

INVESTIGATION OF THE TRIPLE-ALPHA REACTION IN A FULL THREE-BODY
APPROACH

By

Ngoc Bich Nguyen

A DISSERTATION

Submitted to
Michigan State University
in partial fulfillment of the requirements
for the degree of

Physics – Doctor of Philosophy

2013

ABSTRACT

INVESTIGATION OF THE TRIPLE-ALPHA REACTION IN A FULL THREE-BODY APPROACH

By

Ngoc Bich Nguyen

We have developed a new three-body method to compute the triple-alpha reaction rate at low temperatures where measurements are impossible and many numerical attempts have failed before. In this work, the triple-alpha is modeled as a three-body Borromean system in hyperspherical harmonics coordinates. In the low temperature region, the triple-alpha proceeds through a quadrupole transition from the 0^+ continuum to the 2_1^+ bound state in ^{12}C . The 2_1^+ bound state is obtained by solving a set of coupled channels equations in hyper-radius coordinates for negative energy with a boundary condition that requires the wavefunction to go to zero at large distances. The same approach can not be applied to the 0^+ continuum state because it requires an exact boundary condition for the three charged particles. We therefore combine the R-matrix expansion, the R-matrix propagation method, and the screening technique in the hyperspherical harmonics basis to obtain a numerically stable three-body continuum wavefunction for the $\alpha + \alpha + \alpha$ system. We employ the Ali-Bodmer potential for the alpha-alpha interaction which reproduces the low energy phase shifts as well as the 0^+ resonance of ^8Be . We add a three-body force to fit experimental data. Both the 2_1^+ bound state and the 0_2^+ resonant state in ^{12}C are well reproduced in our framework. We find a dominant triangle three-alpha configuration for the Hoyle resonance by studying the density distribution function. The resonant and non-resonant continuum states of $^{12}\text{C}(0^+)$ are obtained simultaneously, allowing us to include these two processes on the same footing. Long range Coulomb interactions show important effects especially in the

low temperature regime. We also present a detailed convergence study of the triple-alpha reaction rate with respect to the screening radius and the size of the model space. The new rate agrees with the NACRE rate for temperatures greater than 0.07 GK, but a large enhancement at lower temperatures is found ($\approx 10^{12}$ at 0.02 GK). We observe a transition between dominance of the non-resonant versus the resonant triple-alpha capture process around 0.06 GK. Our results are then compared to previous calculations where additional approximations were made. We also explore the impact in astrophysics namely, in stellar evolution, helium accreting white dwarfs, and helium accreting neutron stars.

The presence of very narrow two-body and three-body resonances in addition to the strong, long-range Coulomb interaction makes the triple-alpha problem very challenging. Our framework which is the combination of various methods is a new approach to overcome the well known difficulty of the three charged-particle system. This method is particularly suited to the very low energy regime where measurements are impossible. In addition, the method we developed opens new opportunities in addressing three-body, low-energy reactions in other fields (e.g., atomic and molecular physics) where all three particles have charge.

ACKNOWLEDGMENTS

I am heartily thankful to my supervisor, Prof. Filomena Nunes, whose support and guidance have had great impact on both my academic and personal life. I am grateful for her enthusiasm and patience in the beginning of my journey with nuclear reaction theory, her positive attitude and encouragement throughout the years, and her kindness and the care she gave me during difficult times of my life with health issues. I feel very fortunate to have her as my advisor.

I would like to express my gratitude to Prof. Ian Thompson for his expertise on the project and his tremendous help with developing the computer codes. I would like to thank Prof. Edward Brown for many helpful discussions on the astrophysics aspect of the project. Special thanks to my guidance committee members Prof. Pawel Danielewicz, Prof. Hendrik Schatz, Prof. Bhanu Mahanti, Prof. Edward Brown for their comments and helpful suggestions. Their guidance has been invaluable and I owe them my deepest appreciation. I would also like to thank Prof. Vladimir Zelevinsky, who have led me to Nuclear Physics, for his inspiration and excellent lectures. A sincere thank to Prof. Ron Johnson from whom I have learned a lot about reaction theory during his visits.

The Department of Physics and Astronomy at Michigan State University, the National Superconducting Cyclotron Laboratory, and especially the theory group are sincerely acknowledged for providing the financial, academic and technical support, and a great working environment. I would also like to acknowledge the National Science Foundation and the Department of Energy for this support.

I thank my friends and colleagues from Vietnam, United States and other parts of the world for many belated memories we have shared and their company, emotional support

during my long journey. Special thank to my first and current office mate Brent Barker for many sincere conversations, to my dearest friends Seungyun Yook and Winifred Nwaefido for their kindness and great friendship. I would like to thank my group members Neelam Upadhyay, Muslema Pervin and Luke Titus for many good memories and fun time we have together. I also want to thank the Association of Vietnamese Students & Scholars for their strong support and help at the very beginning of my time at Michigan State University.

Last but not least, I am greatly indebted to my family, my parents Chin Nguyen and Duc Nguyen, my sister Nga Nguyen for their unconditional love and support. Without them I would not have been able to make it to this point of my life. My heartfelt thanks are addressed to my husband David Lincoln and his family, especially Lou and Diane Lincoln whose love and encouragement have guided me stepping through all the obstacles of my journey. I hope that this work makes you all proud.

TABLE OF CONTENTS

LIST OF TABLES	ix
LIST OF FIGURES	xi
Chapter 1 Introduction	1
1.1 History of the triple-alpha reaction	1
1.2 The triple-alpha reaction rate and its current status	4
1.3 Three-body reaction methods in solving the triple-alpha problem	11
1.4 Motivation for this work	13
1.5 Outline	13
Chapter 2 The Hyperspherical Harmonics R-matrix (HHR) method	15
2.1 Hyperspherical Harmonics method	15
2.1.1 Hyperspherical coordinates	16
2.1.2 Three-body bound states	18
2.1.2.1 Asymptotic behavior of the three-body Coulomb interaction	21
2.1.3 Three-body continuum states	24
2.1.4 Properties of the three-alpha wavefunction	26
2.2 R-matrix method	29
2.2.1 R-matrix expansion	30
2.2.2 R-matrix propagation	33
2.2.3 Screening technique	39
2.2.4 HHR3a	42
Chapter 3 Three-body reaction rate	45
3.1 Maxwell-Boltzmann energy distribution for a three-body system	46
3.2 The reaction rate formalism for three-body capture	48
3.3 Three-body quadrupole transition function	52
Chapter 4 Results	58
4.1 Interactions	58
4.2 The 2_1^+ bound state	62
4.3 The 0_2^+ Hoyle state	67
4.4 Testing the new code HHR3a	72
4.5 Convergence and uncertainty	74
4.5.1 The impact of using screening potentials	75
4.5.2 Convergence study	78

4.5.3	Interaction uncertainty	83
4.5.4	Rate uncertainty	84
4.6	Rate	87
Chapter 5	Discussion	91
5.1	Comparison with other methods	91
5.2	Long-range Coulomb effects	94
5.3	Reaction dynamics	96
5.4	Astrophysical S-factor	99
Chapter 6	Astrophysics Applications	104
6.1	Evolution of single stars	106
6.2	Binary stars	113
6.2.1	Helium accreting white dwarfs	114
6.2.2	Helium accreting neutron stars	118
Chapter 7	Summary and outlook	121
7.1	Summary	121
7.2	Outlook	124
Appendices		127
Appendix A:	Detailed Derivations of the R-matrix propagation method	128
A.1	Deriving Eq. (2.58)	128
A.2	Deriving Eq. (2.61)	131
A.3	Deriving Eq. (2.63), Eq. (2.64), Eq. (2.65), and Eq. (2.66)	132
Appendix B:	Detailed derivation of the quadrupole transition function	135
B.1	Deriving Eq. (3.32)	135
B.2	Deriving Eq. (3.42)	138
Appendix C:	Inputs for numerical calculations	141
C.1	Bound state calculation	141
C.2	Continuum state calculation	143
Appendix D:	Highlights on the (d,p) reaction projects	145
D.1	Common physical quantities in (d,p) studies	147
D.2	The adiabatic distorted wave approximation	150
D.2.1	Zero-range adiabatic wave approximation (ZR-ADWA)	152
D.2.2	Finite-range adiabatic wave approximation (FR-ADWA)	153
D.3	Finite-range effects in (d,p) reactions	156
D.3.1	Finite-range effects in the potentials	157
D.3.2	Finite-range effects in the transfer cross sections	159
D.4	Testing the dispersive optical model for (d,p) reactions	167
D.4.1	Details of the calculation	168
D.4.2	Transfer cross section	170
D.4.3	Spectroscopic factors	175
D.5	Application of the finite-range adiabatic distorted wave approximation (FR-ADWA)	178

D.6	Conclusion	180
Bibliography	183

LIST OF TABLES

Table 4.1	The three-body interactions to reproduce the experimental energies [69] of the 2_1^+ bound state and 0_2^+ resonant state in ^{12}C	61
Table 4.2	Comparison of the three-body binding energy and the <i>rms</i> radius of the 2_1^+ bound state of ^{12}C obtained from our three-body calculation with other studies: a three-body hyperspherical adiabatic method [26], a microscopic Fermionic Molecular Dynamics method [31] and experimental data [69].	64
Table 4.3	Sources of uncertainty in calculating the triple-alpha reaction rate	86
Table 4.4	Our triple-alpha reaction rate (in $\text{cm}^6\text{s}^{-1}\text{mol}^{-2}$) after being normalized to NACRE for $T \geq 0.5$ GK (the factor of 2 uncertainty is listed for temperature below 0.08 GK above which the triple-alpha rate agrees with NACRE).	88
Table 6.1	Temperature sensitivity of triple-alpha rate	105
Table D.1	The finite-range effects on the deuteron distorting potential are presented as the changes in the diffuseness a_R and a_I of the real and imaginary parts, the depths of the real and imaginary parts V and W_s , as well as the corresponding radii r_R and r_I	158
Table D.2	Finite-range effects in transfer cross sections. Comparisons are performed with respect to the zero-range Johnson and Soper calculation (cases with no existing data are presented by *).	160
Table D.3	Comparison of the DOM overlap function, corrected for non-locality φ_{DOM} with the Woods-Saxon single-particle wavefunction φ_{WS} . In this table we include: n (principal number), ℓ_j (the angular momenta of the valence orbital), S_n (the separation energy), R^{rms} (the root-mean-square radius of the valence orbital), and b_{nlj} (the modulus of the single-particle ANC).	169
Table D.4	Comparison of the spectroscopic factors obtained from the FR-ADWA analysis using different models for optical potentials and overlap functions.	176

Table D.5	ANCs extracted for both the ground state and the first excited state of the $^{14}\text{C}(\text{d},\text{p})^{15}\text{C}$ reaction.	178
-----------	--	-----

LIST OF FIGURES

Figure 1.1	The triple-alpha reaction mechanism: The energy-level diagram of ^{12}C and ^8Be relative to the three-alpha threshold are presented. Two alpha particles combine to form ^8Be which can then capture another alpha particle to produce ^{12}C at the 0_2^+ excited state (or the Hoyle resonance). Here, ^{12}C is likely to decay back into three alpha particles again but it can also decay to the ground state of ^{12}C through two successive gamma ray emissions or the emission of one e^+e^- pair. “For interpretation of the references to color in this and all other figures, the reader is referred to the electronic version of this dissertation.”	3
Figure 1.2	Triple-alpha Jacobi coordinates in CDCC study.	6
Figure 2.1	Three ways to form a Jacobi coordinate set for a system of three particles.	16
Figure 2.2	Coordinates defined for Jacobi set i	16
Figure 2.3	Hyper-radial behavior of the potential couplings $V_{\gamma\gamma'}(\rho)$ in Eq. (2.17). The black solid curve represents the diagonal coupling and the others demonstrate the off-diagonal couplings.	24
Figure 2.4	The hyper-radial scattering wavefunction corresponding to the incoming channel of $K^i l_x^i l_y^i = 000$ and the outgoing channel of $K l_x l_y = 000$ in the hyperspherical expansion (Eq. (2.28)) is calculated at $E = 0.2$ MeV for two different R-matrix box sizes: 50 fm (red) and 100 fm (blue).	34
Figure 2.5	Diagram presenting the sectorization in hyper-radius ρ of the R-matrix propagation method. The subscripts L and R indicate the evaluations at the left and right sector boundary. The R matrix \mathcal{R} of a sector is calculated at the right boundary.	34
Figure 2.6	Schematic diagram of the propagation method in obtaining the three-body scattering wavefunction	37

Figure 2.7	The quadrupole transition strength function $dB(E2)/dE$ is calculated using the global (solid) and local (dashed) representations of the wavefunction propagation method.	39
Figure 2.8	The hyper-radial scattering wavefunction corresponding to the incoming channel of $K^i l_x^i l_y^i = 000$ and the outgoing channel of $K l_x l_y = 000$ in the hyperspherical expansion (Eq. (2.28)) is calculated at $E = 0.5$ MeV for both cases: with screening (red solid) and without screening (blue dashed).	40
Figure 2.9	Relative deviation of the quadrupole transition strength $dB(E2)/dE$ (denoted X in the plot) when diagonal Coulomb screening is introduced.	41
Figure 2.10	Our three-body method is divided into four steps in which we employ the R-matrix expansion, R-matrix propagation and screening technique in Hyperspherical Harmonics coordinates.	42
Figure 4.1	Dependence of the three-body binding energy of the 2_1^+ bound state of ^{12}C on the depth of a three-body force $V_{3b}(\rho) = V_0 e^{-\rho^2/\rho_0^2}$. The maximum hyper-angular momentum K_{max} is taken as 20 for which the results are converged.	60
Figure 4.2	Dependence of the Hoyle resonant energy of ^{12}C on the depth of a three-body force $V_{3b}(\rho) = V_0 e^{-\rho^2/\rho_0^2}$. The maximum hyper-angular momentum K_{max} is taken as 26 for which the results are converged.	61
Figure 4.3	Dependence of the three-body binding energy of the 2_1^+ bound state of ^{12}C on the maximum hyper-angular momentum K_{max}	63
Figure 4.4	Dependence of the r_{rms} radius of the 2_1^+ bound state of ^{12}C on the maximum hyper-angular momentum K_{max}	64
Figure 4.5	The r_{rms} radius as a function of the maximum radius of the box in which the $^{12}\text{C}(2_1^+)$ bound state wavefunction is calculated.	65
Figure 4.6	The density distribution for the 2_1^+ bound state of ^{12}C	66
Figure 4.7	The dominant three-alpha cluster in the $^{12}\text{C}(2_1^+)$ bound state: three alpha particles touch each other and form an equilateral triangle.	66

Figure 4.8	The quadrupole transition strength $dB(E2)/dE$ as a function the three-alpha relative energy E	68
Figure 4.9	The quadrupole transition strength function $dB(E2)/dE$ around the Hoyle resonant energy is calculated with different values of hyper-momentum K_{\max}	69
Figure 4.10	Dependence of the three-body energy of the 0_2^+ Hoyle state of ^{12}C on the maximum hyper-angular momentum K_{\max}	70
Figure 4.11	The density distribution for the 0_2^+ resonance state of ^{12}C	71
Figure 4.12	Three triple-alpha configurations of the 0_2^+ resonance in ^{12}C : the prolate triangle (a), the oblate triangle (b) and the equilateral triangle (c).	71
Figure 4.13	A numerical solution (dashed) of Eq. (2.30) at $E = 0.5$ MeV for the 0^+ scattering wavefunction of the triple-alpha system when only the diagonal Coulomb couplings are taken into account is compared with the analytic solution (solid).	73
Figure 4.14	The triple-alpha reaction rate is computed for the diagonal Coulomb case using the numerical solution of Fig. 4.13 (dashed) and compared to the analytic solution (solid).	74
Figure 4.15	The reaction rate as a function of temperature for the fictitious three-alpha system in which only Coulomb interactions are included: $K_{\max} = 20$ (solid) and $K_{\max} = 26$ (dot-dashed).	75
Figure 4.16	The quadrupole transition strength $dB(E2)/dE$ at $E = 0.01$ MeV as a function of model space K_{\max} when both nuclear and Coulomb interaction (a) and only Coulomb interaction (b) are present in the three-alpha system.	76
Figure 4.17	Relative differences between screening and no screening calculations for the fictitious three-alpha scattering system in which only Coulomb interactions are introduced. The screening calculation is performed for $K_{\max} = 26$ and $\rho_{\text{screen}} = 800$ fm. Calculations without screening are performed for $K_{\max} = 20$ (solid) and $K_{\max} = 26$ (dashed). . . .	77

Figure 4.18	The quadrupole transition strength are computed at low energies using three different values of the diffuseness in screening potentials: $a_{\text{screen}} = 10$ fm (solid), $a_{\text{screen}} = 20$ fm (dashed), $a_{\text{screen}} = 30$ fm (dot-dashed).	79
Figure 4.19	Relative differences between the triple-alpha rate calculated at several screening radii and its converged value. The reaction rates calculated using $\rho_{\text{screen}} = 600$ fm (solid), $\rho_{\text{screen}} = 800$ fm (dashed), $\rho_{\text{screen}} = 1000$ fm (dot-dashed) are compared with the converged rate in Table 4.4.	79
Figure 4.20	Relative differences between the triple-alpha rate calculated at several maximum hyper-momentum K_{max} and its converged value. The reaction rates calculated using $K_{\text{max}} = 20$ (solid), $K_{\text{max}} = 22$ (dashed), $K_{\text{max}} = 24$ (dot-dashed), $K_{\text{max}} = 26$ (dot-dot-dashed) are compared with the converged rate in Table 4.4.	81
Figure 4.21	Convergence of the quadrupole transition strength $dB(E2)/dE$ with hyper-momentum K_{max} for $E = 0.01$ MeV.	81
Figure 4.22	Convergence of the quadrupole transition strength $dB(E2)/dE$ with n_{jac} , number of Gauss-Jacobi quadrature grid point, for a given low energy of 0.01 MeV	82
Figure 4.23	Convergence of the quadrupole transition strength $dB(E2)/dE$ with matching radius ρ_a for a given low energy of 0.01 MeV	83
Figure 4.24	The sensitivity of the triple-alpha rate to the interactions: comparison between $\alpha - \alpha$ Ali-Bodmer+3-body force (solid) and $\alpha - \alpha$ interaction as in [15]+3-body force (dashed)	85
Figure 4.25	The photo-disintegration cross section is fitted to the Breit-Wigner shape to obtained the gamma decay width.	87
Figure 4.26	The integrand $f(E)$ and its energy cumulative sum $Sm(E)$ at a very low temperature of 0.01 GK	89
Figure 4.27	The integrand $f(E)$ and its energy cumulative sum $Sm(E)$ at $T = 0.1$ GK	89
Figure 4.28	Range of energy relevant for the triple-alpha reaction rate at a given temperature.	90

Figure 5.1	Different evaluations of the triple-alpha reaction rate: comparing the Hyperspherical Harmonic R-matrix method (solid) with NACRE (dotted), CDCC (dashed) and the three-body Breit Wigner (dot-dashed).	92
Figure 5.2	The triple-alpha reaction rate: comparing the Hyperspherical Harmonic R-matrix method (solid) with NACRE (dotted), Fynbo (dashed), and CF88 (dot-dashed).	94
Figure 5.3	The long-range Coulomb effects are shown in four different calculations: only diagonal Coulomb couplings (dotted), only Coulomb couplings (dot-dashed), both nuclear and Coulomb interactions with off-diagonal Coulomb couplings up to 30 fm (dashed) and a fully converged calculation with off-diagonal Coulomb couplings up to 800 fm (solid)	95
Figure 5.4	Spatial distribution of function $f_{\gamma^i}(r, R)$ for $E = 0.05$ MeV and $\gamma^i = \{0, 0, 0\}$	97
Figure 5.5	Spatial distribution of function $f_{\gamma^i}(r, R)$ for $E = 0.38$ MeV and $\gamma^i = \{0, 0, 0\}$	97
Figure 5.6	Spatial distribution of function $f_{\gamma^i}(r, R)$ for $E = 0.5$ MeV $\gamma^i = \{0, 0, 0\}$	98
Figure 5.7	Fitting $E_{\gamma}^2 \sigma_{\gamma}$ to an exponential behavior $A e^{\frac{-2\pi B}{\sqrt{E}}}$ for energies below the resonance.	100
Figure 5.8	Comparison between the energy dependence of the cross section σ_{γ} and the three-body astrophysical S-factor S_{3b}	101
Figure 5.9	Comparison between the energy dependence of the cross section σ_{γ} and the astrophysical S-factor S_0 for $K_{\max} = 0$	102
Figure 6.1	Temperature dependence for the HHR rate (solid) and the NACRE rate (dashed).	105
Figure 6.2	Standard evolution curve of $1M_{\odot}$ stars (surface luminosity as a function of surface temperature): 1 - main sequence, 2 - red giant, 3 - core helium flashes, 4 - thermal pulses, 5 - planetary nebula, and 6 - white dwarf.	107

Figure 6.3	Full evolutionary track (luminosity vs. surface temperature) from main sequence to white dwarf of a one solar-mass ($1M_{\odot}$) star for HHR (solid), NACRE (dashed), Fynbo (dotted), and CF88 (dot-dashed).	110
Figure 6.4	Evolutionary track (luminosity vs. surface temperature) from main sequence to the end of asymptotic giant branch of a one solar-mass ($1M_{\odot}$) star for HHR (solid), NACRE (dashed), Fynbo (dotted), and CF88 (dot-dashed).	110
Figure 6.5	Surface luminosity as a function of age: HHR rate (solid) and NACRE rate (dashed).	112
Figure 6.6	Full evolutionary track (luminosity vs. surface temperature) from main sequence to white dwarf of a 0.8 solar-mass ($0.8M_{\odot}$) star for the HHR rate (solid) and the NACRE rate (dashed).	113
Figure 6.7	Binary system and its Roche lobes	113
Figure 6.8	Helium ignition curves for the NACRE rate (blue solid) and the HHR rate (red dashed). Calculations are performed for helium accreting white dwarf with initial mass of $1M_{\odot}$ and several values of accretion rate.	116
Figure 6.9	Helium ignition curves for the NACRE rate (blue solid) and the HHR rate (red dashed). Calculations are performed for helium accreting white dwarf with the accretion rate of $5 \times 10^{-10} M_{\odot} \text{ yr}^{-1}$ and two different initial masses: $0.734M_{\odot}$ and $1.315M_{\odot}$.	117
Figure 6.10	The light curve (luminosity vs. time) for helium accreting a neutron star at accretion rate of $1.75 \times 10^{-10} M_{\odot} \text{ yr}^{-1}$: Comparing the CF88 rate (dashed) and the HHR rate (solid).	119
Figure D.1	(d,p) transfer reaction: (a) incoming channel, (b) outgoing channel	151
Figure D.2	Finite-range effects in sub-Coulomb (d,p) reactions: (a) $^{48}\text{Ca}(d,p)^{49}\text{Ca}(\text{g.s.})$ $E_d = 2$ MeV (data from [124]) and (b) $^{208}\text{Pb}(d,p)^{209}\text{Pb}(\text{g.s.})$ $E_d = 8$ MeV (data from [125]).	163
Figure D.3	Finite-range effects in (d,p) reactions at energies slightly above the Coulomb barrier: (a) $^{86}\text{Kr}(d,p)^{87}\text{Kr}(\text{g.s.})$ $E_d = 11$ MeV (data from [126]) and (b) $^{208}\text{Pb}(d,p)^{209}\text{Pb}(\text{g.s.})$ $E_d = 20$ MeV (data from [127]).	164

Figure D.4	Finite-range effects in (d,p) reactions at high energies: (a) $^{12}\text{C}(\text{d,p})^{13}\text{C}(\text{g.s.})$ $E_d = 56$ MeV (data from [128]) and (b) $^{48}\text{Ca}(\text{d,p})^{49}\text{Ca}(\text{g.s.})$ $E_d = 56$ MeV (data from [129]).	165
Figure D.5	Systematic finite-range effect as a function of beam energy. The effect from the adiabatic potentials is presented as open symbols while that from the evaluation of the matrix elements is plotted as filled symbols.	166
Figure D.6	The square of the single-neutron overlap functions in the Woods-Saxon (solid) and the DOM (dashed) model are compared for ^{49}Ca .	170
Figure D.7	DOM and CH89 optical potentials are compared for n- ^{132}Sn and p- ^{132}Sn at 4.7 MeV: (a) the real part and (b) the imaginary part.	171
Figure D.8	$^{48}\text{Ca}(\text{d,p})^{49}\text{Ca}$ at $E_d = 2$ MeV (angular distributions are normalized to the data at backward angles).	172
Figure D.9	$^{48}\text{Ca}(\text{d,p})^{49}\text{Ca}$ at $E_d = 19.3$ MeV (angular distributions are normalized to the data at the peak).	173
Figure D.10	$^{48}\text{Ca}(\text{d,p})^{49}\text{Ca}$ at $E_d = 56$ MeV (angular distributions are normalized to the data at forward angles).	173
Figure D.11	$^{132}\text{Sn}(\text{d,p})^{133}\text{Sn}$ at $E_d = 9.46$ MeV (angular distributions are normalized at the peak of the experimental cross section).	174
Figure D.12	$^{208}\text{Pb}(\text{d,p})^{209}\text{Pb}$ at $E_d = 20$ MeV (angular distributions are normalized at the peak of the experimental data).	174
Figure D.13	$^{208}\text{Pb}(\text{d,p})^{209}\text{Pb}$ at $E_d = 8$ MeV (angular distributions are normalized at the peak of the experimental data).	177
Figure D.14	Angular distribution for the ground state in the $^{14}\text{C}(\text{d,p})^{15}\text{C}$ reaction.	179

Chapter 1

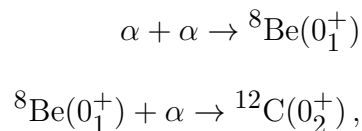
Introduction

1.1 History of the triple-alpha reaction

In the early 1950s, physicists were puzzled by the mystery of nucleosynthesis beyond mass 8 since stable isotopes of mass number 5 and 8 can not be found in nature. To explain the puzzle, Salpeter proposed the theory that stable ^{12}C is formed by alpha capture on ^8Be in equilibrium, and heavier nuclei are then synthesized from ^{12}C [1]. In his theory, two alpha particles first fuse to create an intermediate particle ^8Be which is unstable by only 92 keV against alpha decay. The ground state of ^8Be has a very short lifetime of 2.6×10^{-16} sec which corresponds to a narrow resonance with a width of 2.5 eV [2]. Although short, this lifetime is sufficient for a small amount of ^8Be in equilibrium to build up. For every 10^9 alpha particles, one finds approximately 1 ^8Be nucleus [3]. This modest concentration of ^8Be can then capture another alpha particle to form ^{12}C . However, the corresponding reaction rate was too small to account for the observed abundances of ^{12}C in stars. Because both ^4He and ^8Be nuclei have total spins $J^\pi = 0^+$, the alpha capture on ^8Be would highly increase its rate if the reaction could proceed through a ^{12}C s-wave resonance. Based on that argument,

Fred Hoyle predicted the existence of a 0^+ resonance in the ^{12}C energy spectrum, near the three-alpha threshold, to significantly enhance the reaction rate [4]. This resonant state and its properties were confirmed by experimentalists [5, 6] shortly thereafter. The resonance was then named after Hoyle and located as a second excited state of ^{12}C at 0.38 MeV above the three-alpha threshold. Fig. 1.1 illustrates the energy-level diagram of ^{12}C and ^8Be relative to the three-alpha threshold. The Hoyle resonant state may sequentially decay back into three alpha particles through the intermediate step of the ^8Be ground state. It may also deexcite to the ground state of ^{12}C through two successive gamma ray emissions. While direct decay to the ground state of ^{12}C through a photon emission is forbidden by angular momentum conservation, an emission of a e^+e^- pair is possible. The probability for the photon decay from the Hoyle resonant state to the ground state is much smaller than the probability of three-alpha breakup but significantly larger than the e^+e^- pair decay [6]. A large amount of ^{12}C could therefore be produced in stars through this mechanism.

Thus, the two-step (sequential) mechanism of the triple-alpha capture,



was accepted to explain the mystery of nucleosynthesis and the abundances of ^{12}C in helium burning stars. The capture probability is highly enhanced by the narrow resonances of ^8Be and ^{12}C . The accuracy of this helium burning rate has a big impact on the late stages of stellar evolution. It was shown that there is a strong dependence between the triple-alpha reaction rate and the production of nuclei ^{26}Al , ^{44}Ti , ^{60}Fe in supernova explosions [7]. Over the range of twice its experimental uncertainty ($\sim 12\%$), one finds that the production of

1.2 The triple-alpha reaction rate and its current status

In order for the triple-alpha reaction to happen as a two step process, the stellar environment temperature must be high enough so the alpha particles can reach the resonant energies. At low temperatures, we expect the three-alpha direct capture to become dominant. Even though the current experimental uncertainty of the triple-alpha resonant rate is 12% [7], the theory of this process is well established. The first evaluation of the triple-alpha resonant reaction rate was credited to Caughlan and Fowler [8] in which a Breit-Wigner shape [9] for the two-body resonant cross sections of α - α and α - ^8Be was used:

$$\sigma_{BW}(E) = \frac{\pi}{k^2} \frac{(2J+1)(1+\delta_{12})}{(2j_1+1)(2j_2+1)} \frac{\Gamma_i(E)\Gamma_f(E)}{(E-E_r)^2 + \Gamma(E)^2/4}. \quad (1.1)$$

In Eq. (1.1), the momentum k and the energy E of the two-body system are related by $k = \sqrt{2\mu E}/\hbar$, where μ is the reduced mass of the two particles and \hbar is the Planck constant. j_i are the spins of projectile and target, and J is the spin of the resonance. The Kronecker delta δ_{12} accounts for identical particles in the entrance channel. Γ_i (Γ_f) is the resonance partial width of the entrance (exit) channel, Γ is the total resonance width, and E_r is the resonant energy. The triple-alpha reaction rate was calculated in two steps, through the formation of the intermediate $^8\text{Be}(0_1^+)$ resonance. One first evaluates the reaction rate for alpha capture by ^8Be by integrating the α - ^8Be cross section over its corresponding Maxwell-Boltzmann distribution:

$$N_A \langle \sigma v \rangle^{\alpha^8\text{Be}} = N_A \frac{8\pi}{\mu_{\alpha^8\text{Be}}^2} \left(\frac{\mu_{\alpha^8\text{Be}}}{2\pi k_B T} \right)^{3/2} \int_0^\infty \sigma_{\alpha^8\text{Be}}(E'; E) e^{-\frac{E'}{k_B T}} E' dE', \quad (1.2)$$

where E and E' are the energies of α - α and α - ^8Be systems, respectively; k_B is the Boltzmann constant and T is the temperature at which the triple-alpha reaction rate is evaluated. The triple-alpha reaction rate is then calculated by the Maxwell-Boltzmann averaging of the α - ^8Be capture rate weighted with the α - α fusion cross section which is proportional to the probability of the ^8Be formation:

$$N_A^2 \langle \sigma v \rangle^{\alpha\alpha\alpha} = 3N_A \frac{8\pi\hbar}{\mu_{\alpha\alpha}^2} \left(\frac{\mu_{\alpha\alpha}}{2\pi k_B T} \right)^{3/2} \int_0^\infty \frac{\sigma_{\alpha\alpha}(E)}{\Gamma_\alpha(^8\text{Be}, E)} e^{-\frac{E}{k_B T}} N_A \langle \sigma v \rangle^{\alpha^8\text{Be}} E \, dE. \quad (1.3)$$

Eq. (1.3) clearly indicates the sequential mechanism of the triple-alpha reaction used in this theory. It is important to note that Caughlan and Fowler considered only the Hoyle resonance when calculating the triple-alpha reaction rate. Ten years later, this reaction rate was improved by Angulo [10] when taking into account the contribution of the 2_2^+ resonance. Astrophysicists refer to this new rate as the NACRE (Nuclear Astrophysics Compilation of Reaction Rate) reaction rate. The $^{12}\text{C}(2_2^+)$ resonance contributes significantly to the triple-alpha rate at $T > 1$ GK but has little impact at low temperatures [11]. Uncertainties in the properties of this 2_2^+ state have been recently addressed [12]. The work in [13] found a 0_3^+ broad resonance around 3 MeV above the three-alpha threshold that does not influence the rate at $T \sim 0.1$ GK and is much less dominant than the 2_2^+ resonance at $T \sim 1$ GK. These high lying resonances leads to variation of the triple-alpha rate in [8], [10] and [13]. Throughout this work we will use NACRE [10] as our reference, but comparisons with other rates [8, 13] are presented in [14]. It is important to note that none of these resonances contribute to the triple-alpha rate at low temperatures where the measurements are impossible. To determine the rate at $T < 0.1$ GK, a well founded theory for the three-alpha direct (non-resonant) capture is crucial.

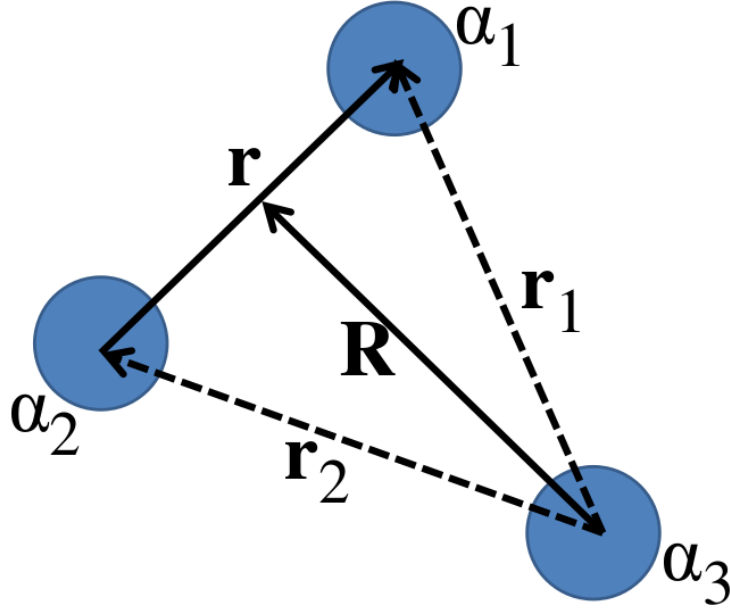


Figure 1.2: Triple-alpha Jacobi coordinates in CDCC study.

The non-resonant triple-alpha rate tabulated in NACRE is obtained by a simple extrapolation to low energies using the tail of the Breit-Wigner cross sections in the sequential model as in Eq. (1.3) and Eq. (1.2). The validity of this approach is doubtful since at low energy the three alpha particles do not have access to the intermediate resonances. The question of how much the direct capture process contributes to the triple-alpha rate at low temperature was not addressed in [10]. Ogata *et al.* [15] was the first group who attempted to tackle this problem without using an ambiguous extrapolation. In order to describe the three-alpha system, they used the Jacobi coordinates \mathbf{r} and \mathbf{R} as shown in Fig. 1.2, which represent the relative radius between α_1 and α_2 and the distance from their center of mass to α_3 , respectively. In their studies, the continuum discretized coupled channel (CDCC) method [16, 17] was employed to solve a three-body scattering equation:

$$[T_{\mathbf{r}} + T_{\mathbf{R}} + v(r) + v(r_1) + v(r_2) - E]\Psi(\mathbf{r}, \mathbf{R}) = 0, \quad (1.4)$$

where E is the total relative energy of the three alpha system, $T_{\mathbf{r}}$ and $T_{\mathbf{R}}$ are the kinetic operators and v is the alpha-alpha potential. The continuum states of the α_1 - α_2 subsystem were first discretized into momentum bins $[k_i, k_{i+1}]$ with corresponding bin wavefunctions $\hat{u}_i(r)$:

$$\hat{u}_i(r) = \int_{k_i}^{k_{i+1}} f_i(k) u(k, r) dk / \left[\int_{k_i}^{k_{i+1}} |f_i(k)|^2 dk \right]^{1/2}, \quad (1.5)$$

where the two-body scattering wavefunction $u(k, r)$ is averaged over the momentum bin $[k_i, k_{i+1}]$ using the weight function $f_i(k)$. The bin wavefunctions $\hat{u}_i(r)$ form a discrete orthonormal basis $\int \hat{u}_i^*(r) \hat{u}_j(r) dr = \delta_{ij}$. The total three-body wavefunction $\Psi(r, R)$ was then expanded in terms of the products between the bin wavefunction of the ${}^8\text{Be}$ continuum states and its relative motion with respect to the third alpha particle:

$$\Psi_{\hat{k}_{i_0}, E}^{0+}(r, R) = \sqrt{\frac{2}{\pi}} \frac{1}{32\pi^2} \frac{1}{\hat{k}_{i_0} \hat{K}_{i_0}} \sum_{i=1}^{i_{\max}} \frac{\hat{u}_i(r)}{r} \frac{\hat{\chi}_i^{(i_0)}(R)}{R}. \quad (1.6)$$

In Eq. (1.6) the bin wavefunction $\hat{u}_i(r)$ describes the α_1 - α_2 continuum while $\hat{\chi}_i^{(i_0)}(R)$ describes the motion of momentum bin $\hat{u}_i(r)$ relative to α_3 . The subscript i_0 indicates the incident channel, \hat{k} is the average bin momentum of the α_1 - α_2 subsystem corresponding to the average bin energy $\hat{\varepsilon}_{12}$, and \hat{K} is the relative momentum between the continuum bin and the third alpha. Using the above wavefunction decomposition technique, the three-body Schrodinger equation becomes a set of coupled channels equations:

$$[T_R + V_{ii}(R) - (E - \hat{\varepsilon}_{12, i})] \hat{\chi}_i^{(i_0)}(R) = - \sum_{i' \neq i} V_{ii'}(R) \hat{\chi}_{i'}^{(i_0)}(R). \quad (1.7)$$

The coupling potential $V_{ii'}(R)$ is defined as:

$$V_{ii'}(R) = \left\langle \frac{\hat{u}_i(r)}{r} |v(r_1) + v(r_2)| \frac{\hat{u}_{i'}(r)}{r} \right\rangle_r. \quad (1.8)$$

In [15], the authors considered the quadrupole transition from the 0^+ continuum states to the 2_1^+ bound state of ^{12}C to be the main contribution to the triple-alpha reaction rate. They adopted a microscopic 2_1^+ bound state wavefunction [18, 19] while numerically solving Eq. (1.7) to obtain a description for the $^{12}\text{C}(0^+)$ continuum states and from there constructed the triple-alpha reaction rate. The advantage of this method was that both the resonant and the non-resonant processes are treated on the same footing. However, the presence of the long-range Coulomb potentials made it a challenging problem since the truncated CDCC wavefunction generally does not have the correct asymptotic form for the scattering of three charged particles [20]. The CDCC results differ from NACRE by 20 orders of magnitude at $T = 0.02$ GK. Ogata *et al.* [15] explained that the Coulomb barrier between the two-alpha subsystem and the third alpha particle is very much quenched at low energies, making the non-resonant capture process dominant and enhancing the reaction rate at low temperatures. Such drastic enhancement of the triple-alpha reaction rate can significantly affect astrophysics. For example, when using the CDCC rate to study the evolution of low and intermediate mass stars, the red giant phase is strongly suppressed or disappears [21, 22], which is incompatible with observation. Also, the studies of He ignition in accreting white dwarfs [23] and accreting neutron stars [24, 25] show that the CDCC rate is barely consistent with the observations of type Ia supernovae and type I X-ray bursts, respectively.

Another attempt to solve the triple-alpha problem was made by the Madrid-Aarhus collaboration [26, 27]. The idea of their work is to solve the Faddeev equations in coordinate

space using the adiabatic hyperspherical expansion method. The hyperspherical coordinates which consist of one radial coordinate ρ and five generalized angles denoted by Ω were adopted in their studies (details on the hyperspherical coordinates will be presented in chapter 2) for an adiabatic expansion of the wavefunction:

$$\Psi^{JM} = \frac{1}{\rho^{5/2}} \sum_n f_n(\rho) \Phi_n^{JM}(\rho, \Omega). \quad (1.9)$$

Here, the expansion coefficient $f_n(\rho)$ is hyper-radial dependent. $\Phi_n^{JM}(\rho, \Omega)$ is the solution of an eigenvalue problem with respect to the five dimensional spin-angular part of the Faddeev operator when considering ρ to be invariant:

$$(T_\Omega - \lambda_n) \Phi_{n,(i)}^{JM} + \frac{2m}{\hbar^2} \rho^2 V_i \Phi_n^{JM} = 0, \quad (1.10)$$

$$\Phi_n^{JM} = \Phi_{n,(1)}^{JM} + \Phi_{n,(2)}^{JM} + \Phi_{n,(3)}^{JM}. \quad (1.11)$$

The index i in $\Phi_{n,(i)}^{JM}$ represents one of the three Jacobi coordinates in the Faddeev representation. T_Ω is the angular part of the kinetic operator and V_i is the two-body interaction in Jacobi i in the Faddeev representation. The eigenvalues λ_n and the eigenfunction Φ_n^{JM} are hyper-radial ρ dependent. A set of coupled channels equations arising from the adiabatic hyperspherical expansion of the wavefunctions is then solved to obtain different states in ^{12}C . The results are used to compute the triple-alpha reaction rate. According to their studies, the formation of ^{12}C from three alpha particles can happen in several paths. At temperatures below 1 GK the quadrupole transition from the 0^+ continuum (both resonant and non-resonant) states to the 2_1^+ bound state dominates. However, contribution from the $2^+ \rightarrow 0_1^+$ transition increases and begins to be dominant at $T \approx 2.5$ GK. Other transi-

tions from the 2^+ continuum states to the 2_1^+ bound state do not contribute significantly to the rate for all temperatures. Although the triple-alpha reaction rate agrees well with what is obtained in NACRE for $T > 0.1$ GK, below that it is not computable due to the numerical limitation of the implementation in [26, 27]. Therefore, in order to estimate the direct triple-alpha rate at low temperatures assuming it captures to the tail of the Hoyle state directly, Garrido *et al.* extrapolated a three-body Breit-Wigner cross section for the three-alpha capture to low energies [28] in a similar manner as done in the sequential process [10]. The reaction rate from that work (named as BW(3B)) shows an increase of 7 orders of magnitude at $T = 0.02$ GK compared to NACRE due to the three-alpha direct capture. There are large discrepancies in the results of [10], [15] and [28], demonstrating uncertainties and ambiguities in our understanding of the low-temperature triple-alpha reaction. We want to develop a theory that provides a better description of the $\alpha + \alpha + \alpha$ system with the correct Coulomb asymptotic behavior, thereby enabling us to compute the reaction rate at very low temperatures without extrapolation. It is demonstrated in chapter 6 of this thesis that the low-temperature triple-alpha rate plays important role in several astrophysical scenarios such as helium accreting white dwarfs and helium accreting neutron stars. We find that the triple-alpha reaction rate at low temperatures dictates the helium ignition on the surface of these objects for very low accretion rates. Since the triple-alpha reaction rate is impossible to measure at low temperatures and can have dramatic effects in astrophysics, a well founded theory is critical.

1.3 Three-body reaction methods in solving the triple-alpha problem

At low temperature, the triple-alpha reaction proceeds through the 0^+ continuum states to the 2_1^+ bound state, which then fully deexcites to form ^{12}C at ground state. In order to construct a reliable non-resonant reaction rate, we need a good description of both 2_1^+ bound states and 0^+ continuum states of ^{12}C . Recent microscopic theories such as the no-core shell model [29] and the Green's function Monte Carlo method [30] struggle to reproduce the Hoyle state of ^{12}C by solving the 12-body problem. Even though the fermionic molecular dynamics method produces both the 2_1^+ bound state as well as the 0_2^+ resonance with significant triple-alpha configurations [31], a microscopic description for the non-resonant continuum states is currently not available. Given the dominant triple-alpha structure in both $^{12}\text{C}(2_1^+)$ and $^{12}\text{C}(0_2^+)$, it is reasonable to construct this as a three-body problem as done in [15, 26, 27].

The three-body problem is an important topic not only in nuclear physics but also in atomic and molecular physics. The first three-body problem was studied for a three-nucleon system with no Coulomb interactions in a formalism invented by Faddeev [32]. With Coulomb interactions present, the problem became much more complicated. Theories for the three-body problem have made significant progress over the last few decades. An accurate solution for a three-body bound state system can now be obtained (e.g. [33]). However, there are still difficulties remaining for a three-body scattering problem because no standard boundary condition for this system exist when including the long-range effects of the Coulomb interaction. Some efforts have been made to solve this problem by using an approximate boundary condition formulated by Merkuriev [34], but the results were limited

to p - d scattering systems [35]. Deltuva *et al.* [36] have developed a screening and renormalization technique for Coulomb interactions in momentum space which can solve a three-body scattering problem but for cases where only one pair of particles have charge [36]. Our triple-alpha problem is more difficult since all three particles are charged.

In this work, we employ the hyperspherical harmonics (HH) method [33, 37, 38] to tackle the triple-alpha problem. The HH method is excellent to reproduce the 2_1^+ bound state of ^{12}C . However, applying it directly to calculate the 0^+ continuum states of ^{12}C is more challenging due to the strong Coulomb interaction that governs the system at large distances. Despite that difficulty, using hyperspherical coordinates offers a natural way to express the asymptotic form for the scattering of this three charged-particle system [20]. We combine the HH method with the R-matrix method and R-matrix propagation (the new method is named HHR) to compute the 0^+ continuum states of ^{12}C . We also implement a technique of screening the off-diagonal Coulomb couplings to ensure numerical stability at very low energies. The scattering wavefunctions for the triple-alpha system are constructed with the correct Coulomb asymptotic behavior. Since the resonant and the non-resonant continuum states come naturally from the solutions of the HHR equations, we are able to treat both resonant and non-resonant, and direct and sequential capture mechanisms on the same footing. The HHR method enables us to obtain numerically stable solutions at low energies and therefore successfully obtain the triple-alpha reaction rate in the low temperature regime where many attempts have failed before.

1.4 Motivation for this work

The triple-alpha reaction has a long history of investigation and is still a current topic of interest because it plays a very important role in many astrophysical processes. Although the theory for the triple-alpha reaction at high-temperatures is well established, our current knowledge for the low temperature regime is very uncertain and ambiguous as seen through the large deviation among [10], [15] and [28]. The aim of this work is to resolve this problem by developing a three-body framework that provides an accurate description of the $\alpha + \alpha + \alpha$ scattering at low temperatures with the correct Coulomb asymptotic behavior. The non-resonant capture mechanism is therefore taken into account naturally without any extrapolation and the role of the non-resonant continuum in the triple-alpha rate will be clarified.

1.5 Outline

In this work we develop a new three-body method for solving the triple-alpha problem. Details on the hyperspherical harmonics R-matrix method are presented in chapter 2. The hyperspherical coordinates will be defined. The R-matrix expansion and the R-matrix propagation method in the hyperspherical harmonic (HH) representation are introduced to tackle the difficulty of three charged particles in the asymptotic region. We also discuss the screening technique for the off-diagonal Coulomb couplings to ensure the numerical stability of the problem at low energies. The three-body quadrupole strength function and the reaction rate formalism are derived in chapter 3. In chapter 4 we present the main results of this work which include a thorough convergence study of the problem, a closer look at the cluster structure of the 2_1^+ bound state and the 0_2^+ Hoyle resonant state of ^{12}C , and the new triple-

alpha reaction rate in which both the resonant and the non-resonant capture mechanisms are naturally taken into account. We then discuss the reaction dynamics of the triple-alpha problem in chapter 5. In this chapter we want to understand the effect of long-range Coulomb effects on the reaction rate at low temperatures as well as the dynamics of the three alpha particles at low energy when intermediate resonances are impossible. We also compare our rate with other studies. In chapter 6 we focus on astrophysics, exploring the impact of the new rate on stars, helium accreting white dwarfs, and helium accreting neutron stars. Will it produce drastic changes as the rate in [15]? The summary of our work and conclusions are drawn in chapter 7.

Chapter 2

The Hyperspherical Harmonics

R-matrix (HHR) method

2.1 Hyperspherical Harmonics method

The hyperspherical harmonics (HH) method originated in atomic and molecular physics [39, 40]. Later, it was extended to few-body systems in nuclear physics by Delves [41, 42]. The theory of the HH method was well developed for Borromean systems [43, 44, 45]. Borromean nuclei are defined as systems of three particles which are loosely bound and have no bound states in any of the two-body subsystems. ^{11}Li and ^6He which have two neutron weakly coupled to the core, are typical examples of Borromean nuclei. In this work, we formulate our problem as a Borromean system of three alpha particles. Many details on the HH method can be found in the literature (e.g., [33], [37], [38]). In the current chapter we will present an overview of the method.

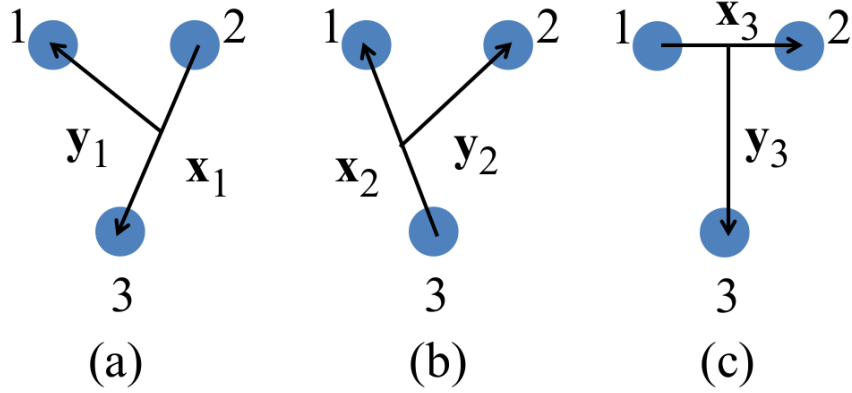


Figure 2.1: Three ways to form a Jacobi coordinate set for a system of three particles.

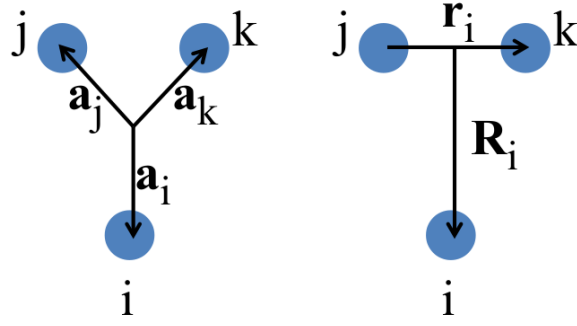


Figure 2.2: Coordinates defined for Jacobi set i

2.1.1 Hyperspherical coordinates

Let us consider a system of three nuclei with masses m_i . For a three-body system there are three ways to form a Jacobi coordinate set $(\mathbf{x}_i, \mathbf{y}_i)$ as presented in Fig. 2.1. For each Jacobi set i , we define the scaled coordinates (see Fig. 2.2):

$$\begin{aligned} \mathbf{x}_i &= \sqrt{\frac{A_j A_k}{A_j + A_k}} \mathbf{r}_i, \\ \mathbf{y}_i &= \sqrt{\frac{A_i (A_j + A_k)}{A_i + A_j + A_k}} \mathbf{R}_i. \end{aligned} \quad (2.1)$$

Here, $\mathbf{r}_i = \mathbf{a}_k - \mathbf{a}_j$ is the relative radius from particle j to particle k and $\mathbf{R}_i = \mathbf{a}_{jk}^{\text{cm}} - \mathbf{a}_i$ is the radius from particle i to the center of mass of the two-body subsystem (jk) . The ratios

$A_i = m_i/m$ are dimensionless and the scaled mass m is usually taken as the nucleon mass.

The hyperspherical coordinates are then defined as functions of x_i and y_i :

$$\begin{aligned}\rho^2 &= x_i^2 + y_i^2, \\ \theta_i &= \arctan \frac{x_i}{y_i}.\end{aligned}\tag{2.2}$$

The hyper-radius ρ is universal in all three Jacobi coordinates. It does not change under translations, rotations, and permutations and therefore provides information about the size of the system:

$$r_{rms}^2 = \frac{\sum_i A_i r_{rms}^2(i)}{A} + \frac{1}{A} \langle \rho^2 \rangle,\tag{2.3}$$

where $A = A_i + A_j + A_k$; r_{rms} and $r_{rms}(i)$ are the root-mean-square (*rms*) radius of the system and particle i , respectively.

The hyper-angle θ_i depends on the selected Jacobi set, containing some insights about the configuration of the system. For example, $\theta_3 \approx 0$ tells us that particle 1 and 2 are much closer to each other than to particle 3. If $\theta_3 \approx \pi/2$, we could say that particle 1 and 2 are very far apart and particle 3 lie between them. For the triple-alpha problem in which three particles are identical, all the Jacobi sets are equivalent, we choose to work with Jacobi set $i = 3$ and drop the index i in our equations from now on for convenience. The scaled coordinates x and y can be reexpressed in terms of the hyperspherical coordinates as

$$\begin{aligned}x &= \rho \sin\theta, \\ y &= \rho \cos\theta.\end{aligned}\tag{2.4}$$

2.1.2 Three-body bound states

In this section we describe a three-body bound system in the hyperspherical harmonics representation. Since the triple-alpha involves only spin-zero particles, all the equations in HH coordinates take this into account because the equations are reduced to much simpler forms. The general case of non-zero spin particles is presented with details in Chapter 9 of [46].

We first write down the three-body Schrodinger equation in the scaled Jacobi coordinates:

$$H_{3b} \Psi^{LM} = [T + V] \Psi^{LM} = E \Psi^{LM}, \quad (2.5)$$

$$T = -\frac{\hbar^2}{2m} [\Delta_{\mathbf{x}}^2 + \Delta_{\mathbf{y}}^2], \quad (2.6)$$

$$V = \sum_{j>i=1}^3 V_{ij} + V_{3b}, \quad (2.7)$$

where, E is the three-body relative energy which is negative for a bound system and positive for a scattering system; m is the scaled mass; \hbar is the Planck's constant. The three-body Hamiltonian H_{3b} is the sum of the kinetic operator T and the potential V . The three-body wavefunction Ψ^{LM} describes a state of total spin and angular momentum L and its projection M .

The hyperspherical expansion separates the radial and angular dependence of the three-body wavefunction. For a bound state, the expansion has the following form:

$$\Psi^{LM} = \rho^{-\frac{5}{2}} \sum_{Kl_xl_y} \chi_{Kl_xl_y}^L(\rho) \varphi_K^{l_xl_y}(\theta) [Y_{l_x} \otimes Y_{l_y}]_{LM}, \quad (2.8)$$

where $\rho^{-5/2}$ cancels out the factor ρ^5 in the volume element $dV = \rho^5 \sin^2\theta \cos^2\theta d\rho d\theta d\Omega_x d\Omega_y$ to simplify the normalization condition of a three-body bound state wavefunction:

$$\int |\Psi^{LM}(\rho, \theta, \hat{\mathbf{x}}, \hat{\mathbf{y}})|^2 dV = \int \sum_{Kl_xl_y} |\chi_{Kl_xl_y}^L(\rho)|^2 d\rho = 1 \quad (2.9)$$

From now on we will drop the L notation in the hyper-radial wavefunction $\chi_{Kl_xl_y}^L(\rho)$ for convenience. Eq. (2.8) is written for the case of zero-spin particles as we discussed above (a more general formula can be found in [37]). $\chi_{Kl_xl_y}(\rho)$, $\varphi_K^{l_xl_y}(\theta)$ and Y are the hyper-radial functions, the hyper-angular functions, and the spherical harmonics functions respectively; l_x and l_y are the orbital angular momenta corresponding to the Jacobi coordinates x and y . This expansion introduces a new quantum number, the hyper-momentum K , an extended concept of angular momentum for a three-body system.

We use the definition of hyperspherical coordinates Eq. (2.4) and the hyperspherical wavefunction expansion Eq. (2.8) to rewrite the kinetic energy in Eq. (2.6) in terms of the hyperspherical variables ρ and θ :

$$T = -\frac{\hbar^2}{2m} \left[\frac{1}{\rho^5} \frac{\partial}{\partial \rho} \left(\rho^5 \frac{\partial}{\partial \rho} \right) + \frac{1}{\rho^2} \Lambda^2 \right], \quad (2.10)$$

$$\Lambda^2 = \frac{1}{\sin^2 2\theta} \frac{\partial}{\partial \theta} \left(\sin^2 2\theta \frac{\partial}{\partial \theta} \right) - \frac{l_x(l_x + 1)}{\sin^2 \theta} - \frac{l_y(l_y + 1)}{\cos^2 \theta}. \quad (2.11)$$

The hyper-angle operator Λ^2 has its eigenvalues as a function of hyper-momentum K and its eigensolutions being the hyper-angular functions $\varphi_K^{l_xl_y}(\theta)$:

$$\Lambda^2 \varphi_K^{l_xl_y}(\theta) = -K(K + 4) \varphi_K^{l_xl_y}(\theta). \quad (2.12)$$

These eigensolutions can be written in terms of Jacobi polynomials $P_n^{l_x+1/2, l_y+1/2}(\cos 2\theta)$:

$$\varphi_K^{l_x l_y}(\theta) = N_K^{l_x l_y} (\sin \theta)^{l_x} (\cos \theta)^{l_y} P_n^{l_x+1/2, l_y+1/2}(\cos 2\theta). \quad (2.13)$$

In order for the hyper-angular functions $\varphi_K^{l_x l_y}(\theta)$ to form an orthonormal set with the weight factor $\sin^2 \theta \cos^2 \theta$:

$$\int_0^{\pi/2} \varphi_K^{l_x l_y}(\theta) \varphi_{K'}^{l_x l_y}(\theta) \sin^2 \theta \cos^2 \theta d\theta = \delta_{KK'} \quad (2.14)$$

the normalization coefficients $N_K^{l_x l_y}$,

$$N_K^{l_x l_y} = \sqrt{2^{l_x+l_y+2n+3} \frac{(l_x + l_y + 2n + 2) n! (l_x + l_y + n + 1)!}{[2(n + l_x) + 1]!! [2(n + l_y) + 1]!! \pi}}, \quad (2.15)$$

can be derived with the help from [47]. Using Eq. (2.12) and Eq. (2.8), the three-body Schrodinger equation for a bound state reduces to a set of coupled channels equations that only depends on the hyper-radius ρ :

$$\left(\frac{\hbar^2}{2m} \left[\frac{d^2}{d\rho^2} - \frac{\Delta_K(\Delta_K+1)}{\rho^2} \right] + E \right) \chi_\gamma(\rho) = \sum_{\gamma'} V_{\gamma\gamma'}(\rho) \chi_{\gamma'}(\rho), \quad (2.16)$$

where $\Delta_K = K + 3/2$ and $\gamma = \{K, l_x, l_y\}$. The coupling potentials $V_{\gamma\gamma'}(\rho)$ are the sum of interactions defined in Eq. (2.7), integrated over all variables but ρ :

$$V_{\gamma\gamma'}(\rho) = \left\langle \Omega_\gamma(\theta, \hat{\mathbf{x}}, \hat{\mathbf{y}}) \left| \sum_{k>j=1}^3 V_{jk} + V_{3b} \right| \Omega_{\gamma'}(\theta, \hat{\mathbf{x}}, \hat{\mathbf{y}}) \right\rangle, \quad (2.17)$$

where $\Omega_\gamma(\theta, \hat{\mathbf{x}}, \hat{\mathbf{y}}) = \varphi_K^{l_x l_y}(\theta) [Y_{l_x}(\hat{\mathbf{x}}) \otimes Y_{l_y}(\hat{\mathbf{y}})]$ are the hyper-harmonic basis functions containing all the angular dependence in coordinate space of Eq. (2.8). For a system of three

charged particles like the triple-alpha, $V_{\gamma\gamma'}(\rho)$ are long-range causing significant difficulties in determining the boundary conditions of the problem. It is thus important to study the properties of these couplings.

2.1.2.1 Asymptotic behavior of the three-body Coulomb interaction

In the asymptotic region ($\rho \rightarrow \infty$), the potential couplings $V_{\gamma\gamma'}(\rho)$ only contains a sum of three pairwise Coulomb interactions. All the nuclear forces as well as the three-body force go to zero at large distance:

$$V_{\gamma\gamma'}^{\text{asy}}(\rho) = V_{\gamma\gamma'}^{C(12)}(\rho) + V_{\gamma\gamma'}^{C(23)}(\rho) + V_{\gamma\gamma'}^{C(31)}(\rho). \quad (2.18)$$

As we choose to present all equations in the T-basis (Jacobi coordinates $i = 3$ (Fig. 2.1c)), calculating $V_{\gamma\gamma'}^{C(12)}(\rho)$ is straight forward. At large radius, the Coulomb interaction between particle 1 and 2 is expressed as $V^{C(12)} = Z^2 e^2/r_3$ where Z is the charge of an alpha particle; e is the elementary electric charge and r_3 is the radius between them. Although this expression is modified at small radii to take into account the finite size of each alpha particle (see Sec. 4.1), it is exact for the two-body Coulomb interaction in the asymptotic region. Using Eq. (2.1) and Eq. (2.4), $V_{\gamma\gamma'}^{C(12)}(\rho)$ is expressed as:

$$\begin{aligned} V_{\gamma\gamma'}^{C(12)}(\rho) &= \frac{Z^2 e^2}{\rho} \sqrt{\frac{A}{2}} \left\langle \gamma, 3 \left| \frac{1}{\sin\theta_3} \right| \gamma', 3 \right\rangle, \\ &= \frac{Z^2 e^2}{\rho} \sqrt{\frac{A}{2}} \int \Omega_\gamma(\theta_3, \hat{\mathbf{x}}_3, \hat{\mathbf{y}}_3) \frac{1}{\sin\theta_3} \Omega_{\gamma'}^*(\theta_3, \hat{\mathbf{x}}_3, \hat{\mathbf{y}}_3) \sin^2\theta_3 \cos^2\theta_3 d\theta_3 d\Omega_{x_3} d\Omega_{y_3}, \end{aligned} \quad (2.19)$$

where A is the atomic number of an alpha particle. We then simplify the integration in Eq. (2.19) to obtain:

$$V_{\gamma\gamma'}^{C(12)}(\rho) = \frac{Z^{12}}{\rho}, \quad (2.20)$$

$$Z_{\gamma\gamma'}^{12} = Z^2 e^2 \sqrt{\frac{A}{2}} \int \varphi_K^{lxly}(\theta_3) \frac{1}{\sin\theta_3} \varphi_{K'}^{*l'x'l'y}(\theta) \sin^2\theta_3 \cos^2\theta_3 d\theta_3, \quad (2.21)$$

It is more difficult to express the other two components $V_{\gamma\gamma'}^{C(23)}(\rho)$ and $V_{\gamma\gamma'}^{C(31)}(\rho)$ in Jacobi $i = 3$ because vectors \mathbf{r}_1 and \mathbf{r}_2 are not proportional to the scaled coordinate \mathbf{x}_3 . The advantage of the HH method is that the hyper-radius ρ is the same for all three Jacobi sets, leading to a possibility of six-dimensional coordinate rotations. For example, Jacobi coordinates $(\mathbf{x}_3, \mathbf{y}_3)$ can be obtained by rotating Jacobi coordinates $(\mathbf{x}_2, \mathbf{y}_2)$ by an angle ϕ :

$$\mathbf{x}_3 = -\cos\phi \mathbf{x}_2 + \sin\phi \mathbf{y}_2, \quad (2.22)$$

$$\mathbf{y}_3 = -\sin\phi \mathbf{x}_2 - \cos\phi \mathbf{y}_2, \quad (2.23)$$

where the rotation angle ϕ is a function of the mass of the three particles. Based on this argument, Raynal and Revai developed a way to rotate the hyper-harmonic basis function $\Omega_\gamma(\theta, \hat{\mathbf{x}}, \hat{\mathbf{y}})$ from one coordinate set to another using the multiplying Raynal-Revai coefficients \mathfrak{R} which can be calculated analytically [48]. The potential couplings $V_{\gamma\gamma'}^{C(23)}(\rho)$ and $V_{\gamma\gamma'}^{C(31)}(\rho)$ are first computed in Jacobi $i = 1$ and $i = 2$ in Fig. 2.1a and Fig. 2.1b respectively and then rotated back to Jacobi $i = 3$ using the Raynal-Revai frame-rotation technique. In the end, the potential couplings $V_{\gamma\gamma'}(\rho)$ in the asymptotic region can then be expressed as:

$$V_{\gamma\gamma'}(\rho) = \frac{Z_{\gamma\gamma'}^{\text{eff}}}{\rho}, \quad (2.24)$$

where $Z_{\gamma\gamma'}^{\text{eff}}$ is constant for any given channel γ and γ' and has a non-trivial expression:

$$Z_{\gamma\gamma'}^{\text{eff}} = Z^2 e^2 \sqrt{\frac{A}{2}} \left[\left\langle \gamma, 3 \left| \frac{1}{\sin\theta_3} \right| \gamma', 3 \right\rangle + \sum_{\alpha\alpha'} \Re_{\gamma\alpha}^{32} \Re_{\alpha'\gamma'}^{23} \left\langle \alpha, 2 \left| \frac{1}{\sin\theta_2} \right| \alpha', 2 \right\rangle + \sum_{\beta\beta'} \Re_{\gamma\beta}^{31} \Re_{\beta'\gamma'}^{13} \left\langle \beta, 1 \left| \frac{1}{\sin\theta_1} \right| \beta', 1 \right\rangle \right], \quad (2.25)$$

where $\Re_{\beta\gamma}^{ij}$ are the Raynal-Revai coefficients [48]; $i = 1, 2, 3$ represent the three Jacobi coordinates $(\mathbf{x}_i, \mathbf{y}_i)$ (Fig. 2.1). Each bra-ket matrix element is calculated as in Eq. (2.19).

Eq. (2.24) shows that both the diagonal and the off-diagonal couplings decay slowly as $1/\rho$ for a three charge system in the HH representation, as seen in [20]. Fig. 2.3 demonstrates the hyper-radial behavior of the potential couplings $V_{\gamma\gamma'}(\rho)$. In this graph, couplings are calculated by fixing $\gamma = (0, 0, 0)$ and varying γ' . Although the diagonal term $\gamma = \gamma' = (0, 0, 0)$ is dominant, all the couplings do not vanish at a large hyper-radius $\rho = 800$ fm. This demonstrates the difficulty of our problem in the asymptotic region.

For neutral Borromean systems, the long range couplings are not present and the three-body bound state wavefunction decays exponentially at large distances [49, 50]:

$$\chi_\gamma(\rho) \xrightarrow{\rho \rightarrow \infty} e^{-\kappa\rho}. \quad (2.26)$$

When introducing Coulomb interactions, a simple analytic expression for the asymptotic bound state wavefunction of three charged particles no longer exists. However, for a well-bound system, imposing the boundary condition that the wavefunction goes to zero at large

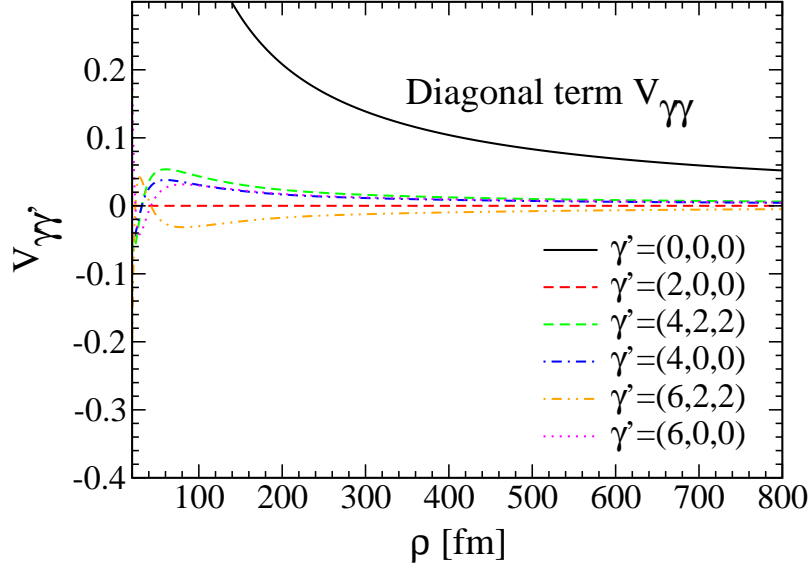


Figure 2.3: Hyper-radial behavior of the potential couplings $V_{\gamma\gamma'}(\rho)$ in Eq. (2.17). The black solid curve represents the diagonal coupling and the others demonstrate the off-diagonal couplings.

distances is sufficient for the numerical calculation [37]:

$$\chi_\gamma(\rho \rightarrow \infty) \rightarrow 0. \quad (2.27)$$

2.1.3 Three-body continuum states

For a three-body scattering wavefunction, an additional set of subscripts $K^i l_x^i l_y^i$ is needed to describe the incoming channels of the system in which three particles come in with direction \mathbf{k} (κ, θ_κ) in momentum space:

$$\Psi^{LM} = \frac{1}{(\kappa\rho)^{5/2}} \sum_{\substack{K^i l_x^i l_y^i \\ Kl_x l_y}} \chi_{Kl_x l_y}^{K^i l_x^i l_y^i}(\kappa\rho) \varphi_K^{l_x l_y}(\theta) [Y_{l_x} \otimes Y_{l_y}]_{LM} \varphi_{K^i}^{l_x^i l_y^i}(\theta_\kappa) [Y_{l_x^i} \otimes Y_{l_y^i}]_{LM}^\kappa, \quad (2.28)$$

where κ is the hyper-radial momentum and relates to the three-body energy E through $\kappa = \sqrt{2mE}/\hbar$. The $(\kappa\rho)^{5/2}$ factor is introduced to simplify the normalization condition of the three-body scattering wavefunction:

$$\int_0^\infty \chi_{\gamma\gamma^i}(\kappa\rho) \chi_{\gamma\gamma^i}(\kappa'\rho) d\rho = \delta(\kappa - \kappa'). \quad (2.29)$$

where $\gamma = (K, l_x, l_y)$ [$\gamma^i = (K^i, l_x^i, l_y^i)$] are the outgoing [incoming] channels. Using this HH expansion, we obtain a set of coupled channels equations for a three-body scattering system:

$$\left(\frac{\hbar^2}{2m} \left[\frac{d^2}{d\rho^2} - \frac{\Delta_K(\Delta_K+1)}{\rho^2} \right] + E \right) \chi_{\gamma\gamma^i}(\kappa\rho) = \sum_{\gamma'} V_{\gamma\gamma'}(\rho) \chi_{\gamma'\gamma^i}(\kappa\rho), \quad (2.30)$$

where $V_{\gamma\gamma'}(\rho)$ are the potential couplings as defined in Eq. (2.17).

Solving Eq. (2.30) for positive energy E to obtain continuum states for a system of three charges is numerically challenging since it requires an exact boundary condition. In order to overcome that difficulty we implement a screening technique in which all the off-diagonal couplings are screened at large distances. Because the diagonal couplings are dominant in the asymptotic region (see Fig. 2.3), the screening method can help to achieve numerical stability and the correct three-body scattering boundary condition while preserving the physics of the three Coulombian particle problem. More details on the screening method will be presented in Sec. 2.2.3. In the region where all the off-diagonal couplings vanish, Eq. (2.30) can be rewritten as:

$$\frac{d^2 \chi_{\gamma\gamma^i}(x)}{dx^2} + \left(1 - \frac{2\eta_\gamma}{x} - \frac{\Delta_K(\Delta_K+1)}{x^2} \right) \chi_{\gamma\gamma^i}(x) = 0, \quad (2.31)$$

where $x = \kappa\rho$ and $\Delta_K = K + 3/2$. The variable η_γ is an equivalent of the Sommerfeld parameter in two-body systems but is more complex and hyper-momentum K dependent. η_γ

is obtained from the parameter $Z_{\gamma\gamma}^{\text{eff}}$ in Eq. (2.25) through the relationship $\eta_\gamma = mZ_{\gamma\gamma}^{\text{eff}}/\hbar^2\kappa$.

It is well known that Eq. (2.31) has analytic solutions which are the regular $F_{K+3/2}(\eta_\gamma, \kappa\rho)$ and irregular $G_{K+3/2}(\eta_\gamma, \kappa\rho)$ three-body Coulomb functions [46]. Therefore, in the asymptotic region where all the off-diagonal couplings are negligible, the $\alpha + \alpha + \alpha$ scattering wavefunction behaves as:

$$\chi_{\gamma\gamma i}^{\text{HHR}}(\rho) \xrightarrow{\rho \rightarrow \infty} H_{K+3/2}^-(\eta_\gamma, \kappa\rho) \delta_{\gamma\gamma i} - H_{K+3/2}^+(\eta_\gamma, \kappa\rho) S_{\gamma\gamma i}. \quad (2.32)$$

In this equation, $H^\pm = G \pm iF$ are the Coulomb functions describing the outgoing and incoming spherical waves and $S_{\gamma\gamma i}$ is the scattering matrix [46].

2.1.4 Properties of the three-alpha wavefunction

In this section we want to discuss about the symmetry properties of the three-alpha wavefunction. An alpha particle is considered as a boson of spin zero, thus the wavefunction must be unchanged for any permutation of these two particles. This selects certain partial waves contributing to the HH wavefunction expansion (Eq. (2.8) and Eq. (2.28)). Next, we derive the relation describing this selection rule. Fig. 2.1 represents three different Jacobi coordinates. These give rise to three representations of the three-body wavefunction:

$$|\Psi_1\rangle = |[l_{x_1}, l_{y_1}]L_1, (s_2, s_3)S_{x_1}]J_1, s_1; J\rangle [[t_1 \otimes t_2] \otimes t_3]_T, \quad (2.33)$$

$$|\Psi_2\rangle = |[l_{x_2}, l_{y_2}]L_2, (s_3, s_1)S_{x_2}]J_2, s_2; J\rangle [[t_1 \otimes t_2] \otimes t_3]_T, \quad (2.34)$$

$$|\Psi_3\rangle = |[l_{x_3}, l_{y_3}]L_3, (s_1, s_2)S_{x_3}]J_3, s_3; J\rangle [[t_1 \otimes t_2] \otimes t_3]_T. \quad (2.35)$$

We denoted $s_i(t_i)$ as the spin (isospin) of particle i and $J(T)$ as the total spin (total isospin) of the three-body system. l_{x_i}, l_{y_i} are the the relative orbital angular momenta of the two-body subsystem in Jacobi i and the orbital angular momenta between its center of mass and particle i respectively. If we interchange the position of particle 1 and particle 2 which are identical, the total wavefunction in the third Jacobi coordinate becomes:

$$|\Psi'_3\rangle = |[(-l_{x_3}, l_{y_3})L_3, (s_2, s_1)S_{x_3}]J_3, s_3; J\rangle [[t_2 \otimes t_1] \otimes t_3]_T. \quad (2.36)$$

We can rewrite this new wavefunction in terms of $|\Psi_3\rangle$ with the aid from [51]:

$$\begin{aligned} |\Psi'_3\rangle &= (-1)^{l_{x_3}} (-1)^{S_{x_3} - s_1 - s_2} (-1)^{T_{21} - t_2 - t_1} \\ &\quad \times |[(l_{x_3}, l_{y_3})L_3, (s_1, s_2)S_{x_3}]J_3, s_3; J\rangle [[t_1 \otimes t_2] \otimes t_3]_T, \\ |\Psi'_3\rangle &= (-1)^{l_{x_3} + S_{x_3} + T_{21}} |\Psi_3\rangle. \end{aligned} \quad (2.37)$$

Since particle 1 and particle 2 are bosons, their spins and isospins are even numbers which can then be dropped from Eq. (2.37). Because the wavefunction is symmetric under the exchange of two identical bosons, Eq. (2.37) requires $l_{x_3} + S_{x_3} + T_{21}$ to be even. Therefore we can conclude that for three identical bosons, expressed in Jacobi coordinates 3, only partial waves satisfying the selection rule $l_x + S_x + T_x = \text{even}$ will contribute to the total wavefunction. Here, l_x , S_x and T_x are the relative angular momentum, the total spin, and total isospin of the two-body subsystem in respect to that Jacobi coordinate system. For the triple-alpha problem, each alpha particle has spin and isospin zero, the selection rule is thus reduced to $l_x = \text{even}$.

Using the same techniques, we could write down the wavefunction $|\Psi_2\rangle$ in the second

Jacobi coordinate after exchange particle 1 and particle 2:

$$|\Psi_2\rangle = |[(-l_{x_1}, l_{y_1})L_1, (s_3, s_2)S_{x_1}]J_1, s_1; J\rangle[[t_2 \otimes t_1] \otimes t_3]_T. \quad (2.38)$$

Rearranging the order of momentum couplings we have:

$$\begin{aligned} |\Psi_2\rangle &= (-1)^{l_{x_1}}(-1)^{S_{x_1}-s_3-s_2}(-1)^{T_{21}-t_2-t_1} \\ &\quad \times |[(l_{x_1}, l_{y_1})L_1, (s_2, s_3)S_{x_1}]J_1, s_1; J\rangle[[t_1 \otimes t_2] \otimes t_3]_T, \\ |\Psi_2\rangle &= (-1)^{l_{x_1}+S_{x_1}+T_{21}}|\Psi_1\rangle. \end{aligned} \quad (2.39)$$

Again, spins and isospins of particle 1 and 2 are even, therefore they can be dropped from Eq. (2.39). From Eq. (2.39), we can generalize a relationship for the wavefunction of a three identical boson system between any pair of Jacobi sets:

$$|\Psi_j\rangle = P_{jk}|\Psi_k\rangle, \quad (2.40)$$

where the permutation operator P_{jk} is defined as $P_{jk} = (-1)^{T_{jk}+l_{x_k}+S_{x_k}}$. For the triple-alpha problem, this quantity equals to one when applying the even partial wave selection rule that we discuss above.

Eq. (2.40) indicates that only one of these wavefunctions should be explicitly included in the three-component Faddeev equations:

$$\begin{pmatrix} T_i + V_i - E & V_i & V_i \\ V_j & T_j + V_j - E & V_j \\ V_k & V_k & T_k + V_k - E \end{pmatrix} \begin{pmatrix} \Psi_i \\ \Psi_j \\ \Psi_k \end{pmatrix} = 0. \quad (2.41)$$

Here, subscript i and the corresponding variables keep their common definitions in Jacobi set i . With the use of Eq. (2.40), we can effectively reduce three sets of Faddeev equations to a set of coupled channel equations in one set of Jacobi coordinates:

$$\langle i|T_i + V_i - E|i\rangle\langle i|\Psi_i\rangle + \langle i|V_i|j\rangle\langle j|\Psi_i\rangle + \langle i|V_i|k\rangle\langle k|\Psi_i\rangle = 0, \quad (2.42)$$

which can be rewritten as:

$$[T_i + V_i + \langle i|V_i|j\rangle\langle j|i\rangle + \langle i|V_i|k\rangle\langle k|i\rangle - E]\Psi_i = 0. \quad (2.43)$$

The constraint condition of the partial wave in combination with the symmetry property of Eq. (2.43) allow us to fully take into account the symmetrization of the system and highly increase the computational efficiency.

2.2 R-matrix method

In order to obtain the continuum states of a three charged-particle system, we need to solve Eq. (2.30) for positive values of energy E . Theoretically, we could integrate N linearly independent solutions of Eq. (2.30) from $\rho = 0$ to a certain large radius ρ_a where the off-diagonal couplings $V_{\gamma\gamma'}(\rho)$ are negligible [43, 52]. Then, a combination of these solutions would be matched with the asymptotic wavefunction Eq. (2.32) at ρ_a to construct the physical continuum wave of a three-body system. However for a three charged-particle system, ρ_a has to be very large (~ 1000 fm) due to the long range Coulomb interaction, making it inefficient to use the direct integration methods. Since we are interested in the low energy region in which the wavefunction is needed below the Coulomb barrier, the direct integration methods are

not numerically stable for solving coupled channels equations with strong repulsive couplings [46]. In this section, we discuss about the R-matrix method in hyperspherical coordinates which enables us to overcome these problems.

Wigner and Eisenbud [53] were the first to introduce the R-matrix method into nuclear physics to study resonances in nuclear scattering. Later on, this method was developed and extended in detail by Lane and Thomas [54]. The general idea of this method is to use an orthonormal basis expansion inside an R-matrix box. An R matrix is then constructed to match to the asymptotic wavefunction outside the box [46]. Even though the R-matrix method was originally developed for a two-body scattering problem, it has been generalized to a three-body system in HH coordinates by I.J. Thompson *et al.* [55].

2.2.1 R-matrix expansion

In the R-matrix expansion, the eigenfunctions of the diagonal parts of the Hamiltonian in each separate channel γ are used as a basis:

$$\left(-\frac{\hbar^2}{2m} \left[\frac{d^2}{d\rho^2} - \frac{(K + \frac{3}{2})(K + \frac{5}{2})}{\rho^2} \right] + V_{\gamma\gamma}(\rho) - \varepsilon_\gamma^n \right) \omega_\gamma^n(\rho) = 0, \quad (2.44)$$

where ε_γ^n is the eigenenergy corresponding to the eigenfunction $\omega_\gamma^n(\rho)$. These basis functions are defined to have the same logarithmic derivatives $\beta = \frac{d \ln \omega_\gamma^n(\rho)}{d\rho}$ at the R-matrix radius ρ_m . The constant feature of the logarithmic derivatives ensures that $\omega_\gamma^n(\rho)$ forms an orthonormal basis set within the range of $[0, \rho_m]$.

$$\int_0^{\rho_m} \omega_n(\rho) \omega_m(\rho) d\rho = \delta_{nm}. \quad (2.45)$$

We then solve the coupled channels equations in the interior region $[0, \rho_m]$:

$$\left(-\frac{\hbar^2}{2m} \left[\frac{d^2}{d\rho^2} - \frac{(K + \frac{3}{2})(K + \frac{5}{2})}{\rho^2} \right] - e^p \right) \phi_\gamma^p(\rho) + \sum_{\gamma'} V_{\gamma\gamma'}(\rho) \phi_{\gamma'}^p(\rho) = 0, \quad (2.46)$$

by expanding the eigensolution ϕ_γ^p at eigenenergy e^p in terms of the orthonormal basis $\omega_\gamma^n(\rho)$:

$$\phi_\gamma^p(\rho) = \sum_{n=1}^N c_\gamma^{pn} \omega_\gamma^n(\rho). \quad (2.47)$$

The expansion coefficients c_γ^{pn} can easily be obtained by solving a set of linear equations:

$$\varepsilon_\gamma^n c_\gamma^{pn} + \sum_{n'\gamma'} \langle \omega_\gamma^n | V_{\gamma\gamma'} | \omega_{\gamma'}^{n'} \rangle c_{\gamma'}^{pn'} = e^p c_\gamma^{pn}. \quad (2.48)$$

These eigenfunctions $\phi_\gamma^p(\rho)$ will also form an orthonormal basis within the R-matrix radius ρ_m . The three-body scattering wavefunction $\chi_{\gamma\gamma i}(\rho)$ at energy E , a solution of Eq. (2.30) in the whole coordinate space, can be expanded in terms of $\phi_\gamma^p(\rho)$:

$$\chi_{\gamma\gamma i} = \sum_p A_{\gamma\gamma i}^p \phi_\gamma^p. \quad (2.49)$$

In our calculation, the logarithmic derivative β is chosen to be zero. This option may lead to the discontinuity of the derivative of the wavefunction at the R-matrix boundary when using a truncated basis as discussed in [56]. However, a sufficiently large basis is employed in our calculation to ensure a smooth behavior of the wavefunction at all energies. In addition, the zero logarithmic derivative highly reduces the complexity of the R-matrix propagation method (Sec. 2.2.2), therefore increasing the efficiency and accuracy of the numerical performance when propagation is needed to a very large radius. All the equations

presented in this thesis consider $\beta = 0$ while more general formulae can be found in [46].

The R matrix at energy E relates the wavefunction $\chi_{\gamma\gamma^i}(\rho)$ and its derivative:

$$\chi_{\gamma\gamma^i}(\rho) = \sum_{\gamma'} \rho \mathcal{R}_{\gamma\gamma'}(E) \chi'_{\gamma'\gamma^i}(\rho). \quad (2.50)$$

The constant logarithmic derivative feature enables us to calculate the R matrix $\mathcal{R}_{\gamma\gamma'}(E)$ from the known eigenfunctions ϕ_γ^p at radius ρ_m :

$$\mathcal{R}_{\gamma\gamma'}(E) = \frac{\hbar^2}{2m\rho_m} \sum_{p=1}^P \frac{\phi_\gamma^p(\rho_m) \phi_{\gamma'}^p(\rho_m)}{e^p - E}. \quad (2.51)$$

where P is the number of poles used in our calculation. If we substitute Eq. (2.49) and Eq. (2.51) into Eq. (2.50), the only missing quantities to calculate the scattering wavefunction are the expansion coefficients $A_{\gamma\gamma^i}^p$. As discussed in Sec. 2.1.3, Eq. (2.32) is the asymptotic form of a continuum wavefunction for the three alpha system when the off-diagonal couplings can be neglected. For sufficiently large ρ_m , the wavefunction will be in the asymptotic regime. The unknown coefficients $A_{\gamma\gamma^i}^p$ are obtained by performing an asymptotic matching of the three-body scattering wavefunction at ρ_m :

$$A_{\gamma\gamma^i}^p = \frac{\hbar^2}{2m} \frac{1}{e_\gamma^p - E} \sum_{\gamma'} \phi_{\gamma'}^p \left(\delta_{\gamma'\gamma^i} H_{K'+3/2}^-(\kappa\rho_m) - S_{\gamma'\gamma^i} H_{K'+3/2}^+(\kappa\rho_m) \right). \quad (2.52)$$

All functions in Eq. (2.52) are evaluated at the R-matrix boundary ρ_m . The scattering matrix $S_{\gamma'\gamma^i}$ and the R matrix are directly related [46]:

$$S_{\gamma'\gamma^i} = \frac{\delta_{\gamma'\gamma^i} H_{K'+3/2}^-(\kappa\rho_m) - \rho_m \mathcal{R}_{\gamma'\gamma^i} H_{K'+3/2}^-(\kappa\rho_m)}{\delta_{\gamma'\gamma^i} H_{K'+3/2}^+(\kappa\rho_m) - \rho_m \mathcal{R}_{\gamma'\gamma^i} H_{K'+3/2}^+(\kappa\rho_m)}. \quad (2.53)$$

2.2.2 R-matrix propagation

The triple-alpha system is driven by a strong Coulomb interaction with long-range off-diagonal couplings. Therefore, the R-matrix radius ρ_m has to be very large to fully capture the physics of the problem. Solving the coupled channels equations in a large R-matrix box will lead to numerical instability. Fig. 2.4 presents the scattering wavefunction calculations at 0.2 MeV using two different R-matrix radius. The red curve corresponds to an R-matrix box of $\rho_m = 50$ fm. The blue curve represents a calculation with $\rho_m = 100$ fm. We observe a numerical instability in the small radius region when using a larger R-matrix box. Large R-matrix box requires more terms in the R-matrix expansion Eq. (2.49) and Eq. (2.51). The R-matrix basis wavefunctions around the origin are expected to be infinitesimally small due to the strong Coulomb barrier. Accumulation error of adding many small numbers could lead to the instability of the solution at small radius as seen in Fig. 2.4.

In order to overcome this difficulty, we employ the R-matrix propagation technique originally developed by Light and Walker for the atom-molecule scattering problem [57, 58, 59]. First, the set of coupled channels equations (2.30) is solved in a small R-matrix box with radius ρ_m . Then the R-matrix at ρ_m is propagated to $\rho_a \gg \rho_m$ where it becomes safe to ignore the off-diagonal couplings, and matching to known Coulomb functions of Eq. (2.32) can be performed. This propagation method is well known for its fast convergence and high numerical stability in atomic and molecular system. We first rewrite Eq. (2.30) as

$$\frac{d^2 \chi_{\gamma\gamma^i}(\rho)}{d\rho^2} = \sum_{\gamma'} \tilde{V}_{\gamma\gamma'} \chi_{\gamma'\gamma^i}(\rho), \quad (2.54)$$

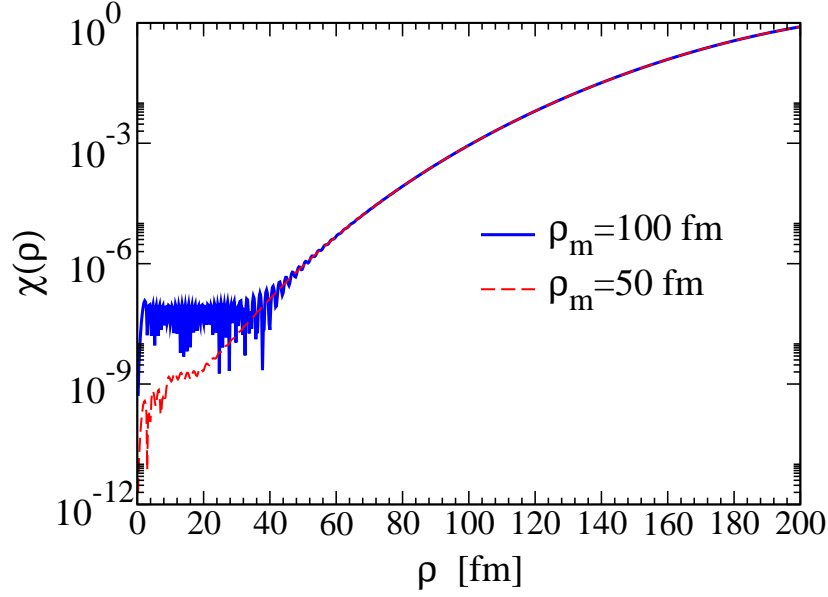


Figure 2.4: The hyper-radial scattering wavefunction corresponding to the incoming channel of $K^i l_x^i l_y^i = 000$ and the outgoing channel of $K l_x l_y = 000$ in the hyperspherical expansion (Eq. (2.28)) is calculated at $E = 0.2$ MeV for two different R-matrix box sizes: 50 fm (red) and 100 fm (blue).

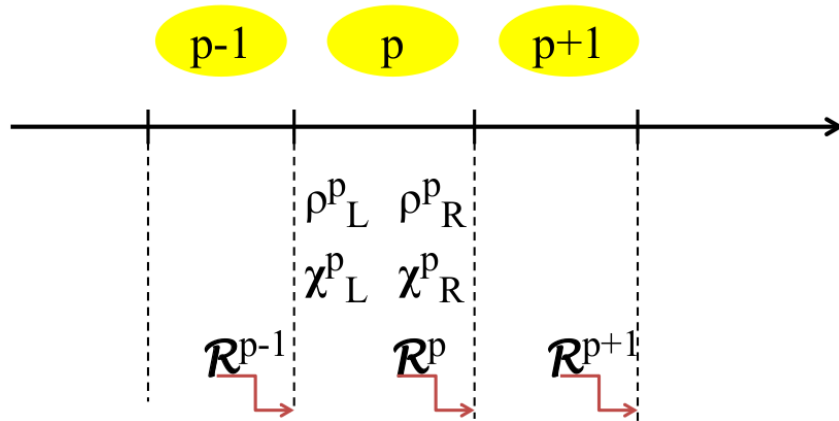


Figure 2.5: Diagram presenting the sectorization in hyper-radius ρ of the R-matrix propagation method. The subscripts L and R indicate the evaluations at the left and right sector boundary. The R matrix \mathcal{R} of a sector is calculated at the right boundary.

where

$$\tilde{V}_{\gamma\gamma'} = \frac{2m}{\hbar^2} V_{\gamma\gamma'} + \left(\frac{\Delta_K(\Delta_K + 1)}{\rho^2} - \frac{2mE}{\hbar^2} \right) \delta_{\gamma\gamma'}. \quad (2.55)$$

The interval from the R-matrix radius ρ_m to the matching radius of the three-body asymptotic wavefunction ρ_a is divided into M sectors, illustrated in Fig. 2.5. We choose the size h_p of sector p to be sufficiently small that the interaction within is considered to be constant $\lambda_\gamma(p)$ in each channel γ . We diagonalize $\tilde{V}_{\gamma\gamma'}$ by solving the equation:

$$(\tilde{\mathbf{T}}^p)^T \tilde{\mathbf{V}}(\rho_p) \mathbf{T}^p = \lambda(p)^2, \quad (2.56)$$

where ρ_p is taken at the center of sector p . The wavefunction and its derivative at the left and right boundary of sector p can be related through a local diagonal representation of the propagating functions \mathbf{G}^p :

$$\begin{bmatrix} \boldsymbol{\chi}_R^p \\ \boldsymbol{\chi}_L^p \end{bmatrix} = \begin{bmatrix} \mathbf{G}_1^p & \mathbf{G}_2^p \\ \mathbf{G}_3^p & \mathbf{G}_4^p \end{bmatrix} \begin{bmatrix} -\boldsymbol{\chi}_R^{p'} \\ \boldsymbol{\chi}_L^{p'} \end{bmatrix}. \quad (2.57)$$

The subscripts R and L imply evaluations at the right and left side of the sector boundary, respectively. In this section, all the equations are written in matrix form for simplicity. The bold letter indicates a matrix quantity, e.g $\boldsymbol{\chi}_R^p$ is the wavefunction matrix of which each matrix element is $(\chi_{\gamma\gamma^i})_R^p$ corresponding to the incoming γ^i and outgoing γ channels. The propagating functions are expressed as $\mathbf{G}_i^p = \mathbf{T}^p \mathbf{g}_i^p \tilde{\mathbf{T}}^p$, where \mathbf{g}^p is a simple function of $\lambda_\gamma(p)$

(see Appendix A for detailed derivation):

$$\begin{aligned}
(g_1^p)_{\gamma\gamma'} = (g_4^p)_{\gamma\gamma'} = \delta_{\gamma\gamma'} & \begin{cases} -\frac{1}{|\lambda_\gamma|} \coth|h_p\lambda_\gamma|, & \lambda_\gamma^2 > 0 \\ \frac{1}{|\lambda_\gamma|} \cot|h_p\lambda_\gamma|, & \lambda_\gamma^2 \leq 0 \end{cases} \\
(g_2^p)_{\gamma\gamma'} = (g_3^p)_{\gamma\gamma'} = \delta_{\gamma\gamma'} & \begin{cases} -\frac{1}{|\lambda_\gamma|} \operatorname{csch}|h_p\lambda_\gamma|, & \lambda_\gamma^2 > 0 \\ \frac{1}{|\lambda_\gamma|} \operatorname{csc}|h_p\lambda_\gamma|, & \lambda_\gamma^2 \leq 0 \end{cases} .
\end{aligned} \tag{2.58}$$

The R matrix of sector p relates the wavefunction and its derivative at the right sector boundary through a matrix equation:

$$\chi_R^p = \rho_R^p \mathcal{R}^p \chi_R^{p'} . \tag{2.59}$$

We can obtain a similar expression for sector $p-1$:

$$\chi_L^p = \rho_R^{p-1} \mathcal{R}^{p-1} \chi_L^{p'} . \tag{2.60}$$

Inserting Eq. (2.59) and Eq. (2.60) into Eq. (2.57), we derive an equation that propagates the R matrix from sector $p-1$ to the next (see Appendix A for detailed derivation):

$$\mathcal{R}^p = \frac{1}{\rho_R^p} \left(\mathbf{G}_2^p [\mathbf{G}_4^p - \rho_R^{p-1} \mathcal{R}^{p-1}]^{-1} \mathbf{G}_3^p - \mathbf{G}_1^p \right) . \tag{2.61}$$

The R-matrix propagation in Eq. (2.61) is the first step in the propagation method to calculate the three-body scattering wavefunction (see Fig. 2.6). We first propagate the R

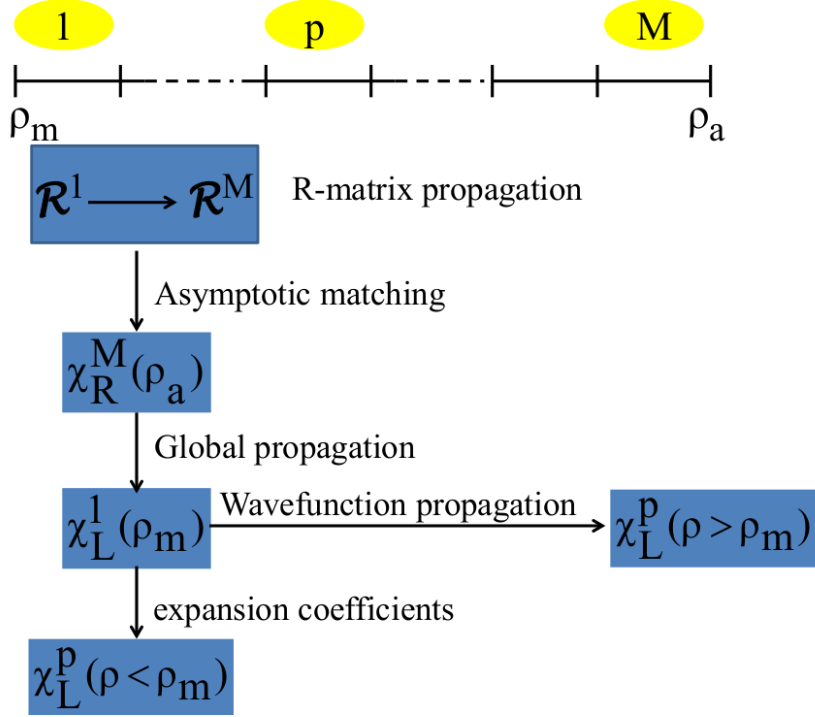


Figure 2.6: Schematic diagram of the propagation method in obtaining the three-body scattering wavefunction

matrix from a small radius ρ_m to a large distance ρ_a where the asymptotic matching can be performed and the wavefunction (χ_R^M) and its derivative ($\chi_R^{M'}$) at the boundary of the final sector M are obtained. These quantities are then used in the global propagation which will be discussed later to compute the wavefunction (χ_L^1) at the R-matrix boundary ρ_m . We use that to determine the wavefunction expansion coefficient $A_{\gamma\gamma'i}$ in Eq. (2.49) from which the three-body scattering wavefunction within the R-matrix radius can be calculated. For $\rho > \rho_m$, its value is obtained by propagating the wavefunction from χ_L^1 to the desired radius instead.

We now discuss the global propagation and the wavefunction propagation which are important in constructing the three-body scattering wavefunction. The global propagation is designed to propagate the wavefunction from an arbitrary sector p to sector 1 and vice versa (see Appendix A for details):

$$\begin{bmatrix} \chi_R^p \\ \chi_L^1 \end{bmatrix} = \begin{bmatrix} \mathcal{G}_1^p & \mathcal{G}_2^p \\ \mathcal{G}_3^p & \mathcal{G}_4^p \end{bmatrix} \begin{bmatrix} -\chi_R^{p'} \\ \chi_L^{1'} \end{bmatrix}, \quad (2.62)$$

where the global propagation functions \mathcal{G}_i^p are calculated by a set of recursive equations:

$$\mathcal{G}_1^p = \mathbf{G}_1^p - \mathbf{G}_2^p[\mathbf{G}_4^p + \mathcal{G}_1^{p-1}]^{-1}\mathbf{G}_3^p, \quad (2.63)$$

$$\mathcal{G}_2^p = \mathbf{G}_2^p[\mathbf{G}_4^p + \mathcal{G}_1^{p-1}]^{-1}\mathcal{G}_2^{p-1}, \quad (2.64)$$

$$\mathcal{G}_3^p = \mathcal{G}_3^{p-1}[\mathbf{G}_4^p + \mathcal{G}_1^{p-1}]^{-1}\mathbf{G}_3^p, \quad (2.65)$$

$$\mathcal{G}_4^p = \mathcal{G}_4^{p-1} - \mathcal{G}_3^{p-1}[\mathbf{G}_4^p + \mathcal{G}_1^{p-1}]^{-1}\mathcal{G}_2^{p-1}. \quad (2.66)$$

Given the wavefunction χ_R^M and its derivative $\chi_R^{M'}$ at the matching radius ρ_a , we can evaluate its value at the R-matrix boundary ρ_m by using Eq. (2.62). The wavefunction is then propagated to larger radius by a sequential application of the local propagation functions \mathbf{G}_i^p in Eq. (2.57):

$$\chi_L^p = \mathbf{G}_1^{p-1}[\mathbf{G}_3^{p-1}]^{-1}\chi_L^{p-1} + \left(\mathbf{G}_2^{p-1} - \mathbf{G}_1^{p-1}[\mathbf{G}_3^{p-1}]^{-1}\mathbf{G}_4^{p-1} \right) \chi_L^{p-1'}, \quad (2.67)$$

or a single application of the global propagation functions \mathcal{G}_i^p in Eq. (2.62):

$$\chi_R^p = \mathcal{G}_1^p[\mathcal{G}_3^p]^{-1}\chi_L^1 + \left(\mathcal{G}_2^p - \mathcal{G}_1^p[\mathcal{G}_3^p]^{-1}\mathcal{G}_4^p \right) \chi_L^{1'}. \quad (2.68)$$

Fig. 2.7 compares the quadruple transition strength functions $dB(E2)/dE$ calculated using the global (solid) and local (dashed) representations of the wavefunction propagation method. Since the two curves are identical, we conclude that these methods are numerically equivalent

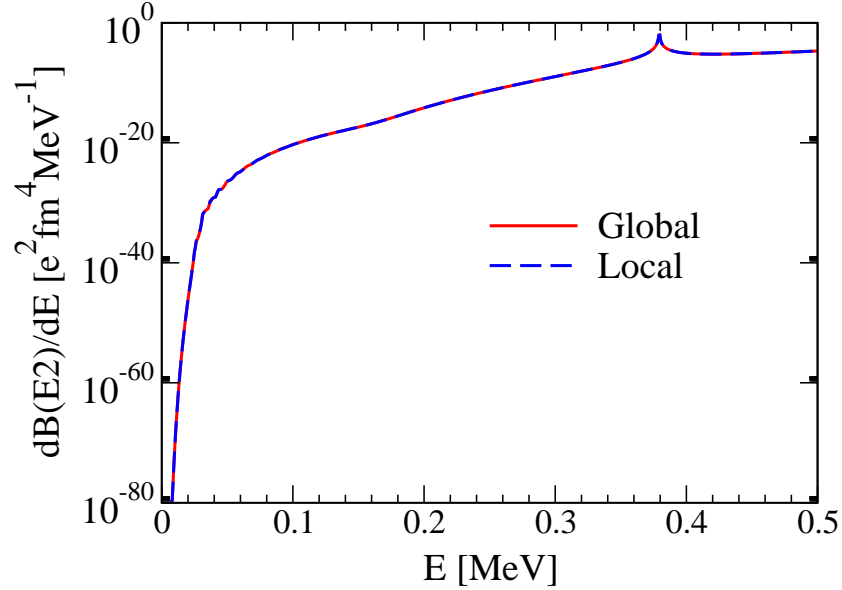


Figure 2.7: The quadrupole transition strength function $dB(E2)/dE$ is calculated using the global (solid) and local (dashed) representations of the wavefunction propagation method.

and provide consistent results.

2.2.3 Screening technique

The R-matrix propagation method is numerically stable when the Coulomb off-diagonal couplings are not introduced. The presence of very narrow two-body and three-body resonances in addition to the strong, long-range Coulomb interaction in our problem creates numerical instabilities in the propagated three-body scattering wavefunctions. The blue dashed curved in Fig. 2.8 represents the first component of the three-alpha scattering wavefunction in the hyperspherical expansion at 0.5 MeV which is calculated when considering both nuclear and Coulomb interactions to all orders. The numerical instability occurs around 90 fm which is also the turning point for this channel. Because the propagation method calculates the wavefunction at a given sector using the previous sector's information, the numerical insta-

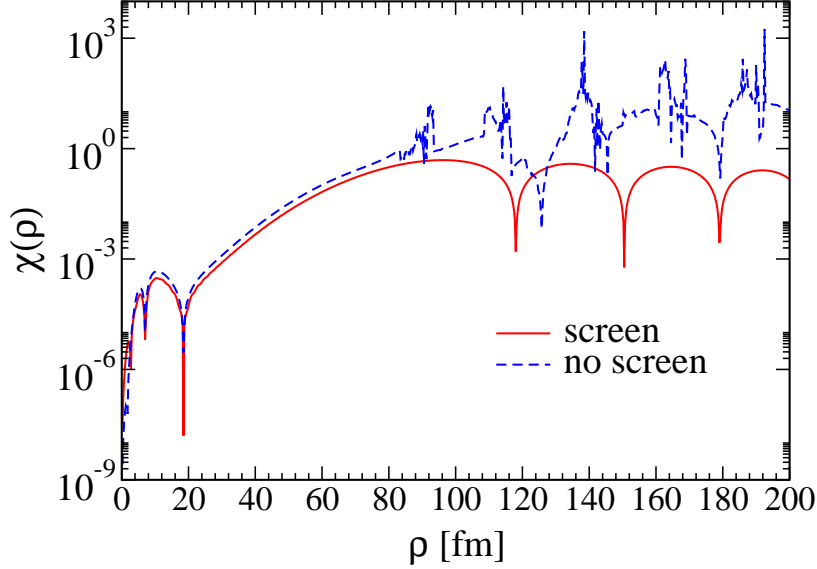


Figure 2.8: The hyper-radial scattering wavefunction corresponding to the incoming channel of $K^i l_x^i l_y^i = 000$ and the outgoing channel of $K l_x l_y = 000$ in the hyperspherical expansion (Eq. (2.28)) is calculated at $E = 0.5$ MeV for both cases: with screening (red solid) and without screening (blue dashed).

bility at the turning point region is propagated outward as seen in Fig. 2.8.

We overcome these difficulties by introducing a Woods-Saxon screening factor on the off-diagonal potentials of Eq. (2.17):

$$V_{\gamma\gamma'} = \frac{V_{\gamma\gamma'}}{1 + \exp\left(\frac{\rho - \rho_{\text{screen}}}{a_{\text{screen}}}\right)}, \quad (2.69)$$

where $\gamma \neq \gamma'$. Fig. 2.3 demonstrates that the diagonal couplings $V_{\gamma\gamma}(\rho)$ are dominant at large radius (\sim factor of 10 larger than the off-diagonal couplings). Even though the off-diagonal couplings are small, the fact that they decay slowly as $1/\rho$ is responsible for the numerical instability of the wavefunctions as shown above. When the off-diagonal couplings are screened, we are able to improve the numerical stability and at the same time retain the long-range asymptotic behavior of the problem. The red solid curve in Fig. 2.8 shows

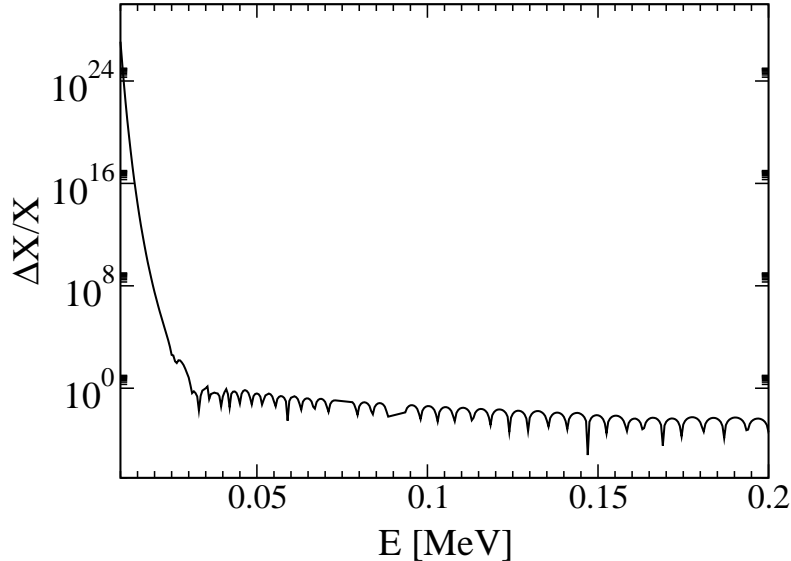


Figure 2.9: Relative deviation of the quadrupole transition strength $dB(E2)/dE$ (denoted X in the plot) when diagonal Coulomb screening is introduced.

an improvement of the scattering wavefunction when using the screening technique. The screening radius ρ_{screen} is chosen sufficiently large to gain convergence, yet small enough to ensure numerical stability. Note that we should not screen the diagonal Coulomb couplings. The additional diagonal Coulomb screening leads to a large changes in the quadrupole transition strength $dB(E2)/dE$ at low energies (see Fig. 2.9).

Fig. 2.10 summarizes the different steps in our method. We divide the hyper-radial space into four regions. The Hyperspherical Harmonics R-matrix expansion is first applied in a small box of radius ρ_m (~ 50 fm). We then use the R-matrix propagation method to much larger distances. All Coulomb couplings are included from ρ_m to ρ_{screen} (~ 800 fm). After that, the off-diagonal couplings are screened up to ρ_a (~ 3000 fm) where it is safe to perform the asymptotic matching with Eq. (2.32).

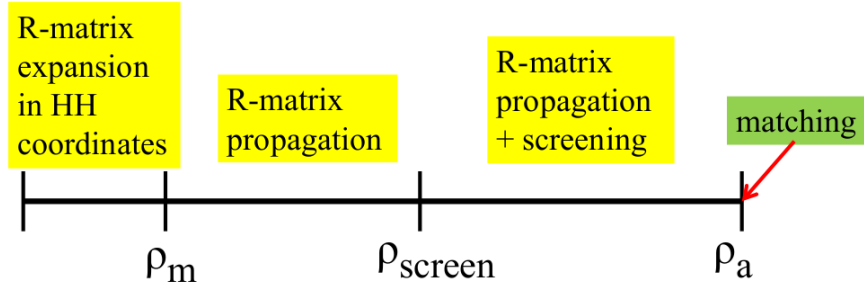


Figure 2.10: Our three-body method is divided into four steps in which we employ the R-matrix expansion, R-matrix propagation and screening technique in Hyperspherical Harmonics coordinates.

2.2.4 HHR3a

A new code named HHR3a is generated to solve Eq. (2.16) for bound states and Eq. (2.30) for continuum states of the triple-alpha system. It is developed from the program FaCE [33] and STURMXX [60] which are originally designed by I. J. Thompson *et al.* for a *core + n + n* system. In FaCE, these coupled equations are solved by expanding the hyper-radial wavefunction in terms of the Laguerre basis introduced in [61] :

$$\chi_\gamma(\rho) = \sum_n a_{n,\gamma} R_n(\rho, \rho_0), \quad (2.70)$$

$$R_n(\rho, \rho_0) = \rho^{5/2} \rho_0^{-3} \left(\frac{n!}{(n+5)!} \right)^{1/2} L_n^5(z) \exp(-z/2), \quad (2.71)$$

where $z = \rho/\rho_0$. ρ_0 is a scaling radius and $L_n(z)$ is the associated Laguerre polynomial of the order $n = 0, 1, 2, \dots$. This basis forms an orthonormal set with respect to the weight function ρ^5 :

$$\int_0^\infty R_n(\rho, \rho_0) R_{n'}(\rho, \rho_0) \rho^5 d\rho = \delta_{n,n'}. \quad (2.72)$$

Using this basis, we can rewrite the coupled equation Eq. (2.16) in matrix form:

$$H\mathbf{v} = E\mathbf{v}. \quad (2.73)$$

Then, a diagonalization method is used to obtain eigenenergies E and eigenvectors \mathbf{v} from this set of linear equations. The boundary condition implemented in FaCE for bound state calculations is that $\chi_\gamma(\rho)$ vanishes at both $\rho = 0$ and $\rho \rightarrow \infty$. This is ensured by the properties of the Laguerre basis in Eq. (2.71).

The hyperspherical harmonics R-matrix (HHR) method is implemented in STURMXX, used to solve the coupled equations Eq. (2.30) for positive energy E . First, the coupling matrix from FaCE is fed to STURMXX which then uses this information to construct an R-matrix expansion basis. The coupled equations Eq. (2.30) are solved in a small R-matrix box by expanding its solutions in terms of that orthonormal basis set built on the diagonal couplings and an R matrix is calculated at the boundary of the box. We then propagate this R matrix to larger radius by the use of the R-matrix propagation method (see Sec. 2.2 for details). At a large enough distance, the asymptotic matching is performed to obtain the three-body continuum wavefunction. STURMXX operates very well for a *core* + n + n system, providing fast converged and highly stable solutions of the scattering problem. Our current problem, involving three identical alpha particles, has different symmetries and is more difficult because of the long-range Coulomb interaction. Therefore, considerable modifications are introduced to the new code HHR3a in order to tackle this problem. First of all, HHR3a is corrected for the symmetry properties given by the three identical bosons. As we discuss in Sec. 2.1.4, only partial waves with $l_x = \text{even}$ will contribute to the total wavefunction. Here, l_x are the relative angular momentum the two identical alpha particles

being interchanged. This constraint is applied for the wavefunction in each of the three Jacobi coordinates. Because the wavefunction is symmetric for any pair of interchanged particles, we are able to reduce three Faddeev components to a set of coupled channel equations in one Jacobi coordinate. We thus highly increase the computational efficiency and fully take into account the symmetrization of the system. In addition, the correct Coulomb asymptotic wavefunctions Eq. (2.32) are used instead of plane waves in STURMXX, since our problem involves charged particles. The propagation method is put to work in our new version of the code. Because for the triple-alpha problem, the R-matrix propagation method is needed for very large radii, a new technique of screening the off-diagonal couplings (see Sec. 2.2.3) is added to the HHR3a code in order to improve the numerical stability of the calculation. When the off-diagonal couplings die off we can perform a matching of the scattering wavefunction with the correct asymptotic behavior Eq. (2.32). We also implement the local representation of the wavefunction propagation in HHR3a to test the validity of this method.

Chapter 3

Three-body reaction rate

Nuclear burning is the main source of energy for a star to maintain its active existence. It is not only the Q-value of a given nuclear reaction but also its reaction rate that is important to determine the amount of energy produced in a star. The nuclear reaction rate is defined as the number of reactions per unit time and unit volume. This quantity is well understood for a two-body reaction. It certainly depends on the nuclear cross section σ , which measures the probability for this reaction to occur with respect to any pair of interacting particles. The reaction rate per particle pair is defined as σv . However in a stellar plasma, the relative velocity v is not the same for all pairs but follows a thermal distribution, namely the Maxwell-Boltzmann distribution $P(v)$:

$$\begin{aligned} P(v) dv &= P(E) dE \\ &= \left(\frac{m_{ab}}{2\pi kT} \right)^{3/2} e^{-\frac{m_{ab}v^2}{2kT}} 4\pi v^2 dv, \\ &= \frac{2}{\sqrt{\pi}} \frac{1}{(kT)^{3/2}} \sqrt{E} e^{-\frac{E}{kT}} dE, \end{aligned} \tag{3.1}$$

where m_{ab} is the reduced mass of the two interacting particles a and b ; k is the Boltzmann constant and T is the stellar temperature. The reaction rate per pair of interacting particles is obtained by averaging the cross section over the thermal distribution of relative velocities $vP(v)$:

$$\begin{aligned} \langle \sigma v \rangle &= \int_0^\infty v P(v) \sigma(v) dv = \int_0^\infty v P(E) \sigma(E) dE, \\ &= \left(\frac{8}{\pi m_{ab}} \right)^{1/2} \frac{1}{(kT)^{3/2}} \int_0^\infty E \sigma(E) e^{-\frac{E}{kT}} dE. \end{aligned} \quad (3.2)$$

At high temperatures, Eq. (3.2) can be used to evaluate the triple-alpha rate since this reaction is considered as two two-body problems [10]. In the low temperature regime where the three-alpha direct capture mechanism is dominant, Eq. (3.2) is no longer applicable. In this chapter we will present a detailed derivation of the three-body reaction rate formula.

3.1 Maxwell-Boltzmann energy distribution for a three-body system

Since the astrophysical reaction rate is calculated by integrating the energy dependent rate over the Maxwell-Boltzmann energy distribution, it is important to derive the formula of this distribution for a three-body system. We define \mathbf{v}_1 as the relative velocity of particle 1 and 2, and \mathbf{v}_2 as the relative velocity between particle 3 and the center of mass of system 12. The probability of finding particle 1, 2, 3 with these relative velocities in the range of $(\mathbf{v}_1, \mathbf{v}_1 + d\mathbf{v}_1)$ and $(\mathbf{v}_2, \mathbf{v}_2 + d\mathbf{v}_2)$ can be expressed as:

$$P(\mathbf{v}_1) d\mathbf{v}_1 P(\mathbf{v}_2) d\mathbf{v}_2 = \left(\frac{m\mu_1}{2\pi kT} \right)^{\frac{3}{2}} e^{-\frac{m\mu_1 v_1^2}{2kT}} \left(\frac{m\mu_2}{2\pi kT} \right)^{\frac{3}{2}} e^{-\frac{m\mu_2 v_2^2}{2kT}} d\mathbf{v}_1 d\mathbf{v}_2, \quad (3.3)$$

where $k = 8.617 \times 10^5 \text{ eV K}^{-1}$ is Boltzmann constant and T is the temperature. μ_1 and μ_2 are defined in terms of the ratio between the mass of particle i and the scaled mass, $A_i = \frac{m_i}{m}$:

$$\mu_1 = \frac{A_1 A_2}{A_1 + A_2}, \quad (3.4)$$

$$\mu_2 = \frac{A_3(A_1 + A_2)}{A_1 + A_2 + A_3}. \quad (3.5)$$

The conjugate Jacobi momenta corresponding to \mathbf{x} and \mathbf{y} coordinates are defined as:

$$\mathbf{k}_x = \frac{\mathbf{p}_1}{\sqrt{\mu_1}} = \frac{m\mu_1 \mathbf{v}_1}{\sqrt{\mu_1}} = m\sqrt{\mu_1} \mathbf{v}_1, \quad (3.6)$$

$$\mathbf{k}_y = \frac{\mathbf{p}_2}{\sqrt{\mu_2}} = \frac{m\mu_2 \mathbf{v}_2}{\sqrt{\mu_2}} = m\sqrt{\mu_2} \mathbf{v}_2. \quad (3.7)$$

Using Eq. (3.6) and Eq. (3.7) we can rewrite Eq. (3.3) as:

$$P(\mathbf{v}_1) d\mathbf{v}_1 P(\mathbf{v}_2) d\mathbf{v}_2 = \frac{1}{(2\pi kT)^3} \frac{1}{m^3} e^{-\frac{k_x^2}{2mkT}} e^{-\frac{k_y^2}{2mkT}} d\mathbf{k}_x d\mathbf{k}_y. \quad (3.8)$$

The fact that $k_x^2 + k_y^2 = \kappa^2$ allows us to simplify the above equation to:

$$P(\mathbf{v}_1) d\mathbf{v}_1 P(\mathbf{v}_2) d\mathbf{v}_2 = \frac{1}{(2\pi kT)^3} \frac{1}{m^3} e^{-\frac{\kappa^2}{2mkT}} \kappa^5 \sin^2\theta_\kappa \cos^2\theta_\kappa d\kappa d\theta_\kappa d\Omega_{k_x} d\Omega_{k_y}. \quad (3.9)$$

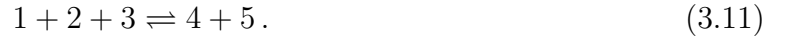
Performing the integration of Eq. (3.9) over all the angles, we obtain the Maxwell Boltzmann distribution for the three-body system:

$$P(E) = \frac{1}{2(kT)^3} e^{-\frac{E}{kT}} E^2. \quad (3.10)$$

Comparing to Eq. (3.1) which is obtained for a two-body system, the three-body Maxwell-Boltzmann distribution has very different energy and temperature dependence. In the next section we will apply this new distribution to derive a general formula for the three-body reaction rate.

3.2 The reaction rate formalism for three-body capture

We first consider a reaction in which three particles 1, 2, 3 fuse to create two new particles 4, 5:



The ratio of the reaction rates between the direct and inverse process is defined as in [62]:

$$\frac{\langle 123 \rangle}{\langle 45 \rangle} = \frac{g_4 g_5}{g_1 g_2 g_3} \left(\frac{A_4 A_5}{A_1 A_2 A_3} \right)^{\frac{3}{2}} \left(\frac{2\pi\hbar^2}{mkT} \right)^{\frac{3}{2}} \frac{1 + \Delta_{123}}{1 + \delta_{45}} e^{-\frac{Q}{kT}}, \quad (3.12)$$

where $\Delta_{123} = \delta_{12} + \delta_{23} + \delta_{31} + 2\delta_{123}$ to account for the effects introduced by the number of identical particles in the reactions; the Q-value of the reaction is defined as $Q = E_{123} - E_{45}$; g_i is the degenerate factor for particle i which can be calculated from its total spin J_i : $g_i = 2J_i + 1$; \hbar , k , A_i and m have their usual meanings as defined before; T is the temperature of the environment.

The three-body $\langle 123 \rangle$ and two-body $\langle 45 \rangle$ reaction rates are defined using Eq. (3.10) and

Eq. (3.1) respectively for averaging over the Maxwell-Boltzmann distribution:

$$\langle 123 \rangle = \frac{1}{2(kT)^3} \int R_{123}(E_{123}) e^{-\frac{E_{123}}{kT}} E_{123}^2 dE_{123}, \quad (3.13)$$

$$\langle 45 \rangle = \left(\frac{8}{\pi m_{45}} \right)^{\frac{1}{2}} \frac{1}{(kT)^{\frac{3}{2}}} \int \sigma(E_{45}) e^{-\frac{E_{45}}{kT}} E_{45} dE_{45}. \quad (3.14)$$

In these equations, E_{123} and E_{45} are the three-body and the two-body relative energies, respectively. $\sigma(E_{45})$ is the reaction cross section of system (4, 5) which is equivalent to $R_{123}(E_{123})$ in the three-body case and $m_{45} = \frac{m_4 m_5}{m_4 + m_5}$ is the reduced mass of a two-body system (4, 5).

Using the Q-value definition, we rewrite Eq. (3.13) in terms of an integration over the two-body energy E_{45} :

$$\langle 123 \rangle = \frac{1}{2(kT)^3} e^{-\frac{Q}{kT}} \int R_{123}(E_{123}) e^{-\frac{E_{45}}{kT}} E_{123}^2 dE_{45}. \quad (3.15)$$

Inserting Eq. (3.15) and Eq. (3.14) into Eq. (3.12) and after some simple algebraic reduction, we obtain:

$$\frac{\int R_{123}(E_{123}) e^{-\frac{E_{45}}{kT}} E_{123}^2 dE_{45}}{\int \sigma(E_{45}) e^{-\frac{E_{45}}{kT}} E_{45} dE_{45}} = \frac{g_4 g_5}{g_1 g_2 g_3} \left(\frac{A_4 A_5}{A_1 A_2 A_3} \right)^{\frac{3}{2}} \frac{1 + \Delta_{123}}{1 + \delta_{45}} \left(\frac{2\pi \hbar^2}{mkT} \right)^{\frac{3}{2}} \left(\frac{32}{\pi m_{45}} \right)^{\frac{1}{2}}. \quad (3.16)$$

In order for Eq. (3.16) to be valid with all reactions as described by Eq. (3.11), the integrands themselves have to satisfy:

$$R_{123}(E_{123}) E_{123}^2 = \frac{g_4 g_5}{g_1 g_2 g_3} \left(\frac{A_4 A_5}{A_1 A_2 A_3} \right)^{\frac{3}{2}} \frac{1 + \Delta_{123}}{1 + \delta_{45}} \left(\frac{2\pi \hbar^2}{mkT} \right)^{\frac{3}{2}} \left(\frac{32}{\pi m_{45}} \right)^{\frac{1}{2}} \sigma(E_{45}) E_{45}. \quad (3.17)$$

This formula is correct when all 1, 2, 3, 4, and 5 are particles. In our triple-alpha reaction, one of the products is a photon, so the formula for this case is slightly different. We now need to transform the cross section σ_{45} for the case of two real particles into the photo-disintegration cross section where one of these particles is a photon. Let us consider a two-body process:

$$4 + 5 \rightleftharpoons \gamma + 0. \quad (3.18)$$

The ratio between the direct and inverse cross section is defined in [9]:

$$\frac{\sigma(E_{45})}{\sigma_\gamma(E_\gamma)} = \frac{g_\gamma g_0}{g_4 g_5} \frac{E_\gamma^2}{2 m_{45} c^2 E_{45}} (1 + \delta_{45}), \quad (3.19)$$

where all the variables in this equation have the same meaning as described before.

Inserting Eq. (3.19) into Eq. (3.17) we have:

$$R_{123}(E_{123}) E_{123}^2 = \frac{g_\gamma g_0}{g_1 g_2 g_3} \left(\frac{A_4 A_5}{A_1 A_2 A_3} \right)^{\frac{3}{2}} (1 + \Delta_{123}) \left(\frac{2\pi \hbar^2}{mkT} \right)^{\frac{3}{2}} \left(\frac{32}{\pi m_{45}} \right)^{\frac{1}{2}} \frac{E_\gamma^2}{2m_{45}c^2} \sigma_\gamma(E_\gamma). \quad (3.20)$$

Expressing m_{45} in terms of A_4 and A_5 , we could further reduce Eq. (3.20) to a simpler form:

$$R_{123}(E_{123}) = \frac{\hbar^3}{c^2} \frac{8\pi}{m^3 (\mu_1 \mu_2)^{\frac{3}{2}}} (1 + \Delta_{123}) \frac{g_\gamma g_0}{g_1 g_2 g_3} \frac{E_\gamma^2}{E_{123}^2} \sigma_\gamma(E_\gamma). \quad (3.21)$$

Eq. (3.21) is the energy dependent rate for the fusion of three particles 1, 2, 3 into particle 0 with the emission of a photon γ :

$$1 + 2 + 3 \rightleftharpoons \gamma + 0. \quad (3.22)$$

We denote $E = E_{123}$ for convenience and then integrate $R_{123}(E)$ over the three-body Maxwell-Boltzmann distribution Eq. (3.10) to obtain the astrophysical three-body reaction rate:

$$\langle R_{123} \rangle = N_A^2 \frac{1}{2(kT)^3} \int_0^\infty e^{-\frac{E}{kT}} E^2 R_{123}(E) dE. \quad (3.23)$$

Inserting Eq. (3.21) into Eq. (3.23) and using the expression for the reaction Q-value ($Q = E - E_\gamma$), we have:

$$\langle R_{123} \rangle = (1 + \Delta_{123}) N_A^2 \frac{1}{2(kT)^3} e^{-\frac{Q}{kT}} \frac{\hbar^3}{c^2} \frac{8\pi}{m^3 (\mu_1 \mu_2)^{\frac{3}{2}}} \frac{g_\gamma g_0}{g_1 g_2 g_3} \int_{|Q|}^\infty e^{-\frac{E_\gamma}{kT}} E_\gamma^2 \sigma_\gamma(E_\gamma) dE_\gamma. \quad (3.24)$$

Since the photon has only 2 polarization directions, we have $g_\gamma = 2$. We replace $(1 + \Delta_{123})$ by $p!$ where p is the number of identical particles. Eq. (3.24) is now reduced to:

$$\langle R_{123} \rangle = p! N_A^2 \frac{\hbar^3}{c^2} \frac{8\pi}{m^3 (\mu_1 \mu_2)^{\frac{3}{2}}} \frac{g_0}{g_1 g_2 g_3} e^{-\frac{Q}{kT}} \frac{1}{(kT)^3} \int_{|Q|}^\infty e^{-\frac{E_\gamma}{kT}} E_\gamma^2 \sigma_\gamma(E_\gamma) dE_\gamma. \quad (3.25)$$

Eq. (3.25) relates the radiative capture reaction rate to the photo-disintegration cross section σ_γ which depends on the electromagnetic transition strength $dB(E\lambda)/dE$ through which the reaction occurs [11, 27, 46, 63]:

$$\sigma_\gamma = \frac{(2\pi)^3 (\lambda + 1)}{\lambda [(2\lambda + 1)!!]^2} \left(\frac{E_\gamma}{\hbar c} \right)^{2\lambda - 1} \frac{dB(E\lambda)}{dE}. \quad (3.26)$$

The missing ingredient to calculate the three-body reaction rate (Eq. (3.25)) is the electromagnetic transition strength $dB(E\lambda)/dE$. In the next section, we will discuss how to calculate this quantity for a three-body system in the HH representation.

3.3 Three-body quadrupole transition function

At low energies, the triple-alpha reaction proceeds through a quadrupole transition from the 0^+ continuum to the 2_1^+ bound state in ^{12}C . The quadrupole transition operator $E2$ for any three-body system has the general form in coordinate space:

$$E_{2m} = e[Z_1 a_1^2 Y_{2m}(\hat{\mathbf{a}}_1) + Z_2 a_2^2 Y_{2m}(\hat{\mathbf{a}}_2) + Z_3 a_3^2 Y_{2m}(\hat{\mathbf{a}}_3)], \quad (3.27)$$

Where, Z_i is the charge of particle i and Y is the spherical harmonic function and $m = -2, -1, 0, 1, 2$ are the projections of angular momentum $l = 2$; a_1, a_2 , and a_3 are the distances from the center of mass of the three-body system to each particle as seen in Fig. 2.2. Vectors \mathbf{a}_i can be expressed in terms of the scaled Jacobi coordinates (\mathbf{x}, \mathbf{y}) :

$$\mathbf{a}_1 = -\frac{\sqrt{\mu_1}}{A_1} \mathbf{x} - \frac{\sqrt{\mu_2}}{A_1 + A_2} \mathbf{y}, \quad (3.28)$$

$$\mathbf{a}_2 = \frac{\sqrt{\mu_1}}{A_2} \mathbf{x} - \frac{\sqrt{\mu_2}}{A_1 + A_2} \mathbf{y}, \quad (3.29)$$

$$\mathbf{a}_3 = \frac{\sqrt{\mu_2}}{A_3} \mathbf{y}. \quad (3.30)$$

For a given vector relationship $\mathbf{a} = \mathbf{a}_1 + \mathbf{a}_2$, we have the following properties for spherical functions as proven in [51]:

$$a^l C_{lm}(\hat{\mathbf{a}}) = \sum_{\lambda, \mu} \left(\frac{2l!}{2\lambda! 2(l-\lambda)!} \right)^{\frac{1}{2}} a_1^{l-\lambda} a_2^\lambda C_{l-\lambda, m-\mu}(\hat{\mathbf{a}}_1) C_{\lambda, \mu}(\hat{\mathbf{a}}_2) \langle l-\lambda \ m-\mu \ \lambda \ \mu | l \ m \rangle, \quad (3.31)$$

where $C_{lm} = \left(\frac{2l+1}{4\pi} \right)^{-1/2} Y_{lm}$.

Applying Eq. (3.31) to Eq. (3.28), Eq. (3.29) and Eq. (3.30) we can express the transition operator $E2$ in terms of hyperspherical coordinates (ρ, θ) . For the triple-alpha system in

which three particles are identical: $A_1 = A_2 = A_3 = A$ and $Z_1 = Z_2 = Z_3 = Z$, the quadruple transition operator reduces to much simpler form (see Appendix B for details):

$$E_{2m} = \frac{eZ}{A} \left[(\rho \sin\theta)^2 Y_{2m}(\hat{\mathbf{x}}) + (\rho \cos\theta)^2 Y_{2m}(\hat{\mathbf{y}}) \right]. \quad (3.32)$$

A quadrupole transition from the initial continuum state of total spin L and momentum κ to the final bound state of spin L' is characterized by the strength function:

$$\frac{dB(E2, L \rightarrow L')}{d\kappa d\Omega_5^\kappa} = \sum_{mM'M} |\langle L'M' | E_{2m} | LM; \kappa \rangle|^2, \quad (3.33)$$

where $d\Omega_5^\kappa = \sin^2\theta_\kappa \cos^2\theta_\kappa d\theta_\kappa d\Omega_{\kappa x} d\Omega_{\kappa y}$. Because our system is composed of spin zero particles, the total angular momentum L also indicates the total spin. The total $B(E2)$ is computed by integrating over all the continuum states $|LM, \kappa\rangle$:

$$B(E2, L \rightarrow L') = \int \frac{dB(E2, L \rightarrow L')}{d\kappa d\Omega_5^\kappa} \kappa^5 d\kappa d\Omega_5^\kappa. \quad (3.34)$$

Applying the relationship $\kappa = \frac{\sqrt{2mE}}{\hbar}$ to Eq. (3.34) we obtain:

$$B(E2, L \rightarrow L') = \int \frac{dB(E2, L \rightarrow L')}{d\kappa d\Omega_5^\kappa} \frac{E^2}{2} \left(\frac{2m}{\hbar^2} \right)^3 d\Omega_5^\kappa dE. \quad (3.35)$$

Using Eq. (3.33) and comparing Eq. (3.35) with the following equation:

$$B(E2, L \rightarrow L') = \int \frac{dB(E2, L \rightarrow L')}{dE} dE, \quad (3.36)$$

we obtain the energy dependent strength function:

$$\frac{dB(E2, L \rightarrow L')}{dE} = \frac{E^2}{2} \left(\frac{2m}{\hbar^2} \right)^3 \int \sum_{mM'M} |\langle L'M' | E_{2m} | LM; \kappa \rangle|^2 d\Omega_5^\kappa. \quad (3.37)$$

We use the hyperspherical expansion of the wavefunctions in Eq. (2.8) and Eq. (2.28) to expand the squared modulus in Eq. (3.37):

$$\begin{aligned} \langle L'M' | (E2)_m | LM; \kappa \rangle &= \sum_{K^i l_x^i l_y^i} \sum_{K l_x l_y} \sum_{K' l'_x l'_y} \left(\varphi_{K^i}^{l_x^i l_y^i} \left[Y_{l_x^i} \otimes Y_{l_y^i} \right]_{LM} \right)_\kappa^* \\ &\times \langle K' l'_x l'_y L'M' | (E2)_m | K l_x l_y K^i l_x^i l_y^i LM \rangle_s, \end{aligned} \quad (3.38)$$

where the subscript s denotes the spatial part (ρ, θ, Ω_5) in the wavefunction expansions.

The integration in Eq. (3.37) is then simplified using the following properties of spherical harmonics functions Y_{lm} and hyper-angular functions $\varphi_K^{l_x l_y}$:

$$\int d\Omega_{k_x} Y_{l_x^i m_x^i}^*(\Omega_{k_x}) Y_{l_x^i m_x^i}(\Omega_{k_x}) = \delta_{l_x^i l_x^i} \delta_{m_x^i m_x^i}, \quad (3.39)$$

$$\int d\Omega_{k_y} Y_{l_y^i m_y^i}^*(\Omega_{k_y}) Y_{l_y^i m_y^i}(\Omega_{k_y}) = \delta_{l_y^i l_y^i} \delta_{m_y^i m_y^i}, \quad (3.40)$$

$$\int \sin^2 \theta_\kappa \cos^2 \theta_\kappa d\theta_\kappa (\varphi_{K^i}^{l_x^i l_y^i}(\theta_\kappa))^* \varphi_{K_1^i}^{l_x^i l_y^i}(\theta_\kappa) = \delta_{K^i, K_1^i}. \quad (3.41)$$

The integration in Eq. (3.37) is reduced to (see Appendix B for details):

$$\begin{aligned} &\int |\langle L'M' | (E2)_m | LM; \kappa \rangle|^2 d\Omega_5^\kappa \\ &= \sum_{K^i l_x^i l_y^i} \left| \sum_{K l_x l_y} \sum_{K' l'_x l'_y} \langle K' l'_x l'_y L'M' | E_{2m} | K l_x l_y K^i l_x^i l_y^i LM \rangle_s \right|^2. \end{aligned} \quad (3.42)$$

Inserting Eq. (3.42) into Eq. (3.37) and employing the Wigner-Eckart theorem from [51] we obtain:

$$\frac{dB(E2, L \rightarrow L')}{dE} = \frac{E^2}{2} \left(\frac{2m}{\hbar^2} \right)^3 \frac{\hat{L}'^2}{\hat{L}^2} \times \sum_{K^i l_x^i l_y^i} \left| \sum_{K l_x l_y} \sum_{K' l'_x l'_y} \langle K' l'_x l'_y L' || E_{2m} || K l_x l_y K^i l_x^i l_y^i L \rangle_s \right|^2, \quad (3.43)$$

where $\hat{L}^2 = 2L + 1$. Let's first calculate the matrix element in Eq. (3.43) using Eq. (3.32):

$$\begin{aligned} \langle K' l'_x l'_y L' || E_{2m} || K l_x l_y K^i l_x^i l_y^i L \rangle_s &= \frac{eZ}{A} \langle K' l'_x l'_y L' || (\rho \sin\theta)^2 Y_2(\hat{\mathbf{x}}) || K l_x l_y K^i l_x^i l_y^i L \rangle_s \\ &+ \frac{eZ}{A} \langle K' l'_x l'_y L' || (\rho \cos\theta)^2 Y_2(\hat{\mathbf{y}}) || K l_x l_y K^i l_x^i l_y^i L \rangle_s. \end{aligned} \quad (3.44)$$

We denote *M.E.1* and *M.E.2* as the first and second term on the *r.h.s* of Eq. (3.44). *M.E.1* can be factorized into two terms of which one contains the hyper-variable dependence and the other is angular momentum dependent:

$$M.E.1 = \frac{eZ}{A} \langle K' l'_x l'_y | (\rho \sin\theta)^2 | K l_x l_y K^i l_x^i l_y^i \rangle \langle l'_x l'_y L' || Y_2(\hat{x}) || l_x l_y L \rangle. \quad (3.45)$$

The first bra-ket term on the *r.h.s* of Eq. (3.45) is calculated by taking an integral over the hyper-radial and hyper-angular parts of the wavefunctions:

$$\langle K' l'_x l'_y | (\rho \sin\theta)^2 | K l_x l_y K^i l_x^i l_y^i \rangle = \left(\frac{2mE}{\hbar^2} \right)^{-5/4} I_\rho I_{1,\theta}, \quad (3.46)$$

where we define:

$$I_\rho = \int d\rho \chi_{K'l'_x l'_y}^*(\rho) \rho^2 \chi_{Kl_x l_y}^{K'l'_x l'_y}(\rho), \quad (3.47)$$

$$I_{1,\theta} = \int \sin^2\theta \cos^2\theta d\theta (\varphi_{K'}^{l'_x l'_y}(\theta))^* \sin^2\theta \varphi_K^{l_x l_y}(\theta). \quad (3.48)$$

The second bra-ket term on the *r.h.s* of Eq. (3.45) can be explicitly calculated using angular momentum algebra [51] as:

$$\langle l'_x l'_y L' || Y_2(\hat{x}) || l_x l_y L \rangle = \delta(l_y, l'_y) \sqrt{\frac{5}{4\pi}} \hat{L} \hat{l}_x \hat{l}_x (-1)^{2+l'_y+L+2l'_x} \left\{ \begin{matrix} L' & L & 2 \\ l_x & l'_x & l'_y \end{matrix} \right\} \left(\begin{matrix} l'_x & 2 & l_x \\ 0 & 0 & 0 \end{matrix} \right). \quad (3.49)$$

Performing a similar calculation for the second term on the *r.h.s* of of Eq. (3.44) (*M.E.2*), we obtain the final result for a three-body quadrupole transition strength function:

$$\frac{dB(E2, L \rightarrow L')}{dE} = \sqrt{\frac{m}{2\hbar^2}} \frac{1}{\sqrt{E}} \hat{L}'^2 \left(\frac{eZ}{A} \right)^2 \sum_{K'l'_x l'_y} \left| \sum_{Kl_x l_y} \sum_{K'l'_x l'_y} I_\rho (I_{1,\theta} A_1 + I_{2,\theta} A_2) \right|^2, \quad (3.50)$$

where

$$I_\rho = \int d\rho \chi_{K'l'_x l'_y}^*(\rho) \rho^2 \chi_{Kl_x l_y}^{K'l'_x l'_y}(\rho), \quad (3.51)$$

$$I_{1,\theta} = \int \sin^2\theta \cos^2\theta d\theta (\varphi_{K'}^{l'_x l'_y}(\theta))^* \sin^2\theta \varphi_K^{l_x l_y}(\theta), \quad (3.52)$$

$$I_{2,\theta} = \int \sin^2\theta \cos^2\theta d\theta (\varphi_{K'}^{l'_x l'_y}(\theta))^* \cos^2\theta \varphi_K^{l_x l_y}(\theta), \quad (3.53)$$

with coefficients:

$$A_1 = \delta(l_y, l'_y) \sqrt{\frac{5}{4\pi}} \hat{l}_x \hat{l}'_x (-1)^{2+l'_y+L+2l'_x} \begin{Bmatrix} L' & L & 2 \\ l_x & l'_x & l'_y \end{Bmatrix} \begin{pmatrix} l'_x & 2 & l_x \\ 0 & 0 & 0 \end{pmatrix}, \quad (3.54)$$

$$A_2 = \delta(l_x, l'_x) \sqrt{\frac{5}{4\pi}} \hat{l}_y \hat{l}'_y (-1)^{2+l'_x+L'+l'_y+l_y} \begin{Bmatrix} L' & L & 2 \\ l_y & l'_y & l'_x \end{Bmatrix} \begin{pmatrix} l'_y & 2 & l_y \\ 0 & 0 & 0 \end{pmatrix}. \quad (3.55)$$

The quadrupole transition strength in Eq. (3.50) is used to obtain the triple-alpha reaction rate. Calculation of Eq.(3.50) requires correct solutions of the 2_1^+ bound state and the 0^+ continuum states of ^{12}C . The convergence study will focus of these quantities of our interest.

Chapter 4

Results

4.1 Interactions

Although there has been progress in many body techniques as discussed in Sec. 1.3, the non-resonant continuum description of ^{12}C at a microscopic 12 body level is not yet attainable. Since the alpha particle is the strongest bound nucleus among few-nucleon systems, it is reasonable to formulate the 12-body problem of ^{12}C as an effective three-body system. This argument is supported by the dominant triple-alpha structure found in the microscopic calculation of both the 2_1^+ bound state and the Hoyle resonant state of ^{12}C [31]. In order to obtain a good description for this three-body system, a well-constrained effective two-body interaction for any pair of alpha particles is necessary. Ali and Bodmer [64] had developed a phenomenological alpha-alpha potential for s , d and g waves by fitting the experimental phase shifts at low energies. We employ the effective alpha-alpha interaction from [65] which modified the Ali-Bodmer potential to exactly reproduced the ^8Be s-wave resonance:

$$V_{\alpha\alpha} = (125\hat{P}_{l=0} + 20\hat{P}_{l=2}) e^{-r^2/1.53^2} - 30.18 e^{-r^2/2.85^2}. \quad (4.1)$$

This l -dependent potential has a very strong repulsive core in the s-wave to simulate the Pauli exclusion principle in the alpha-alpha system. It reproduces successfully the low energy phase shifts as well as the 0^+ resonant state of ${}^8\text{Be}$ at 0.092 MeV.

Another interaction we investigated is a local Gaussian alpha-alpha interaction independent of energy and angular momentum [66]. Even though this interaction fits the scattering data very well, it creates deep s-wave states which are forbidden and need to be projected out of the model space. Although the handling of forbidden states in computing the ${}^{12}\text{C}(2_1^+)$ bound state was possible, this additional difficulty was hard to overcome within the three-body continuum.

In order to describe the triple-alpha system, a three-body force V_{3b} is introduced to the sum of three pairwise alpha-alpha interactions $V_{\alpha\alpha}$. It is important to understand the physical interpretation of an effective three-body force used in our calculation. The three-body force was first considered in nuclear physics to explain the discrepancy between the measured binding energy of the triton and the theoretical calculations using different realistic nucleon-nucleon interactions [67, 68]. Although the triton is one of the simplest systems in nuclear physics, treating nucleons as fundamental particles that interact via a two-body potential gave rise to such discrepancy. An effective three-body force was then needed to account for this simplification. Our triple-alpha system is largely reduced since each alpha particle is composed of four nucleons. We introduce a three-body force in our model to compensate for the reduction of the model space, allowing us to reproduce the experimental observable of a three-alpha system. In this work, a three-body interaction $V_{3b}(\rho) = V_0 e^{-\rho^2/\rho_0^2}$ is added to the Hamiltonian to reproduce the experimental bound state energy of the 2_1^+ state as well as the Hoyle resonant state 0_2^+ of ${}^{12}\text{C}$ (similarly to [65]). Since the effective three-body force originates from the fact that the alpha particle is not a fundamental particle, we expect the

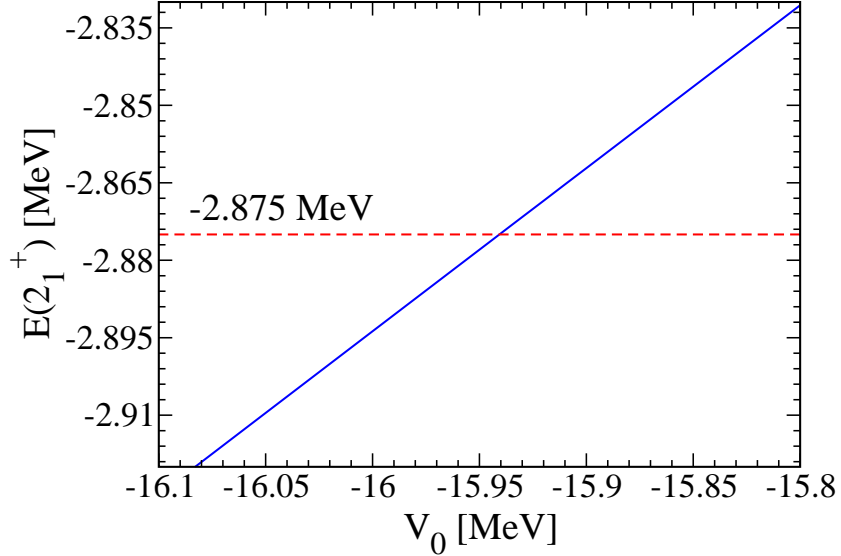


Figure 4.1: Dependence of the three-body binding energy of the 2_1^+ bound state of ^{12}C on the depth of a three-body force $V_{3b}(\rho) = V_0 e^{-\rho^2/\rho_0^2}$. The maximum hyper-angular momentum K_{max} is taken as 20 for which the results are converged.

range of this interaction to be approximately the overall size of the three-alpha system. We therefore take $\rho_0 = 6$ fm as the position where the three alpha particles touch each other and adjust the depth V_0 of the three-body interaction to measurements.

The blue solid curve in Fig. 4.1 represents the dependence of the $^{12}\text{C}(2_1^+)$ binding energy on the three-body potential depth V_0 for a fixed alpha-alpha interaction. The red dash line is the experimental value -2.875 MeV of this state [69]. As can be seen, we need $V_0 = -15.94$ MeV to reproduce the measured excitation energy of the 2_1^+ bound state. The same story applies to the Hoyle state. Fig. 4.2 shows a dependence of the resonant energy on the depth of a three-body force V_0 (blue curve). The red curve is again the experimental energy (0.3795 MeV) [69]. A depth of $V_0 = -19.46$ MeV reproduces the measured Hoyle state. This interaction is then used to calculate all the 0^+ continuum states. In Table 4.1, we summarize the parameters for the three-body interactions used in our calculations.

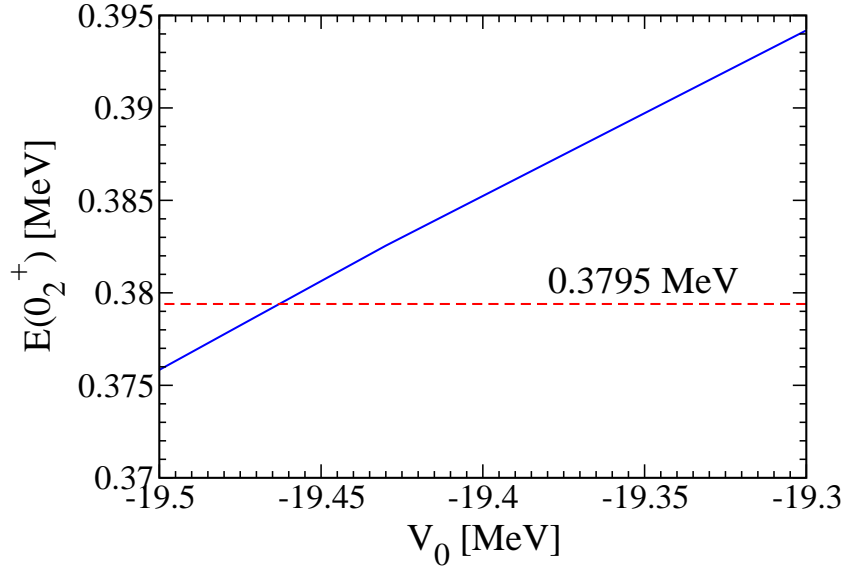


Figure 4.2: Dependence of the Hoyle resonant energy of ^{12}C on the depth of a three-body force $V_{3b}(\rho) = V_0 e^{-\rho^2/\rho_0^2}$. The maximum hyper-angular momentum K_{max} is taken as 26 for which the results are converged.

Table 4.1: The three-body interactions to reproduce the experimental energies [69] of the 2_1^+ bound state and 0_2^+ resonant state in ^{12}C .

J^Π	$V_0(\text{MeV})$	$\rho_0(\text{fm})$	$E(\text{MeV})$
2_1^+	-15.94	6	-2.875
0_2^+	-19.46	6	0.380

In addition to the nuclear interaction we include the Coulomb potential:

$$V_{\alpha\alpha}^{Coul}(r) = Z^2 e^2 \times \begin{cases} \left(\frac{3}{2} - \frac{r^2}{2r_{Coul}^2} \right) \frac{1}{r_{Coul}} & r \leq r_{Coul} \\ \frac{1}{r} & r \geq r_{Coul} \end{cases} \quad (4.2)$$

Here, Z is the charge of an alpha particle, r is the distance between two alpha particles, and r_{Coul} is the Coulomb radius which is taken as twice the alpha particle radius $r_{Coul} = 2.94$ fm.

4.2 The 2_1^+ bound state

A three-body bound state is obtained by solving the set of coupled channels equations (Eq. (2.16)) with a boundary condition that the wavefunction goes to zero at large ρ [33]. These coupled equations are solved by expanding the hyper-radial wavefunction in terms of the Laguerre basis [61] which forms a complete and orthogonal set (Sec. 2.2.4). The matrix diagonalization is then applied to obtain eigenenergies and eigenvectors. We choose the scaling radius ρ_0 in Eq. (2.71) for the Laguerre polynomial to be 0.3 fm. The standard mass m is taken as the nucleon mass (939 MeV). The hyper-angular integrations are performed using Gauss-Jacobi quadrature on a grid with 70 points. The hyper-radial integrations are performed using Gauss-Laguerre quadrature on a grid with 180 points. 40 basis polynomials are used in the hyper-radial wave expansion Eq. (2.70). A actual input file with all the necessary variables for a bound state calculation can be seen in Appendix C.

Fig. 4.3 shows the convergence of the three-body binding energy of the 2_1^+ bound state of ^{12}C with the size of the model space represented here by the maximum hyper-angular momentum K_{max} . For a given K_{max} we can calculate how many channels are included in the wavefunction expansion (Eq. (2.8)), e.g., $K_{\text{max}} = 20$ produces 36 channels in the expansion. From Fig. 4.3, the bound state energy starts converging at $K_{\text{max}} = 12$. Therefore, energy convergence is guaranteed by choosing $K_{\text{max}} = 20$. The bound state energy of the 2^+ state of ^{12}C converges to the experimental value $E = -2.875$ MeV [69] with respect to

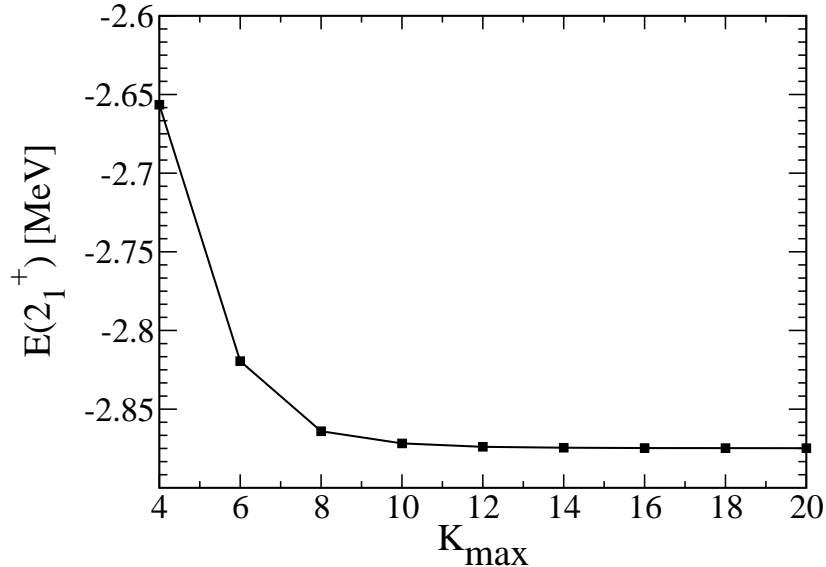


Figure 4.3: Dependence of the three-body binding energy of the 2_1^+ bound state of ^{12}C on the maximum hyper-angular momentum K_{\max} .

the three-alpha threshold.

The convergence of the *rms* radius of the $^{12}\text{C}(2_1^+)$ bound state with respect to K_{\max} is shown in Fig. 4.4. Again, the result converges very well for $K_{\max} = 20$. Our final value for the *rms* radius is 2.459 fm which is close to 2.50 fm obtained in a microscopic calculation done by Chernykh *et al.*[31]. This agreement validates the three-body approximation for the 2^+ bound state.

In Table 4.2, we compare the three-body binding energy and the *rms* radius of the 2_1^+ bound state of ^{12}C obtained from our three-body calculation with experimental data and other studies. Our results reproduce the experimental data and agree very well with an independent three-body study using the hyperspherical adiabatic method [26]. The microscopic calculations in [31] overestimate the binding energy of the $^{12}\text{C}(2_1^+)$ state but provide a similar *rms* radius.

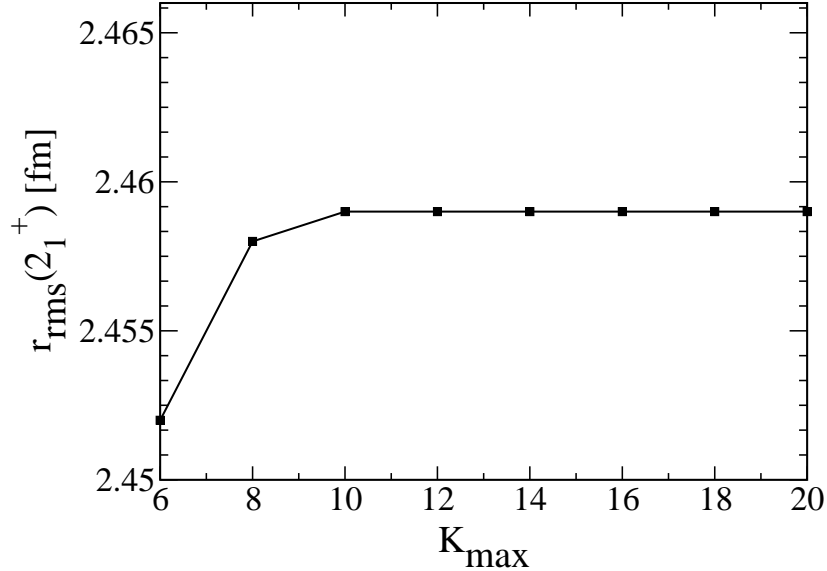


Figure 4.4: Dependence of the r_{rms} radius of the 2_1^+ bound state of ^{12}C on the maximum hyper-angular momentum K_{\max} .

Table 4.2: Comparison of the three-body binding energy and the rms radius of the 2_1^+ bound state of ^{12}C obtained from our three-body calculation with other studies: a three-body hyperspherical adiabatic method [26], a microscopic Fermionic Molecular Dynamics method [31] and experimental data [69].

	This work	[26]	[31]	Exp [69]
E (MeV)	-2.875	-2.875	-3.74	-2.875
r_{rms} (fm)	2.459	2.45	2.50	

In Fig. 4.5, we plot the r_{rms} radius as a function of the maximum radius ρ_{\max} of the calculated 2_1^+ bound state wavefunction. As can be seen, the r_{rms} no longer depends on the maximum radius of the bound state wavefunction for $\rho_{\max} > 20$ fm. All the calculations through out this work employ a bound state wavefunction up to 200 fm, thus the correct

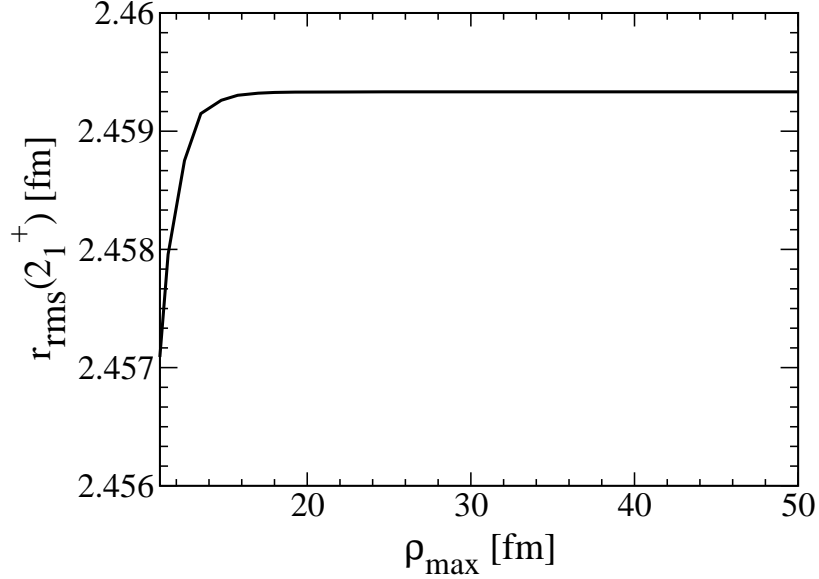


Figure 4.5: The r_{rms} radius as a function of the maximum radius of the box in which the $^{12}\text{C}(2_1^+)$ bound state wavefunction is calculated.

contribution from the long-range part of the wavefunction to the rate at low temperatures is ensured.

Given that the wavefunction of the $^{12}\text{C}(2_1^+)$ bound state is available in our work, it is interesting to look at the cluster structure of this state. We next construct the density distribution function from the 2_1^+ wavefunction to study its structure:

$$P(r, R) = \int |\Psi(\mathbf{r}, \mathbf{R})|^2 d\hat{\mathbf{r}} d\hat{\mathbf{R}}. \quad (4.3)$$

Here r is the radius between the two alpha particles and R is the distance from its center of mass to the third alpha. In Fig. 4.6 we present the density distribution $P(r, R)$ for the 2_1^+ bound state of ^{12}C in contour color style. We observe a maximum in the density distribution at $r \sim R \sim 3$ fm. This indicates that the dominant configuration for the $^{12}\text{C}(2_1^+)$ bound state is a nearly equilateral triangle in which each pair of particles is ~ 3 fm apart. Since an

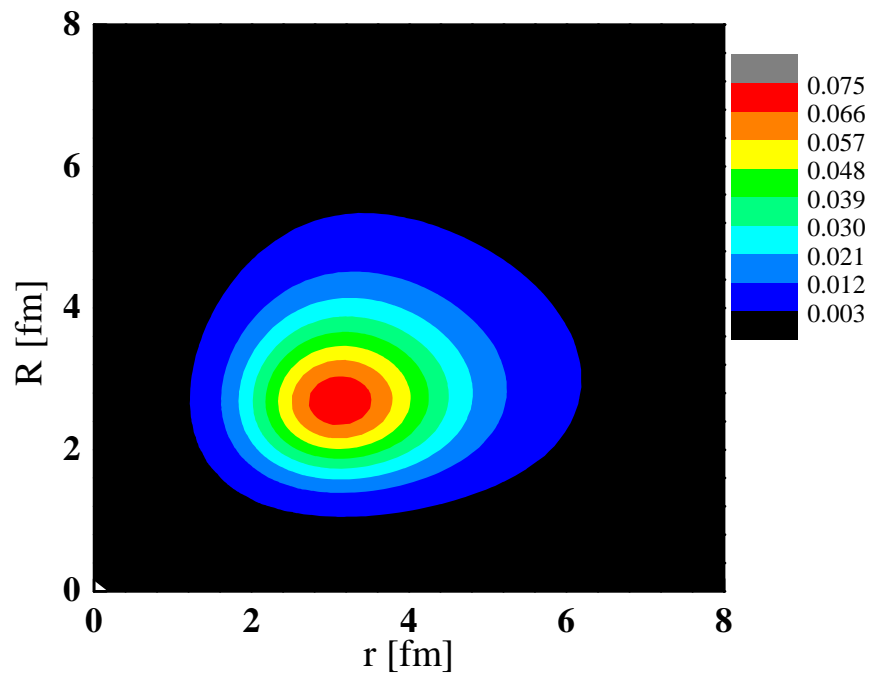


Figure 4.6: The density distribution for the 2_1^+ bound state of ^{12}C .

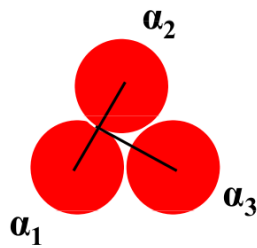


Figure 4.7: The dominant three-alpha cluster in the $^{12}\text{C}(2_1^+)$ bound state: three alpha particles touch each other and form an equilateral triangle.

alpha particle has a radius of 1.47 fm, three alpha particles almost touch each other in this dominant configuration. This configuration is described in Fig. 4.7.

4.3 The 0_2^+ Hoyle state

The three alpha particle system is driven by a strong Coulomb interaction of which the off-diagonal couplings are long-range in the HH representation. Therefore, solving the coupled channels equations (Eq. (2.30)) for positive energy E is not a trivial task. The HHR method which combines the R-matrix expansion and R-matrix propagation in the HH basis is employed to overcome this difficulty. Details of this method are presented in Sec. 2.2. The numerical calculations are performed using our HHR3a code (see Sec. 2.2.4). We use an R-matrix box size of 50 fm with 50 poles included in the R-matrix expansion and a radial step size of 0.05 fm. The hyper-angular integrations are performed using Gauss-Jacobi quadrature on a grid with 100 points. As mentioned before, the fixed logarithmic derivative in the R-matrix calculation is selected to be zero. Our converged calculation is obtained with the maximum hyper-momentum $K_{\max} = 26$, the screening radius $\rho_{\text{screen}} = 800$ fm and the screening diffuseness $a_{\text{screen}} = 10$ fm. The convergence of these quantities are thoroughly tested. The R matrix is propagated out to 3000 fm, sufficiently large to perform the Coulomb asymptotic matching. A detailed input file for the calculation of 0^+ continuum states can be viewed in Appendix C.

The 0^+ continuum states of ^{12}C are calculated for $E = 0.01 - 0.5$ MeV. The quadrupole transition strength Eq. (3.37) is then constructed using the 2_1^+ bound state wavefunction and the 0^+ resonant and non-resonant continuum states. Therefore, in our calculations we treat the resonant and non-resonant process on the same footing. Fig. 4.8 shows the quadrupole

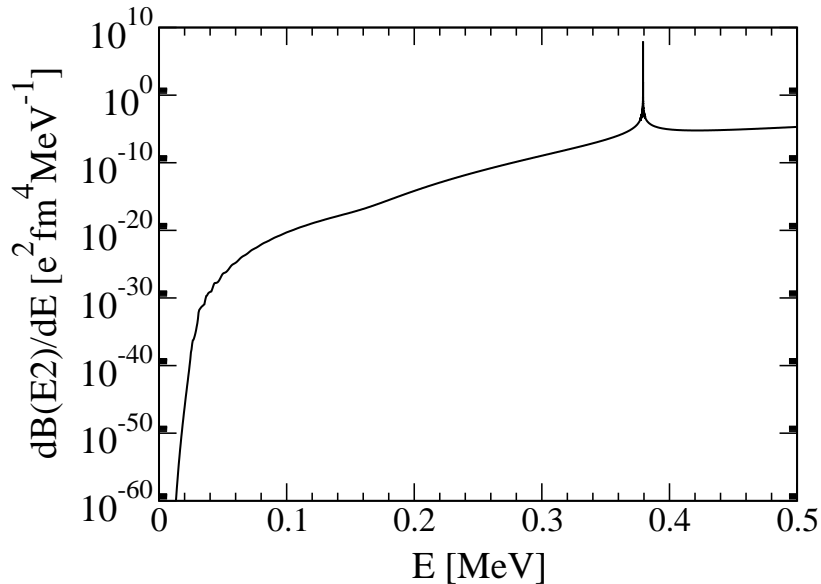


Figure 4.8: The quadrupole transition strength $dB(E2)/dE$ as a function the three-alpha relative energy E .

transition strength as a function of the relative energy for the three interacting alpha particles. The curve peaks at the measured Hoyle resonance energy ($E = 0.38$ MeV). As we expect, the strength function decreases as it approaches the lower energy regime. Below 0.05 MeV there is a sharp reduction of the transition strength below which the formation of ^{12}C becomes unlikely.

It is important to discuss our method to extract the Hoyle resonant energy as well as its convergence. We repeated the calculation of the quadrupole transition strength function around the 0_2^+ resonant energy in Fig. 4.8 for different values of K_{max} . The results are presented in Fig. 4.9. As can be verified, the position of the peak in the quadrupole transition strength curve is sensitive to the size of our model space. As K_{max} increases the discrepancy between the two consecutive curves is reduced which indicates a converged behavior. For each K_{max} , the resonant energy is obtained from the maximum of the transition

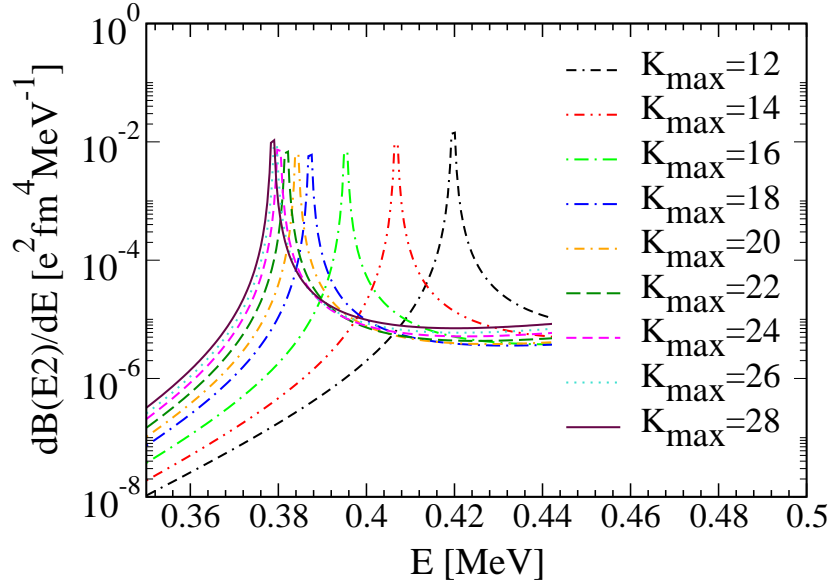


Figure 4.9: The quadrupole transition strength function $dB(E2)/dE$ around the Hoyle resonant energy is calculated with different values of hyper-momentum K_{\max} .

strength function and plotted in Fig. 4.10. A clearer convergence pattern of the $^{12}\text{C}(0_2^+)$ Hoyle resonant energy with respect to the size of the model space is depicted in this graph. As expected, we find that the convergence for the Hoyle resonant state is slower than for the bound state. The result begins to converge at $K_{\max} = 26$ and this is the point we choose to fit the three-body force to reproduce the experimental energy of 0.38 MeV [69] with respect to the three-alpha threshold. One might wonder why can we use the phase-shift analysis to extract the resonant energy instead? Because the problem involves so many channels, it is not possible for us to continuously link the eigenphases at various energies. In addition one cannot associate the eigenphases with certain hyper-spherical harmonics channels. A specific algorithm would need to be developed to tackle those challenges.

In order to estimate the uncertainty in extracting the Hoyle resonant energy, the data in Fig. 4.10 is fitted to an exponential function $y = A + Be^{-Cx}$. When K_{\max} goes to infinity

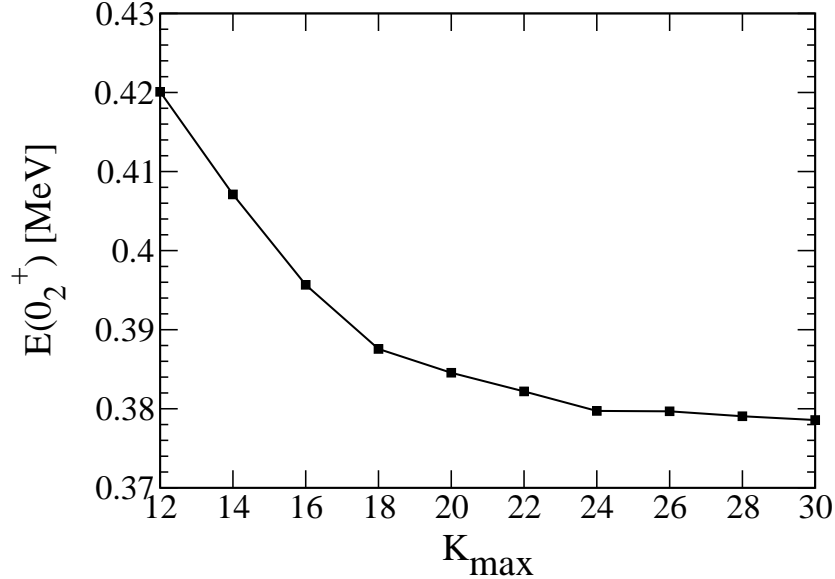


Figure 4.10: Dependence of the three-body energy of the 0_2^+ Hoyle state of ^{12}C on the maximum hyper-angular momentum K_{\max} .

this function approaches its converged value which is then compared to the value of the energy at $K_{\max} = 26$ to obtain an uncertainty of 4%.

By using the wavefunction at the Hoyle resonance energy we are able to construct the density distribution function as in Eq. (4.3) for the 0_2^+ state in ^{12}C . This quantity illustrates the spatial structure of the Hoyle state, a topic of tremendous interest for many years [31, 70, 71, 72, 73]. Fig. 4.11 depicts the density distribution in a color contour plot. The dominant configuration for the Hoyle state, corresponding to the biggest maxima in the density plot, is the prolate triangle in which two alpha particles are near each other (~ 3.7 fm) and further away from the third alpha (~ 5.2 fm). This result is in agreement with the finding in [65, 73] and the alpha cluster configuration for this case is presented in Fig. 4.12a. Thus, a $^8\text{Be}-\alpha$ like structure dominates the ^{12}C Hoyle resonant state as expected. We also observe two smaller maxima for the density distribution function. One of them supports

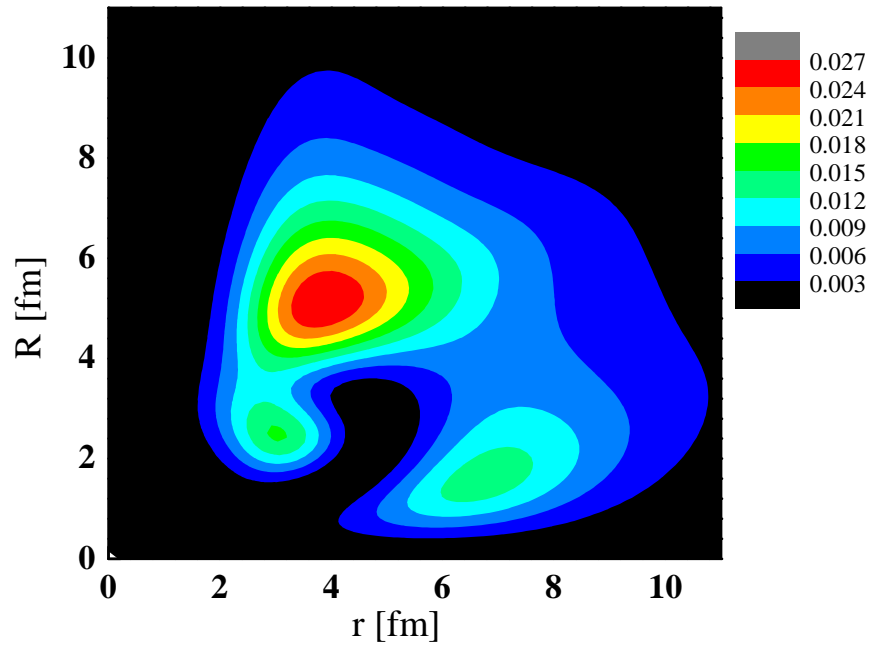


Figure 4.11: The density distribution for the 0_2^+ resonance state of ^{12}C .

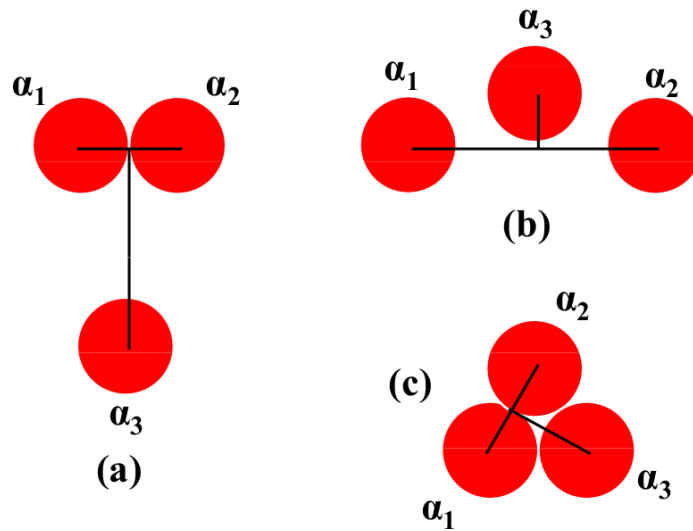


Figure 4.12: Three triple-alpha configurations of the 0_2^+ resonance in ^{12}C : the prolate triangle (a), the oblate triangle (b) and the equilateral triangle (c).

an oblate triangle configuration of three alpha particles, where two alpha particles are ~ 7 fm apart and its center of mass is ~ 1.5 fm from the third alpha. This configuration forms an almost chain-like structure as depicted in Fig. 4.12b. An *ab initio* calculation using lattice effective field theory method [72] also supports the existence of this three-alpha cluster structure for the Hoyle state. The other small maximum indicates an almost equilateral triangle with a distance of ~ 3 fm between any pair of alpha particles. This is the same structure obtained for the 2_1^+ bound state and is presented in Fig. 4.12c. The weights of these two latter configurations are about two times smaller than that of the prolate triangle configuration. In conclusion, we find three different configurations for the triple-alpha in which the prolate triangle is dominant, but the oblate triangle (almost chain-like) and the equilateral triangle also contribute significantly to the structure of the Hoyle state of ^{12}C . Note that our results are limited to the relative magnitudes of r and R only. The average angle between these two vectors requires further investigation. Fig. 4.12 does not consider the angular orientation of the two radius vectors.

4.4 Testing the new code HHR3a

HHR3a is developed from the programs FaCE [33] and STURMXX [60], which are originally designed for a *core + n + n* problem, to introduce the correct symmetry and the right boundary conditions for the three identical charged-particle system. It is important to ensure that the new code operates properly. When only the diagonal Coulomb couplings are considered, Eq. (2.30) becomes Eq. (2.31) which has analytic solutions as seen in Sec. 2.1.3. We therefore can use this case to test our numerical method. In Fig. 4.13, we compare the numerical solution of Eq. (2.31) calculated at $E = 0.5$ MeV for the 0^+ scattering wavefunction of the

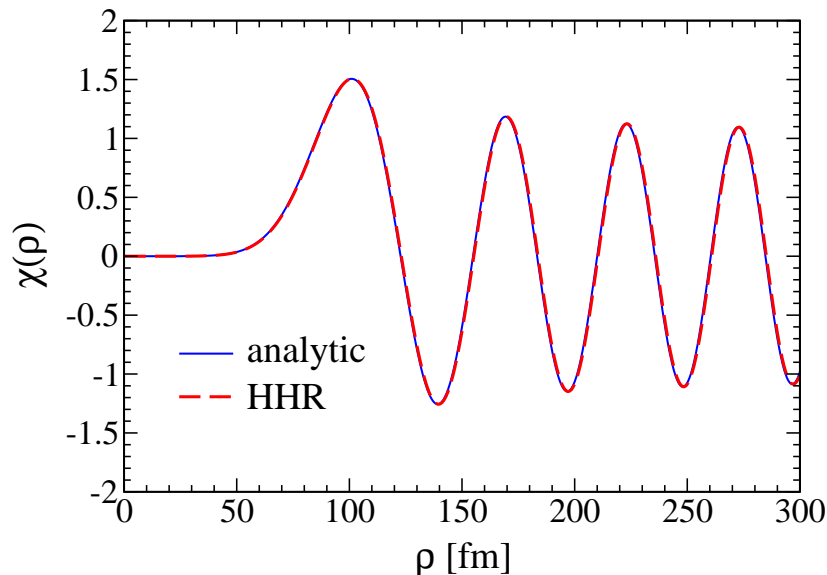


Figure 4.13: A numerical solution (dashed) of Eq. (2.30) at $E = 0.5$ MeV for the 0^+ scattering wavefunction of the triple-alpha system when only the diagonal Coulomb couplings are taken into account is compared with the analytic solution (solid).

three-alpha system with its analytic solution expressed in terms of the confluent hypergeometric function of the first kind [74]. We observe a fine agreement between the two curves indicating the correct behavior of the codes in the absence of off-diagonal couplings. In this graph we only present one component of the wavefunction in the hyperspherical expansion of which the incoming channel and the outgoing channel are characterized by the set of quantum numbers $Kl_xl_y = 000$, however all other components show equal level of agreement.

We then perform a calculation for the triple-alpha rate when only the diagonal Coulomb couplings are taken into account by employing the 0^+ continuum wavefunctions above, obtained both numerically and analytically. The results are compared and plotted in Fig. 4.14. We find that the reaction rate calculated from our numerical solutions produced by HHR3a agrees very well with that obtain using the analytic wavefunctions. Therefore, we conclude that the new code is able to reproduce the analytic results for a simplified three-alpha prob-

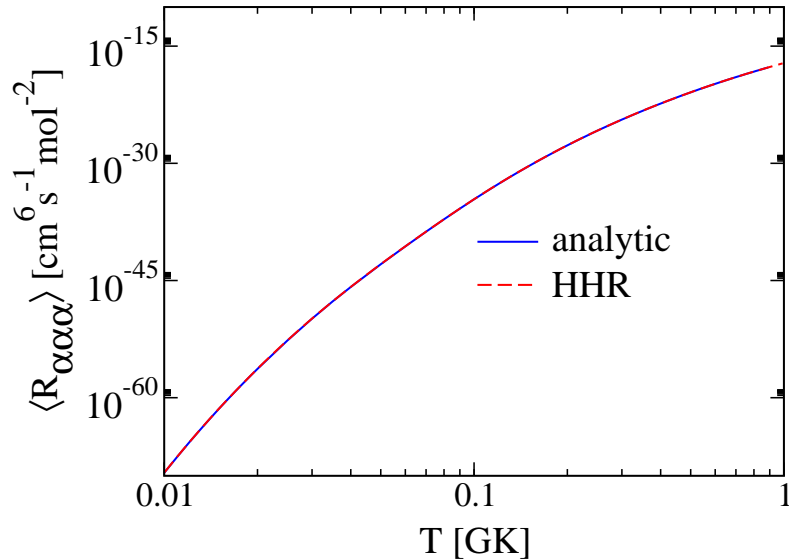


Figure 4.14: The triple-alpha reaction rate is computed for the diagonal Coulomb case using the numerical solution of Fig. 4.13 (dashed) and compared to the analytic solution (solid).

lem in which only the diagonal Coulomb interaction is present.

We also test the new code for a realistic case when both nuclear and Coulomb interactions are included. The HHR3a code produces the Hoyle resonant state at the right energy and the results agree well with an independent study in [26] given the same interactions. We also reproduce the results from [75] for the bound states as well as the resonant states of $^{12}\text{C}(0^+)$. These reinforce the validity of our new code.

4.5 Convergence and uncertainty

It is important for us to carefully study the convergence properties of our method, given the well known difficulty of the three charged-particle problem. Since the 2^+ bound state wavefunction is easily obtained and fully converged for the effective three-alpha system when both the nuclear and Coulomb interactions are present, in all of our tests presented in this

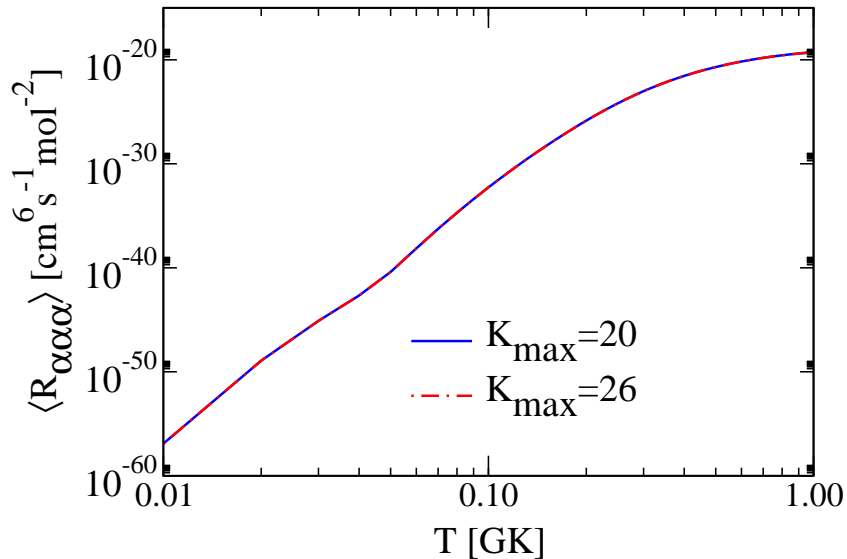


Figure 4.15: The reaction rate as a function of temperature for the fictitious three-alpha system in which only Coulomb interactions are included: $K_{\text{max}} = 20$ (solid) and $K_{\text{max}} = 26$ (dot-dashed).

section we will fix the bound state wavefunction and only study the convergence of the solutions of the coupled channels equations (Eq. (2.30)) for scattering states.

4.5.1 The impact of using screening potentials

With the help of the R-matrix propagation method we are able to perform calculations out to a very large radius and obtain stable results with Coulomb interactions only. Fig. 4.15 presents the calculated reaction rate for a fictitious three-alpha system in which only the Coulomb interactions play a role. We perform two calculations of the rate with different sizes of the model space $K_{\text{max}} = 20$ and $K_{\text{max}} = 26$ in order to study the convergence of this system when just long-range couplings are introduced. It is important to note that the bound state wavefunction which is employed to compute the rate is obtained using a realistic triple-alpha model where the nuclear and Coulomb interactions are fully coupled. For the

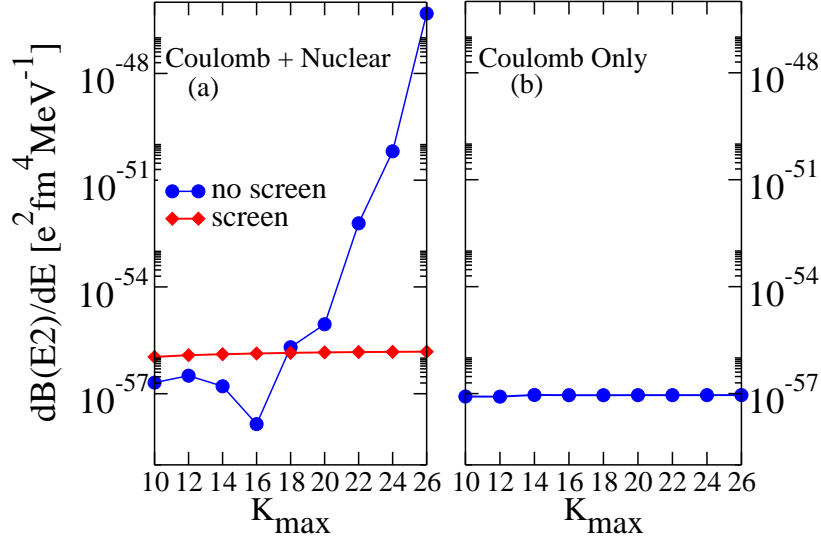


Figure 4.16: The quadrupole transition strength $dB(E2)/dE$ at $E = 0.01$ MeV as a function of model space K_{\max} when both nuclear and Coulomb interaction (a) and only Coulomb interaction (b) are present in the three-alpha system.

0^+ continuum, the R matrix is propagated out to a very large radius (3000 fm) in order for the rate to be fully converged. This demonstrates the challenge of our problem. The two calculations in Fig. 4.15 are different by 0.3% indicating a very good convergence of the triple-alpha rate with respect to K_{\max} when only the Coulomb interaction is considered. It is important to note that the results converge faster when no nuclear interaction is taken into account. In fact, we only need $K_{\max} = 20$ for this case to converge while $K_{\max} = 26$ is required for the realistic triple-alpha system.

When nuclear interactions are introduced, the very narrow resonances occur in both the two-body and three-body systems, and lead to a degradation of our propagation technique, increasing numerical instabilities, especially in the turning point region. This is confirmed in Fig. 4.16 in which the quadrupole transition strength $dB(E2)/dE$ at $E = 0.01$ MeV from the 0^+ continuum states to the 2_1^+ bound state of ^{12}C is plotted as a function of K_{\max} .

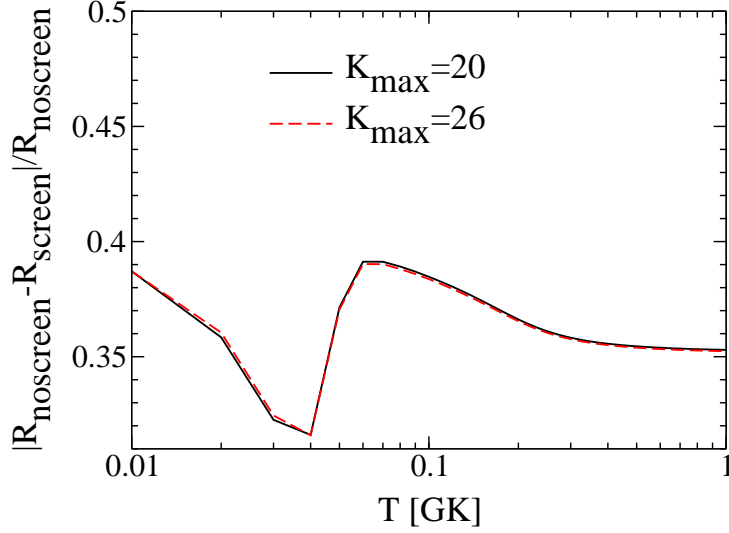


Figure 4.17: Relative differences between screening and no screening calculations for the fictitious three-alpha scattering system in which only Coulomb interactions are introduced. The screening calculation is performed for $K_{\max} = 26$ and $\rho_{\text{screen}} = 800$ fm. Calculations without screening are performed for $K_{\max} = 20$ (solid) and $K_{\max} = 26$ (dashed).

$dB(E2)/dE$ on the left panel (Fig. 4.16a, blue-circle curve) is computed for a real triple-alpha system where both nuclear and Coulomb interactions are present and no screening potential is used. Unlike the Coulomb only case (Fig. 4.16b), the result does not converge as we increase the size of our model space.

As mentioned before, we tackle this problem by screening the off-diagonal couplings by a Woods-Saxon multiplying factor $[1 + \exp((\rho - \rho_{\text{screen}})/a_{\text{screen}})]^{-1}$. Note that this only affects the Coulomb part of the couplings. The red-diamond curve in Fig. 4.16a shows a much more stable behavior of the quadrupole transition strength $dB(E2)/dE$ when screening is introduced. However, it is necessary for us to ensure that important physics is not left out. We therefore compare in Fig. 4.17 screening and no screening calculations for a scattering system of three alpha particles when only Coulomb interactions are included. For this case, there are no resonances in either the two-body or three-body system, thus the

propagation technique is stable and we are able to determine the impact of introducing screening potentials. We perform a calculation of the triple-alpha rate using the screening technique with $\rho_{\text{screen}} = 800$ fm. This calculation fully converges at $K_{\text{max}} = 26$. This result is then compared to calculations with no screening, presented as the solid and dashed curves for $K_{\text{max}} = 20$ and $K_{\text{max}} = 26$, respectively. Uncertainty of the reaction rate due to the screening technique ranges from 35% to 39% for temperatures within 0.01 – 1 GK. These are very small numbers given the many orders of magnitude involved in the problem.

4.5.2 Convergence study

It was shown in Fig. 4.16a that when the screening technique is not used, the quadrupole transition strength $dB(E2)/dE$ at 0.01 MeV diverges as the size of the model space increases. However if one screens the off-diagonal couplings at large radii, the result becomes more stable and a converged triple-alpha rate can be obtained (see red-diamond line in Fig. 4.16a). The convergence study of our triple-alpha rate is performed carefully.

Although using screening improves the numerical stability and the convergence of the result, unfortunately it also introduces an approximation into our calculation. It is important to verify that the triple-alpha rate converges with screening radius and we capture the important physics of our problem. In Fig. 4.18 we present three calculations of the quadrupole transition strength $dB(E2)/dE$ at low energies by varying the diffuseness a_{screen} of the Woods-saxon screening potential from 10 fm to 30 fm while fixing the screening radius at 800 fm. The results are not sensitive to this parameter, we thus fix the diffuseness of 10 fm throughout this work.

In order to study the convergence of the triple-alpha rate with respect to the screening radius ρ_{screen} , we perform calculations of the triple-alpha rate using three different screening

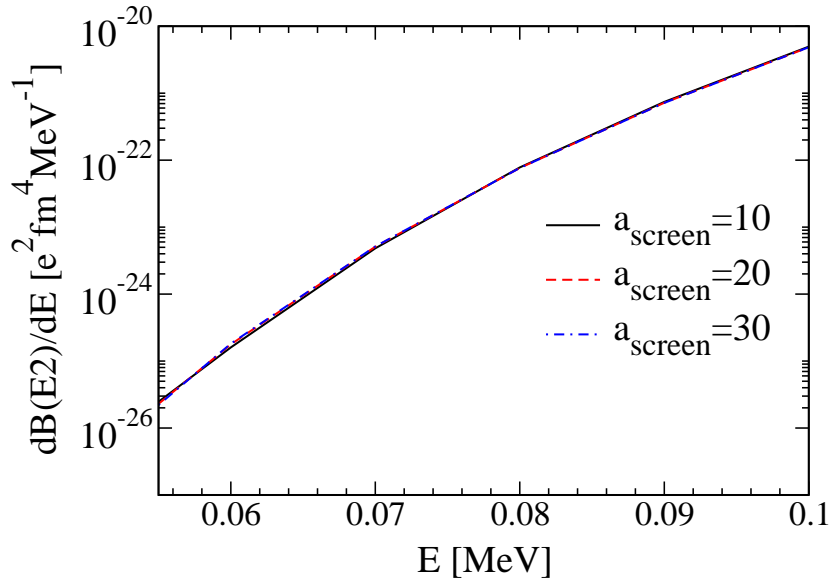


Figure 4.18: The quadrupole transition strength are computed at low energies using three different values of the diffuseness in screening potentials: $a_{\text{screen}} = 10$ fm (solid), $a_{\text{screen}} = 20$ fm (dashed), $a_{\text{screen}} = 30$ fm (dot-dashed).

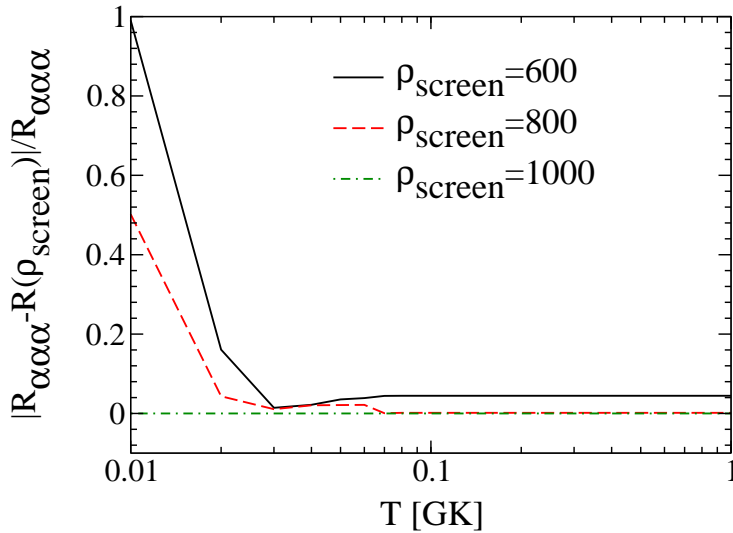


Figure 4.19: Relative differences between the triple-alpha rate calculated at several screening radii and its converged value. The reaction rates calculated using $\rho_{\text{screen}} = 600$ fm (solid), $\rho_{\text{screen}} = 800$ fm (dashed), $\rho_{\text{screen}} = 1000$ fm (dot-dashed) are compared with the converged rate in Table 4.4.

radii: 600, 800 and 1000 fm. These results are plotted in comparison with the converged rate in Table 4.4. As seen from Fig. 4.19, the triple-alpha reaction rate in general converges for $\rho_{\text{screen}} \geq 800$ fm with a small uncertainty of 5% for temperature within 0.02 – 1 GK. Only at $T = 0.01$ GK, the uncertainty gets much larger ($\sim 50\%$). At those low temperatures, a larger screening radius is needed because the capture happens at much larger distances. We will see in chapter 6 that the triple-alpha reaction rate at $T = 0.01$ GK does not have significant impact on many astrophysical phenomena.

Fig. 4.20 shows the convergence of the triple-alpha reaction rate with hyper-momentum K_{max} . We perform four calculations of the rate as a function of temperature by varying K_{max} from 20 to 26. The results are plotted in comparison with the converged rate in Table 4.4. $K_{\text{max}} = 20$ is not large enough to reproduce the experimental 0_2^+ Hoyle resonant state, therefore the reaction rate for this case is larger than other curves for $T > 0.1$ GK. The uncertainty of the triple-alpha rate is larger at high temperatures due to the sensitivity of the Hoyle resonant energy with K_{max} . The uncertainty is less than 20% for $K_{\text{max}} = 26$.

In Fig. 4.21 we look at the quadrupole strength function, which is a principal ingredient for calculating the reaction rate, at a specific energy of $E = 0.01$ MeV. If $dB(E2)/dE$ converges, then the cross section and the reaction rate will also converge. Since the $dB(E2)/dE$ has an exponential behavior, namely $y = A - Be^{-Cx}$ as a function of hyper-momentum K_{max} , we are able to extrapolate the converged value of $dB(E2)/dE$ when $K_{\text{max}} \rightarrow \infty$. For this very low energy, the extrapolated value of the rate differs from that at $K_{\text{max}} = 26$ by only 4%. Our calculation is therefore very well converged with the size of the model space.

Although the screening radius ρ_{screen} and the size of the model space K_{max} are the major sources of uncertainties in our calculation due to the difficulty of the long-range behavior in a three charged-particle system, we have fully tested the convergence of our results with other

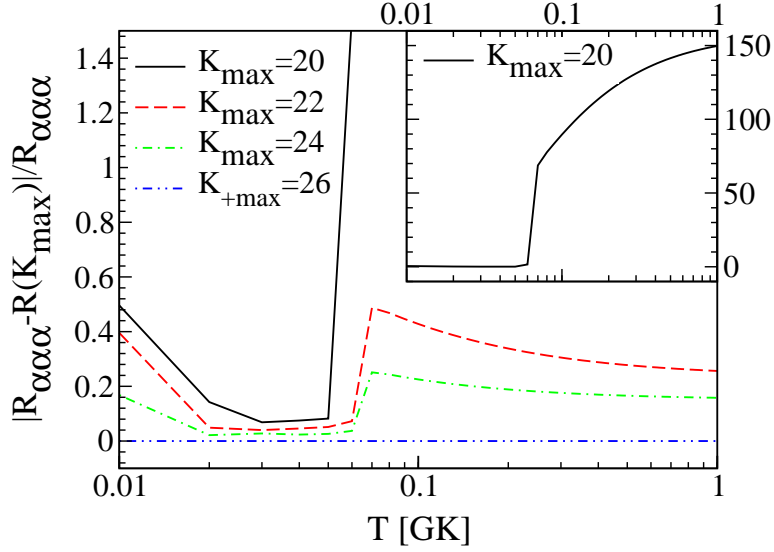


Figure 4.20: Relative differences between the triple-alpha rate calculated at several maximum hyper-momentum K_{\max} and its converged value. The reaction rates calculated using $K_{\max} = 20$ (solid), $K_{\max} = 22$ (dashed), $K_{\max} = 24$ (dot-dashed), $K_{\max} = 26$ (dot-dot-dashed) are compared with the converged rate in Table 4.4.

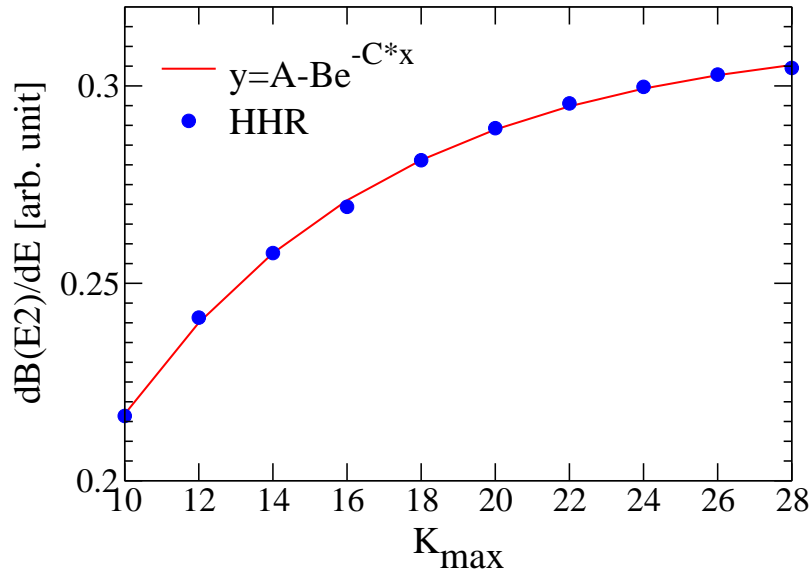


Figure 4.21: Convergence of the quadrupole transition strength $dB(E2)/dE$ with hyper-momentum K_{\max} for $E = 0.01$ MeV.

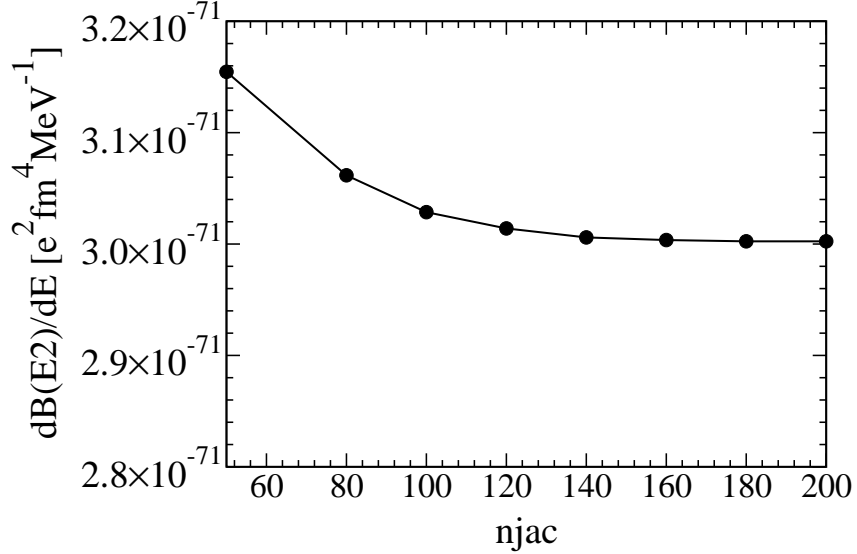


Figure 4.22: Convergence of the quadrupole transition strength $\frac{dB(E2)}{dE}$ with n_{jac} , number of Gauss-Jacobi quadrature grid point, for a given low energy of 0.01 MeV

variables in the numerical method for completeness. In Fig. 4.22, we study the convergence of the quadrupole transition strength $\frac{dB(E2)}{dE}$ with n_{jac} , the size of the Gauss-Jacobi quadrature grid for the hyper-angular integrations, for a given low energy of 0.01 MeV. The result converges very well for $n_{jac} \geq 100$. As mention earlier we use $n_{jac}=100$ in our calculation of the triple-alpha rate.

It is important that the matching radius ρ_a is large enough so that we can match the interior wavefunction with the diagonal Coulomb wavefunction in the asymptotic region. We perform a calculation of the quadrupole strength $\frac{dB(E2)}{dE}$ at very low energy (0.01 MeV) for which case the matching radius is expected to be very large. Different values of the matching radius are used to compute $\frac{dB(E2)}{dE}$. The results are plotted in Fig. 4.23 and it is clear that our calculation converges with the matching radius for $\rho_a \geq 2000$ fm. We use a matching radius of 3000 fm in our calculation of the triple-alpha rate.

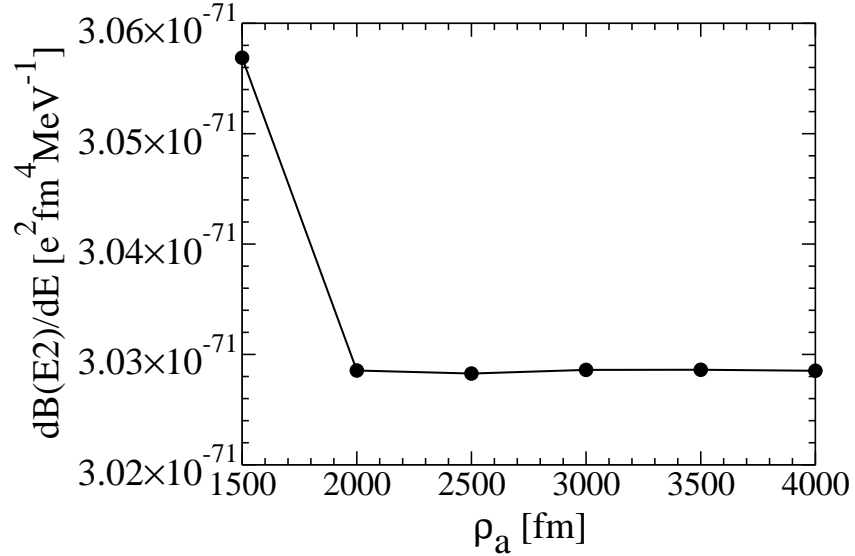


Figure 4.23: Convergence of the quadrupole transition strength $\text{dB}(E2)/dE$ with matching radius ρ_a for a given low energy of 0.01 MeV

4.5.3 Interaction uncertainty

Since the alpha-alpha interaction is phenomenological based, there are ambiguities that need to be considered. In order to study the sensitivity of the triple-alpha rate to the nuclear interaction and the three-body force, we consider employing the same Hamiltonian as [15] to calculate the 0^+ continuum. In [15] the alpha-alpha interaction is given as:

$$V_{\alpha\alpha}(r) = 100.0 e^{-r^2/1.00^2} - 30.35 e^{-r^2/2.13^2} . \quad (4.4)$$

Unlike in [15], we find that a three-body interaction is needed to reproduce the relevant Hoyle state. As seen from Fig. 4.24, the new interaction produces a triple-alpha reaction rate at low temperatures 4 orders of magnitude higher than that obtained with the Ali-Bodmer interaction [64, 65]. While the Ali-Bodmer potential reproduces the α - α phase shifts, the

interaction in [15] does not. It therefore provides an upper limit for the error associated with $V_{\alpha\alpha}$ ambiguities.

Another issue concerning the uncertainty of the alpha-alpha interactions is as discussed in [75]. It was stated in [75] that additional narrow resonances are produced when using the shallow potentials as compared to the deep alpha-alpha interaction. This may lead to unexpected contributions to the triple-alpha reaction rate. As seen from Fig. 4.8, no other peaks in addition to the Hoyle state is found in the quadrupole transition strength function plot in the low energy regime. Therefore the enhancement in our low-temperature triple-alpha rate purely comes from the three-alpha non-resonant contribution. The difference in the spectroscopic properties between the deep and shallow alpha-alpha interactions may have larger impact in the evaluation of the triple-alpha rate at high temperatures where high lying resonances play an important role. However, we expect this effect to be too small to be detected in our temperature region of interest, given the many orders of magnitude involved in the problem.

4.5.4 Rate uncertainty

Our final rate is normalized to the standard rate from NACRE for temperatures $T \geq 0.5$ GK, where the Hoyle resonance completely dominates. At this temperature, the triple-alpha reaction proceeds through the very narrow Hoyle resonance and its rate is proportional to the gamma decay width Γ_γ [9], known experimentally $\Gamma_\gamma = 3.7 \times 10^{-9}$ MeV [69]. In our calculation we fit the photo-disintegration cross section σ_γ to a Breit-Wigner shape:

$$\sigma_\gamma = \frac{1}{2} \frac{\pi \hbar^2 c^2}{E_\gamma^2} \frac{\Gamma_{\alpha\alpha\alpha} \Gamma_\gamma}{(E - E_R)^2 + \Gamma^2/4}, \quad (4.5)$$

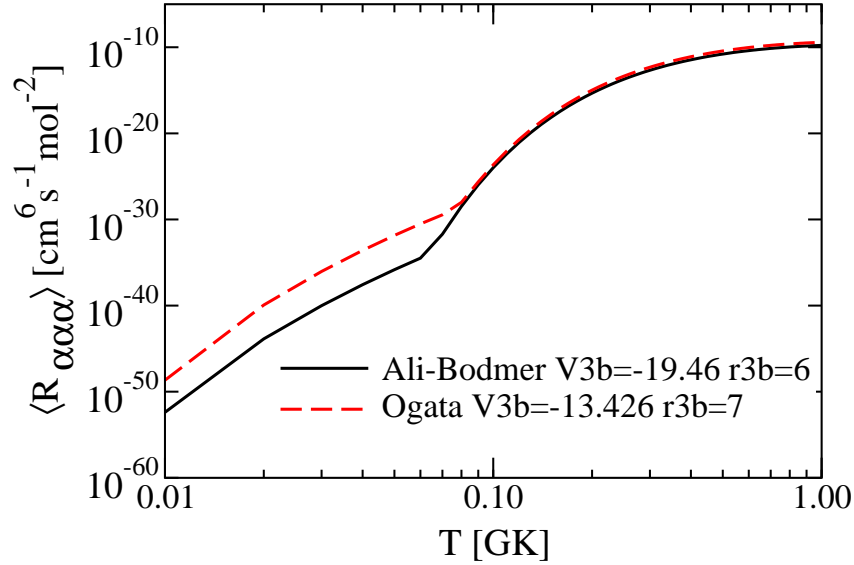


Figure 4.24: The sensitivity of the triple-alpha rate to the interactions: comparison between $\alpha-\alpha$ Ali-Bodmer+3-body force (solid) and $\alpha-\alpha$ interaction as in [15]+3-body force (dashed)

where $\Gamma_{\alpha\alpha\alpha}$ and Γ_{γ} are the particle and gamma decay widths respectively; $\Gamma = \Gamma_{\alpha\alpha\alpha} + \Gamma_{\gamma}$ is the total width.

As shown in Fig. 4.25, we fit our calculated cross sections to a Breit-Wigner shape and obtain a value of $\sim 10^{-9}$ MeV for the partial decay width, which is the same order of magnitude as experiment. In practice, a factor of 2 is needed for normalizing to the NACRE rate, counting for both the uncertainty of the decay width and the convergence of the problem. In Table 4.3, we summarize different sources of uncertainty in calculating the triple-alpha reaction rate. At low temperatures the uncertainty mostly comes from the screening technique. Errors coming from K_{\max} increase for higher temperatures when the contribution from the Hoyle resonance becomes important because such a narrow resonance is very sensitive to the maximum hyper-momentum. Table 4.3 shows that the total uncertainty

Table 4.3: Sources of uncertainty in calculating the triple-alpha reaction rate

T (GK)	Uncertainty			Total
	Screening	ρ_{screen}	K_{max}	
0.01	38%	50%	16%	65%
0.02	36%	4%	2%	36%
0.03	32%	1%	2%	32%
0.04	31%	2%	2%	31%
0.05	37%	2%	2%	37%
0.06	39%	2%	3%	39%
0.07	39%	0.1%	25%	46%
0.08	39%	0.2%	24%	46%
0.09	38%	0.2%	23%	44%
0.1	38%	0.2%	22%	44%
> 0.1	36%	0.2%	16%	39%

of the triple-alpha rate is much smaller than the normalization factor, we therefore consider this factor of 2 to be our conservative error of this problem.

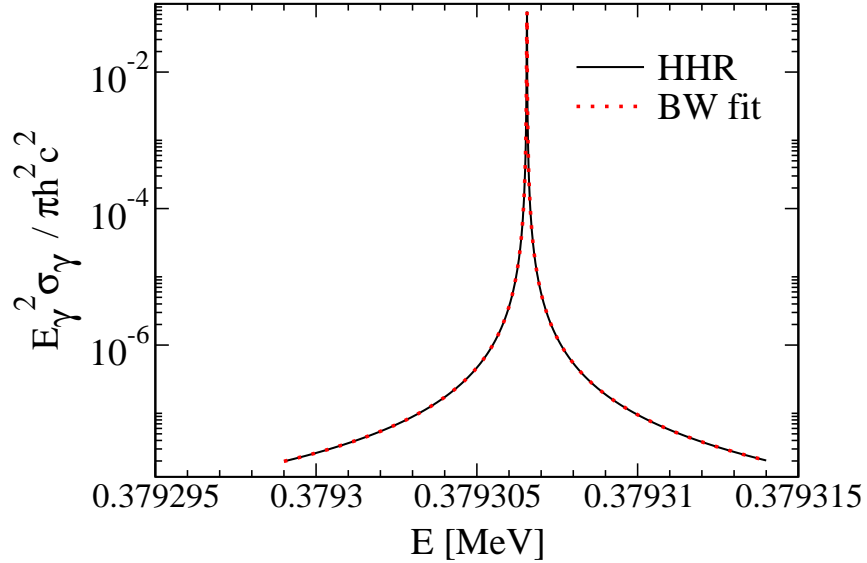


Figure 4.25: The photo-disintegration cross section is fitted to the Breit-Wigner shape to obtain the gamma decay width.

4.6 Rate

With the 2_1^+ bound state and the 0^+ continuum states of ^{12}C obtained in Sec. 4.2 and Sec. 4.3, we are able to compute the triple-alpha reaction rate at different temperatures. Since both the resonant and the non-resonant continuum 0^+ states come naturally from solving the coupled channels equation (Eq. (2.30)), the HHR method enables us to treat the resonant and non-resonant processes on the same footing. We present our new triple-alpha rate in Table 4.4 for temperatures ranging from 0.01 GK to 1.0 GK beyond which we need to consider other high lying resonances.

The triple-alpha reaction proceeds primarily through either the resonant or the non-resonant path depending on the temperature of the stellar environment. In order to have a full understanding of the triple-alpha reaction mechanism, we estimate the energy range relevant for the reaction rate at a given temperature. For convenience we denote the integrand

Table 4.4: Our triple-alpha reaction rate (in $cm^6s^{-1}mol^{-2}$) after being normalized to NACRE for $T \geq 0.5$ GK (the factor of 2 uncertainty is listed for temperature below 0.08 GK above which the triple-alpha rate agrees with NACRE).

T (GK)	$\langle R_{\alpha\alpha\alpha} \rangle$	Uncertainty	T (GK)	$\langle R_{\alpha\alpha\alpha} \rangle$
0.010	8.47×10^{-53}	x2	0.15	1.53×10^{-18}
0.015	2.11×10^{-47}	x2	0.20	9.90×10^{-16}
0.020	2.86×10^{-44}	x2	0.25	4.13×10^{-14}
0.025	4.44×10^{-42}	x2	0.30	4.50×10^{-13}
0.030	2.08×10^{-40}	x2	0.35	2.31×10^{-12}
0.04	5.72×10^{-38}	x2	0.4	7.44×10^{-12}
0.05	3.11×10^{-36}	x2	0.5	3.44×10^{-11}
0.06	6.79×10^{-35}	x2	0.6	8.63×10^{-11}
0.07	4.18×10^{-32}	x2	0.7	1.55×10^{-10}
0.08	7.12×10^{-29}		0.8	2.28×10^{-10}
0.09	2.26×10^{-26}		0.9	2.95×10^{-10}
0.10	2.19×10^{-24}		1.0	3.51×10^{-10}

of Eq. (3.25) as function $f(E)$:

$$f(E) = (E - Q)^2 \sigma_\gamma(E) e^{-\frac{E}{k_B T}}. \quad (4.6)$$

At a given temperature, there is a certain range of energy that dominates the integrand $f(E)$. In Fig. 4.26 we plot in dashed-blue the integrand f as a function of the three-alpha relative energy E at low temperature (0.01 GK). The energy cumulative sum of this

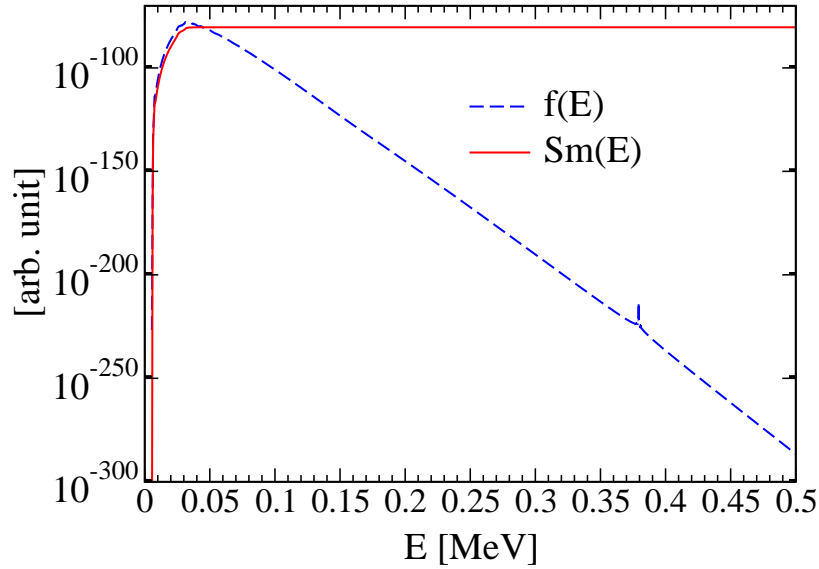


Figure 4.26: The integrand $f(E)$ and its energy cumulative sum $Sm(E)$ at a very low temperature of 0.01 GK

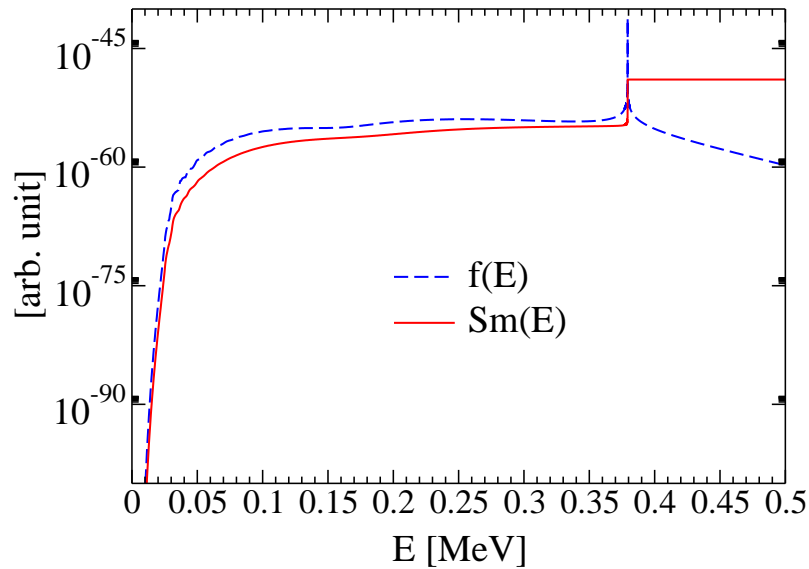


Figure 4.27: The integrand $f(E)$ and its energy cumulative sum $Sm(E)$ at $T = 0.1$ GK

function ($Sm(E) = \int_{0.01}^E f(E')dE'$) is presented in red. This gives us an estimation for the energy range that is relevant to calculate the triple-alpha rate at a given temperature. From

Fig. 4.26, one concludes that the contribution from the Hoyle resonance to the triple-alpha rate is negligible at $T = 0.01$ GK.

A similar calculation is presented in Fig. 4.27 but for a higher temperature $T = 0.1$

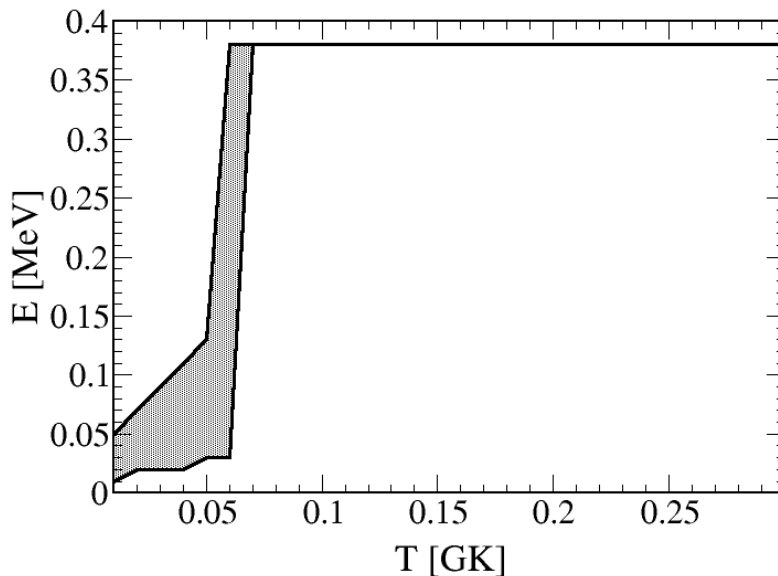


Figure 4.28: Range of energy relevant for the triple-alpha reaction rate at a given temperature.

GK. The energy cumulative sum of function $f(E)$ in this case indicates that the dominant contribution to the triple-alpha rate comes indeed from the Hoyle state.

We summarize our results in Fig. 4.28. The shaded area represents the energy range relevant for the evaluation of the triple-alpha reaction rate at a given temperature. As we can see the resonant energy at 0.38 MeV completely dominates the integration for $T \geq 0.07$ GK. This is valid for temperatures below 1 GK because when $T > 1$ GK additional high lying resonances contribute significant. For $T = 0.06 - 0.07$ GK, there is a competition between the resonant and the non-resonant processes, marking the transition region between those. The non-resonant capture mechanism dominates for $T < 0.06$ GK.

Chapter 5

Discussion

The HHR method which combines the R-matrix expansion and the R-matrix propagation in the hyperspherical harmonics representation is developed to solve an exact three-body problem. We have succeeded in providing the triple-alpha reaction rate for $T < 1$ GK, including temperatures below 0.1 GK. In this section we compare our result with other studies ([10], [15], [28]) and discuss different aspects of the reaction mechanism.

5.1 Comparison with other methods

Fig. 5.1 presents our results (solid line) in comparison with other studies: NACRE, CDCC and BW(3B). Although the new rate (HHR) is slightly reduced below 0.07 GK, it is significantly enhanced for $T < 0.06$ GK as compared to NACRE. We also obtained a very different temperature dependence in this region. In NACRE, the triple-alpha reaction is assumed as a two-step process for all temperatures. An enhancement of the rate at low temperatures in our calculation is attributed to the non-resonant three-body direct capture which is not considered in NACRE. The results assuming an extrapolation of a three-body Breit-Wigner

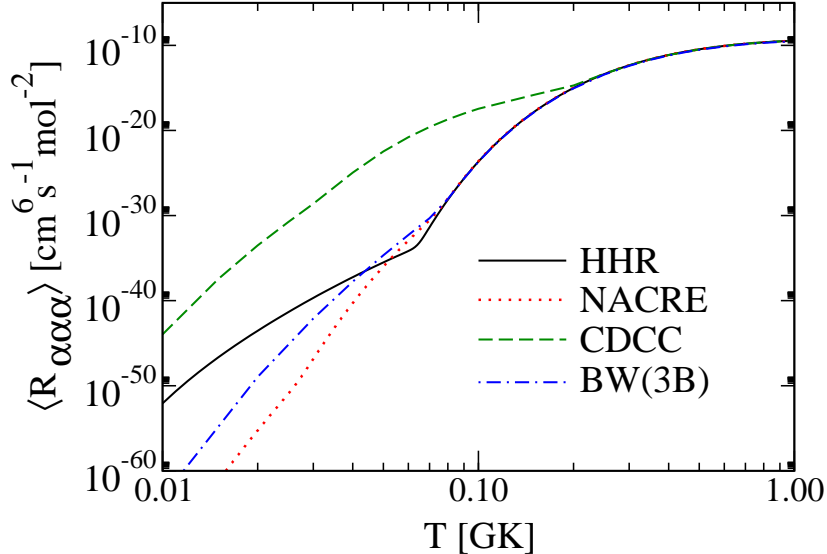


Figure 5.1: Different evaluations of the triple-alpha reaction rate: comparing the Hyper-spherical Harmonic R-matrix method (solid) with NACRE (dotted), CDCC (dashed) and the three-body Breit Wigner (dot-dashed).

cross section to low energies BW(3B) (dot-dashed line) [28] have a similar behavior but the reaction rate increases to a lesser extent. Although the non-resonant treatment in [28] is crude by assuming the low temperature triple-alpha reaction is driven by the tail of a three-alpha Breit-Wigner resonance, without the intermediate ${}^8\text{Be}$ resonant state, that work shares the same finding as ours, namely that an enhancement of the rate is expected in the low temperature regime due to the direct capture mechanism. The CDCC calculation in [15] (long-dashed) produces a large enhancement of the triple-alpha rate for temperatures up to 0.2 GK when comparing with NACRE. That is the first attempt to include the non-resonant contribution in the triple-alpha reaction rate at low temperatures. However, the effect in [15] is much stronger than what is seen in our studies. In [15], the three-body wavefunction is expanded in terms of the continuum states in the two-body subsystem (${}^8\text{Be}$), approximately reducing a three-body problem to a 2 + 1 body problem. In practise, truncation in

maximum excitation energy and angular momentum of the two-body subsystem is necessary for numerical performance. Our hypothesis is that this leads to the incorrect asymptotic form for the three-body scattering wavefunction when all particles have charge [20]. The CDCC calculation in [15] are combined with a 2_1^+ bound state from a microscopic cluster model (not the same framework). However, we do not expect this would introduce the many orders of magnitude difference that we observe. Our HHR method approaches the triple-alpha problem in a different way, expanding the total three-body wavefunction in terms of hyperspherical harmonics, equally considering all the possible configurations of the three alpha particles, and highly improving the asymptotic treatment of the three charged-particle system as compared to the CDCC method. We know that the results in [15] overestimate the enhancement of the rate leading to a failure of the description of the red giant phase in the evolution of low mass stars [21].

There exists a kink in the HHR curve around $T \approx 0.06$ GK as seen in Fig. 5.1. This marks the transition between the resonant and the non-resonant processes for which the temperature dependences are different. Above $T \approx 0.06$ GK the resonant process dominates, while below there is mostly direct non-resonant capture. This agrees with the finding in Fig. 4.28.

Although we consider the NACRE rate as our reference, there exist other rates that are commonly used in astrophysics such as CF88 from [8] and Fynbo from [13]. The theory behind these rates are the same, assuming the triple-alpha reaction proceeds through a sequential two-step process for all energies. However, the treatment of the high energy resonances of ^{12}C causes deviation between them. In Fig. 5.2 we compare the HHR rate with others namely NACRE, Fynbo and CF88. It is shown that the difference in the rates typically used in astrophysics is insignificant to the large enhancement that we obtain in the HHR rate for $T < 0.06$ GK. The result is published in [14].

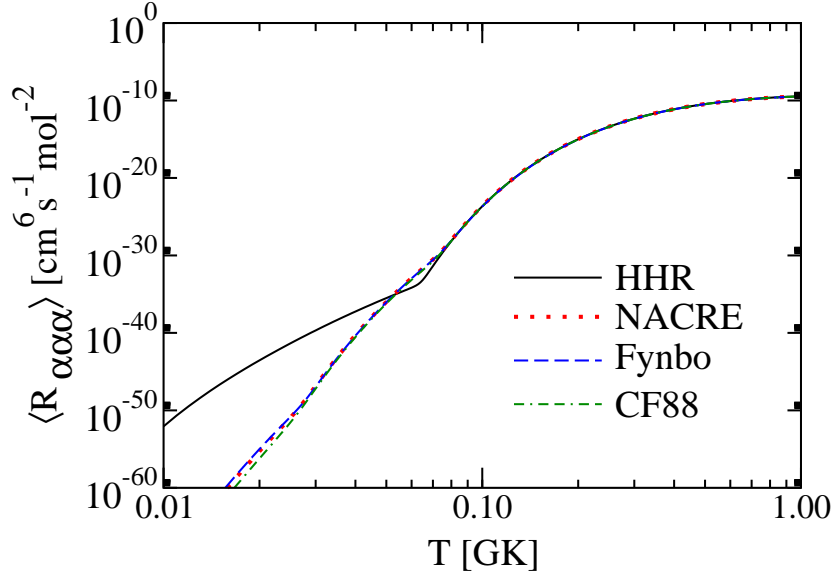


Figure 5.2: The triple-alpha reaction rate: comparing the Hyperspherical Harmonic R-matrix method (solid) with NACRE (dotted), Fynbo (dashed), and CF88 (dot-dashed).

5.2 Long-range Coulomb effects

Since we obtain a large enhancement for the triple-alpha reaction rate at low temperatures, it is important to isolate the source of this effect. We therefore perform calculations of the $^{12}\text{C}(0^+)$ continuum states for cases in which only the diagonal Coulomb couplings $V_{\gamma\gamma}^C$ or the full Coulomb couplings $V_{\gamma\gamma}^C$ are included. The results are then compared to calculations including both nuclear and Coulomb interactions $(V^C + V^N)_{\gamma\gamma'}$ with the off-diagonal Coulomb couplings up to 30 fm and 800 fm. The reaction rate for each case is then constructed by using those scattering wavefunctions and fixing the $^{12}\text{C}(2_1^+)$ bound state. Fig. 5.3 shows the results of these calculations. When only the diagonal Coulomb couplings are present (dotted line), we are able to obtain an analytic solution of Eq. (2.32) (Sec. 2.1.3). The inclusion of the off-diagonal Coulomb couplings (dot-dashed line) significantly increases the reaction rate at low temperatures. When both nuclear and Coulomb couplings are fully included

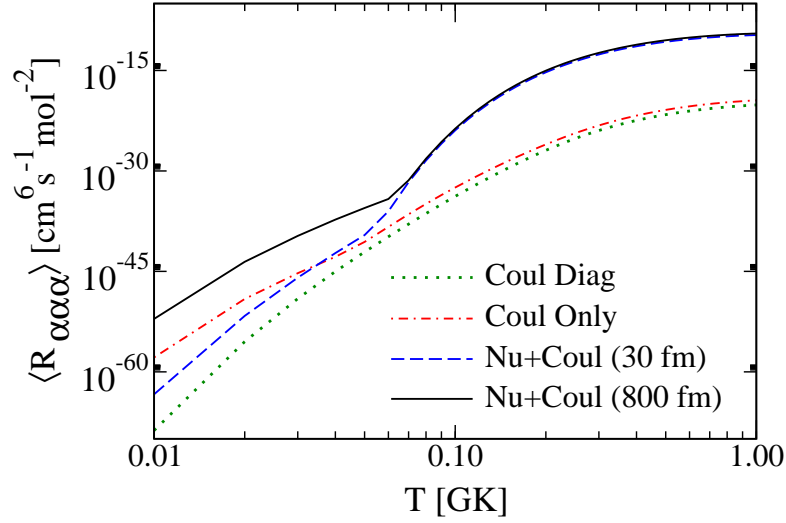


Figure 5.3: The long-range Coulomb effects are shown in four different calculations: only diagonal Coulomb couplings (dotted), only Coulomb couplings (dot-dashed), both nuclear and Coulomb interactions with off-diagonal Coulomb couplings up to 30 fm (dashed) and a fully converged calculation with off-diagonal Coulomb couplings up to 800 fm (solid)

in our calculation (dashed and solid lines), we observe an increase in the reaction rate at high temperatures due to the resonant contribution. Comparison between the solid and the dashed curves confirms that long-range off-diagonal Coulomb couplings drive the increase in the triple-alpha reaction rate at low temperatures. Fig. 5.3 indicates that the effect of off-diagonal long-range couplings are relatively small at high temperatures but very important in the low temperature regime. About 10 orders of magnitude enhancement in the rate is found at $T = 0.01$ GK due to these effects, demonstrating the importance of including Coulomb correctly.

5.3 Reaction dynamics

In order to understand the mechanism for ^{12}C production in more detail, we rewrite Eq. (3.37) as

$$\frac{dB(E2)}{dE} \sim \sum_{\gamma^i} \left| \int f_{\gamma^i}(r, R) dr dR \right|^2, \quad (5.1)$$

where r is the radius between two alpha particles and R is the distance from their center of mass to the third alpha particle. $\gamma^i = \{K^i, l_x^i, l_y^i\}$ indicates an incoming channel in the hyperspherical wave expansion for a scattering state. The spatial distribution of function $f_{\gamma^i}(r, R)$ at different three-body kinetic energies E contains information about the dynamics of the triple-alpha reaction. Fig. 5.4, 5.5, and 5.6 illustrate the spatial distributions of $f_{\gamma^i}(r, R)$ at a very low energy $E = 0.05$ MeV, at the resonant energy $E = 0.38$ MeV, and at an energy well above the resonance $E = 0.5$ MeV, respectively. We just present here the distribution functions corresponding to the first incoming channel ($K^i = 0$, $l_x^i = 0$, and $l_y^i = 0$) which is the dominant contribution to the quadrupole strength function $dB(E2)/dE$. Other channels exhibit the same trends.

At low energy $E = 0.05$ MeV, the spatial distribution of function $f_{\gamma^i}(r, R)$ shown in Fig. 5.4 has a different symmetry in comparison with the higher energies (Fig. 5.5, 5.6). We observe comparable contributions coming from two different triple-alpha configurations: the prolate triangle and the oblate triangle as shown in Fig. 4.12a and Fig. 4.12b, respectively. There is a large cancellation between these two contributions resulting in a small value of $dB(E2)/dE$ at low energies (for example, the two contributions are $\sim 10^{-12}$ but their sum is $\sim 10^{-16}$). Nevertheless these cancellations are well within the numerical accuracy of our computations.

Fig. 5.5 and Fig. 5.6 illustrate the spatial distribution of function $f_{\gamma^i}(r, R)$ at the res-

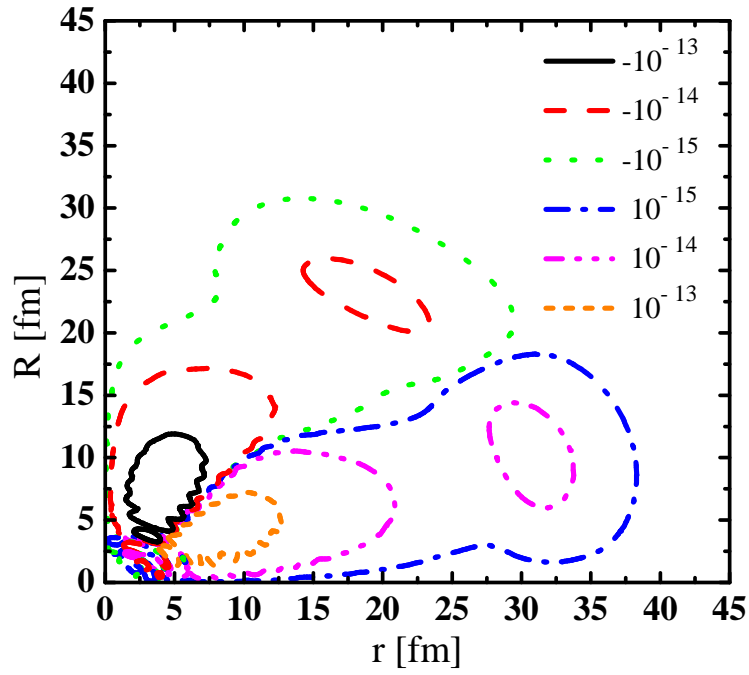


Figure 5.4: Spatial distribution of function $f_{\gamma^i}(r, R)$ for $E = 0.05$ MeV and $\gamma^i = \{0, 0, 0\}$.

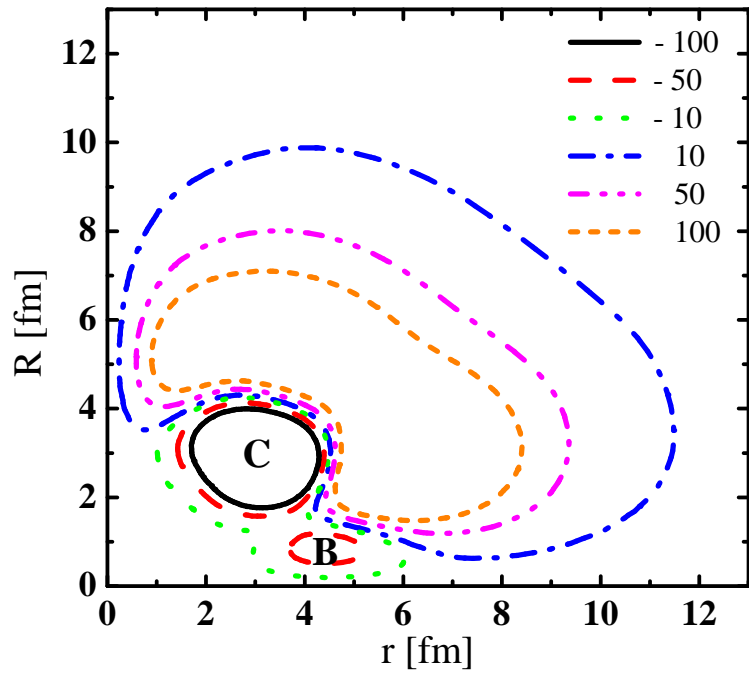


Figure 5.5: Spatial distribution of function $f_{\gamma^i}(r, R)$ for $E = 0.38$ MeV and $\gamma^i = \{0, 0, 0\}$.

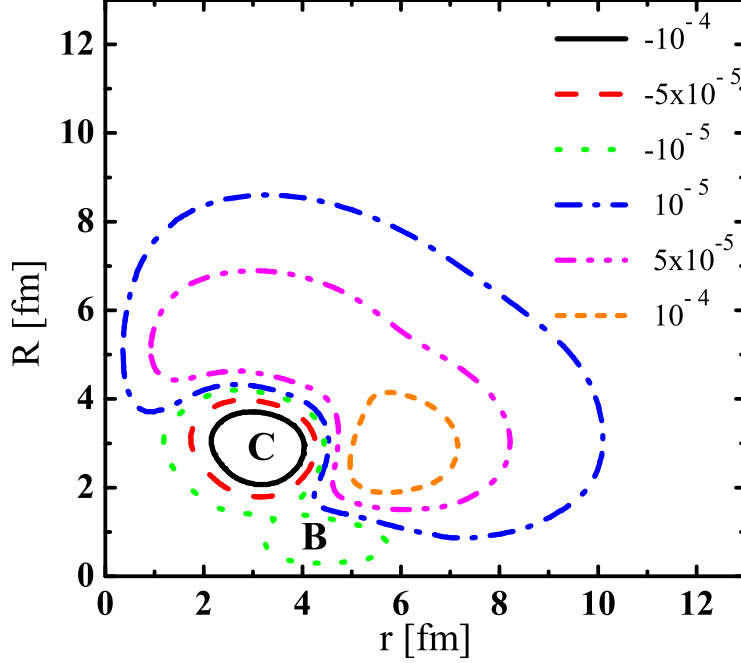


Figure 5.6: Spatial distribution of function $f_{\gamma^i}(r, R)$ for $E = 0.5$ MeV $\gamma^i = \{0, 0, 0\}$.

onant energy $E = 0.38$ MeV and higher $E = 0.5$ MeV. These two cases share the same symmetry. The dominant contribution to the quadrupole strength function $dB(E2)/dE$ comes from the region within the smallest contour in Fig. 5.5 and Fig. 5.6 that contains both maxima **B** and **C**. The maximum **C** in the spatial distribution of function $f_{\gamma^i}(r, R)$ is caused by the triple-alpha equilateral triangle configuration in both the 2_1^+ bound state and the Hoyle resonant state (see the density distribution for each state in Fig. 4.6 and Fig. 4.11). The contribution to the maximum **B** mostly comes from the three-alpha oblate configuration which only appears in the Hoyle resonant state. Even though the three-alpha prolate configuration dominates the Hoyle state's structure, it does not contribute significantly to the strength function because the 2_1^+ bound state wavefunction is zero in that region.

5.4 Astrophysical S-factor

The astrophysical S-factor is often introduced to facilitate the calculation of the reaction rate at low temperatures in a two-body reaction in which the reaction rate is defined as:

$$\langle \sigma v \rangle = \left(\frac{8}{\pi m_{ab}} \right)^{1/2} \frac{1}{(kT)^{3/2}} \int_0^\infty E \sigma(E) e^{-\frac{E}{kT}} dE. \quad (5.2)$$

The cross section $\sigma(E)$ is expressed in terms of the astrophysical S-factor $S(E)$:

$$\sigma(E) = \frac{1}{E} e^{-2\pi\eta} S(E), \quad (5.3)$$

where η is the two-body Sommerfeld parameter measuring the strength of the Coulomb barrier $\eta = \frac{Z_a Z_b e^2}{\hbar} \left(\frac{m_{ab}}{2E} \right)^{1/2}$. Eq. (5.3) removes explicitly the penetration factor, resulting on an astrophysical S-factor $S(E)$ with weak energy dependence. This improves the quality of the extrapolation of the cross section to low energies where measurements are not possible or a simplification in calculating the reaction rate [9, 46]. If this property holds for a three-body S-factor, we will be able to estimate the low-temperature triple-alpha rate in a simpler way. As derived in Sec. 3.2, the three-body reaction rate has the formula:

$$\langle R_{123} \rangle = p! N_A^2 \frac{\hbar^3}{c^2} \frac{8\pi}{m^3 (\mu_1 \mu_2)^{3/2}} \frac{g_0}{919293} \frac{1}{(kT)^3} \int_0^\infty e^{-\frac{E}{kT}} E_\gamma^2 \sigma_\gamma(E_\gamma) dE. \quad (5.4)$$

We apply the same analogy in the two-body problem to obtain the relationship between the three-body astrophysical S-factor $S_{3b}(E)$ and the photo-disintegration cross section σ_γ :

$$\sigma_\gamma(E_\gamma) = \frac{1}{E_\gamma^2} e^{-2\pi\zeta} S_{3b}(E), \quad (5.5)$$

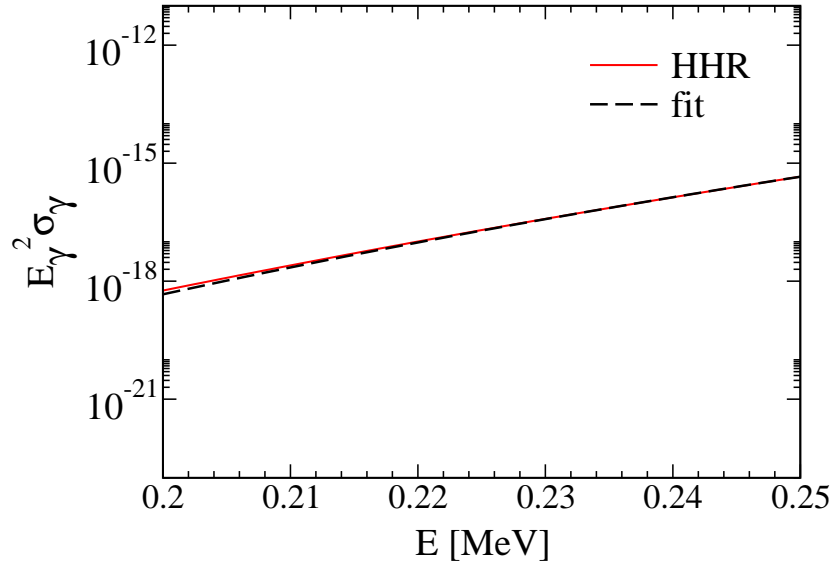


Figure 5.7: Fitting $E_\gamma^2 \sigma_\gamma$ to an exponential behavior $A e^{\frac{-2\pi B}{\sqrt{E}}}$ for energies below the resonance.

where ζ is an equivalent to the Sommerfeld parameter in the two-body case.

For a three-body system, the picture of Coulomb interaction is more complex. As seen from Eq. (2.25) in Sec. 2.1.2, the strength of the Coulomb barrier in a three-body system is not a constant as in the two-body case but rather depends on the incoming and outgoing channels in the HH representation. We thus do not have an exact expression for ζ except the fact that ζ should be proportional to $1/\sqrt{E}$ because the three-body Coulomb couplings also vary as $1/\rho$ in our method. We estimate ζ by fitting $E_\gamma^2 \sigma_\gamma$ to an exponential behavior $A e^{\frac{-2\pi B}{\sqrt{E}}}$ for energies below the Hoyle resonance. A and B are fitting parameters. As seen from Fig. 5.7, the fitting procedure is performed for the energy range (0.2-0.25) MeV, below which we are not able to obtain any reasonable fit. The result from this fit is then used to construct the three-body S-factor as in Eq. (5.5). In Fig. 5.8, we plot the energy dependence of both the cross section σ_γ and the three-body astrophysical S-factor S_{3b} . A significant

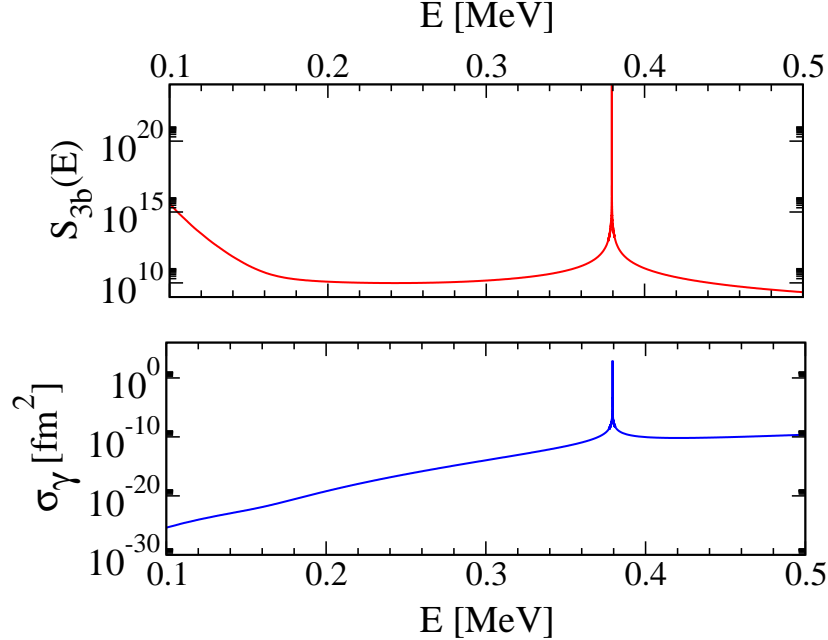


Figure 5.8: Comparison between the energy dependence of the cross section σ_γ and the three-body astrophysical S-factor S_{3b} .

reduction in the energy dependence is observed for the S-factor in the low energy range (0.15-0.33) MeV. For energies below 0.15 MeV, the astrophysical S-factor strongly varies with energy. This is not fixable by fitting ζ to the lower energy range since no reasonable fit can be obtained. In conclusion, we are not able to construct a three-body astrophysical S-factor for the triple-alpha system at very low energies that has weak energy dependence. For the intermediate energies (0.15-0.33) MeV, a desired three-body S-factor in the same two-body analogy is possible.

As stated above, the parameter ζ varies with the HH channels causing difficulty in extracting the three-body Sfactor. In order to verify that statement, we perform similar calculations but only include the first incoming and outgoing channels (0,0,0). This allows us to uniquely define ζ :

$$\zeta = \frac{Z_{00}^{\text{eff}}}{\hbar} \sqrt{\frac{m}{2E}}, \quad (5.6)$$

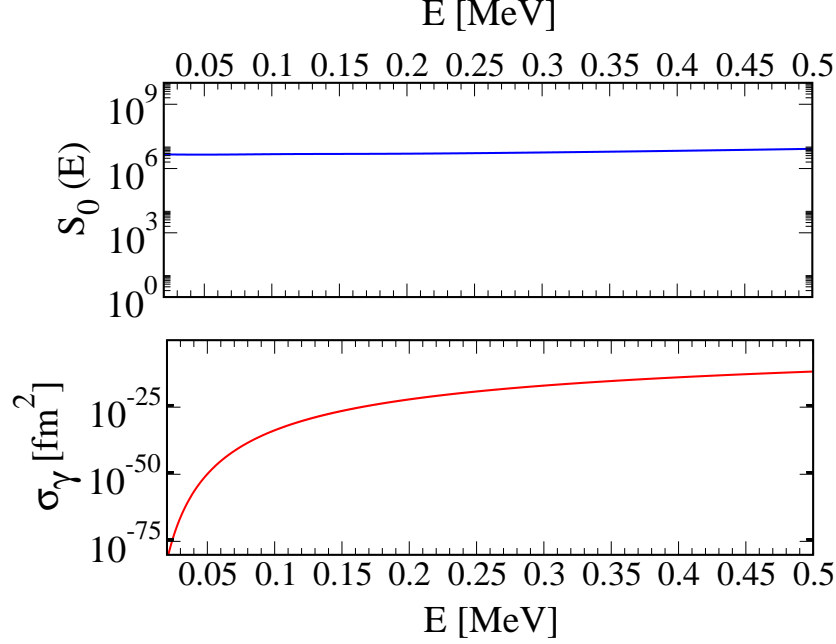


Figure 5.9: Comparison between the energy dependence of the cross section σ_γ and the astrophysical S-factor S_0 for $K_{\max} = 0$.

where Z_{00}^{eff} is calculated from Eq. (2.25). We therefore expect to obtain an S-factor with much weaker energy dependence for this case. The results are presented in Fig. 5.9. As you can see, the extracted S-factor is almost constant with relative energy, reinforcing our conclusion on the difficulty in obtaining a three-body astrophysical S-factor. We also explore different fitting functions which are commonly used in an effort to extract a desired three-body S-factor. For example, we slightly modify the energy dependence of ζ :

$$\sigma_\gamma(E_\gamma) = \frac{1}{E_\gamma^2} e^{-\frac{2\pi B}{E^C}} S_{3b}(E), \quad (5.7)$$

or introduce a polynomial into the S-factor formula:

$$\sigma_\gamma(E_\gamma) = \frac{1}{E_\gamma^2} e^{-\frac{2\pi B}{\sqrt{E}}} (A_0 + A_1 * E + A_2 * E^2). \quad (5.8)$$

However, we continue to find difficulty in obtaining a three-body S-factor with weak energy dependence using these simple expressions.

Chapter 6

Astrophysics Applications

As mentioned in chapter 1, the triple-alpha reaction is one of the key reactions in astrophysics. It is responsible for the creation of ^{12}C and provides a mechanism to overcome the difficulty in nucleosynthesis of heavy elements due to the instability of nuclei with mass 5 and 8. Helium burning is a critical source of energy for horizontal branch stars, a significant phase in the life of a low-mass star. Its rate determines the tip of the red giant branch in a normal star's evolution. Competition between the triple-alpha rate and the $^{12}\text{C}(\alpha,\gamma)$ rate determines the C/O ratio in the core of a star with mass ranging from $0.4M_{\odot}$ to $2M_{\odot}$ [9]. Helium burning can also be found in helium accreting white dwarfs and helium accreting neutron stars in compact binary systems. If the accretion rate is sufficiently low, the evolution of these binary systems could lead to very rare energetic events such as type Ia supernovae and superbursts of which many related studies are based on computational simulations. It is critical that the triple-alpha rate and other inputs in these models are well constrained.

We obtain a large enhancement of the triple-alpha reaction rate at $T < 0.06$ GK as compared to NACRE. The new rate also has a very different temperature dependence. In Table. 6.1, we present the temperature dependence of different rates by evaluating $d \ln \langle R_{\alpha\alpha\alpha} \rangle / d \ln T$.

Table 6.1: Temperature sensitivity of triple-alpha rate

T (GK)	$d \ln \langle R_{\alpha\alpha\alpha} \rangle / d \ln T$	
	HHR	NACRE
0.01	34.1	56.5
0.02	23.3	45.5
0.04	18.5	47.7
0.08	51.7	48.3
0.16	24.4	24.4

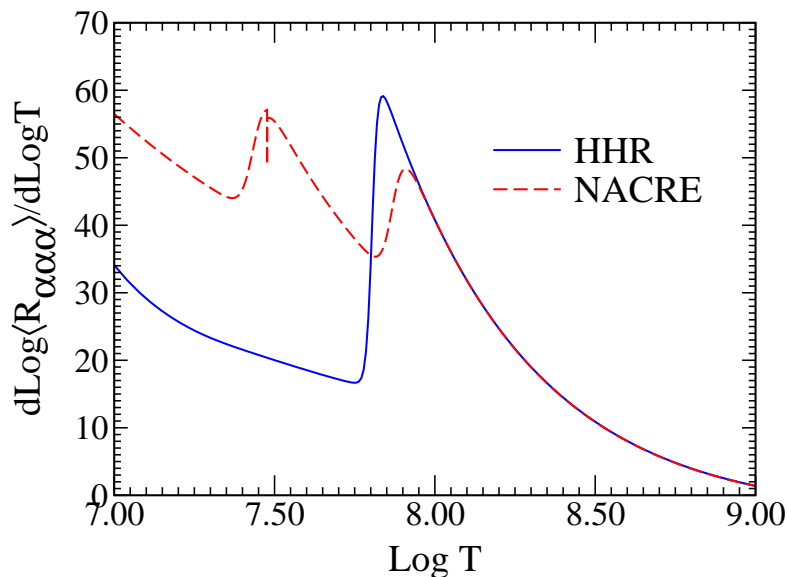


Figure 6.1: Temperature dependence for the HHR rate (solid) and the NACRE rate (dashed).

Fig. 6.1 plots the temperature dependence of the HHR rate (solid line) and the NACRE rate (dashed line). As we can see, the HHR rate has a much weaker temperature dependence than the NACRE rate for temperatures below 0.06 GK. Beyond this point, the two rates have the same temperature sensitivity. Since our rate significantly differs from the standard NACRE rate at low temperatures, we want to investigate its influence on important astrophysical events.

6.1 Evolution of single stars

In this section, we describe a general picture of the evolution of a normal star with solar metallicity Z_{\odot} and initial mass ranging from $0.4M_{\odot}$ to $2M_{\odot}$ (M_{\odot} is the solar mass). For heavier stars, we do not expect our rate would have significant impact because helium burns at higher temperatures [9]. In Fig. 6.2 we present the standard evolution curve of a $1M_{\odot}$ star. Stars are first formed from an interstellar gas cloud which is mainly composed of hydrogen and helium. In the first stage of their lives as pre-main-sequence stars, they undergo gravitational contraction. This leads to the increase of density, causing the temperature in the star to rise. The gas cloud is hot enough that some primordial nuclei start to burn. The nuclear energy generated at this stage is small but sufficient to halt the gravitational collapse of the central part of the cloud, forming the core of the star. When the core temperature reaches ~ 0.01 GK, hydrogen burning starts. It becomes the only energy supply of the core when the star approaches its main-sequence stage (label “1” in Fig. 6.2). Depending on the mass of the star, hydrogen fusion can proceed via the pp chain or the CNO cycle. Stars with $M \gtrsim 1.5M_{\odot}$ burn hydrogen at higher temperature through the CNO cycle, whereas lighter stars do it through the pp chain. The energy produced in the core is carried outward and increases the surface luminosity.

A significant amount of helium is accumulated in the core due to hydrogen fusion. The star eventually runs out of hydrogen in the core. It starts burning hydrogen in a shell surrounding the inert helium core. The star begins to leave the main sequence. Because there is no energy generated in the core, the helium core contracts again due to gravity. This increases the temperature in the core as well as in the hydrogen burning shell. More energy is produced in the shell causing a rapid increase in the surface luminosity. The star’s envelope

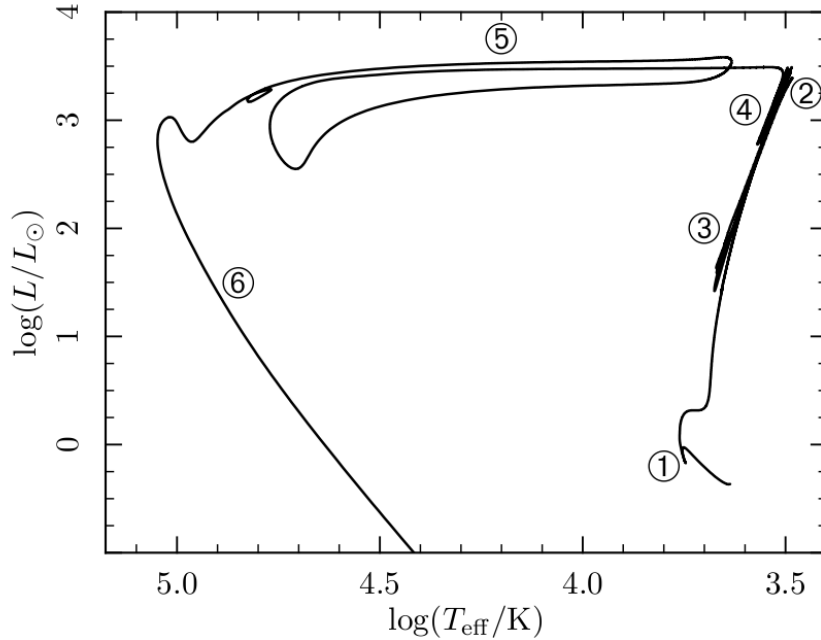


Figure 6.2: Standard evolution curve of $1M_{\odot}$ stars (surface luminosity as a function of surface temperature): 1 - main sequence, 2 - red giant, 3 - core helium flashes, 4 - thermal pulses, 5 - planetary nebula, and 6 - white dwarf.

becomes fully convective and expands dramatically. The drastic expansion together with the star's surface reddening indicates that the star enters a new phase in its evolution process, the so-called red giant stage (label "2" in Fig. 6.2). The maximum luminosity is achieved when the star gets to the tip of the red giant branch.

The gravitational contraction of the core leads to an increase in the central temperature and density. Around 0.1 GK, the star starts burning helium in the core. Since the central density is too high, matter becomes electron degenerate and therefore does not respond to the increasing temperature in the core due to helium fusion. The degenerate pressure prevents the star's surface expansion while the temperature keeps rising. More and more energy is generated inside the star. Eventually the rising temperature produces a thermonuclear runaway, or a core helium flash (label "3" in Fig. 6.2). This lifts the degeneracy and the star is able to expand and cool off to a stable state. The star settles at the horizontal branch

and burns the remaining core helium in a stable manner.

When helium in the core runs out, gravitational contraction starts again and heats up the stellar interior. The increasing temperature ignites the helium shell next to the carbon-oxygen core. The hydrogen shell next to the helium burning region also begins to burn. The star enters the asymptotic giant branch. The hydrogen shell burning is so active that more and more helium produced by hydrogen fusion in this shell is added to the helium zone, causing its density and temperature to increase. However, the inner helium shell is such a thin layer that energy generated can not be carried outward fast enough by radiative diffusion. As a result, a thermonuclear runaway occurs. This unstable helium shell burning is also called helium shell flash or thermal pulse (label “4” in Fig. 6.2).

Eventually, hydrogen and helium in the shell are exhausted, and the star leaves the asymptotic giant branch. Due to a strong stellar wind, most of the star’s envelope is ejected. The star enters the planetary nebula stage (label “5” in Fig. 6.2). The surface temperature of the star keeps increasing because hotter layers are now exposed.

When there is no hydrogen envelope left and the hydrogen shell burning completely dies out, the star begins to lose its luminosity (label “6” in Fig. 6.2). The star will end its life as a white dwarf which is mainly composed of carbon and oxygen. The electron degeneracy pressure prevents the white dwarf from gravitational collapse. It eventually cools by radiating away the thermal energy.

It is clear that the triple-alpha reaction plays an important role in the evolution of a star. Changes in the rate can lead to a very different evolution of the star. When Ogata *et al.* [15] first claimed a drastic enhancement in the reaction rate due to the non-resonant contribution, an investigation of the impact of that finding on the evolution of a single star was performed immediately thereafter. In [21] Dotter *et al.* compared the evolutionary tracks

obtained using the standard NACRE rate and the rate from [15] (denoted as OKK in [21] and CDCC in our work). Using the OKK (CDCC) rate severely shortens the red giant phase. This is because the drastic enhancement of the triple-alpha rate in OKK (CDCC) results in core helium burning at much lower luminosity and temperature. Since the predictions from the stellar evolution model using the NACRE rate agree very well with observations of red giant branch (RGB) stars [76], Dotter *et al.* [21] conclude that the OKK (CDCC) result is inconsistent with observations.

In this work we obtain a new triple-alpha rate that is significantly larger than the standard NACRE rate for $T < 0.06$ GK. The rate enhancement is less than that of Ref. [15]. It is important to explore the impact of our new rate on the stellar evolution. We repeat the calculation in [21] for a $1M_{\odot}$ star with standard composition of 0.02 metallicity (Z_{\odot}) and 0.7 hydrogen using our HHR rate. A code named MESA (Modules for Experiments in Stellar Astrophysics) is used for the calculations [77, 78]. The result is then compared to those using NACRE rate.

Fig. 6.3 presents the full evolutionary track of a $1M_{\odot}$ star calculated using our HHR rate (solid curve) and the NACRE rate (dashed curve). We also include the results using the Fynbo (dotted curve) and the CF88 (dot-dashed) rates for completeness. The star evolves from the main sequence through the red giant phase, the asymptotic giant branch, the planetary nebula stage and ends its life as a white dwarf. Fig. 6.4 blows up a small portion of the track in which the star goes from the main sequence to the end of thermal pulsation in the asymptotic giant branch. Because the HHR rate is normalized to the NACRE rate at high temperature, the difference in the evolutionary tracks reflects the impact of our rate in the low temperature region. It is clear that both curves are identical from the main sequence to the end of the red giant branch. This is not the case for the reaction rate from [15], for

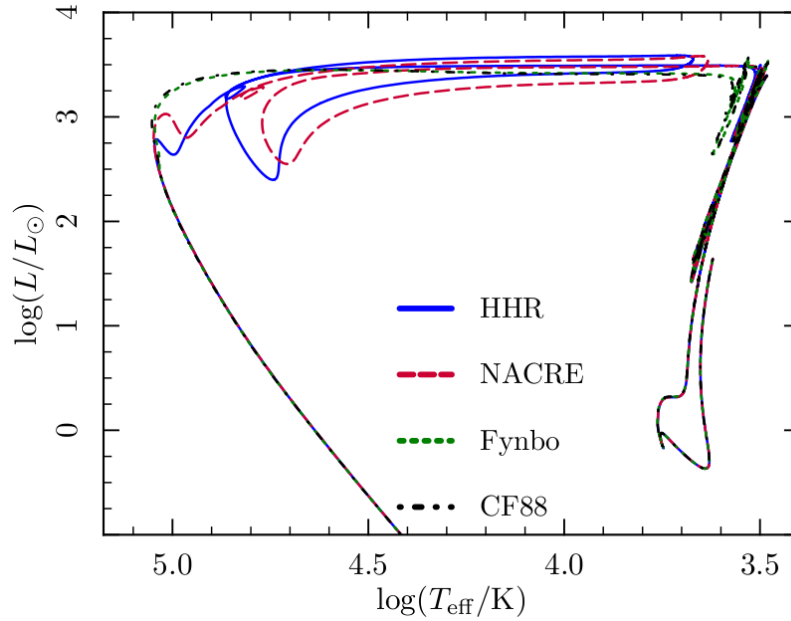


Figure 6.3: Full evolutionary track (luminosity vs. surface temperature) from main sequence to white dwarf of a one solar-mass ($1M_{\odot}$) star for HHR (solid), NACRE (dashed), Fynbo (dotted), and CF88 (dot-dashed).

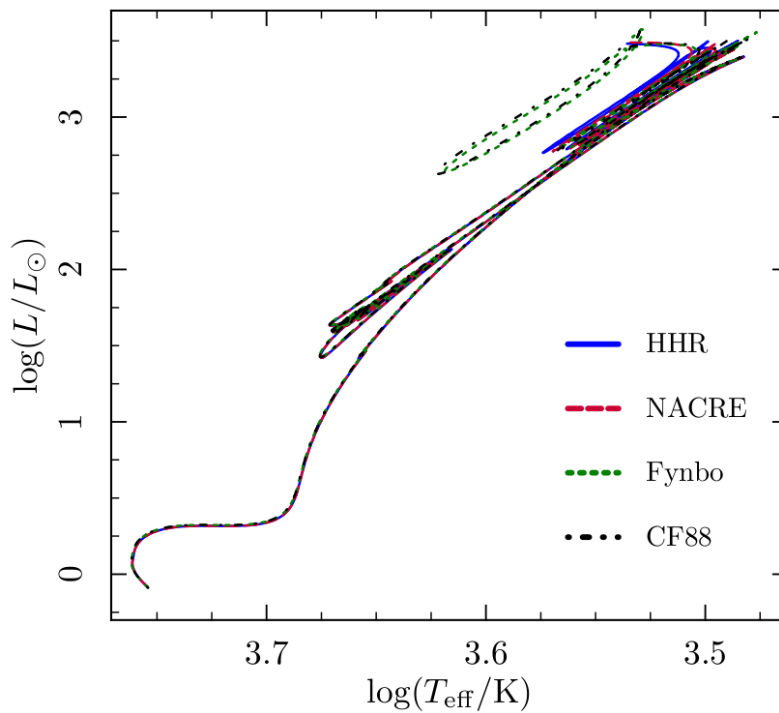


Figure 6.4: Evolutionary track (luminosity vs. surface temperature) from main sequence to the end of asymptotic giant branch of a one solar-mass ($1M_{\odot}$) star for HHR (solid), NACRE (dashed), Fynbo (dotted), and CF88 (dot-dashed).

which the red giant phase either severely shortens or completely vanishes. We observe a small difference beginning at the thermal pulsation phase in the asymptotic giant branch, as the enhanced HHR rate at $T < 0.06$ GK tends to produce a slightly larger convective zone during helium shell flashes. The difference at the onset of hydrogen and helium thermal shell flashes causes the two tracks to depart from each other during the planetary nebula phase. However those differences are probably smaller than the inherent uncertainties in using a one-dimensional code to simulate this highly unstable stage. The two tracks rejoin when the star cools off and dies as a white dwarf. The final white dwarfs obtained in both calculations (HHR and NACRE) has the same carbon-oxygen (C/O) ratio of 1 : 2.08.

The Fynbo and CF88 tracks are identical but noticeably differ from the NACRE track in the asymptotic giant branch. Because these rates are relatively consistent at low temperatures, the above differences must come from the treatment of the high lying resonances in ^{12}C . Using the Fynbo or the CF88 rate, the final white dwarf of a $1M_{\odot}$ star obtains a C/O ratio of 1 : 2.37 which is $\sim 12\%$ smaller than that from NACRE. This issue, which does not arise from the low-temperature behavior, must be addressed because many astrophysical scenarios burn helium at higher temperatures.

Fig. 6.5 plots the surface luminosity as a function of the stellar age for our HHR rate (solid curve) and the NACRE rate (dashed curve). The peak of the surface luminosity when using the HHR rate occurs at about a million years earlier than for the results using the NACRE rate. This is because the HHR rate is much larger than the NACRE rate for temperatures below 0.06 GK. At this low temperature, the star with HHR rate will burn helium faster than that with the NACRE rate.

For completeness, we also perform comparisons between HHR and NACRE for other stars with mass $M = 0.08M_{\odot}$, $1.25M_{\odot}$ and $1.5M_{\odot}$. The evolutionary track for a $1.25M_{\odot}$

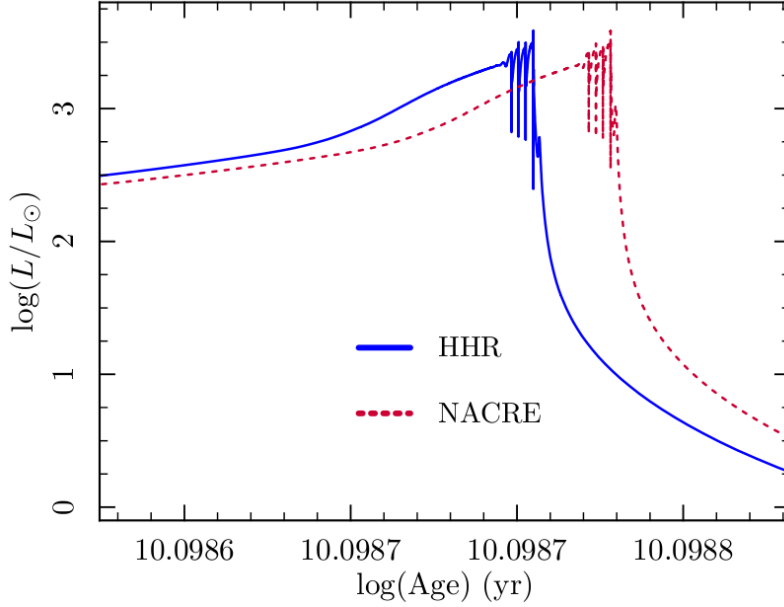


Figure 6.5: Surface luminosity as a function of age: HHR rate (solid) and NACRE rate (dashed).

star exhibits similar behavior as seen in the $1M_{\odot}$ case. In Fig. 6.6, we show the full evolutionary track of a $0.8M_{\odot}$ star calculated using our HHR rate (solid curve) and the NACRE rate (dashed curve). For this case, helium burning happens at temperatures above 0.07 GK, where our rate and NACRE are the same, and we therefore obtain identical evolutionary tracks. The same result is obtained for a $1.5M_{\odot}$ star. In conclusion, a large enhancement in the HHR rate at $T < 0.06$ GK does not produce severe changes in the evolutionary tracks of normal stars with solar metallicity, contrary to what happens when the CDCC rate is used. Our rate preserves the evolution of stars from main sequence to the red giant branch. Only small differences are obtained during the thermal pulsation phase for stars of mass $1M_{\odot}$ and $1.25M_{\odot}$.

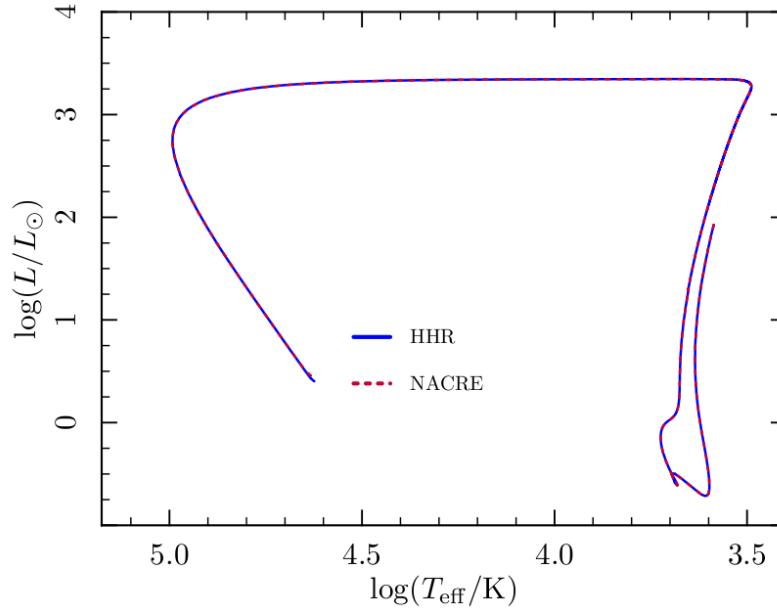


Figure 6.6: Full evolutionary track (luminosity vs. surface temperature) from main sequence to white dwarf of a 0.8 solar-mass ($0.8M_{\odot}$) star for the HHR rate (solid) and the NACRE rate (dashed).

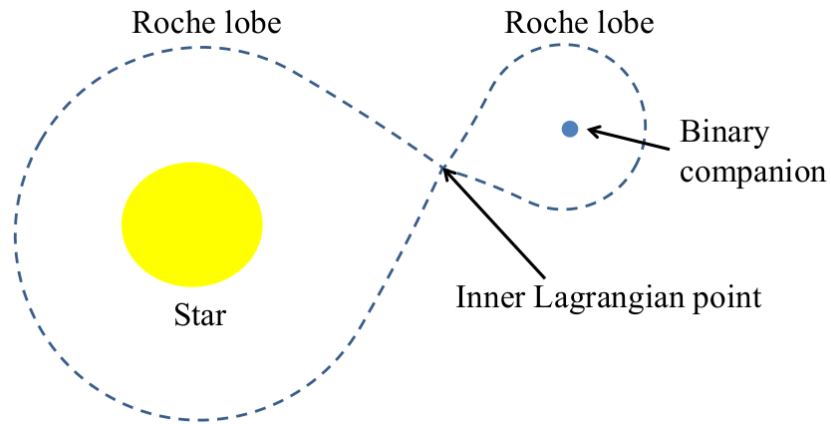


Figure 6.7: Binary system and its Roche lobes

6.2 Binary stars

A binary star system is defined as a pair of gravitationally bound stars. In a close binary system, the evolution of one star can strongly affect the other. A binary system is characterized by the Roche lobe, which forms a teardrop-shaped region in space (see Fig. 6.7).

It is defined as the equipotential surface of the binary system due to the gravitational and centrifugal forces when considering a rotating coordinate frame of the center of mass. Materials confined in this region are bound to the corresponding stars by gravity. The point of contact between the two Roche lobes is called the inner Lagrangian point. If one star fills its Roche lobe, material from that star can flow through the inner Lagrangian point to the other companion. This gives rise to some interesting astrophysical phenomena such as type .Ia supernovae in helium accreting white dwarfs and superbursts in helium accreting neutron stars. In this work we explore the influence of the new triple-alpha rate in these types of astrophysical events.

6.2.1 Helium accreting white dwarfs

We consider a binary system consisting of a helium donor and a carbon-oxygen white dwarf accretor which is often called AM Canum Venaticorum (AM CVn) binary [79]. Helium from the donor is transferred onto the white dwarf through the inner Lagrangian point. It is accumulated on the white dwarf's surface. Due to the intensive gravitational contraction, the helium layer is strongly compressed. As a result, the temperature at the bottom of the helium layer keeps rising as more and more helium is added to the white dwarf's surface. When the temperature is high enough, helium burning occurs. The bottom layer density is so high that matter becomes electron degenerate and therefore a thermonuclear runaway ensues. During this process a very bright outburst is produced. Depending on the mass of the accreted layer when the explosion occurs, these phenomena are classified as helium nova or type .Ia supernovae.

The ignition of helium at the base of the accreted layer is closely related to the nuclear

heating time scale:

$$\tau_n = \frac{C_p T}{\epsilon_{\alpha\alpha\alpha}}, \quad (6.1)$$

where T is the star's temperature and C_p is the specific heat calculated at constant pressure.

The triple-alpha generation rate $\epsilon_{\alpha\alpha\alpha}$ is given as:

$$\epsilon_{\alpha\alpha\alpha} = N_A \frac{Q}{6} \rho^2 \left(\frac{Y}{4}\right)^3 f_{scr} \langle R_{\alpha\alpha\alpha} \rangle. \quad (6.2)$$

In this equation, N_A is Avogadro number; Q is the Q-value of the triple-alpha reaction; ρ is the density of the star; Y is the helium mass fraction; f_{scr} is the screening factor and $\langle R_{\alpha\alpha\alpha} \rangle$ is the triple-alpha reaction rate.

The work in [80] found that the condition for helium ignition to occur is when $\tau_n = 10^6$ yrs. Solving Eq. (6.1), one obtains a set of ignition points (ρ, T) which show the density and temperature of the star when the helium flash triggers. It is clear from Eq. (6.1) and Eq. (6.2) that the helium ignition depends on the triple-alpha reaction rate. It is interesting to see if our new rate produces significant changes of helium ignition in these dynamical events.

For uncertainty estimation, two values of the nuclear heating time scale $\tau_n = 10^5$ yrs and $\tau_n = 10^7$ yrs are used to produce the helium ignition curve. Calculations are performed with both NACRE and HHR rates. It is important to mention that the screening factor f_{scr} in Eq. (6.2) is taken from MESA [81]. This screening factor is constructed as if the triple-alpha reaction is a two-step process, which is not a valid assumption at low temperatures. Given that the direct triple-alpha screening description is not yet available, using a consistent screening factor from MESA in both calculations will provide some insight of the impact that the HHR rate may have on helium accreting white dwarfs. In Fig. 6.8, we plot the

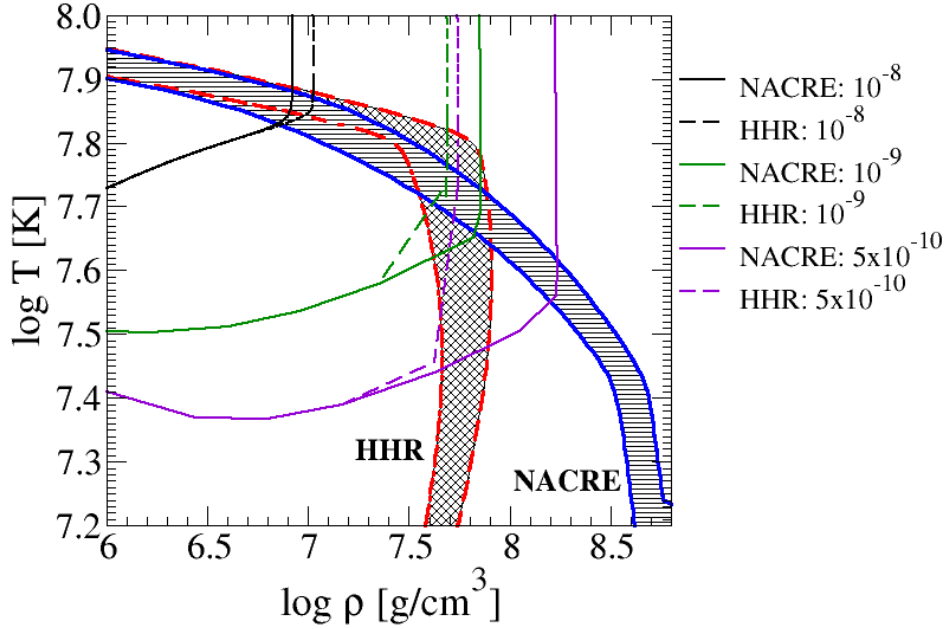


Figure 6.8: Helium ignition curves for the NACRE rate (blue solid) and the HHR rate (red dashed). Calculations are performed for helium accreting white dwarf with initial mass of $1M_{\odot}$ and several values of accretion rate.

helium ignition curves calculated using the NACRE rate (blue solid curve) and the HHR rate (red dashed curve). The helium shell flashes are expected to occur in the shaded region for each case [23]. At high temperatures, the HHR and the NACRE rates are identical resulting in a very good agreement between the two corresponding ignition curves. These curves diverge as the ignition temperature decreases. As seen from Fig. 6.8, the differences are significant between the NACRE and HHR calculations. At the same temperature, the helium ignition in the HHR calculation occurs at much lower density as compared to the NACRE calculation. When does this difference become important? In order to answer that question, we show in Fig. 6.8 the evolutionary tracks at the base of the helium accreted layer, for three different accretion rates $dM/dt (M_{\odot} \text{ yr}^{-1}) = 10^{-8}, 10^{-9}$ and 5×10^{-10} . The ignition of helium in all cases falls within the predicted ignition curves. At high accretion

rate $dM/dt = 10^{-8} M_{\odot} \text{yr}^{-1}$, the NACRE and HHR evolutionary tracks are almost identical. Helium ignition in this case occurs at higher temperature where the NACRE and our rate are the same. As expected, as the accretion rate decreases, the ignition happens at lower temperature. The evolutionary tracks are significantly different between NACRE and HHR. For the lowest accretion rate in which we see the most difference between our rate and NACRE, the ignition occurs when the mass of the helium accreted layer is about $0.315 M_{\odot}$ for HHR rate and $0.360 M_{\odot}$ for NACRE rate. These events fall into the type Ia supernova category.

In Fig. 6.9 we study the dependence of helium ignition on the initial mass of the white

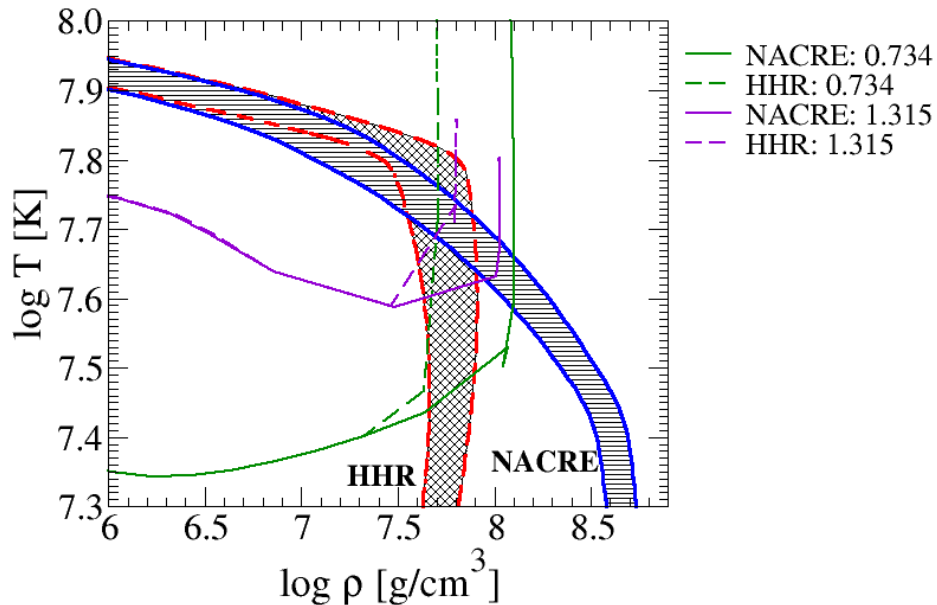


Figure 6.9: Helium ignition curves for the NACRE rate (blue solid) and the HHR rate (red dashed). Calculations are performed for helium accreting white dwarf with the accretion rate of $5 \times 10^{-10} M_{\odot} \text{yr}^{-1}$ and two different initial masses: $0.734 M_{\odot}$ and $1.315 M_{\odot}$.

dwarf accretor. Two different initial masses of $0.734 M_{\odot}$ and $1.315 M_{\odot}$ are employed. The calculations are performed using a low accretion rate of $5 \times 10^{-10} M_{\odot} \text{yr}^{-1}$ where the HHR

rate is likely to differ from the NACRE rate. The evolutionary tracks at the bottom of the helium accreted layer and the ignition curves are plotted in the same graph (Fig. 6.9) similarly to Fig. 6.8. As expected, we obtain significant differences in the evolutionary tracks between the NACRE and the HHR calculations for both masses. The helium ignitions happen at much lower density when using the HHR rate. It is also seen that the ignition temperature is higher for a white dwarf with larger initial mass. This is because a stronger gravitational force is exerted on the accreted materials causing the bottom layer to heat up faster when the white dwarf is larger.

Type .Ia supernovae were predicted by theoretical calculations [82]. They should last for about 10 days and have one-tenth the luminosity of a normal type Ia supernova, hence the name. We find that our triple-alpha rate produces very different results from NACRE for this type of explosive scenarios. However, type .Ia supernovae are very rare events that are predicted to occur once every 5000-15000 yr in a galaxy of $10^{11}M_{\odot}$ [82]. There are so far only two observed candidates for type .Ia supernovae: SN 2002bj [83] and 2010X [84]. The properties of those have not been fully understood. In addition, the current one-dimensional code is not designed to simulate such energetic explosion. Therefore comparison between our calculated type .Ia supernova and observations are not yet available. We hope our results would motivate astronomers to collect more data of these phenomena.

6.2.2 Helium accreting neutron stars

In a binary system consisting of a neutron star and a helium companion, helium is transferred from the donor and accretes onto the neutron star's surface. This accreted layer is strongly compressed by the gravitational force causing the temperature at its base to rise. At some point helium ignites, and the thin shell instability [85] enhanced by electron degeneracy

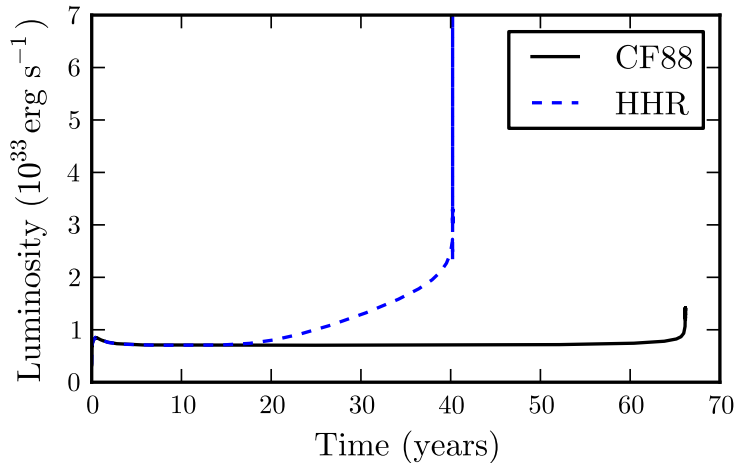


Figure 6.10: The light curve (luminosity vs. time) for helium accreting a neutron star at accretion rate of $1.75 \times 10^{-10} M_{\odot} \text{ yr}^{-1}$: Comparing the CF88 rate (dashed) and the HHR rate (solid).

leads to a thermonuclear runaway. The neutron star releases an extensive amount of energy. During this process an outburst of X-rays is produced. This phenomena is called a type I X-ray burst. Depending on the duration, bursts are classified as normal, intermediate or superbursts. Note that many superburst theories favor the ignition of a thick carbon layer instead [86].

We explore the impact of our new rate on helium accreting neutron stars. We expect to see the effect of our results most strongly at low accretion rates because helium burning then occurs at lower temperatures, where the HHR rate is different from NACRE and other rate predictions. Simulations are performed by L. Keek [87] for a helium accreting neutron star, at an accretion rate of $1.75 \times 10^{-10} M_{\odot} \text{ yr}^{-1}$ and a low crustal heating of 0.056 MeV/nucleon. We compare results obtained with our HHR rate and the CF88 rate [8]. The results are presented in Fig. 6.10. While the CF88 calculation exhibits a sudden increase in the luminosity once the X-ray burst ignites, we observe a slow rise of the light curve in the HHR calculation for half of the burst recurrence time. In addition, the recurrence

time obtained from the HHR calculation is substantially shorter than that from the CF88 calculation. We attain an ignition mass of $0.704 \times 10^{-8} M_{\odot}$ for the HHR rate and $1.156 \times 10^{-8} M_{\odot}$ for the NACRE rate. Based on the thermal timescale of the ignited helium layer, the duration of this burst would fall into the superburst category. In the HHR calculation, helium is ignited first due to a large enhancement in the rate at low temperatures, leading to a smaller amount of helium piled up on the neutron star's surface. As a result, the burst is less energetic than that in the CF88 calculation, which explains a slower increase in the luminosity of the light curve (Fig. 6.10). Our preliminary results demonstrate the large impact of the new triple-alpha rate on this burst.

Because of its long recurrence time, the number of observed instances for this burst is very low. In our model, we use approximately the same low accretion rate as the system with the observed superburst 0614+091 [88]. Because the event is too energetic, we are not able to simulate the entire burst. Therefore, the peak luminosity of this burst is not obtained. In addition, the start of the 0614+091 [88] superburst was not observed. For these two reasons, no comparison between the simulated and the observed superburst can be made at this stage. We certainly hope more data of this event would be collected in the future. Also, the upcoming advanced telescopes may be able to detect the slow rise of the light curve produced by HHR.

Chapter 7

Summary and outlook

7.1 Summary

We have successfully calculated the triple-alpha reaction rate in the low temperature regime $T < 0.1$ GK, where many numerical attempts have failed before. In this work, the triple-alpha reaction is modeled as a three-body problem. We use the hyperspherical harmonics (HH) method to tackle this problem. In the low temperature region, the triple-alpha reaction proceeds through a quadrupole transition from the 0^+ continuum to the 2_1^+ bound state in ^{12}C . The 2_1^+ bound state is obtained by solving a set of coupled channels equations in hyper-radius coordinates for negative energy, under the condition that the wavefunction goes to zero at large distances. The same approach can not be applied to the 0^+ continuum states because they require an exact boundary condition for the three charged particles. We overcome this difficulty by combining the R-matrix expansion and the R-matrix propagation method in the hyperspherical harmonics basis. We first solve a set of coupled channels equations for a positive energy in a small R-matrix box with fixed logarithmic derivatives. The R-matrix at the boundary of the box is then propagated to a sufficiently large radius,

where the Coulomb asymptotic matching can be performed. We also implement a technique of screening the off-diagonal Coulomb couplings to ensure numerical stability at very low energies. The screening technique allows us to obtain analytic solutions for the Coulomb asymptotic wavefunction, which are then used in the matching procedure. We also study the symmetry properties of our problem. Since an alpha particle can be considered as a boson of spin zero, the wavefunction must be unchanged for any permutation of the alpha-alpha pair. This only allows even partial waves to contribute to the total wavefunction. The symmetrization also enables us to reduce three Faddeev components to a set of coupled channel equations in the hyper-radius formed from one pair of Jacobi coordinates. This strongly increases the computational efficiency.

For the alpha-alpha interaction we use the Ali-Bodmer potential, which reproduces the low energy phase shifts as well as the 0^+ resonance of ^8Be . A three-body force is necessary to fit experimental data. We obtain good convergence for the binding energy and the root-mean-square radius of the 2_1^+ bound state in ^{12}C . Our binding energy agrees with measurements and the root-mean-square radius is compatible with a microscopic study, supporting the correct structure for the bound state wavefunction. In the HHR framework, we are not only able to calculate the 0^+ non-resonant continuum states in ^{12}C , but also reproduce its well known Hoyle state. Therefore, this method allows us to include the resonant and non-resonant process on the same footing. The density distribution function for the Hoyle state is constructed to study its structure. We find the prolate triangle configuration of the triple-alpha to be dominant.

When both the 2_1^+ bound state and the 0^+ continuum states of ^{12}C are obtained, we are able to construct the quadrupole transition function and the cross section, from which we determine the triple-alpha reaction rate. A careful assessment of different sources of

uncertainty for this rate, arising from the numerical calculation is also provided. We first check our method for the pure Coulomb case where no resonances are present in either the two-body or three-body systems. The propagation method for this case is stable without screening. An relatively small uncertainty of 35% due to the screening technique is introduced in the calculation of the reaction rate at low temperatures. A thorough convergence study is then performed for the realistic triple-alpha problem. Our reaction rate converges well with screening radius ρ_{screen} and the size of our model space K_{max} . We estimate an overall uncertainty of a factor of 2 for our triple-alpha rate, due to the screening approximation and the resonant width estimation.

Our triple-alpha reaction rate obtained by the HHR method agrees with NACRE at high temperatures but increases significantly at temperatures below 0.06 GK, accompanied by a very different temperature dependence. The enhancement of the HHR rate at low energy is not as strong as that seen in the CDCC result of [15]. We find a dominant contribution of the non-resonant continuum to the triple-alpha rate at low temperatures. Our study shows that this non-resonant contribution is driven by the long-range Coulomb effects. In this work we include the Coulomb couplings to all orders, up to sufficiently large radius (800 fm). The transition between the resonant and non-resonant process occurs around 0.06 GK.

Our triple-alpha rate differs strongly from previous predictions. While the CDCC rate does not reproduce the red giant phase in the evolution of low-mass stars, our HHR rate does. The evolutionary tracks are very similar between the HHR and the NACRE calculations. Using our new rate, stars still undergo the red giant phase, contrary to the results using the CDCC rate. We observe small differences in the thermal pulsation and the planetary nebula stages. However, we expect these differences to be smaller than the inherent uncertainties in the astrophysical model. In conclusion, our rate does not drastically change the evolution

of low-mass stars, opposed to the CDCC rate. The implication of our new rate is also investigated for other astrophysical scenarios that burn helium at lower temperatures. We look at helium accreting white dwarfs and helium accreting neutron stars with small accretion rates, which can give rise to very energetic events like type Ia supernovae and superbursts. Helium burning in these scenarios occurs at lower temperatures where the HHR rate and the NACRE rate are very different. We find that helium ignition conditions are very different between the HHR and the NACRE rates. At a given temperature, the helium shell flash ignites at much lower density when the HHR rate is used. As a result, the ignition mass in the HHR calculation is smaller than that in the NACRE calculation. There is also significant difference in the light curve of a helium accreting neutron star between the HHR rate and the NACRE rate. The recurrence time of the burst is much shorter using the HHR rate. Because the current one-dimensional codes are not designed for such energetic events like type Ia supernovae and superbursts, where our rate demonstrates large impact, full simulations of these explosive scenarios are not possible. We should also note that, until today, the number of observed instances for such events is very low, therefore comparison with our calculation is not yet available at this stage. Our results serve as an additional stimulus to collect more data on these types of phenomena.

7.2 Outlook

The presence of very narrow two-body and three-body resonances, in addition to the strong, long range Coulomb interaction makes the triple-alpha problem very challenging. Our HHR framework which is the combination of various methods is a new approach to overcome the well known difficulty of the three charged-particle system. This method allows us to approach

the very low energy regime where measurements are impossible without using extrapolation and results obtained have an impact in astrophysics. Our success in solving the triple-alpha problem opens the opportunity for further applications of the method to other three-body systems.

Within the triple-alpha system, there is still room for further developments. Throughout this work, we employ a fixed zero logarithmic derivative for the R-matrix method due to its mathematical simplicity. One might extend the R-matrix propagation method for arbitrary values of the logarithmic derivative β . This could improve the numerical stability of the method and free us from using the screening technique. Because the aim of this work is to calculate the triple-alpha rate at low temperatures, our convergence study is currently performed with respect to this quantity. One can further explore the convergence of the three-body scattering wavefunction from phase-shift and scattering matrix analyses. Because the problem involves so many channels, it is not trivial to continuously link the eigenphases at various energies and associate the eigenphases with certain hyper-spherical harmonics channels. A specific algorithm would need to be developed. The scattering matrix and phase-shift analyses can also improve the accuracy of extracting the properties of the Hoyle resonant state of ^{12}C . Cluster structures of the 2_1^+ bound state and the 0_2^+ resonant state can be further investigated to obtain information about the angular orientation between the three alpha particles. A recent *ab initio* lattice calculation [89] finds a “bent-arm” triangle configuration for the Hoyle state when taking into account the effect of rotational excitation. It will be interesting to compare that, with results obtained from our three-body framework.

Although specifically designed for the triple-alpha problem, the HHR method can be applied to other three-body systems. It has a large application for many important reactions in astrophysics. For example, one can use this method to directly calculate the production

rate of elements that are relevant in particular astrophysical environments such as ${}^6\text{He}$ and ${}^9\text{Be}$. The study of dineutron decay in nuclear reactions (such as ${}^{16}\text{Be}$ in [90]) can be studied using the same framework. Because these three-body systems do not involve the Coulomb interaction, the calculations are expected to converge much faster. Also important, it opens new opportunities in addressing three-body, low energy reactions for particles with charge where the physics is more challenging. For example, the diproton decay experiment of ${}^6\text{Be}$ [91] can be analyzed using this method. The HHR method can be extended to any three-body problem in atomic and molecular physics. The work in [92] employs a three-body approach to calculate the ground state energy of the two electron atoms and ions such as negatively charged hydrogen, helium, and positively charged lithium. The results can be further improved by using our method.

APPENDICES

Appendix A

Detailed Derivations of the R-matrix propagation method

A.1 Deriving Eq. (2.58)

In this section, we will present the detailed derivation of the propagating functions \mathbf{g}_i in Eq. (2.58). This is the key element in the R-matrix propagation method. First, we insert Eq. (2.56) into Eq. (2.54) for sector p to obtain:

$$\frac{d^2 \chi_{\gamma\gamma i}^p(\rho)}{d\rho^2} = \sum_{\alpha\gamma'} T_{\gamma\alpha}^p \lambda_\alpha^2(p) \tilde{T}_{\alpha\gamma'}^p \chi_{\gamma'\gamma i}^p(\rho). \quad (\text{A.1})$$

Because \mathbf{T} is a unitary matrix which means $\sum_{\gamma'} \tilde{T}_{\alpha\gamma'}^p T_{\gamma'\beta}^p = \delta_{\alpha\beta}$, we can define:

$$\begin{aligned} F_{\alpha\gamma i}^p(\rho) &= \sum_{\gamma'} \tilde{T}_{\alpha\gamma'}^p \chi_{\gamma'\gamma i}^p(\rho), \\ \chi_{\gamma\gamma i}^p &= \sum_{\alpha} T_{\gamma\alpha}^p F_{\alpha\gamma i}^p(\rho). \end{aligned} \quad (\text{A.2})$$

Inserting Eq. (A.2) into Eq. (A.1), we obtain a simpler equation:

$$\frac{d^2 F_{\alpha\gamma i}^p(\rho)}{d\rho^2} = \lambda_\alpha^2(p) F_{\alpha\gamma i}^p(\rho). \quad (\text{A.3})$$

The general solutions of Eq. (A.1) are well known:

$$F_{\alpha\gamma i}^p(\rho) = \begin{cases} A_\alpha^p \sinh(|\lambda_\alpha(p)|\rho) + B_\alpha^p \cosh(|\lambda_\alpha(p)|\rho), & \lambda_\alpha^2(p) > 0 \\ A_\alpha^p \sin(|\lambda_\alpha(p)|\rho) + B_\alpha^p \cos(|\lambda_\alpha(p)|\rho), & \lambda_\alpha^2(p) \leq 0 \end{cases}. \quad (\text{A.4})$$

From now on we will drop the index p for convenience and keep in mind that these are the solutions for sector p . The constants A_α and B_α are determined by the boundary conditions of sector p at ρ_L and ρ_R (see Fig. 2.5):

$$\begin{bmatrix} \mathbf{F}_R \\ \mathbf{F}_L \end{bmatrix} = \begin{bmatrix} \mathbf{g}_1 & \mathbf{g}_2 \\ \mathbf{g}_3 & \mathbf{g}_4 \end{bmatrix} \begin{bmatrix} -\mathbf{F}'_R \\ \mathbf{F}'_L \end{bmatrix}, \quad (\text{A.5})$$

where \mathbf{g}_i are the diagonal matrices. Eq. (A.5) for \mathbf{F} is equivalent to Eq. (2.57) for $\boldsymbol{\chi}$ due to the relationship in Eq. (A.2). We rewrite Eq. (A.5) in the following form:

$$\begin{aligned} (F_{\alpha\gamma i})_R &= -(g_1)_{\alpha\alpha} (F_{\alpha\gamma i})'_R + (g_2)_{\alpha\alpha} (F_{\alpha\gamma i})'_L, \\ (F_{\alpha\gamma i})_L &= -(g_3)_{\alpha\alpha} (F_{\alpha\gamma i})'_R + (g_4)_{\alpha\alpha} (F_{\alpha\gamma i})'_L. \end{aligned} \quad (\text{A.6})$$

For simplicity, we assume $\rho_L = 0$ and $\rho_R = \rho_R - \rho_L = h_p$ without losing the generality of the problem.

For $\lambda_\alpha^2 > 0$:

We first evaluate Eq. (A.4) at the two boundaries of sector p and then plug the results into Eq. (A.6):

$$A_\alpha \sinh|\lambda_\alpha h_p| + B_\alpha \cosh|\lambda_\alpha h_p| =$$

$$- (g_1)_{\alpha\alpha} (A_\alpha |\lambda_\alpha| \cosh|\lambda_\alpha h_p| + B_\alpha |\lambda_\alpha| \sinh|\lambda_\alpha h_p|) + (g_2)_{\alpha\alpha} A_\alpha, \quad (\text{A.7})$$

$$B_\alpha = - (g_3)_{\alpha\alpha} (A_\alpha |\lambda_\alpha| \cosh|\lambda_\alpha h_p| + B_\alpha |\lambda_\alpha| \sinh|\lambda_\alpha h_p|) + (g_4)_{\alpha\alpha} A_\alpha. \quad (\text{A.8})$$

In order for Eq. (A.7) and Eq. (A.8) to be satisfied with all values of A_α and B_α , we have to constrain $(g_i)_{\alpha\alpha}$ by the following equations:

$$(g_1)_{\alpha\alpha} |\lambda_\alpha| \cosh|\lambda_\alpha h_p| - (g_2)_{\alpha\alpha} + \sinh|\lambda_\alpha h_p| = 0, \quad (\text{A.9})$$

$$(g_1)_{\alpha\alpha} |\lambda_\alpha| \sinh|\lambda_\alpha h_p| + \cosh|\lambda_\alpha h_p| = 0, \quad (\text{A.10})$$

$$(g_3)_{\alpha\alpha} |\lambda_\alpha| \cosh|\lambda_\alpha h_p| - (g_4)_{\alpha\alpha} = 0, \quad (\text{A.11})$$

$$(g_3)_{\alpha\alpha} |\lambda_\alpha| \sinh|\lambda_\alpha h_p| + 1 = 0. \quad (\text{A.12})$$

Solving these equations we obtain the sector propagating functions \mathbf{g}_i :

$$(g_1^p)_{\alpha\alpha'} = (g_4^p)_{\alpha\alpha'} = -\delta_{\alpha\alpha'} \frac{\coth|\lambda_\alpha h_p|}{|\lambda_\alpha|}, \quad (\text{A.13})$$

$$(g_2^p)_{\alpha\alpha'} = (g_3^p)_{\alpha\alpha'} = -\delta_{\alpha\alpha'} \frac{1}{|\lambda_\alpha| \sinh|\lambda_\alpha h_p|}. \quad (\text{A.14})$$

For $\lambda_\alpha^2 \leq 0$:

In a very similar manner we obtain the sector propagating functions \mathbf{g}_i for this case:

$$(g_1^p)_{\alpha\alpha'} = (g_4^p)_{\alpha\alpha'} = \delta_{\alpha\alpha'} \frac{\cot|\lambda_\alpha h_p|}{|\lambda_\alpha|}, \quad (\text{A.15})$$

$$(g_2^p)_{\alpha\alpha'} = (g_3^p)_{\alpha\alpha'} = \delta_{\alpha\alpha'} \frac{1}{|\lambda_\alpha| \sin|\lambda_\alpha h_p|}. \quad (\text{A.16})$$

The results in Eq. (A.13), Eq. (A.14), Eq. (A.15) and Eq. (A.16) are briefly presented in Eq. (2.58) in Sec. 2.2.2

A.2 Deriving Eq. (2.61)

In this section, we derive the propagating equation of the R-matrix: Eq. (2.61). In order to that we first insert Eq. (2.59) and Eq. (2.60) into Eq. (2.57):

$$\rho_R^p \mathcal{R}^p \chi_R^{p'} = -\mathbf{G}_1^p \chi_R^{p'} + \mathbf{G}_2^p \chi_L^{p'}, \quad (\text{A.17})$$

$$\rho_R^{p-1} \mathcal{R}^{p-1} \chi_L^{p'} = -\mathbf{G}_3^p \chi_R^{p'} + \mathbf{G}_4^p \chi_L^{p'}, \quad (\text{A.18})$$

Arranging Eq. (A.17) and Eq. (A.18) we obtain:

$$(-\mathbf{G}_1^p + \rho_R^p \mathcal{R}^p) \chi_R^{p'} = \mathbf{G}_2^p \chi_L^{p'}, \quad (\text{A.19})$$

$$\mathbf{G}_3^p \chi_R^{p'} = (\mathbf{G}_4^p - \rho_R^{p-1} \mathcal{R}^{p-1}) \chi_L^{p'}, \quad (\text{A.20})$$

We first multiply both sides of Eq. (A.20) with $(\mathbf{G}_4^p - \rho_R^{p-1} \mathcal{R}^{p-1})^{-1}$ to the left and then with \mathbf{G}_2^p also to the left. Afterward, we compare the new equation with Eq. (A.19) and

obtain:

$$(-\mathbf{G}_1^p + \rho_R^p \mathbf{R}^p) = \mathbf{G}_2^p (\mathbf{G}_4^p - \rho_R^{p-1} \mathbf{R}^{p-1})^{-1} \mathbf{G}_3^p. \quad (\text{A.21})$$

Eq. (A.21) reduces to Eq. (2.61) in Sec. 2.2.2, after trivial manipulation.

A.3 Deriving Eq. (2.63), Eq. (2.64), Eq. (2.65), and Eq. (2.66)

This section presents the detailed derivation of several equations namely Eq. (2.63), Eq. (2.64), Eq. (2.65), and Eq. (2.66) which result in the propagation of the three-body scattering wavefunctions. We first rewrite Eq. (2.62):

$$\chi_R^p = -\mathcal{G}_1^p \chi_R^{p'} + \mathcal{G}_2^p \chi_L^{1'}, \quad (\text{A.22})$$

$$\chi_L^1 = -\mathcal{G}_3^p \chi_R^{p'} + \mathcal{G}_4^p \chi_L^{1'}, \quad (\text{A.23})$$

We obtain a similar set of equations for sector $p - 1$:

$$\chi_R^{p-1} = -\mathcal{G}_1^{p-1} \chi_R^{p-1'} + \mathcal{G}_2^{p-1} \chi_L^{1'}, \quad (\text{A.24})$$

$$\chi_L^1 = -\mathcal{G}_3^{p-1} \chi_R^{p-1'} + \mathcal{G}_4^{p-1} \chi_L^{1'}, \quad (\text{A.25})$$

Because the wavefunctions are continuous at the sector boundaries, i.e. $\chi_R^{p-1} = \chi_L^p$ and $\chi_R^{p-1'} = \chi_L^{p'}$, we can express the Eq. (2.57) in the following form:

$$\chi_R^p = -\mathbf{G}_1^p \chi_R^{p'} + \mathbf{G}_2^p \chi_R^{p-1'}, \quad (\text{A.26})$$

$$\chi_R^{p-1} = -\mathbf{G}_3^p \chi_R^{p'} + \mathbf{G}_4^p \chi_R^{p-1'}. \quad (\text{A.27})$$

We multiply to the left of both sides of Eq. (A.22) and Eq. (A.24) with $[\mathcal{G}_2^p]^{-1}$ and $[\mathcal{G}_2^{p-1}]^{-1}$ respectively and then subtract the results:

$$[\mathcal{G}_2^p]^{-1} \chi_R^p - [\mathcal{G}_2^{p-1}]^{-1} \chi_R^{p-1} = [\mathcal{G}_2^{p-1}]^{-1} \mathcal{G}_1^{p-1} \chi_R^{p-1'} - [\mathcal{G}_2^p]^{-1} \mathcal{G}_1^p \chi_R^{p'}. \quad (\text{A.28})$$

Inserting Eq. (A.27) into Eq. (A.28) we obtain:

$$[\mathcal{G}_2^p]^{-1} \chi_R^p = ([\mathcal{G}_2^{p-1}]^{-1} \mathbf{G}_4^p + [\mathcal{G}_2^{p-1}]^{-1} \mathcal{G}_1^{p-1}) \chi_R^{p-1'} - ([\mathcal{G}_2^{p-1}]^{-1} \mathbf{G}_3^p + [\mathcal{G}_2^p]^{-1} \mathcal{G}_1^p) \chi_R^{p'}. \quad (\text{A.29})$$

Multiplying \mathcal{G}_2^p to the left of both sides of Eq. (A.29) and comparing with Eq. A.26 we have:

$$\mathbf{G}_1^p = \mathcal{G}_2^p ([\mathcal{G}_2^{p-1}]^{-1} \mathbf{G}_3^p + [\mathcal{G}_2^p]^{-1} \mathcal{G}_1^p), \quad (\text{A.30})$$

$$\mathbf{G}_2^p = \mathcal{G}_2^p ([\mathcal{G}_2^{p-1}]^{-1} \mathbf{G}_4^p + [\mathcal{G}_2^{p-1}]^{-1} \mathcal{G}_1^{p-1}). \quad (\text{A.31})$$

Eq. (A.31) is equivalent to Eq. (2.64):

$$\mathcal{G}_2^p = \mathbf{G}_2^p [\mathbf{G}_4^p + \mathcal{G}_1^{p-1}]^{-1} \mathcal{G}_2^{p-1}. \quad (\text{A.32})$$

Inserting Eq. (A.32) into Eq. (A.30) we arrive at Eq. (2.63):

$$\mathcal{G}_1^p = \mathbf{G}_1^p - \mathbf{G}_2^p [\mathbf{G}_4^p + \mathcal{G}_1^{p-1}]^{-1} \mathbf{G}_3^p. \quad (\text{A.33})$$

Comparing Eq. (A.23) and Eq. (A.25) we have:

$$\chi_L^{1'} = [\mathcal{G}_4^p - \mathcal{G}_4^{p-1}]^{-1} (\mathcal{G}_3^p \chi_R^{p'} - \mathcal{G}_3^{p-1} \chi_R^{p-1'}). \quad (\text{A.34})$$

Inserting Eq. (A.34) into Eq. (A.24) we obtain:

$$\chi_R^{p-1} = \mathcal{G}_2^{p-1} [\mathcal{G}_4^p - \mathcal{G}_4^{p-1}]^{-1} \mathcal{G}_3^p \chi_R^{p'} - (\mathcal{G}_1^{p-1} + \mathcal{G}_2^{p-1} [\mathcal{G}_4^p - \mathcal{G}_4^{p-1}]^{-1} \mathcal{G}_3^{p-1}) \chi_R^{p-1'}. \quad (\text{A.35})$$

Comparing Eq. (A.35) and Eq. (A.27) we have:

$$\mathbf{G}_3^p = -\mathcal{G}_2^{p-1} [\mathcal{G}_4^p - \mathcal{G}_4^{p-1}]^{-1} \mathcal{G}_3^p, \quad (\text{A.36})$$

$$\mathbf{G}_4^p = -\mathcal{G}_1^{p-1} - \mathcal{G}_2^{p-1} [\mathcal{G}_4^p - \mathcal{G}_4^{p-1}]^{-1} \mathcal{G}_3^{p-1}. \quad (\text{A.37})$$

Eq. (A.37) reduces to Eq. (2.66), after trivial algebra :

$$\mathcal{G}_4^p = \mathcal{G}_4^{p-1} - \mathcal{G}_3^{p-1} [\mathbf{G}_4^p + \mathcal{G}_1^{p-1}]^{-1} \mathcal{G}_2^{p-1}. \quad (\text{A.38})$$

Inserting Eq. (A.38) into Eq. (A.36) we obtain Eq. (2.65):

$$\mathcal{G}_3^p = \mathcal{G}_3^{p-1} [\mathbf{G}_4^p + \mathcal{G}_1^{p-1}]^{-1} \mathbf{G}_3^p. \quad (\text{A.39})$$

Appendix B

Detailed derivation of the quadrupole transition function

B.1 Deriving Eq. (3.32)

In this section, we derive the quadrupole transition operator E_{2m} (Eq. (3.32)) in the hyperspherical harmonics representation. This is an important step in constructing the three-body transition strength function. First, we apply Eq. (3.31) to Eq. (3.28) and obtain:

$$\begin{aligned} Z_1 a_1^2 Y_{2m}(\hat{\mathbf{a}}_1) &= Z_1 \sqrt{\frac{5}{4\pi}} a_1^2 C_{2m}(\hat{\mathbf{a}}_1), \\ &= Z_1 \sqrt{\frac{5}{4\pi}} \sum_{\lambda,\mu} \left(\frac{4!}{2\lambda!2(2-\lambda)!} \right)^{\frac{1}{2}} \left(-\frac{\sqrt{\mu_1}}{A_1} x \right)^{2-\lambda} \left(-\frac{\sqrt{\mu_2}}{A_1 + A_2} y \right)^\lambda \\ &\times C_{2-\lambda, m-\mu}(\hat{\mathbf{x}}) C_{\lambda,\mu}(\hat{\mathbf{y}}) \langle 2-\lambda \ m-\mu \ \lambda \ \mu | 2 \ m \rangle. \end{aligned} \tag{B.1}$$

We do the same with Eq. (3.29):

$$\begin{aligned}
Z_2 a_2^2 Y_{2m}(\hat{\mathbf{a}}_2) &= Z_2 \sqrt{\frac{5}{4\pi}} a_2^2 C_{2m}(\hat{\mathbf{a}}_2), \\
&= Z_2 \sqrt{\frac{5}{4\pi}} \sum_{\lambda,\mu} \left(\frac{4!}{2\lambda!2(2-\lambda)!} \right)^{\frac{1}{2}} \left(\frac{\sqrt{\mu_1}}{A_2} x \right)^{2-\lambda} \left(-\frac{\sqrt{\mu_2}}{A_1+A_2} y \right)^\lambda \\
&\quad \times C_{2-\lambda,m-\mu}(\hat{\mathbf{x}}) C_{\lambda,\mu}(\hat{\mathbf{y}}) \langle 2-\lambda \ m-\mu \ \lambda \ \mu | 2 \ m \rangle.
\end{aligned} \tag{B.2}$$

Adding Eq. (B.1) and Eq. (B.2), we arrive at:

$$\begin{aligned}
&Z_1 a_1^2 Y_{2m}(\hat{\mathbf{a}}_1) + Z_2 a_2^2 Y_{2m}(\hat{\mathbf{a}}_2) \\
&= \sqrt{\frac{5}{4\pi}} \sum_{\lambda,\mu} \left(\frac{4!}{2\lambda!2(2-\lambda)!} \right)^{\frac{1}{2}} (\sqrt{\mu_1} x)^{2-\lambda} \left(-\frac{\sqrt{\mu_2}}{A_1+A_2} y \right)^\lambda \\
&\quad \times C_{2-\lambda,m-\mu}(\hat{\mathbf{x}}) C_{\lambda,\mu}(\hat{\mathbf{y}}) \langle 2-\lambda \ m-\mu \ \lambda \ \mu | 2 \ m \rangle \left[Z_1 \left(-\frac{1}{A_1} \right)^{2-\lambda} + Z_2 \left(\frac{1}{A_2} \right)^{2-\lambda} \right].
\end{aligned} \tag{B.3}$$

Due to the properties of angular momentum, λ can only be 0,1,2. Firstly, we calculate the *r.h.s* of Eq. (B.3) for $\lambda = 0$:

$$\begin{aligned}
r.h.s &= \sqrt{\frac{5}{4\pi}} \left(\frac{4!}{0!4!} \right)^{\frac{1}{2}} (\sqrt{\mu_1} x)^2 \left(-\frac{\sqrt{\mu_2}}{A_1+A_2} y \right)^0 \\
&\quad \times C_{2m}(\hat{\mathbf{x}}) C_{00}(\hat{\mathbf{y}}) \langle 2 \ m \ 0 \ 0 | 2 \ m \rangle \left[Z_1 \left(-\frac{1}{A_1} \right)^2 + Z_2 \left(\frac{1}{A_2} \right)^2 \right] \\
&= \mu_1 x^2 Y_{2m}(\hat{\mathbf{x}}) \left[\frac{Z_1}{A_1^2} + \frac{Z_2}{A_2^2} \right].
\end{aligned} \tag{B.4}$$

For $\lambda = 1$, the *r.h.s* of Eq. (B.3) becomes:

$$\begin{aligned}
r.h.s &= \sqrt{\frac{5}{4\pi}} \left(\frac{4!}{2!2!} \right)^{\frac{1}{2}} (\sqrt{\mu_1} x)^1 \left(-\frac{\sqrt{\mu_2}}{A_1 + A_2} y \right)^1 \left[Z_1 \left(-\frac{1}{A_1} \right)^1 + Z_2 \left(\frac{1}{A_2} \right)^1 \right] \\
&\times \sum_{\mu} \langle 1 \ m - \mu \ 1 \ \mu | 2 \ m \rangle C_{1 \ m - \mu}(\hat{\mathbf{x}}) C_{1\mu}(\hat{\mathbf{y}}) \\
&= 2\sqrt{\frac{6\pi}{5}} \frac{\sqrt{\mu_1\mu_2}}{A_1 + A_2} \left[\frac{Z_1}{A_1} - \frac{Z_2}{A_2} \right] x y \sum_{\mu} \langle 1 \ m - \mu \ 1 \ \mu | 2 \ m \rangle Y_{1 \ m - \mu}(\hat{\mathbf{x}}) Y_{1\mu}(\hat{\mathbf{y}}). \quad (\text{B.5})
\end{aligned}$$

We do the same thing for the case of $\lambda = 2$

$$\begin{aligned}
r.h.s &= \sqrt{\frac{5}{4\pi}} \left(\frac{4!}{4!0!} \right)^{\frac{1}{2}} (\sqrt{\mu_1} x)^0 \left(-\frac{\sqrt{\mu_2}}{A_1 + A_2} y \right)^2 \\
&\times C_{00}(\hat{\mathbf{x}}) C_{2m}(\hat{\mathbf{y}}) \langle 0 \ 0 \ 2 \ m | 2 \ m \rangle \left[Z_1 \left(-\frac{1}{A_1} \right)^0 + Z_2 \left(\frac{1}{A_2} \right)^0 \right] \\
&= \left(\frac{\mu_2}{(A_1 + A_2)^2} y^2 \right) Y_{2m}(\hat{\mathbf{y}}) [Z_1 + Z_2]. \quad (\text{B.6})
\end{aligned}$$

Putting Eq. (B.4), Eq. (B.5), and Eq. (B.6) together we have:

$$\begin{aligned}
&Z_1 a_1^2 Y_{2m}(\hat{\mathbf{a}}_1) + Z_2 a_2^2 Y_{2m}(\hat{\mathbf{a}}_2) + Z_3 a_3^2 Y_{2m}(\hat{\mathbf{a}}_3) \\
&= \mu_1 x^2 \left[\frac{Z_1}{A_1^2} + \frac{Z_2}{A_2^2} \right] Y_{2m}(\hat{\mathbf{x}}) + \frac{\mu_2}{(A_1 + A_2)^2} y^2 [Z_1 + Z_2] Y_{2m}(\hat{\mathbf{y}}) \\
&+ 2\sqrt{\frac{6\pi}{5}} \frac{\sqrt{\mu_1\mu_2}}{A_1 + A_2} \left[\frac{Z_1}{A_1} - \frac{Z_2}{A_2} \right] x y \sum_{\mu} \langle 1 \ m - \mu \ 1 \ \mu | 2 \ m \rangle Y_{1 \ m - \mu}(\hat{\mathbf{x}}) Y_{1\mu}(\hat{\mathbf{y}}) \\
&+ Z_3 \frac{\mu_2}{A_3^2} y^2 Y_{2m}(\hat{\mathbf{y}}). \quad (\text{B.7})
\end{aligned}$$

Inserting Eq. (B.7) into Eq. (3.27) we obtain an expression for the quadrupole transition operator in a three-body hyperspherical approach:

$$\begin{aligned}
E_{2m} = & e\mu_1 \left[\frac{Z_1}{A_1^2} + \frac{Z_2}{A_2^2} \right] x^2 Y_{2m}(\hat{\mathbf{x}}) + e\mu_2 \left(\frac{Z_3}{A_3^2} + \frac{Z_1 + Z_2}{(A_1 + A_2)^2} \right) y^2 Y_{2m}(\hat{\mathbf{y}}) \\
& + 2e\sqrt{\frac{6\pi}{5}} \frac{\sqrt{\mu_1\mu_2}}{A_1 + A_2} \left[\frac{Z_1}{A_1} - \frac{Z_2}{A_2} \right] x y \sum_{\mu} \langle 1 \ m - \mu \ 1 \ \mu | 2 \ m \rangle Y_{1 \ m - \mu}(\hat{\mathbf{x}}) Y_{1\mu}(\hat{\mathbf{y}}). \quad (\text{B.8})
\end{aligned}$$

For the triple- α problem we have $A_1 = A_2 = A_3 = A$ (4) and $Z_1 = Z_2 = Z_3 = Z$ (2), the quadrupole transition operator formulae can be simplified:

$$\begin{aligned}
E_{2m} = & \frac{eZ}{A} \left[x^2 Y_{2m}(\hat{\mathbf{x}}) + y^2 Y_{2m}(\hat{\mathbf{y}}) \right], \\
= & \frac{eZ}{A} \left[(\rho \sin\theta)^2 Y_{2m}(\hat{\mathbf{x}}) + (\rho \cos\theta)^2 Y_{2m}(\hat{\mathbf{y}}) \right]. \quad (\text{B.9})
\end{aligned}$$

B.2 Deriving Eq. (3.42)

This section present the missing steps in deriving Eq. (3.42). We first take the squared modulus of both sides of Eq. (3.38) we have:

$$\begin{aligned}
|\langle L'M' | E_{2m} | LM; \kappa \rangle|^2 = & \sum_{Kl_x l_y} \sum_{K'l'_x l'_y} \sum_{K_1 l_{1x} l_{1y}} \sum_{K'_1 l'_{1x} l'_{1y}} \sum_{K^i l_x^i l_y^i} \sum_{K_1^i l_{1x}^i l_{1y}^i} \\
& \left(\varphi_{K^i}^{l_x^i l_y^i}(\theta_\kappa) \right)^* \varphi_{K_1^i}^{l_{1x}^i l_{1y}^i}(\theta_\kappa) \left(\left[Y_{l_x^i}^i \otimes Y_{l_y^i}^i \right]_{LM}^\kappa \right)^* \left[Y_{l_{1x}^i}^i \otimes Y_{l_{1y}^i}^i \right]_{LM}^\kappa \\
& \times \langle K'l'_x l'_y L'M' | (E2)_m | Kl_x l_y K^i l_x^i l_y^i LM \rangle_s \\
& \times \langle K'_1 l'_{1x} l'_{1y} L'M' | (E2)_m | K_1 l_{1x} l_{1y} K_1^i l_{1x}^i l_{1y}^i LM \rangle_s^*. \quad (\text{B.10})
\end{aligned}$$

In order to simplify Eq. (B.10), we first consider its angular part in momentum space. The coupling between two angular momentums can be expressed in term of Clebsch-Gordan coefficients and spherical harmonics functions:

$$\begin{aligned}
& \left(\left[Y_{l_x^i}^i \otimes Y_{l_y^i}^i \right]_{LM}^\kappa \right)^* \left[Y_{l_{1x}^i}^i \otimes Y_{l_{1y}^i}^i \right]_{LM}^\kappa \\
&= \sum_{m_x^i m_y^i} \sum_{m_{1x}^i m_{1y}^i} \langle l_x^i m_x^i l_y^i m_y^i | LM \rangle^* \langle l_{1x}^i m_{1x}^i l_{1y}^i m_{1y}^i | LM \rangle \\
&\times Y_{l_x^i m_x^i}^*(\Omega_{k_x}) Y_{l_y^i m_y^i}^*(\Omega_{k_y}) Y_{l_{1x}^i m_{1x}^i}(\Omega_{k_x}) Y_{l_{1y}^i m_{1y}^i}(\Omega_{k_y}). \tag{B.11}
\end{aligned}$$

Using Eq. (3.39), Eq. (3.40) and Eq. (3.41) to integrate Eq. (B.10) over $d\Omega_r^\kappa$ we obtain:

$$\begin{aligned}
& \int |\langle L'M' | E_{2m} | LM; \kappa \rangle|^2 d\Omega_r^\kappa = \sum_{K l_x l_y} \sum_{K' l'_x l'_y} \sum_{K_1 l_{1x} l_{1y}} \sum_{K'_1 l'_{1x} l'_{1y}} \sum_{K^i l_x^i l_y^i} \\
& \left(\sum_{m_x^i m_y^i} \left| \langle l_x^i m_x^i l_y^i m_y^i | LM \rangle \right|^2 \right) \langle K' l'_x l'_y L' M' | E_{2m} | K l_x l_y K^i l_x^i l_y^i LM \rangle_s \\
& \times \langle K'_1 l'_{1x} l'_{1y} L' M' | E_{2m} | K_1 l_{1x} l_{1y} K^i l_x^i l_y^i LM \rangle_s^*. \tag{B.12}
\end{aligned}$$

There exists a sum rule for the Clebsch-Gordan coefficients

$$\sum_{m_x^i m_y^i} \left| \langle l_x^i m_x^i l_y^i m_y^i | LM \rangle \right|^2 = 1, \tag{B.13}$$

which reduces Eq. (B.12) to:

$$\begin{aligned}
& \int |\langle L'M' | E_{2m} | LM; \kappa \rangle|^2 d\Omega_r^\kappa = \sum_{Kl_x l_y} \sum_{K'l'_x l'_y} \sum_{K_1 l_{1x} l_{1y}} \sum_{K'_1 l'_{1x} l'_{1y}} \sum_{K^i l_x^i l_y^i} \\
& \times \langle K'l'_x l'_y L'M' | E_{2m} | Kl_x l_y K^i l_x^i l_y^i LM \rangle_s \\
& \times \langle K'_1 l'_{1x} l'_{1y} L'M' | E_{2m} | K_1 l_{1x} l_{1y} K^i l_x^i l_y^i LM \rangle_s^* .
\end{aligned} \tag{B.14}$$

Applying further algebraic simplification we arrive at Eq. (3.42):

$$\begin{aligned}
& \int |\langle L'M' | E_{2m} | LM; \kappa \rangle|^2 d\Omega_5^\kappa \\
& = \sum_{K^i l_x^i l_y^i} \left| \sum_{Kl_x l_y} \sum_{K'l'_x l'_y} \langle K'l'_x l'_y L'M' | E_{2m} | Kl_x l_y K^i l_x^i l_y^i LM \rangle_s \right|^2 .
\end{aligned} \tag{B.15}$$

Appendix C

Inputs for numerical calculations

C.1 Bound state calculation

```
&fname
  nfile='2bs'
  desc= '2bs: triple-alpha' /
&scale
  amn=939. hc=197.3/
&nuclei
  name= 'alpha', 'alpha', 'alpha'
  mass= 4 4 4
  z= 2 2 2
  radius=1.47 1.47 1.47 /
&identical
  id=F, F, T, iso=0.0, 0.0, 0.0 /
&total
  ngt = 1, gtot(1)=2.0, gparity(1)=+1 /
&particles
  ns(1)=1, spin(1,1)= 0.0, parity(1,1)=1, energy(1,1)=0.0,
  ns(2)=1, spin(1,2)= 0.0, parity(1,2)=1, energy(1,2)=0.0,
  ns(3)=1, spin(1,3)= 0.0, parity(1,3)=1, energy(1,3)=0.0/
&em
  corek(1)=0.0 def(2,1)=0.0 Qmom(1)=0.0 Mmom(1)=0.0
  corek(2)=0.0 def(2,2)=0.0 Qmom(2)=0.0 Mmom(2)=0.0
  corek(3)=0.0 def(2,3)=0.0 Qmom(3)=0.0 Mmom(3)=0.0 /
&waves
```

```

auto(1)=T, kmaxa(1)=10, lxmax(1)=20, lymax(1)=20,
auto(2)=T, kmaxa(2)=10, lxmax(2)=20, lymax(2)=20,
auto(3)=T, kmaxa(3)=10, lxmax(3)=20, lymax(3)=20/
&poten
detail(1) = '2alpha '
rcoul(1)=2.94
typc(1) = 'gau '
ps(1,1)=125.0 ps(2,1)=1.53 ps(3,1)=-30.18 ps(4,1)=2.85,
pd(1,1)=20 pd(2,1)=1.53 pd(3,1)=-30.18 pd(4,1)=2.85,
pa(1,1)=-30.18 pa(2,1)=2.85,
typso(1)='nul '
typss(1)='nul '
typt(1) = 'nul '
detail(2) = '2alpha '
rcoul(2)=2.94
typc(2) = 'gau '
ps(1,2)=125.0 ps(2,2)=1.53 ps(3,2)=-30.18 ps(4,2)=2.85,
pd(1,2)=20 pd(2,2)=1.53 pd(3,2)=-30.18 pd(4,2)=2.85,
pa(1,2)=-30.18 pa(2,2)=2.85,
typso(2)='nul '
typss(2)='nul '
typt(2) = 'nul '
detail(3) = '2alpha '
rcoul(3)=2.94
typc(3) = 'gau '
ps(1,3)=125.0 ps(2,3)=1.53 ps(3,3)=-30.18 ps(4,3)=2.85,
pd(1,3)=20 pd(2,3)=1.53 pd(3,3)=-30.18 pd(4,3)=2.85,
pa(1,3)=-30.18 pa(2,3)=2.85,
typso(3)='nul '
typss(3)='nul '
typt(3) = 'nul ' /
&pot3b typ3b='gau ', s3b(1)=-15.94, r3b(1)=6.0 /
&gamso gamso1=0,0,0, gamso2=0,0,0 /
&grids rr=0.3 nlag=180 njac=70 / /Methods:
&trace /
&continuum docont=F /
&b2states n2states=0 /
&solve eimin = -5.0, eimax=0, eqn='T' nbmax=40 meigs=1 /
EOF
#timer
face13c3 < data.$$ > 2bs.out

```

C.2 Continuum state calculation

```
&fname
  nfile='0exc'
  desc='0exc: triple-alpha' /
&scale
  amn=939. hc=197.3/
&nuclei
  name='alpha','alpha','alpha'
  mass= 4 4 4
  z= 2 2 2
  radius=1.47 1.47 1.47 /
&identical
  id=F, F, T, iso=0.0, 0.0, 0.0 /
&total
  ngt = 1, gtot(1)=0.0, gparity(1)=+1 /
&particles
  ns(1)=1, spin(1,1)= 0.0, parity(1,1)=1, energy(1,1)=0.0,
  ns(2)=1, spin(1,2)= 0.0, parity(1,2)=1, energy(1,2)=0.0,
  ns(3)=1, spin(1,3)= 0.0, parity(1,3)=1, energy(1,3)=0.0/
&em
  corek(1)=0.0 def(2,1)=0.0 Qmom(1)=0.0 Mmom(1)=0.0
  corek(2)=0.0 def(2,2)=0.0 Qmom(2)=0.0 Mmom(2)=0.0
  corek(3)=0.0 def(2,3)=0.0 Qmom(3)=0.0 Mmom(3)=0.0 /
&waves
  auto(1)=T, kmaxa(1)=26, lxmax(1)=20,
  auto(2)=T, kmaxa(2)=26, lxmax(2)=20,
  auto(3)=T, kmaxa(3)=26, lxmax(3)=20/
&poten
  detail(1) ='2alpha'
  rcoul(1)=2.94
  typec(1) ='gau'
  ps(1,1)=125.0 ps(2,1)=1.53 ps(3,1)=-30.18 ps(4,1)=2.85,
  pd(1,1)=20 pd(2,1)=1.53 pd(3,1)=-30.18 pd(4,1)=2.85,
  pa(1,1)=-30.18 pa(2,1)=2.85,
  typso(1)='nul'
  typss(1)='nul'
  typt(1) ='nul'
  detail(2) ='2alpha'
  rcoul(2)=2.94
  typec(2) ='gau'
  ps(1,2)=125.0 ps(2,2)=1.53 ps(3,2)=-30.18 ps(4,2)=2.85,
  pd(1,2)=20 pd(2,2)=1.53 pd(3,2)=-30.18 pd(4,2)=2.85,
  pa(1,2)=-30.18 pa(2,2)=2.85,
```

```

typso(2)='nul'
typss(2)='nul'
typt(2)='nul'
detail(3)='2alpha'
rcoul(3)=2.94
typc(3)='gau'
    ps(1,3)=125.0 ps(2,3)=1.53 ps(3,3)=-30.18 ps(4,3)=2.85,
    pd(1,3)=20 pd(2,3)=1.53 pd(3,3)=-30.18 pd(4,3)=2.85,
    pa(1,3)=-30.18 pa(2,3)=2.85,
typso(3)='nul'
typss(3)='nul'
typt(3)='nul' /
&pot3b typ3b='gau', s3b(1)=-19.46, r3b(1)=6.0 /
&gamso gamso1=0,0,0, gamso2=0,0,0 /
&grids rr=0.3 nlag=3000 njac=100 rscreen=800 ascreen=10 /Methods:
&trace /
&continuum docont=F /
&b2states n2states=0 /
&solve eimin = -6.0, eimax=0, eqn='T' nbmax=0 meigs=0 /
EOF
#timer
face13c3c < data.$$>0excface.out
$mefile
FPOT = '0exc'
$end
$sturmin
Eo(1)=0.00 egsmin=-6.0 egsmax=3.0 sturm(1)='F' ngsmax=0
stepi = 0.05, rmax=50, steps=0.25, eeigmax=5000.0 lprwf=3 wfrmax=200
nsturm=50, buttle=5 rafin=3000 meigs=0 maxnop=100
ebeg=0.3525 estep=0.0005 emax=0.5 wfs=T numax=5 strfun=F
nogscat=F elinear=T betalw=1e-10
flwp ='/tmp/0exc.lwra', flwpr='/tmp/0exc.lwrmats'
$end
$bstate
kpole = 1, emin = 1.0, emax=0.0 ne = 30 numaxgs=10
$end
'EOF'
#timer
sturmxx96 < data.$$ > 0exc.out

```

Appendix D

Highlights on the (d,p) reaction projects

Transfer reactions have been considered as an effective tool to extract the single-particle structure and the properties of nuclei across the nuclear chart [93, 94, 95, 96]. Systematic studies on (d,p) reactions have provided a better understanding about the properties of nuclear interactions. For example, the work [96] on Sn isotopes using single-nucleon transfer reactions discovers the reduction of the spin-orbit strength when approaching the neutron drip line.

Transfer reactions also play an important role in astrophysics since they provide an indirect method to measure the (n, γ) rates which are crucial for the r-process nucleosynthesis. Neutron capture reactions (n, γ) on unstable nuclei are not possible to measure in the laboratory because both the beam and the target are unstable. Recently, the neutron transfer (d,p) inverse kinematics reactions on unstable targets has become possible due to the development of rare isotope facilities and detector technical advances [97, 98, 99]. Studies in

[100, 101] show that the neutron capture rates can be derived indirectly from (d,p) reactions. Significant effort has been invested in reducing the theoretical uncertainty of this indirect method [102, 103].

In the late 70s the single-particle structure of almost all stable nuclei has been successfully mapped out using (d,p) transfer reactions. Nuclear science has now shifted toward unstable rare isotopes, and this imposes severe challenges. The inverse kinematics technique is employed to study the structure and properties of exotic nuclei. Pioneering studies [97, 98, 99, 104, 105, 106, 107] showed promising results in applying this technique to unstable nuclei. With the development of new-generation rare-isotope facilities where beam rates will be enhanced, our possibility to have a detailed understanding of the exotic nuclei and the underlying nucleon-nucleon force is highly increased. In parallel with the experimental development, a well founded theory for (d,p) transfer reactions is crucial.

The traditional method to study transfer reactions is the distorted wave Born approximation (DWBA) [108, 109, 110] in which the T-matrix is truncated after the first term in the Born series. This method does not take into account deuteron break-up since it uses the deuteron-target elastic scattering wavefunction as an input [111]. At energies above 2.23 MeV (deuteron binding energy), deuteron tends to breakup as an intermediate step in transfer processes. For these cases, the break-up effects can be significant and the DWBA method is likely to fail to describe the data. In order to tackle this shortcoming of the DWBA method, Johnson and Soper [112] introduced the adiabatic distorted wave approximation (ADWA) framework which provides a practical prescription for including the deuteron break-up effects. In [112] the zero-range approximation is made for the n - p interaction, and this reduces the transfer matrix element to a form similar to that in the DWBA method. However, in the ADWA method the incoming wave is the adiabatic three-body wavefunction instead of

the elastic deuteron wavefunction. Using this method to analyze single-nucleon transfer reactions one often finds improvement in the description of experimental data [113]. Another formal development on the ADWA method was later introduced by Johnson and Tandy [114] to take into account the finite-range effects of the n - p interaction. However, the numerical implementation and application has not been systematically explored.

In the past, the zero-range (ZR-ADWA) approximation was used to perform (d,p) calculations due to computational limitations. The finite-range effects were then corrected by the local energy approximation (LEA) procedure which was developed by Buttle and Goldfarb [115]. The resulting codes persist to this day. It is not clear that this approximated correction still holds at high deuteron beam energies. In this appendix we will address this issue and further explore the implication of the FR-ADWA method.

Appendix D is organized into six sections. In section D.1, we discuss the physical quantities that are commonly investigated in (d,p) studies. Section D.2 presents the theory of the ADWA method. We then summarize our results on the study of the finite-range effects in (d,p) reactions in section D.3. The dispersive optical model is tested for (d,p) reactions using the FR-ADWA framework in section D.4. An application of the finite-range adiabatic distorted wave approximation (FR-ADWA) method for extracting the normalization coefficients from the $^{14}\text{C}(\text{d,p})^{15}\text{C}$ reaction is presented thereafter in section D.5. In the last section (D.6) of this appendix, we draw the general conclusions from our (d,p) studies.

D.1 Common physical quantities in (d,p) studies

Deuteron transfer reactions are considered as one of the most effective methods to study the single-particle structure of nuclei. A quantity of relevance for this process, in which nucleus

B is formed by the transfer of a neutron from deuteron projectile to the target nucleus A (see Fig. D.1) is the spectroscopic factor, defined as the square of the norm of the overlap function $\phi_{I_A:I_B}^{lj}(\vec{r})$:

$$S_{lsj}^{IAIB} = \int |\phi_{I_A:I_B}^{lj}(\vec{r})|^2 d\vec{r}, \quad (\text{D.1})$$

where,

$$\phi_{I_A:I_B}^{lj}(\vec{r}) = \langle \Phi_{I_A}^A(\xi_A) | \Phi_{I_B}^B(\xi_A, \vec{r}) \rangle. \quad (\text{D.2})$$

Here $\Phi_{I_A}^A$ and $\Phi_{I_B}^B$ are the many-body wave functions of nucleus A and B , respectively. I_A (I_B) is the spin state of nucleus A (B) and ξ_A denotes the internal A coordinates. lsj refers to the quantum state of the transferred neutron. \vec{r} is defined as the vector radius from the target nucleus A to the neutron. The spectroscopic factor S_{lsj}^{IAIB} therefore measures the probability to form a nucleus B in quantum state I_B having a single-particle structure with core nucleus A in quantum state I_A and valence neutron n in quantum state lsj . Since at large radius ($r \rightarrow \infty$) the overlap function goes to zero, contribution to the integration in Eq. (D.1) comes mostly from the nuclear interior ($r < r_N$). The spectroscopic factor is dominated by the radial behavior of the overlap function within the nucleus, thus probing reactions at intermediate and high energies.

Another structure quantity relevant in peripheral (d,p) reactions is the asymptotic normalization coefficient (ANC) C_{lsj}^{IAIB} which determines the strength of the tail of the overlap function:

$$\phi_{I_A:I_B}^{lj}(r) \xrightarrow{r \rightarrow \infty} C_{lsj}^{IAIB} W_{-\eta, l + \frac{1}{2}}(-2k_B r), \quad (\text{D.3})$$

where, $W_{-\eta, l + \frac{1}{2}}$ is the Whittaker function; the Coulomb Sommerfeld parameter η is taken as zero in our study because the transferred particle is neutral; k_B relates to the binding

energy ϵ_B of nucleus B through $k_B = \sqrt{2m_B\epsilon_B}/\hbar$; m_B is the mass of the nucleus and \hbar is Planck's constant. The ANC reflects the peripheral properties of the bound state, therefore it is the relevant ingredient in evaluating reactions occurring at low energies.

In order to obtain the overlap function $\phi_{I_A:I_B}^{lj}(r)$, one needs to solve a many-body problem which is highly complex and numerically difficult. Traditionally in (d,p) studies one replaces the many-body overlap function by a single-particle overlap function:

$$\phi_{I_A:I_B}^{lj}(r) \approx \phi_{I_A:I_B}^{lj(sp)}(r) = [S_{lsj}^{IAIB(sp)}]^{1/2} \varphi_{(lsj)I_B}(r), \quad (\text{D.4})$$

where $\varphi_{(lsj)I_B}(r)$ is the normalized single-particle bound state wave function of nucleus B . Since $\varphi_{(lsj)I_B}(r)$ is normalized to one, the single-particle spectroscopic factor $S_{lsj}^{IAIB(sp)}$ is equal to the many-body spectroscopic factor S_{lsj}^{IAIB} in Eq. (D.1) if the bound state wave function and the overlap function have similar radial behavior in both the interior and exterior of the nucleus. The asymptotic behavior of the bound state wave function is given by:

$$\varphi_{(lsj)I_B}(r) \xrightarrow{r \rightarrow \infty} b_{lsj}^{IB} W_{-\eta, l+1/2}(-2k_B r), \quad (\text{D.5})$$

where b_{lsj}^{IB} is the single-particle ANC which defines the amplitude of the tail of the neutron bound state wave function. From Eq. (D.3), Eq. (D.4), and Eq. (D.5) we can derive a relationship between the single-particle spectroscopic factor, the ANC, and the single-particle ANC:

$$S_{lsj}^{IAIB(sp)} = \frac{(C_{lsj}^{IAIB})^2}{(b_{lsj}^{IB})^2}. \quad (\text{D.6})$$

In practice, an experimental spectroscopic factor is determined by the normalization of the calculated cross section to the experimental cross section at the first peak of the angular

distribution:

$$S^{exp} = \frac{\left[\frac{d\sigma}{d\Omega}\right]_{exp}}{\left[\frac{d\sigma}{d\Omega}\right]_{th}}. \quad (\text{D.7})$$

While S^{exp} is not an observable, $d\sigma/d\Omega$ is.

Because ANC is a peripheral quantity, probing the region outside the nuclear radius r_N , it is best extracted using reactions at very low energies. This quantity should not depend on the choice of the neutron-target binding potential. The spectroscopic factor on contrary contains the nuclear interior information, therefore is commonly determined from high-energy reactions. As indicated in Eq. (D.6), the spectroscopic factor is sensitive to the assumptions made on the geometry of the neutron-target binding interaction, which leads to large ambiguities. The work in [116] provides a method to extract both the ANC and the spectroscopic factor in a more consistent and less ambiguous way. In our (d,p) study, we will often refer to these two quantities.

D.2 The adiabatic distorted wave approximation

Let us consider a (d,p) transfer reaction: $d + A \rightarrow B + p$. The incoming and outgoing channel for this reaction are presented in Fig. D.1. In the adiabatic model of [112, 114], a three-body problem is considered for the $n + p + A$ system in which the deuteron scattering wavefunction $\Psi^{(+)}(\vec{r}, \vec{R})$ in the incident channel is obtained by solving the inhomogeneous differential equation:

$$[E + i\epsilon - T_{\vec{r}} - T_{\vec{R}} - U_{nA} - U_{pA} - V_{np}]\Psi^{(+)}(\vec{r}, \vec{R}) = i\epsilon\phi_d(\vec{r})\exp(i\vec{K}_d \cdot \vec{R}), \quad (\text{D.8})$$

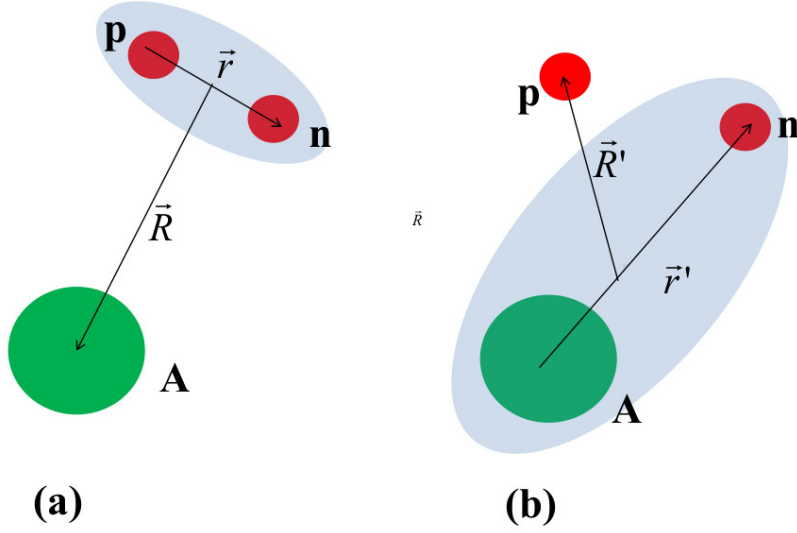


Figure D.1: (d,p) transfer reaction: (a) incoming channel, (b) outgoing channel

where

$$T_{\vec{r}} = -\frac{\hbar^2}{2\mu_{np}} \nabla_{\vec{r}}^2 \quad (\text{D.9})$$

$$T_{\vec{R}} = -\frac{\hbar^2}{2\mu_{dA}} \nabla_{\vec{R}}^2 \quad (\text{D.10})$$

In Eq. (D.8,D.9,D.10), we define $T_{\vec{r}}$ and $T_{\vec{R}}$ as the kinetic energy operators describing the n - p relative motion and the motion of its center of mass relative to the target. μ_{np} and μ_{dA} are the reduced mass of the n - p and d - A systems, respectively. $\vec{r} = \vec{r}_p - \vec{r}_n$ [$\vec{R} = (\vec{r}_n + \vec{r}_p)/2$] is the relative coordinate (center-of-mass coordinate) of the n - p system with \vec{r}_p and \vec{r}_n being the neutron and proton coordinates relative to the center of mass of target A . We take $U_{nA}(\vec{r}_n)$, $U_{pA}(\vec{r}_p)$ and $V_{np}(\vec{r})$ to be the neutron-target, proton-target and neutron-proton interactions, respectively. The term proportional to $i\epsilon$ on the *r.h.s* of Eq. (D.8) ensures that there is an incoming wave only in the deuteron channel.

In this approach, the exact T matrix is:

$$T = \langle \phi_{nA} \chi_{pB}^{(-)} | V_{np} + U_{pA} - U_{pB} | \Psi^{(+)} \rangle, \quad (\text{D.11})$$

where ϕ_{nA} is the neutron-target bound state wavefunction, and $\chi_{pB}^{(-)}$ is the proton scattering distorted wave in the outgoing channel. Note that the T matrix in Eq. (D.11) is exact; the three-body deuteron wavefunction $\Psi^{(+)}(\vec{r}, \vec{R})$ of Eq. (D.8) is used instead of the deuteron elastic scattering wave as in DWBA. In Eq. (D.11) the remnant term $U_{pA} - U_{pB}$ is often small and thus can be neglected except for light nuclei. If that is valid, then it is noted from Eq. (D.11) that the exact solution of the three-body wavefunction $\Psi^{(+)}(\vec{r}, \vec{R})$ in Eq. (D.8) is only necessary within the range of the n - p interaction. This important realization in both [112] and [114] allows the construction of an adiabatic method for (d,p) reactions.

D.2.1 Zero-range adiabatic wave approximation (ZR-ADWA)

This method is developed by Johnson and Soper [112] in which the three-body wavefunction $\Psi^{(+)}(\vec{r}, \vec{R})$ is expanded in term of the eigenstates of the n - p Hamiltonian:

$$\Psi^{(+)}(\vec{r}, \vec{R}) = \phi_d(\vec{r}) \chi_d(\vec{R}) + \int d\vec{k} \phi_k^{(+)}(\vec{r}) \chi_k(\vec{R}), \quad (\text{D.12})$$

where the wave function $\phi(\vec{r})$ describes the two nucleon motion, while $\chi(\vec{R})$ is the wave function of the $n + p$ center of mass and target A system. The scattering states $\phi_k(\vec{r})$ of the n - p system and the deuteron bound state $\phi_d(\vec{r})$ form a complete set since they are eigensolutions of the n - p Schrodinger equation:

$$\begin{aligned} (T_r + V_{np}) \phi_d(\vec{r}) &= -\varepsilon_d \phi_d(\vec{r}), \\ (T_r + V_{np}) \phi_k(\vec{r}) &= +\varepsilon_k \phi_k(\vec{r}). \end{aligned} \quad (\text{D.13})$$

In Eq. (D.13), ε_d and ε_k are the bound and scattering eigenenergies for the n - p system. In ZR-ADWA, the deuteron excitation energies $\varepsilon_k + \varepsilon_d$ is assumed to be much smaller than the deuteron kinetic energy E . Inserting Eq. (D.12) into Eq. (D.8) in the zero-range limit of the n - p interaction and using the adiabatic assumption, we arrive at an optical model equation:

$$(E + \varepsilon_d - T_R - U_{JS}(R))\chi_d^{JS}(\vec{R}) = 0, \quad (\text{D.14})$$

where the effective potential U_{JS} does not describe deuteron elastic scattering, but rather incorporates deuteron breakup effects within the range of V_{np} :

$$U_{JS}(R) = U_{nA}(R) + U_{pA}(R). \quad (\text{D.15})$$

Within this model, the transfer amplitude reduces to

$$T_{JS} = D_0 \int d\vec{R} \phi_{nA}^*(\vec{R}) \chi_{pB}^*(\vec{R}) \chi_d^{JS}(\vec{R}) \quad (\text{D.16})$$

where D_0 is the zero-range constant of the deuteron:

$$D_0 = \int d\vec{r} V_{np}(\vec{r}) \phi_d(\vec{r}). \quad (\text{D.17})$$

D.2.2 Finite-range adiabatic wave approximation (FR-ADWA)

This method is developed by Johnson and Tandy [114] in order to take into account the finite-range effects of the n - p interaction. Instead of using a set of H_{np} eigenstates for the wave function expansion as done in the ZR-ADWA method, they employ the Weinberg representation. Since the exact three-body wavefunction is only needed within the range of

V_{np} , the Weinberg basis is an excellent choice because they form a complete square integrable set over this range. The Weinberg basis is defined as:

$$(T_r + \alpha_i V_{np})\phi_i(\vec{r}) = -\epsilon_d \phi_i(\vec{r}), \quad (\text{D.18})$$

where ϵ_d is the deuteron binding energy and α_i are the eigenvalues which are real and increase with $i = 1, 2, \dots$. Here $\phi_i(\vec{r})$ denote the Weinberg states and satisfy the orthonormality relation:

$$\langle \phi_i | V_{np} | \phi_j \rangle = -\delta_{ij}. \quad (\text{D.19})$$

The three-body wavefunction is then expanded as:

$$\Psi^{(+)}(\vec{r}, \vec{R}) = \sum_{i=1}^{\infty} \phi_i(\vec{r}) \chi_i(\vec{R}). \quad (\text{D.20})$$

Inserting this expansion into the three-body equation Eq. (D.8), one arrives at a set of coupled channel equations:

$$[E + i\epsilon - T_{\vec{R}} - \bar{U}_{ii}(\vec{R})]\chi_i(\vec{R}) = \iota\epsilon\delta_{i1}N_d \exp(\iota\vec{K}_d \cdot \vec{R}) + \sum_{j \neq i} \bar{U}_{ij}(\vec{R})\chi_j(\vec{R}). \quad (\text{D.21})$$

In Eq. (D.21), one defines the coupling potentials $\bar{U}_{ij}(\vec{R})$ as:

$$\bar{U}_{ij}(\vec{R}) = U_{ij}(\vec{R}) + \beta_{ij}(\alpha_j - 1), \quad (\text{D.22})$$

where $U_{ij}(\vec{R})$ and β_{ij} are derived from the nucleon optical potentials U_{nA} and U_{pA} and the n - p interaction V_{np} , in a complex folding procedure:

$$\begin{aligned} U_{ij}(\vec{R}) &= -\langle \phi_i | V_{np}(U_{nA} + U_{pA}) | \phi_j \rangle, \\ \beta_{ij} &= \langle \phi_i | V_{np}^2 | \phi_j \rangle. \end{aligned} \quad (\text{D.23})$$

The normalization coefficient N_d appearing on the *r.h.s* of Eq. (D.21) is computed as:

$$N_d = -\langle \phi_1 | V_{np} | \phi_d \rangle. \quad (\text{D.24})$$

It is not trivial to solve Eq. (D.21) exactly as seen in [117]. However if only the first term in the Weinberg expansion Eq. (D.20) is needed to describe the three-body wave function in the range of V_{np} , Eq. (D.21) can be reduced to a single-channel optical-model like equation:

$$(E + \epsilon_d + i\varepsilon - T_R - U_{11}(R))\chi_1^{JT}(\vec{R}) = i\varepsilon N_d \exp(i\vec{K}_d \cdot \vec{R}). \quad (\text{D.25})$$

In this case, the effective deuteron potential $U_{11}(R)$ is calculated in a more elaborate manner in comparison to that in the ZR-ADWA method:

$$U_{11}(R) = -\langle \phi_1(\vec{r}) | V_{np}(U_{nA} + U_{pA}) | \phi_1(\vec{r}) \rangle. \quad (\text{D.26})$$

The first Weinberg state ϕ_1 is different from the deuteron ground state wavefunction ϕ_d by a normalization coefficient N_d : $|\phi_d\rangle = N_d |\phi_1\rangle$. Therefore one can rewrite the potential

$U_{11}(R)$ in terms of ϕ_d :

$$U_{11}(R) \equiv U_{JT}(R) = \frac{\langle \phi_d(\vec{r}) | V_{np}(U_{nA} + U_{pA}) | \phi_d(\vec{r}) \rangle}{\langle \phi_d(\vec{r}) | V_{np} | \phi_d(\vec{r}) \rangle}. \quad (\text{D.27})$$

When taking into account the finite-range effects of the n - p interaction, the transfer amplitude Eq. (D.11) now has a complex 6-dimensional integral formula:

$$\begin{aligned} T_{JT} &= \langle \phi_{nA} \chi_{pB}^{(-)} | V_{np} + U_{pA} - U_{pB} | \phi_1 \chi_1^{JT}(\vec{R}) \rangle \\ &= \langle \phi_{nA} \chi_{pB}^{(-)} | V_{np} + U_{pA} - U_{pB} | \phi_d \chi_1^{JT}(\vec{R}) / N_d \rangle. \end{aligned} \quad (\text{D.28})$$

D.3 Finite-range effects in (d,p) reactions

In order to explore the finite-range effects we perform a systematic study of 26 (d,p) reactions on stable targets [118], involving nuclei with masses ranging $A = 12 - 208$ and deuteron energies $E_d = 2 - 70$ MeV within the framework of ADWA. For all calculations throughout this appendix, we use the Reid soft-core potential [119] as the n - p interaction. The nucleon optical potentials are taken from the Chapel Hill global parameterization [120]. The neutron-target final bound state is produced by a Woods-Saxon potential with the standard radius $r = 1.25$ fm and diffuseness $a = 0.65$ fm. The depth of this potential is adjusted to reproduce the known neutron separation energy. We employ a subroutine contained in the code TWOFNR [121] to generate the adiabatic potential for the deuteron in the incident channel. The cross section for each case is obtained using the code FRESKO [122].

The finite-range effects introduced by the n - p interaction are presented in both the adiabatic deuteron potential Eq. (D.27) and the evaluation of the transfer matrix element

Eq. (D.28). By comparing U_{JT} (Eq. (D.27)) and U_{JS} (Eq. (D.15)), T_{JT} (Eq. (D.28)) and T_{JS} (Eq. (D.16)) we can disentangle the separate effects of the finite-range. We also study the accuracy of the LEA method.

D.3.1 Finite-range effects in the potentials

Before looking at the changes in cross section due to the finite-range effect, we analyze the effect on the adiabatic potentials by comparing U_{JS} and U_{JT} . In order to simplify the comparison, the real part and imaginary part of the potential are fitted to a volume and surface Woods-Saxon shape, respectively. The finite-range effects in the potentials are obtained by comparing the Woods-Saxon parameters of U_{JS} and U_{JT} . The results are presented in Table D.1. We also compare our results with an approximate method developed by Wales and Johnson [123] to estimate the finite-range effects in the deuteron potential (denoted U_{WJ}). In Table D.1, WJ and JT represent the percentage difference in the potential of the Wales and Johnson method and finite-range adiabatic approach, relative to the zero-range adiabatic prescription. The main difference between the finite-range and zero-range potentials in the adiabatic method is a constant increase in diffuseness and a slight systematic decrease in radius. In the Wales and Johnson study, although the radius is fixed, the main features of the finite-range effects in potentials are captured. The diffuseness also increases but to a lesser extent. We find that the differences in the depths of the real and imaginary parts of the potentials in the adiabatic approach are more subtle and vary case to case while Wales and Johnson obtains a small systematic decrease in the depth of the potential.

Table D.1: The finite-range effects on the deuteron distorting potential are presented as the changes in the diffuseness a_R and a_I of the real and imaginary parts, the depths of the real and imaginary parts V and W_s , as well as the corresponding radii r_R and r_I .

target	parameter	WJ	JT
all	Δa_R	+4%	+7%
	Δa_I	+3%	+8-9%
^{12}C	ΔV	-5.6%	-1.98%
	Δr_R	0%	-1.25%
	ΔW_s	-4.6%	-4.52%
	Δr_I	0%	+0.72%
^{48}Ca	ΔV	-2.1%	-0.04%
	Δr_R	0%	-0.93%
	ΔW_s	-3.7%	+1.6%
	Δr_I	0%	-0.97%
^{208}Pb	ΔV	-0.7%	+0.06%
	Δr_R	0%	-0.35%
	ΔW_s	-3.3%	+1.2%
	Δr_I	0%	-0.35%

D.3.2 Finite-range effects in the transfer cross sections

In this section, we study the differences in the cross section for several model calculations to disentangle the finite-range effects in the deuteron potential and in the evaluation of the transfer matrix element. All the cross section calculations are performed by the code FRESKO [122] with the interaction inputs generated by the code TWOFNR [121]. We consider four different types of calculation for each reaction: U_{JS} deuteron potential and zero-range transfer matrix Eq. (D.16) (ZR-JS, the reference), U_{JS} deuteron potential and finite-range transfer matrix Eq. (D.28) (FR-JS), U_{JT} deuteron potential and finite-range transfer matrix Eq. (D.16) (FR-JT) and a zero-range calculation for both deuteron potential and transfer matrix with a local energy approximation (LEA) finite-range correction [115]. Since LEA method has been widely used in the past, it is important to study the validity of this approximation at different deuteron beam energies.

We summarize our results for all 26 reactions in Table D.2. The last four columns present different aspects of the finite-range effects. $\Delta(\text{LEA})$ shows the effect of finite-range introduced by LEA to the evaluation of the transfer matrix. $\Delta(\text{FR-JS})$ represents the effect of finite-range only in the calculation of the transfer matrix. $\Delta(\text{FR-JT})$ shows the total finite-range effects in both the deuteron adiabatic potential and the evaluation of the transfer matrix. $\Delta(\text{JS-JT})$ is the finite-range effects coming only from the adiabatic potential. All the percentage differences are evaluated at the first peak of the angular distribution for energies above the Coulomb threshold and at the backward angles otherwise. The peak angles are also presented in Table D.2. In all cases, we compute the percentage differences of cross sections relative to the zero-range Johnson and Soper method in which U_{JS} and Eq. (D.16) are used.

Table D.2: Finite-range effects in transfer cross sections. Comparisons are performed with respect to the zero-range Johnson and Soper calculation (cases with no existing data are presented by *).

Target	E_d	θ	$\Delta(\text{LEA})$	$\Delta(\text{FR-JS})$	$\Delta(\text{FR-JT})$	$\Delta(\text{JT-JS})$
^{12}C	4	25	+5.6%	+5.5%	+4.5%	-1.0%
^{12}C	12	13	+2.6%	+2.9%	-1.5%	-4.3%
^{12}C	19.6	10	+11%	+13%	+7.7%	-4.2%
^{12}C	56	6	-37%	-27%	-36%	-12%
^{48}Ca	2	180	+6.5%	+6.3%	+2.6%	-3.5%
^{48}Ca	13	12	+4.9%	+3.8%	-2.8%	-6.2%
^{48}Ca	19	8	+5.0%	+4.0%	-0.30%	-4.1%
$^{48}\text{Ca}^*$	30	4		+7.3%	+4.8%	-2.3%
$^{48}\text{Ca}^*$	40	0		-5.4%	-5.9%	-10%
$^{48}\text{Ca}^*$	50	0		-1.9%	-19%	-18%
^{48}Ca	56	0	-5.2%	-6.5%	-24%	-18.6%
^{69}Ga	12	14	+4.3%	+4.7%	-1.1%	-5.49%
^{86}Kr	11	25	+4.8%	+5.5%	-0.40%	-5.63%

The results in Table D.2 can be divided into three groups. The first group is the sub-Coulomb reactions which occur at very low energies under the Coulomb barrier. In this case, we find the finite-range effects are only a few percent and mostly come from the evaluation of the transfer matrix. The contribution from the adiabatic potential is small. In

Table D.2 (cont'd)

Target	E_d	θ	$\Delta(\text{LEA})$	$\Delta(\text{FR-JS})$	$\Delta(\text{FR-JT})$	$\Delta(\text{JT-JS})$
^{90}Zr	2.7	138	+6.2%	+7.3%	+5.5%	-1.7%
^{90}Zr	11	26	+5.4%	+5.0%	-0.90%	-5.6%
^{124}Sn	5.6	175	+6.1%	+11%	+7.5%	-2.8%
^{124}Sn	33.3	0	+2.9%	+4.6%	0%	-4.4%
$^{124}\text{Sn}^*$	40	12		-1.1%	-2.4%	-1.4%
$^{124}\text{Sn}^*$	50	11		-3.9%	-4.3%	-0.44%
$^{124}\text{Sn}^*$	60	9		-11%	-30%	-21%
$^{124}\text{Sn}^*$	70	0	+5.1%	-29%	-44%	-21%
^{208}Pb	8	180	+6.1%	+7.2%	+6.1%	-0.96%
^{208}Pb	12	98	+5.7%	+8.8%	+2.2%	-6.1%
$^{208}\text{Pb}^*$	20	30		+4.5%	-2.3%	-6.6%
$^{208}\text{Pb}^*$	40	9		+1.4%	-6.9%	-8.1%
$^{208}\text{Pb}^*$	60	0		+0.14%	-8.8%	-9.0%
$^{208}\text{Pb}^*$	80	0		-62%	-86%	-63%

Fig. D.2 we plot two examples:(a) $^{48}\text{Ca}(d,p)^{49}\text{Ca}$ at $E_d = 2$ MeV and b) $^{208}\text{Pb}(d,p)^{209}\text{Pb}$ at $E_d = 8$ MeV. The angular distributions of these two reactions peak at backward angles as expected. Since extracting the spectroscopic information is not the purpose of this work, the data presented here is just to indicate that the ingredients of our model are realistic. The finite-range effects are 3% in ^{48}Ca and 6% in ^{208}Pb . The LEA corrections to the finite-range effects for sub-Coulomb reactions are below 5%. The LEA method is able to capture most of the finite-range effects in this low energy regime.

We then look at the reactions that happen at intermediate deuteron beam energies (10-20 MeV). In Fig. D.3 we present the angular distributions for $^{86}\text{Kr}(d,p)^{87}\text{Kr}$ at $E_d = 11$ MeV (a) and $^{208}\text{Pb}(d,p)^{209}\text{Pb}$ at $E_d = 20$ MeV (b). The finite-range effect from the deuteron potential reduces the cross section while that from the evaluation of the transfer matrix element increases the cross section. Although the two separate finite-range effects are significantly large, the overall effect is small for these cases due to cancellation. For example, we obtain the overall finite-range effect of -1% for the ^{69}Ga at $E_d = 12$ MeV, 0.4% for the ^{86}Kr at $E_d = 11$ MeV and 6% in ^{208}Pb at $E_d = 20$ MeV. In this energy regime, the LEA method starts to deviate from the full finite-range calculation.

Finally we study the reactions at high deuteron beam energies (50-80 MeV). There are only two studied cases in which the experimental data at these energies are available: $^{12}\text{C}(d,p)^{13}\text{C}$ at $E_d = 56$ MeV and $^{48}\text{Ca}(d,p)^{49}\text{Ca}$ at $E_d = 56$ MeV. The angular distributions for these two reactions are plotted in Fig. D.4. In order to ensure that our results are not biased by low-mass systems, we perform the same calculations for ^{124}Sn and ^{208}Pb at high deuteron energies. The dominant contribution to the finite-range effects in this case comes from the adiabatic potential which largely reduces the cross section. We find that the finite-range effects from the evaluation of the transfer matrix is in the same direction but

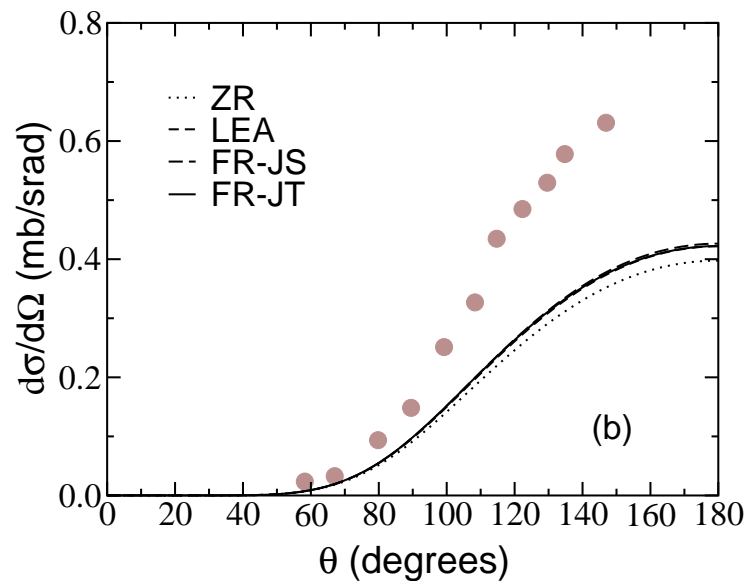
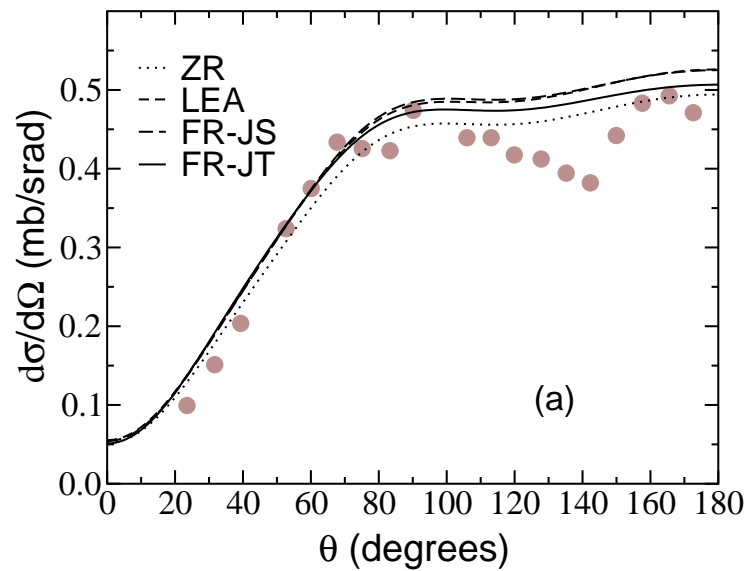


Figure D.2: Finite-range effects in sub-Coulomb (d,p) reactions: (a) $^{48}\text{Ca}(d,p)^{49}\text{Ca}(g.s.)$ $E_d = 2$ MeV (data from [124]) and (b) $^{208}\text{Pb}(d,p)^{209}\text{Pb}(g.s.)$ $E_d = 8$ MeV (data from [125]).

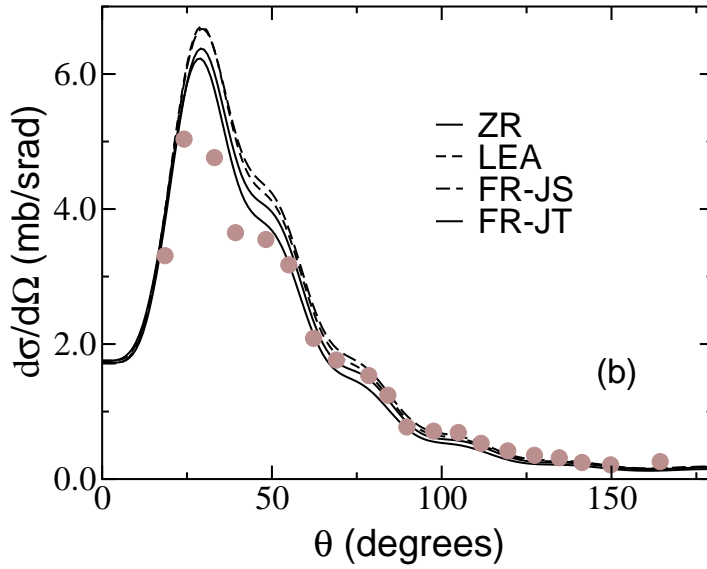
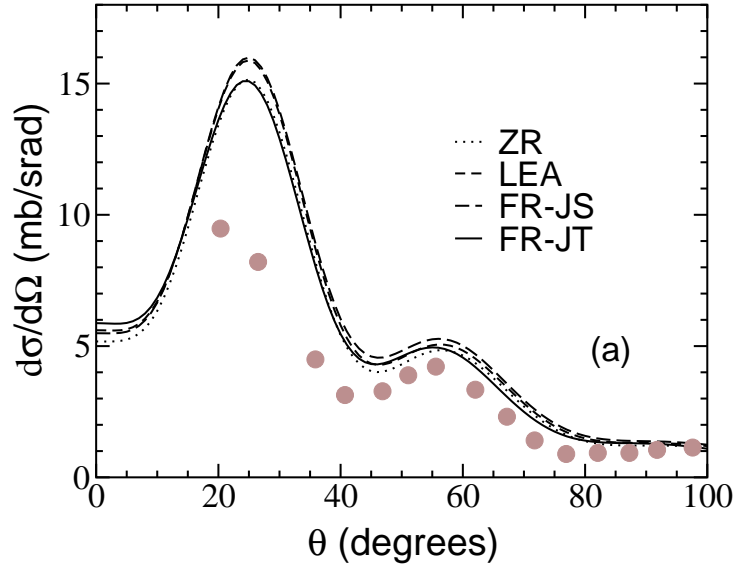


Figure D.3: Finite-range effects in (d,p) reactions at energies slightly above the Coulomb barrier: (a) $^{86}\text{Kr}(d,p)^{87}\text{Kr}(\text{g.s.})$ $E_d = 11$ MeV (data from [126]) and (b) $^{208}\text{Pb}(d,p)^{209}\text{Pb}(\text{g.s.})$ $E_d = 20$ MeV (data from [127]).

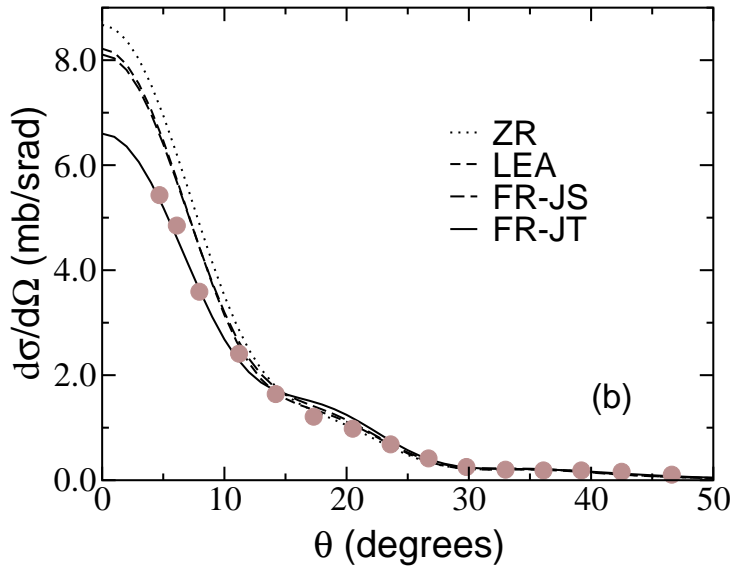
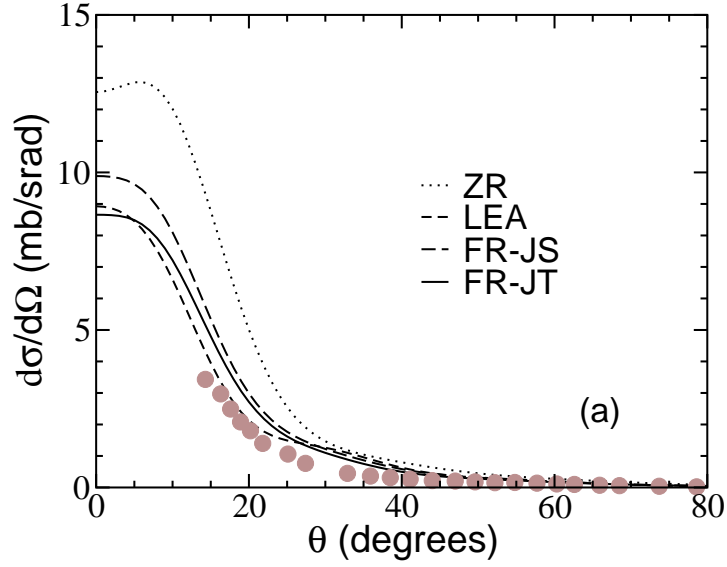


Figure D.4: Finite-range effects in (d,p) reactions at high energies: (a) $^{12}\text{C}(d,p)^{13}\text{C}(\text{g.s.})$ $E_d = 56$ MeV (data from [128]) and (b) $^{48}\text{Ca}(d,p)^{49}\text{Ca}(\text{g.s.})$ $E_d = 56$ MeV (data from [129]).

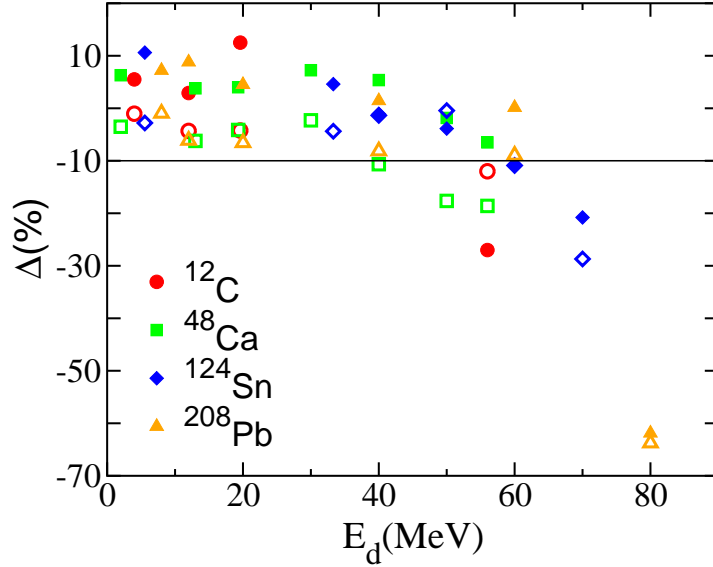


Figure D.5: Systematic finite-range effect as a function of beam energy. The effect from the adiabatic potentials is presented as open symbols while that from the evaluation of the matrix elements is plotted as filled symbols.

smaller. The overall finite-range effects are important for (d,p) reactions at high deuteron beam energies and should not be neglected. The effects are about -36% for ^{12}C at 56 MeV beam, -24% for ^{48}Ca at 56 MeV beam and -43.5% for ^{124}Sn at 70 MeV beam. We find that the LEA method is no longer accurate to estimate the finite-range correction in this high energy regime. The results from the LEA method largely deviate from and sometimes are in the opposite direction of the full finite-range calculation.

In Fig. D.5 we plot the two separate finite-range effects as a function of the beam energy for four different (d,p) reactions. The solid symbols represent the finite-range effects attributed to the evaluation of the transfer matrix element while the open symbols indicate the finite-range effects coming from the deuteron potential. This figure summarizes all the main features of our study. We can see that the finite-range effects are less than 10% for reactions at low energies. These effects become more important as the deuteron beam energy

increases. We estimate the transition at which finite-range effects cannot be neglected to be around 20 MeV/u for lighter systems ($A < 50$) and 30 MeV/u for the heavy systems. We also obtain similar results when performing a systematic study of (d,p) reactions in which the outgoing target populates excited states [130, 131].

D.4 Testing the dispersive optical model for (d,p) reactions

In the conventional approach to study (d,p) reactions, a global deuteron optical potential fitted to elastic scattering is employed for the deuteron-target interaction in the entrance channel. Similarly, a global proton optical potential fitted to p+A elastic scattering is used for the proton-target interaction in the exit channel. In our framework (the FR-ADWA method), the deuteron adiabatic potential is constructed from the neutron and proton optical potentials (Eq. (D.27)). Although these nucleon optical potentials are less ambiguous than the deuteron optical potentials in the DWBA framework and the deuteron binding is well constrained, there remains concern about the effective interaction used for the final neutron bound state. Currently V_{nA} is modeled by an attractive single-particle potential with Woods-Saxon shape in the FR-ADWA method. We employ standard parameters for the radius $r = 1.25$ fm and the diffuseness $a = 0.65$ fm. The depth of this effective potential is then adjusted to reproduce the experimental binding energy of the final nucleus. However, the procedure of choosing the neutron binding potential is not connected to the nucleon optical potentials mentioned above. The disconnect between these two types of interaction is unsatisfying.

Recently, a group of scientists at Washington University have successfully implemented

the dispersive optical model (DOM) [132, 133, 134] which naturally connects the continuum and bound state information of the nucleon-target interaction, thus overcoming the inconsistency of the standard applications of the FR-ADWA method. As opposed to the global optical model where only elastic scattering data are fitted, the DOM method fits simultaneously the nucleon elastic, total and reaction cross section data, as well as bound-state properties extracted from $(e, e'p)$ experiments. The nonlocality correction is also implemented in the fit. The study in [134] observes a nucleon asymmetry dependence of the DOM potentials, opening a possibility for an extrapolation to exotic nuclei. Because of its very promising features, we want to explore the validity of the DOM method for (d,p) transfer reactions using the FR-ADWA framework [135]. In this work we study several cases of doubly magic nuclei for which the experimental data exist: $^{40}\text{Ca}(d,p)^{41}\text{Ca}$ at $E_d = 20$ and 56 MeV, $^{48}\text{Ca}(d,p)^{49}\text{Ca}$ at $E_d = 2, 13, 19.3$ and 56 MeV, $^{132}\text{Sn}(d,p)^{133}\text{Sn}$ at $E_d = 9.46$ MeV, and $^{208}\text{Pb}(d,p)^{209}\text{Pb}$ at $E_d = 8$ and 20 MeV. We used the Reid potential for V_{np} [119] and the DOM potentials for all nucleon-target interactions. The results are also compared with those produced using the CH89 nucleon optical potential [120] and the standard neutron single-particle binding interaction.

D.4.1 Details of the calculation

In this work we employ the DOM fits for the Ca, Sn and Pb isotopes [134]. They include both nucleon scattering and bound state data for $Z = 20, 28$ and $N = 28$ nuclei in the fit for the Ca isotopes. The DOM fit for Sn isotopes includes the proton and $^{112-124}\text{Sn}$ elastic scattering data and the neutron elastic-scattering data on ^{116}Sn , ^{118}Sn , ^{120}Sn , and ^{124}Sn . Data for nuclei with $Z = 82$ are used for the DOM fit of Pb isotopes. For this study, the DOM group provides us all optical potentials necessary to describe $A(d, p)B$ reaction in the

Table D.3: Comparison of the DOM overlap function, corrected for non-locality φ_{DOM} with the Woods-Saxon single-particle wavefunction φ_{WS} . In this table we include: n (principal number), ℓj (the angular momenta of the valence orbital), S_n (the separation energy), R^{rms} (the root-mean-square radius of the valence orbital), and b_{nlj} (the modulus of the single-particle ANC).

Nucleus	Overlap	$n\ell j$	S_n [MeV]	R^{rms} [fm]	$ b_{nlj} $ [fm $^{-1/2}$]
^{41}Ca	φ_{WS}	$0f_{7/2}$	8.362	3.985	2.285
	φ_{DOM}			3.965	2.261
^{49}Ca	φ_{WS}	$1p_{3/2}$	5.146	4.606	5.818
	φ_{DOM}			4.820	6.098
^{133}Sn	φ_{WS}	$1f_{7/2}$	2.469	6.080	0.844
	φ_{DOM}			6.513	0.831
^{209}Pb	φ_{WS}	$1g_{9/2}$	3.936	6.498	1.650
	φ_{DOM}			6.746	1.827

FR-ADWA framework, namely U_{nA} , U_{pA} , U_{pB} , and the neutron binding interaction V_{nA} .

In Table D.3 we present the properties of the final neutron-target bound state. The DOM potentials generated for Ca isotopes have a radius parameter of 1.18 fm while that of the standard Woods-Saxon (WS) is 1.25 fm. For the ^{41}Ca case, the nonlocality correction in the DOM cancels this difference causing the DOM overlap function φ_{DOM} to be almost identical to the Woods-Saxon overlap function φ_{WS} , thus the root-mean-square radius R^{rms} from the two models are exactly the same. The same results are not seen in other cases where a node is present in the overlap function ($n \neq 0$). We find that the nonlocality correction is more pronounced when the number of nodes in the overlap function differs from zero, making the DOM rms radius larger than its WS counterpart. An illustration of this effect is plotted for the ^{49}Ca in Fig. D.6. Here, the nonlocality increases the single-nucleon overlap function at large radii.

In Fig. D.7 we present the difference between the DOM and CH89 nucleon optical potential evaluated at 4.7 MeV for ^{132}Sn . For both the real part and the imaginary part of

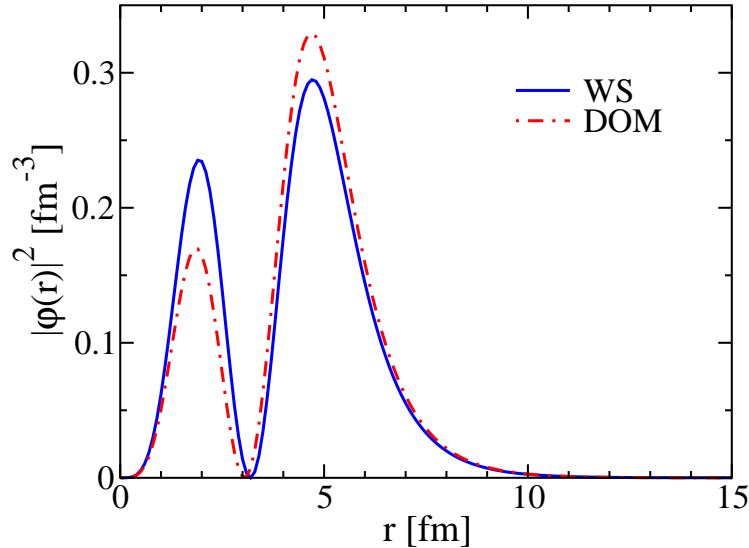


Figure D.6: The square of the single-neutron overlap functions in the Woods-Saxon (solid) and the DOM (dashed) model are compared for ^{49}Ca .

the potentials, we find a reduction (enhancement) in the strength of the neutron (proton) potential in the DOM as compared to the CH89. While the radius parameters are the same for the real part of the neutron and proton potentials in CH89, this is not the case in the DOM model. In this model, the real proton potential has a larger radius than that for the neutron. This is due to the difference between the neutron and proton surface absorption. As indicated in [134], for Sn DOM potentials the proton imaginary surface term has a linear asymmetry dependence while this dependency is insignificant for the neutron.

D.4.2 Transfer cross section

For each reaction we perform three calculations using the FR-ADWA framework but different inputs: (i) the nucleon optical potentials from CH89 and the standard Woods-Saxon (WS) overlap function φ_{WS} for the neutron bound state (CH89+WS); (ii) DOM optical potentials

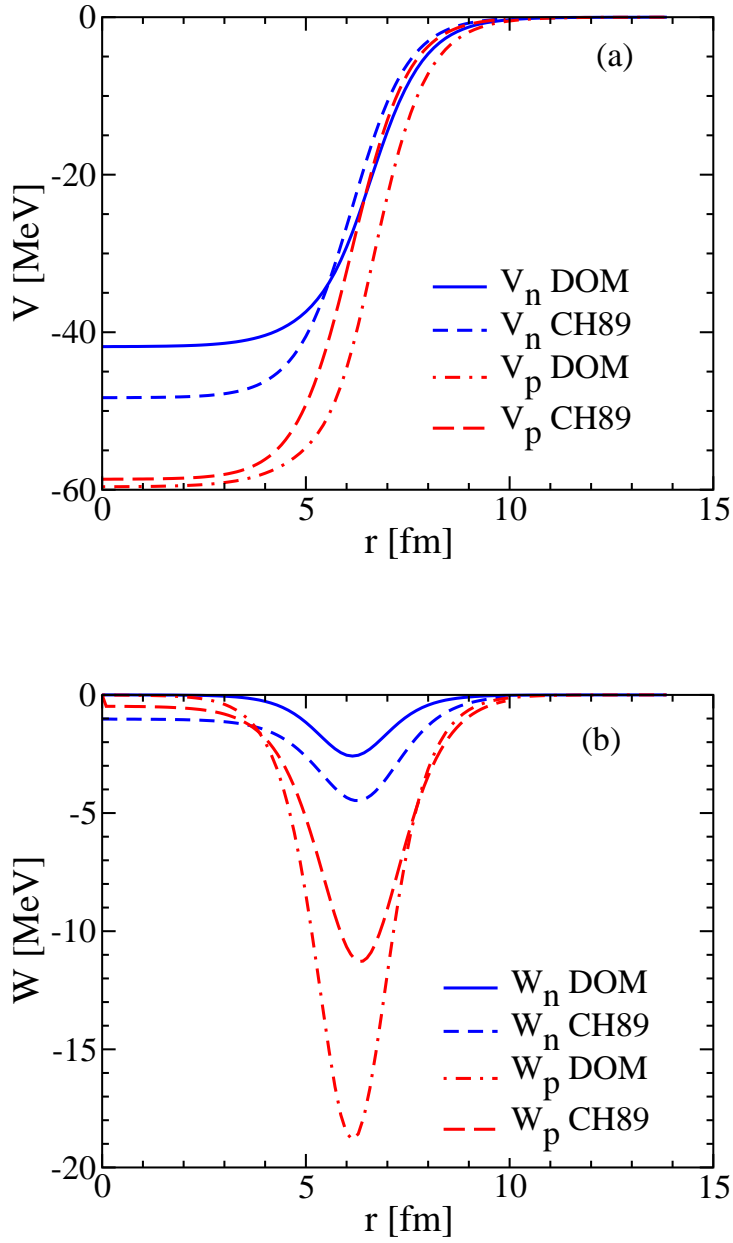


Figure D.7: DOM and CH89 optical potentials are compared for n - ^{132}Sn and p - ^{132}Sn at 4.7 MeV: (a) the real part and (b) the imaginary part.

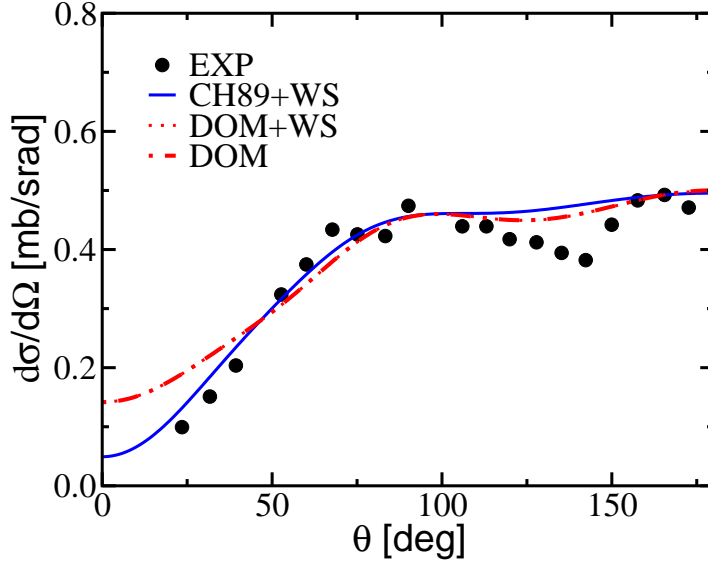


Figure D.8: $^{48}\text{Ca}(d,p)^{49}\text{Ca}$ at $E_d = 2$ MeV (angular distributions are normalized to the data at backward angles).

and the WS neutron overlap function φ_{WS} (DOM+WS); and (iii) both the optical potentials and the neutron overlap function corrected for nonlocality φ_{DOM} from DOM (DOM).

In Fig. D.8, D.9, and D.10 we plot the angular distributions for the $^{48}\text{Ca}(d,p)^{49}\text{Ca}$ reaction at three different deuteron beam energies $E_d = 2, 19.3$ and 56 MeV respectively. The calculated cross sections are normalized to data at the first peak of the angular distribution for energies above the Coulomb threshold and at the backward angles otherwise. It is important to note that the DOM is able to reproduce well the shape of the angular distribution for these cases. Although there are differences in the shape of the neutron overlap functions, we do not obtain significant changes in the shape of the angular distribution between the three calculations: CH89+WS, DOM+WS and DOM. We observe the same behavior for the $^{40}\text{Ca}(d,p)^{41}\text{Ca}$ reaction in which DOM performs as well as CH89+WS.

Fig. D.11 and Fig. D.12 display the results for the $^{132}\text{Sn}(d,p)^{133}\text{Sn}$ and $^{208}\text{Pb}(d,p)^{209}\text{Pb}$

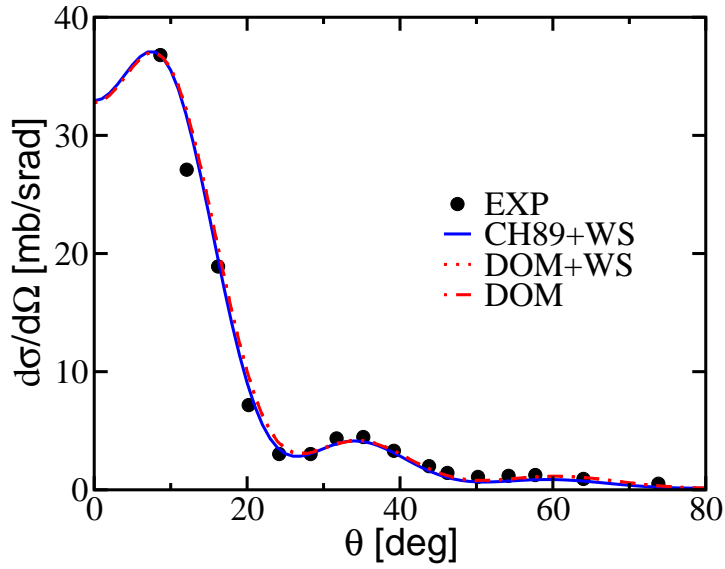


Figure D.9: $^{48}\text{Ca}(d,p)^{49}\text{Ca}$ at $E_d = 19.3$ MeV (angular distributions are normalized to the data at the peak).

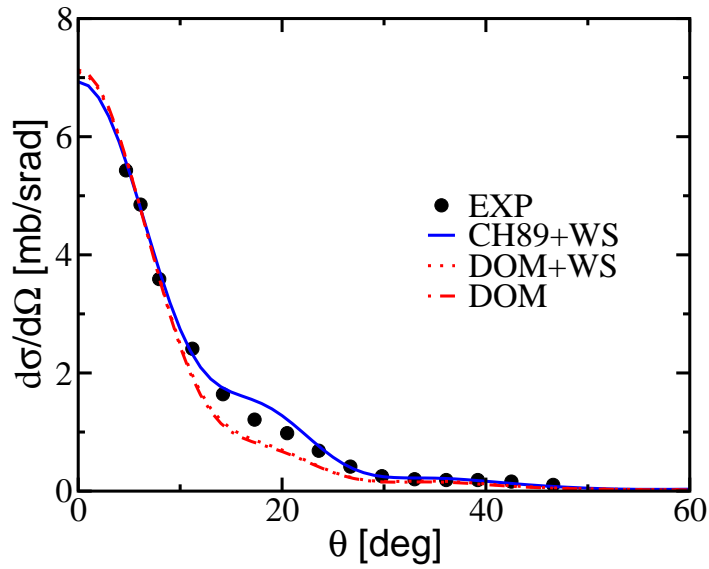


Figure D.10: $^{48}\text{Ca}(d,p)^{49}\text{Ca}$ at $E_d = 56$ MeV (angular distributions are normalized to the data at forward angles).

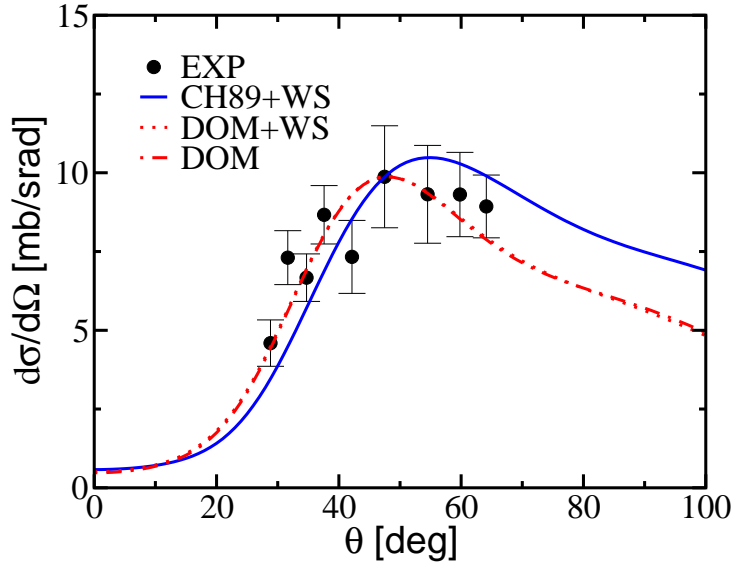


Figure D.11: $^{132}\text{Sn}(d,p)^{133}\text{Sn}$ at $E_d = 9.46$ MeV (angular distributions are normalized at the peak of the experimental cross section).

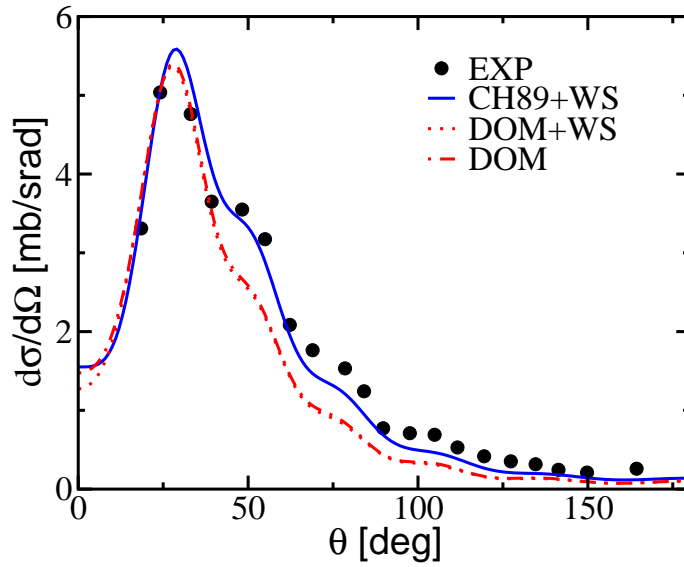


Figure D.12: $^{208}\text{Pb}(d,p)^{209}\text{Pb}$ at $E_d = 20$ MeV (angular distributions are normalized at the peak of the experimental data).

reactions. The calculated cross sections are also normalized to data in each graph. We observe a considerable change in shape of the angular distribution between the DOM and CH89 for these two cases. The diffraction pattern is shifted toward smaller angles when the interactions from the DOM are used. Since DOM+WS and DOM provide the same angular distribution after normalization to data, the modification in the shape of the angular distribution is not caused by the neutron overlap function but rather by the optical potentials. The real part of DOM potentials have a larger radius than that of the CH89, causing the angular distribution to peak at more forward angles. The larger radius of the DOM neutron overlap function only changes the magnitude of the calculated cross section. The DOM method improves the angular distribution for the $^{132}\text{Sn}(d,p)^{133}\text{Sn}$ reaction but deviates further from data for $^{208}\text{Pb}(d,p)^{209}\text{Pb}$ case.

D.4.3 Spectroscopic factors

In this section we study the impact of using the DOM potentials in extracting spectroscopic factors, as in Eq. (D.7). In Table D.4 we present the spectroscopic factors extracted from CH89+WS, DOM+WS and DOM calculations.

The conventional approach CH89+WS which employs the CH89 optical potentials and the standard WS for the neutron overlap function, provides a wide range of spectroscopic factors depending on beam energy. One can see that the spectroscopic factor varies from 0.77 to 1.1 within the energy range of 2 – 56 MeV for the $^{48}\text{Ca}(d,p)^{49}\text{Ca}$ reaction. A weaker energy dependence of the spectroscopic factor is obtained for the DOM calculations with the exception of the $^{208}\text{Pb}(d,p)^{209}\text{Pb}$ reaction. The comparison between CH89+WS and DOM+WS shows a significant reduction of the spectroscopic factor. This is due to the optical potentials alone because the neutron overlap functions are the same (WS) in the

two calculations. Using the overlap function from the DOM instead of the standard WS can further reduce the spectroscopic factors for all cases except the $^{40}\text{Ca}(d,p)^{41}\text{Ca}$ reaction. This is expected: while the DOM and WS overlap functions are the same for ^{41}Ca , this is not the case for ^{49}Ca , ^{133}Sn and ^{209}Pb . There, the nonlocality in the DOM causes a shift of the overlap functions toward the surface region which leads to larger cross sections and smaller spectroscopic factors. The results using DOM inputs are in better agreement with those extracted from knockout measurements ($e, e'p$) [141] except for the Pb cases.

Through out this work, the $^{208}\text{Pb}(d,p)^{209}\text{Pb}$ reaction is proved to be the bad represen-

Table D.4: Comparison of the spectroscopic factors obtained from the FR-ADWA analysis using different models for optical potentials and overlap functions.

Nucleus	E_d	data	CH89+WS	DOM+WS	DOM
^{41}Ca	20	[136]	0.96	0.85	0.86
	56	[137]	0.88	0.73	0.74
^{49}Ca	2	[124]	0.94	0.72	0.66
	13	[138]	0.82	0.67	0.61
	19.3	[139]	0.77	0.68	0.62
	56	[129]	1.1	0.70	0.62
^{133}Sn	9.46	[140]	1.1	1.0	0.72
^{209}Pb	8	[125]	1.7	1.5	1.2
	20	[127]	0.89	0.61	0.51

tative case for the DOM study. We obtain a large discrepancy in extracting spectroscopic factors at $E_d = 8$ MeV and $E_d = 20$ MeV. The same behavior is seen for the extracted ANCs in this case. In addition, the spectroscopic factor for the sub-Coulomb reaction is much larger than unity although the shape of the angular distribution is reproduced (see Fig. D.13). These two problems appear not only in the DOM calculation but also in the traditional CH89+WS approach. In order to investigate the possible cause for these issues, we look into the reaction mechanism. Coupled-channel Born approximation (CCBA)

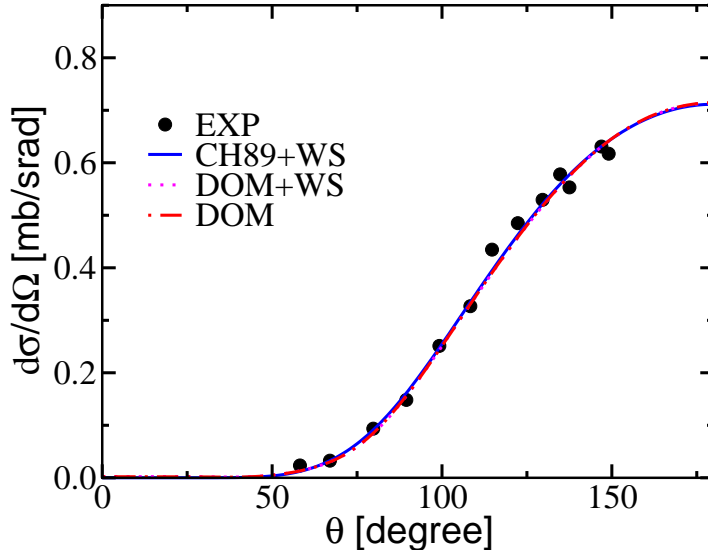


Figure D.13: $^{208}\text{Pb}(d,p)^{209}\text{Pb}$ at $E_d = 8$ MeV (angular distributions are normalized at the peak of the experimental data).

calculations including the low-lying 3^- and 2^+ states in ^{208}Pb are performed using the deuteron global optical potentials [142] to explore if this problem comes from target excitation. Although this CCBA approach is not meant to extract the spectroscopic factor, a better understanding of the reaction mechanism can be obtained. The results show a strong effect of target excitation for $^{208}\text{Pb}(d,p)^{209}\text{Pb}$ at 20 MeV. The effect is rather weak at the low energy of 8 MeV. We can conclude that at least for high deuteron energies, the mechanism of the $^{208}\text{Pb}(d,p)^{209}\text{Pb}$ reaction can not be described by the present ADWA framework. The unrealistically large spectroscopic factor at $E_d = 8$ MeV could indicate the failure of the present ADWA method at this low energy. It may also question the optical potentials or the overlap functions in general. Unfortunately we can not verify that by comparing with the exact Faddeev calculation because the reaction involves a very strong Coulomb field. The exact Faddeev calculation is presently limited for nuclei with $Z \leq 20$ [143].

Table D.5: ANCs extracted for both the ground state and the first excited state of the $^{14}\text{C}(\text{d,p})^{15}\text{C}$ reaction.

State	Method	C_{lj}^2 (fm^{-1})	Uncertainty			
			Experiment	Potentials	Peripherality	Total
$s_{1/2}$	FR-ADWA	1.64 ± 0.26	10%	7%	11%	16%
$d_{5/2}$	FR-ADWA	$(3.55 \pm 0.43) 10^{-3}$	10%	6%	4%	12%

D.5 Application of the finite-range adiabatic distorted wave approximation (FR-ADWA)

As an illustration of the application of the FR-ADWA method, we extract the normalization coefficient (ANC) from the $^{14}\text{C}(\text{d,p})^{15}\text{C}$ reaction data [144]. This is our work in collaboration with a group of physicists at Texas A&M University and experimentalists at Czech Academy of Sciences who provide a measurement of $^{14}\text{C}(\text{d,p})^{15}\text{C}$ reaction at 17.06 MeV deuteron beam for both the ground state and the first excited state of ^{15}C . The single nucleon transfer reaction $^{14}\text{C}(\text{d,p})^{15}\text{C}$ allows an indirect measurement of the $^{14}\text{C}(\text{n},\gamma)^{15}\text{C}$ reaction which in some scenarios, is very important in the nucleosynthesis of heavy nuclei. A direct measurement of the $^{14}\text{C}(\text{n},\gamma)^{15}\text{C}$ reaction cross section is difficult because both neutron and ^{14}C are unstable and radioactive. At low energies relevant for astrophysics where $^{14}\text{C}(\text{d,p})^{15}\text{C}$ reaction is peripheral, the ANC can be extracted and is used to estimate $^{14}\text{C}(\text{n},\gamma)^{15}\text{C}$ cross section.

In this work, we employ the FR-ADWA method to extract the ANC from these new measurements. We first calculate the experimental spectroscopic factor as defined in Eq. (D.7).

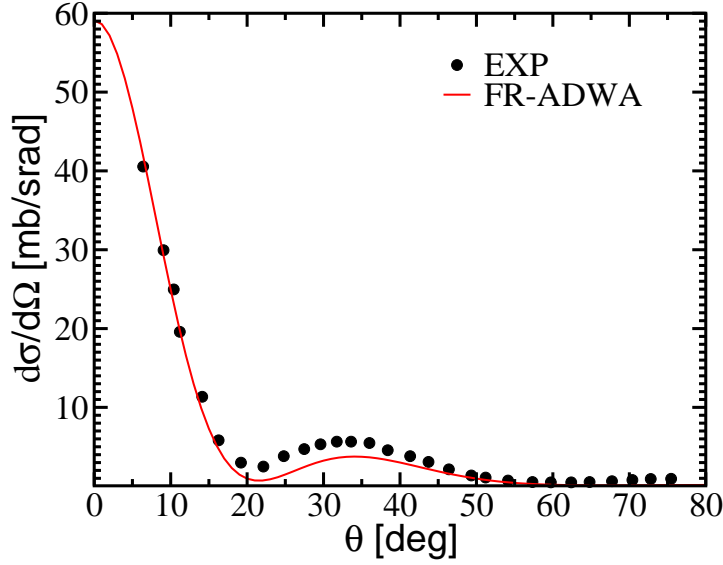


Figure D.14: Angular distribution for the ground state in the $^{14}\text{C}(\text{d},\text{p})^{15}\text{C}$ reaction.

Eq. (D.6) is then used to extract the nuclear ANC. In order to obtain an accurate ANC, it is important to make sure that the reaction is peripheral. We check the peripherality of the reaction by cutting 3 fm of the interior, leading to 11% change in the cross section for the ground state and 4% for the first excited state of ^{15}C . In order to estimate the uncertainty due to the optical potentials we perform FR-ADWA calculations using both CH89 [145] and KD [146] optical potentials. This leads to 7% (6%) standard deviation of the ANC for the ground state (first excited state). We also include 10% experimental systematic error in evaluating the total uncertainty of the calculation. In Table. D.5, we present the square of the ANC and its associate sources of uncertainty for both the ground state and the first excited state. The total uncertainty of the square of the ANC is 16% (12%) for the ground state (excited state) obtained by adding in quadrature all the listed uncertainties.

The square of the ANC $C_{01/2}^2 = 1.64 \pm 0.26 \text{ fm}^{-1}$ obtained from our analysis shows a very good agreement with the results extracted from the Coulomb dissociation of ^{15}C on

^{208}Pb [100] and also agrees with the measurement of a direct radiative capture in [147].

In Fig. D.14 we plot the $^{14}\text{C}(\text{d,p})^{15}\text{C}$ angular distributions for the transition to the ground state of ^{15}C . The FR-ADWA calculation when rescaled by the appropriate normalization factors reproduces well the first peak of the experimental angular distribution which is important in extracting the ANC. There is a discrepancy between the experimental data and the FR-ADWA calculation at large angles, but we expect this contribution is insignificant compared to the large cross section at the forward peak. Note that the cross section at the first peak is 20 times greater than at the first minimum.

D.6 Conclusion

We explore the effect of finite-range introduced by the n - p interaction by performing a systematic study on (d,p) reactions. The adiabatic approach for zero-range [112] and finite-range [114] calculations is used to evaluate this effect. We take into account the contributions from both adiabatic distorting potential and the transfer matrix evaluation. Our findings show significant reduction in the cross section due to the finite-range effect for reactions at high energy ($E_d > 30$ MeV/u). We also find that the LEA method which is traditionally applied to compensate for the finite-range effect is no longer valid for heavy systems and high energy reactions. Our results clarify the role of finite-range effects in (d,p) reaction. It is one of the many efforts in reducing the uncertainty in (d,p) studies. For example, the work in [148] evaluates the uncertainties in the optical potentials, [149] considers the effects of coupling to excited states of the target, ambiguities due to the single particle wave functions are studied in [116, 150], and recently new ways of calculating overlap functions are introduced by Timofeyuk and Barbieri [151, 152]. We looked at a different aspect of

the reaction theory, namely: the finite-range effect. We now have a better understanding of different sources of uncertainty in our theory for transfer reactions. Applying the finite-range adiabatic method to extract the ANC from $^{14}\text{C}(\text{d,p})^{15}\text{C}$ data, we obtain consistent results with other independent studies [100, 147].

We then use the finite-range adiabatic framework to test the performance of the dispersive optical model potentials and the corresponding overlap functions developed by the physicists from Washington University, St. Louis. In general, our work shows that DOM can be used in the study of (d,p) transfer reactions. It produces the angular distributions as well as the CH89 global optical potentials and the extracted spectroscopic factors have weaker energy dependence. An interesting feature of this method is that the asymmetry dependence of the potentials obtained can be used to extrapolate toward more exotic nuclei. The successful application of this feature to the case of ^{132}Sn indicates that DOM can provide a promising path to pin down optical potentials and therefore improves the uncertainty of (d,p) cross section .

BIBLIOGRAPHY

BIBLIOGRAPHY

- [1] E. E. Salpeter, *Astrophys. J.* **115**, 326 (1952).
- [2] D. D. Clayton, *Principles of stellar evolution and nucleosynthesis*, McGraw-Hill Book Company, United States of America, 1968.
- [3] J. Audouze and S. Vauclair, *An introduction to nuclear astrophysics*, D. Reidel Publishing Company, Netherlands, 1980.
- [4] F. Hoyle, *Astrophys. J. Suppl. Ser.* **1**, 121 (1954).
- [5] D. N. F. Dunbar, R. E. Pixley, W. A. Wenzel, and W. Whaling, *Phys. Rev.* **92**, 649 (1953).
- [6] C. W. Cook, W. A. Fowler, C. C. Lauritsen, and T. Lauritsen, *Phys. Rev.* **107**, 508 (1957).
- [7] S. M. Austin, *Nucl. Phys. A* **758**, 375c (2005).
- [8] G. R. Caughlan and W. A. Fowler, *At. Nucl. Data Tables* **40**, 238 (1988).
- [9] C. Iliadis, *Nuclear Physics of Stars*, Germany, 2007.
- [10] C. Angulo *et al.*, *Nucl. Phys. A* **656**, 3 (1999).
- [11] R. de Diego, E. Garrido, D. V. Fedorov, and A. S. Jensen, *Phys. Lett. B* **695**, 324 (2011).
- [12] M. Freer *et al.*, *Phys. Rev. C* **80**, 041303(R) (2009).
- [13] H. O. U. Fynbo *et al.*, *Nature* **433**, 136 (2005).

- [14] N. B. Nguyen, F. M. Nunes, I. J. Thompson, and E. F. Brown, PoS NIC XII, being published.
- [15] K. Ogata, M. Kan, and M. Kamimura, Prog. Theor. Phys. **122**, 1055 (2009).
- [16] N. Austern, Y. Iseri, M. Kamimura, G. Rawitscher, and M. Yahiro, Phys. Rep. **154**, 125 (1987).
- [17] M. Yahiro, N. Nakano, Y. Iseri, and M. Kamimura, Prog. Theo. Phys. **67**, 1464 (1982).
- [18] E. Hiyama, M. Kamimura, T. Motoba, T. Yamada, and Y. Yamamoto, Prog. Theor. Phys. **97**, 881 (1997).
- [19] E. Hiyama, Y. Kino, and M. Kamimura, Prog. Part. Nucl. Phys. **51**, 223 (2003).
- [20] V. Vasilevsky, A. V. Nesterov, F. Arickx, and J. Broeckhove, Phys. Rev. C **63**, 034606 (2001).
- [21] A. Dotter and B. Paxton, Astron. Astrophys. **507**, 1617 (2009).
- [22] T. Suda, R. Hirschi, and M. Fujimoto, Astrophys. J. **741**, 61 (2011).
- [23] M. Saruwatari and M. Hashimoto, Prog. Theor. Phys. **124**, 925 (2010).
- [24] Y. Matsuo *et al.*, Prog. Theor. Phys. **126**, 1177 (2011).
- [25] F. Peng, and C. D. Ott, Astrophys. J. **725**, 309 (2010).
- [26] R. Alvarez-Rodriguez, E. Garrido, A. S. Jensen, D. V. Fedorov, and H. O. U. Fynbo, Eur. Phys. J. A **31**, 303 (2007).
- [27] R. de Diego, E. Garrido, D. V. Fedorov, and A. S. Jensen, Eur. Phys. Lett. **90**, 52001 (2010).
- [28] E. Garrido, R. de Diego, D. V. Fedorov, and A. S. Jensen, Eur. Phys. J. A **47**, 102 (2011).
- [29] P. Maris, J. P. Vary, and A. M. Shirokov, Phys. Rev. C **79**, 014308 (2009).

- [30] S.C. Pieper, Nucl. Phys. A **751**, 516 (2005).
- [31] M. Chernykh, H. Feldmeier, T. Neff, P. von Neumann-Cosel, and A. Richter, Phys. Rev. Lett. **98**, 032501 (2007).
- [32] L. D. Faddeev, Zh. Eksp. Teor. Fiz. **39**, 1459 (1960); Sov. Phys. JETP **12**, 1014 (1961).
- [33] I. J. Thompson, F. M. Nunes, and B. V. Danilin, Comp. Phys. Comm. **161**, 87 (2004).
- [34] S. P. Merkuriev, Ann. Phys. **130**, 395 (1980).
- [35] A. Kievsky, M. Viviani, S. Rosati, Phys. Rev. C **56**, 2987 (1997).
- [36] A. Deltuva, A. C. Fonseca, P. U. Sauer, Phys. Rev. C **71**, 054005 (2005).
- [37] F. M. Nunes, J. A. Christley, I. J. Thompson, R. C. Johnson, and V. D. Efros, Nucl. Phys. A **609**, 43 (1996).
- [38] F. M. Nunes, *Core excitation in few-body systems: Application to light exotic nuclei*, PhD thesis, University of Surrey, England, 1995.
- [39] T. H. Gronwall, Phys. Rev. **51**, 655 (1937).
- [40] C. D. Lin, Phys. Rep. **257**, 1 (1995).
- [41] L. M. Delves, Nucl. Phys. **9**, 391 (1959).
- [42] L. M. Delves, Nucl. Phys. **20**, 268 (1962).
- [43] M. Zhukov, B. Danilin, D. Fedorov, J. Bang, I. Thompson, and J. Vaagen, Phys. Rep. **231**, 151 (1993).
- [44] T. Tarutina, I. Thompson, and J. Tostevin, Nucl. Phys. A **733**, 53 (2004).
- [45] P. Descouvemont, C. Daniel, and D. Baye, Phys. Rev. C **67**, 044309 (2003).
- [46] I. J. Thompson and F. M. Nunes, *Nuclear Reactions for Astrophysics*, Cambridge University Press, United Kingdom, 2009.

- [47] M. Abramowitz and I. A. Stegun, *Handbook of mathematical functions*, Dover Publications, 1972.
- [48] J. Raynal and J. Revai, *Nuovo Cimento A* **68**, 612 (1970).
- [49] S. P. Merkuriev, C. Gignoux and A. Laverne, *Ann. Phys. (NY)* **99**, 1 (1976).
- [50] S. P. Merkuriev, *Sov. J. Nucl. Phys.* **19**, 447 (1974).
- [51] D. M. Brink and G. R. Satchler, *Angular Momentum*, Oxford Science Publications, 1994.
- [52] B. V. Danilin and M. V. Zhukov, *Phys. At. Nucl.* **56**, 460 (1993).
- [53] E. P. Wigner, L. Eisenbud, *Phys. Rev.* **72**, 29 (1947).
- [54] A. M. Lane, R. G. Thomas, *Rev. Mod. Phys.* **30**, 257 (1958).
- [55] I. J. Thompson, B. V. Danilin, V. D. Efros, J. S. Vaagen, J. M. Bang and M. V. Zhukov, *Phys. Rev. C* **61**, 24318 (2000).
- [56] P. Descouvemont and D. Baye, *Rep. Prog. Phys.* **73**, 036301 (2010).
- [57] J. C. Light, R. B. Walker, *J. Chem. Phys.* **65**, 4272 (1976).
- [58] E. B. Stechel, R. B. Walker, J. C. Light, *J. Chem. Phys.* **69**, 3518 (1978).
- [59] B. I. Schneider, R. B. Walker, *J. Chem. Phys.* **70**, 2466 (1979).
- [60] I. J. Thompson, <http://www.ianthompson.org/computation.htm>, version **92**.
- [61] G. Erens, J. L. Visschers, and R. van Wageningen, *Ann. Phys.* **67**, 461 (1971).
- [62] W. A. Fowler, G. E. Caughlin, and B. A. Zimmerman, *Annu. Rev. Astron. Astrophys.* **5**, 525 (1967).
- [63] C. Forssén, N. B. Shul'gina, and M. V. Zhukov, *Phys. Rev. C* **67**, 045801 (2003).
- [64] S. Ali and A. R. Bodmer, *Nucl. Phys.* **80**, 99 (1966).

- [65] D. V. Fedorov, A. S. Jensen, Phys. Lett. B **389**, 631 (1996).
- [66] B. Buck, H. Friedrich and C. Wheatley, Nucl. Phys. A **275**, 246 (1977).
- [67] J. L. Friar, B. F. Gibson, and G. L. Payne, Phys. Rev. C **37**, 2869 (1988).
- [68] T. Y. Saito and I. R. Afnan, Phys. Rev. C **50**, 2756 (1994).
- [69] F. Ajzenberg-Selove and J. H. Kelley, Nucl. Phys. A **506**, 1 (1990).
- [70] G. S. Anagnostatos, Phys. Rev. C **51**, 152 (1995).
- [71] T. Neff and H. Feldmeier, Nucl. Phys. A **738**, 357 (2004).
- [72] E. Epelbaum, H. Krebs, D. Lee, and Ulf-G. Meissner, Phys. Rev. Lett. **106**, 192501 (2011).
- [73] V. Vasilevsky, F. Arickx, W. Vanroose, and J. Broeckhove, Phys. Rev. C **85**, 034318 (2012).
- [74] <http://mathworld.wolfram.com/CoulombWaveFunction.html>.
- [75] P. Descouvemont, J. Phys. G **37**, 064010 (2010).
- [76] M. Salaris, S. Cassisi, and A. Weiss, PASP, **114**, 375 (2002).
- [77] B. Paxton, L. Bildsten, A. Dotter, F. Herwig, P. Lesaffre, and F. Timmes, Astrophys. J. Suppl. Ser. **192**, 3 (2011).
- [78] <http://mesa.sourceforge.net/> (version 4442).
- [79] K. J. Shen and L. Bildsten, Astrophys. J. **699**, 1365 (2009).
- [80] K. Nomoto, Astrophys. J. **253**, 798 (1982).
- [81] H. Graboske *et al.*, Astrophys. J. **181**, 457 (1973).
- [82] L. Bildsten, K. J. Shen, Astrophys. J. **662**, L95 (2007).

- [83] D. Poznanski *et al.*, *Science*, **327**, 58 (2010)
- [84] M. M. Kasliwal *et al.*, *Astrophys. J. Lett*, **723**, L98 (2010)
- [85] C. J. Hansen and H. M. van Horn, *Astrophys. J.* **195**, 735 (1975).
- [86] L. Keek, J. J. M. In't Zand, *PoS INTEGRAL08*, 032 (2008).
- [87] L. Keek, private communication, 2012.
- [88] E. Kuulkers *et al.*, *A&A*, **514**, A65 (2010).
- [89] E. Epelbaum, H. Krebs, T. Lahde, D. Lee, and Ulf-G. Meissner, *arxiv:1208.1328v2*, 2012.
- [90] A. Spyrou *et al.*, *Phys. Rev. Lett* **108**, 102501 (2012).
- [91] I. A. Egorova *et al.*, *Phys. Rev. Lett* **109**, 202502 (2012).
- [92] Md. A. Khan, *Few-body Syst.* **52**, 53 (2012).
- [93] H. Niewodniczanski, J. Nurzynski, A. Strzalkowski and G. R. Satchler, *Phys. Rev.* **146**, 799 (1966).
- [94] W. W. Daehnick and Y.S. Park, *Phys. Rev.* **180**, 1062 (1969).
- [95] D. E. Bainum, R. W. Finlay, J. Rapaport, J. D. Carlson and W. G. Love, *Phys. Rev. C* **16**, 1377 (1977).
- [96] J. P. Schiffer *et al.*, *Phys. Rev. Lett* **92**, 162501 (2004).
- [97] K.L. Jones *et al.*, *Phys. Rev. C* **70**, 067602 (2004).
- [98] J. S. Thomas *et al.*, *Phys. Rev. C* **71**, 021302(R) (2005).
- [99] J. S. Thomas *et al.*, *Phys. Rev. C* **76**, 044302 (2007).
- [100] N. C. Summers and F. M. Nunes, *Phys. Rev. C* **78**, 011601(R) (2008).

- [101] R. L. Kozub *et al.*, Phys. Rev. Lett. **109**, 172501 (2012).
- [102] D. Y. Pang, F. M. Nunes, and A. M. Mukhamedzhanov, Phys. Rev. C **75**, 024601 (2007).
- [103] A. M. Mukhamedzhanov, F. M. Nunes, and P. Mohr, Phys. Rev. C **77**, 051601(R) (2008).
- [104] A. H. Wuosmaa *et al.*, Phys. Lett. **94**, 082502 (2005).
- [105] A. H. Wuosmaa *et al.*, Phys. Rev. C **72**, 061301 (2005).
- [106] H. B. Jeppesen *et al.*, Phys. Lett. B **642**, 449 (2006).
- [107] W. N. Catford *et al.*, J. Phys. G **31**, S1655 (2005).
- [108] N. Austern, *Direct Nuclear Reaction Theories*, John Wiley & Sons, New York, 1970.
- [109] G. R. Satchler, *Direct Nuclear Reactions*, Oxford University Press, Oxford, 1983.
- [110] N. K. Glendenning, *Direct Nuclear Reactions*, World Scientific Publishing, 2004.
- [111] P. G. Roos *et al.*, Nucl. Phys. A **225**, 187 (1975).
- [112] R. C. Johnson and P. J. R. Soper, Phys. Rev. C **1**, 976 (1970).
- [113] R. C. Johnson, AIP Conf. Conf. Procs. **79**, 128 (2005).
- [114] R. C. Johnson and P. C. Tandy, Nucl. Phys. A **235**, 56 (1974).
- [115] P. J. A. Buttle and L. J. B. Goldfarb, Proc. Phys. Soc. **83**, 701 (1964).
- [116] A. M. Mukhamedzhanov and F. M. Nunes, Phys. Rev. C **72**, 017602 (2005).
- [117] A. Laid, J. A. Tostevin, and R. C. Johnson, Phys. Rev. C **48**, 1307 (1993).
- [118] N. B. Nguyen, F. M. Nunes, and R. C. Johnson, Phys. Rev. C **82**, 014611 (2010).
- [119] V. Reid, Ann. Phys. (N.Y.) **50**, 411 (1968).

- [120] R. L. Varner *et al.*, Phys. Rep. **201**, 57 (1991).
- [121] M. Igarashi *et al.*, computer program TWOFNR, University of Surrey version, 2008.
- [122] I. J. Thompson, Comput. Phys. Rep. **7**, 167 (1988).
- [123] G. L. Wales and R. C. Johnson, Nucl. Phys. A **274**, 168 (1976).
- [124] J. Rapaport, A. Sperduto, and M. Salomaa, Nucl. Phys. A **197**, 337 (1972).
- [125] G. M. Crawley, B. V. N. Rao, and D. L. Powell, Nucl. Phys. A **112**, 223(1968).
- [126] K. Haravu, C. L. Hollas, P. J. Riley, and W. R. Coker, Phys. Rev. C **1**, 938 (1970).
- [127] D. G. Kovar, N. Stein, and C. K. Bockelman, Nucl. Phys. A **231**, 266 (1974).
- [128] K. Hatanaka *et al.*, Nucl. Phys. A **419**, 530 (1984).
- [129] Y. Uozumi *et al.*, Nucl. Phys. A **576**, 123 (1994).
- [130] J. Liu, N.B. Nguyen, and F.M. Nunes, internal report, NSCL/MSU August 2012.
- [131] F. M. Nunes, J. Liu, N. B. Nguyen, L. Titus, and N. J. Upadhyay, *Proceedings of 13th International Conference on Nuclear Reaction Mechanism*, Varenna, June (2012)
- [132] R. J. Charity, L. G. Sobotka, and W. H. Dickhoff, Phys. Rev. Lett. **97**, 162503 (2006).
- [133] R. J. Charity, J. M. Mueller, L. G. Sobotka, and W. H. Dickhoff, Phys. Rev. C **76**, 044314 (2007).
- [134] J. M. Mueller *et al.*, Phys. Rev. C **83**, 064605 (2011).
- [135] N. B. Nguyen, S. J. Waldecker, F. M. Nunes, R. J. Charity, and W. H. Dickhoff, Phys. Rev. C **84**, 044611 (2011).
- [136] F. J. Eckle *et al.*, Nucl. Phys. A **506**, 159 (1990).
- [137] K. Hatanaka *et al.*, Nucl. Phys. A **419**, 530 (1984).

- [138] W. D. Metz et. al, Phys. Rev. C **12**, 827 (1975).
- [139] W. D. Metz et. al, Phys. Rev. C **12**, 827 (1975).
- [140] K. Jones et al., Nature **465**, 454 (2010).
- [141] L. Lapikás, Nucl. Phys. A **553**, 297c (1993).
- [142] J.M. Lohr and W. Haeberli, Nucl. Phys. A **232**, 381 (1974).
- [143] N. J. Upadhyay, A. Deltuva, and F. M. Nunes, Phys. Rev. C **85**, 054621 (2012).
- [144] A. M. Mukhamedzhanov, V. Burjan, M. Gulino, Z. Hons, V. Kroha, M. McCleskey, J. Mrazek, N. Nguyen, F. M. Nunes, S. Piskor, S. Romano, M. L. Sergi, C. Spitaleri, and R. E. Tribble, Phys. Rev. C **84**, 024616 (2011).
- [145] R. L. Varner *et al.*, Phys. Rep. **201**, 57 (1991).
- [146] A. J. Koning, J. P. Delaroche, Nucl. Phys. A **713**, 231(2003).
- [147] R. Reifarth *et al.*, Phys. Rev. C **77**, 015804 (2008).
- [148] X. D. Liu, M. A. Famiano, W. G. Lynch, M. B. Tsang, and J. A. Tostevin, Phys. Rev. C **69**, 064313 (2004).
- [149] F. Delaunay, F. M. Nunes, W. G. Lynch, and M. B. Tsang, Phys. Rev. C **72**, 014610 (2005).
- [150] D. Y. Pang, F. M. Nunes, and A. M. Mukhamedzhanov, Phys. Rev. C **75**, 024601 (2007).
- [151] N. K. Timofeyuk, Phys. Rev. Lett. **103**, 242501 (2009).
- [152] C. Barbieri, Phys. Rev. Lett. **103**, 202502 (2009).